

# **Rheology of Arrested Colloids: A parameter study using novel experimental methods**

Dissertation  
zur Erlangung des Grades  
**Doktor rerum naturalium**  
(Dr. rer. nat.)

vorgelegt dem  
Fachbereich Physik, Mathematik und Informatik der



JOHANNES GUTENBERG  
UNIVERSITÄT MAINZ

von

**Marcel Roth**  
geb. in Limburg/Lahn

Mainz, 2011

Dekan:

1. Gutachter:

2. Gutachter:

3. Gutachter:

4. Gutachter:

5. Gutachter:

Tag der Promotion: 14.12.2011

# Table of Contents

|   |           |
|---|-----------|
| <b>1. Introduction and Motivation</b>   | <b>1</b>  |
| 1.1. Basic concepts and terminology . . . . .   | 2         |
| 1.1.1. Diffusion and sedimentation . . . . .  | 2         |
| 1.1.2. Particle interactions and equilibrium phase behavior . . . . .                             | 4         |
| 1.1.3. Arrested states: Aggregation, gelation and crowding . . . . .                              | 7         |
| 1.2. Rheology of the dispersed state . . . . .  | 9         |
| 1.2.1. Constitutive relations . . . . .   | 9         |
| 1.2.2. Viscosity modification . . . . .   | 11        |
| 1.2.3. Non-linearity and visco-elasticity . . . . .   | 12        |
| 1.3. Aggregated colloids in the arrested state . . . . .  | 15        |
| 1.3.1. Glass transition and mode-coupling theory . . . . .  | 15        |
| 1.3.2. Attractive glass and gelation . . . . .  | 19        |
| 1.3.3. Exploring Parameters: interaction mechanisms, structure, and particle properties . . . . . | 22        |
| 1.4. Current challenges and objectives of the present work . . . . .                              | 24        |
| 1.4.1. Diversity of colloidal dispersions . . . . .   | 24        |
| 1.4.2. Unified theories and alternative approaches . . . . .                                      | 25        |
| 1.4.3. Development of experimental techniques . . . . .   | 26        |
| <b>2. Experimental methods</b>  | <b>27</b> |
| 2.1. Laser scanning confocal fluorescence microscope . . . . .                                    | 27        |
| 2.1.1. General working principle . . . . .  | 27        |
| 2.1.2. Characteristics of the home-made setup . . . . .   | 29        |
| 2.1.3. Localization of particles . . . . .  | 32        |
| 2.1.4. Tracking of particles . . . . .  | 35        |
| 2.2. Rheometry . . . . .  | 35        |
| 2.2.1. Piezo-Rheometer . . . . .  | 37        |
| 2.2.2. Nanoindentation . . . . .  | 42        |
| 2.3. Other methods . . . . .  | 47        |
| 2.3.1. Dielectric spectroscopy . . . . .  | 47        |
| 2.3.2. Differential scanning calorimetry . . . . .  | 50        |
| 2.3.3. Dynamical light scattering of diluted colloidal suspensions . . . . .                      | 50        |
| 2.3.4. Scanning electron microscope . . . . .   | 51        |
| 2.3.5. Polarization optical microscopy . . . . .  | 52        |

|  |           |
|--|-----------|
| <b>3. Liquid crystal based colloidal suspensions</b>   | <b>55</b> |
| 3.1. Solvent mediated mechanisms of particle aggregation . . . . .                               | 55        |
| 3.1.1. Particles in binary mixtures of liquids . . . . .   | 56        |
| 3.1.2. Particle interactions in liquid crystals . . . . .  | 58        |
| 3.2. Previous Works . . . . .  | 61        |
| 3.2.1. Theoretical modeling and phase diagram . . . . .  | 62        |
| 3.2.2. Phase separation process . . . . .  | 64        |
| 3.2.3. Rheological properties . . . . .  | 64        |
| 3.2.4. Testing of the model and open problems . . . . .  | 67        |
| 3.3. Preparation techniques . . . . .  | 70        |
| 3.4. Phase separation: From a fluid suspension to an arrested state . . . . .                    | 71        |
| 3.4.1. Correlation of the structural and mechanical evolution . . . . .                          | 71        |
| 3.4.2. Relaxation time spectrum . . . . .  | 73        |
| 3.4.3. Dependency on cooling rate . . . . .  | 74        |
| 3.5. Rheology at intermediate temperatures: Relation between frequency and temperature . . . . . | 76        |
| 3.5.1. Time-temperature-superposition and master curve . . . . .                                 | 76        |
| 3.5.2. Reversibility and aging phenomena . . . . .   | 77        |
| 3.6. Rheology at low temperatures: Parameter study and morphology . . . . .                      | 79        |
| 3.6.1. Dependency on colloid parameters . . . . .  | 79        |
| 3.6.2. Dependency on network morphology . . . . .  | 80        |
| 3.7. Swelling and dissolution: Influence of sample age . . . . .                                 | 81        |
| 3.7.1. Dynamics light scattering study . . . . .   | 82        |
| 3.7.2. Effect on the network properties . . . . .  | 84        |
| 3.8. A detailed look on the network composition . . . . .  | 86        |
| 3.8.1. Extension of the previous model . . . . .   | 86        |
| 3.8.2. Network rheology revised . . . . .  | 87        |
| 3.8.3. Evidences for polymer dynamics . . . . .  | 88        |
| 3.8.4. Thermodynamic equilibrium . . . . .   | 89        |
| 3.9. Conclusions and Outlook . . . . .   | 90        |
| 3.9.1. Mechanical properties of aggregated soft colloids . . . . .                               | 90        |
| 3.9.2. Benefits of piezo-rheometry and simultaneous confocal microscopy . . . . .                | 91        |
| 3.9.3. Future prospects . . . . .  | 92        |
| <b>4. Polymer dispersed liquid crystals</b>  | <b>93</b> |
| 4.1. Introduction . . . . .  | 94        |
| 4.2. Sample preparation and general characterization . . . . .                                   | 95        |
| 4.2.1. Preparation methods . . . . .   | 95        |
| 4.2.2. Phase behavior . . . . .  | 96        |
| 4.3. Rheological properties . . . . .  | 101       |
| 4.3.1. Time-concentration-superposition in the isotropic phase . . . . .                         | 101       |

|           |  |            |
|-----------|--|------------|
| 4.3.2.    | Superposition behavior during phase separation . . . . .                             | 105        |
| 4.3.3.    | Concentration gauging . . . . .  | 106        |
| 4.4.      | A complementary approach: Dielectric spectroscopy . . . . .                          | 107        |
| 4.4.1.    | General measurement idea . . . . .   | 107        |
| 4.4.2.    | Rotation relaxation spectrum . . . . .   | 108        |
| 4.4.3.    | Restricted motion of 5CB in the PMMA matrix . . . . .                                | 111        |
| 4.5.      | Conclusions and Outlook . . . . .  | 112        |
| 4.5.1.    | Generality of time-concentration-superposition . . . . .                             | 113        |
| 4.5.2.    | Comparison with colloidal-LC composites . . . . .                                    | 114        |
| <b>5.</b> | <b>Nanoindentation of aggregated particles</b>                                       | <b>115</b> |
| 5.1.      | Industrial motivation . . . . .  | 116        |
| 5.2.      | Materials and methods . . . . .  | 117        |
| 5.2.1.    | Sample Preparation . . . . .   | 117        |
| 5.2.2.    | Structural characterization . . . . .  | 119        |
| 5.2.3.    | Indentation modes . . . . .  | 122        |
| 5.3.      | Microscopic deformation analysis . . . . .   | 123        |
| 5.3.1.    | Displacement and strain field of the amorphous structure . . . . .                   | 126        |
| 5.3.2.    | Comparison to continuum models . . . . .   | 128        |
| 5.3.3.    | Microscopic processes . . . . .  | 131        |
| 5.3.4.    | Heterogeneities in semi-crystalline structures . . . . .                             | 132        |
| 5.4.      | Macroscopic material properties . . . . .  | 135        |
| 5.4.1.    | Deformation works and elastic recovery . . . . .                                     | 135        |
| 5.4.2.    | Hardness and effective elastic modulus . . . . .                                     | 137        |
| 5.4.3.    | Correlation of microscopic deformation and macroscopic material properties . . . . . | 139        |
| 5.4.4.    | Universality . . . . .   | 141        |
| 5.5.      | Conclusions and Outlook . . . . .  | 141        |
| 5.5.1.    | Nanoindentation as a mechanical test method for colloidal aggregates . . . . .       | 141        |
| 5.5.2.    | Further insight into microscopic processes . . . . .                                 | 143        |
| <b>6.</b> | <b>Deformation and rotation of single particles</b>                                  | <b>145</b> |
| 6.1.      | Deformation analysis of hollow spheres . . . . .                                     | 147        |
| 6.1.1.    | Sample preparation . . . . .   | 147        |
| 6.1.2.    | Localization of hollow particles . . . . .   | 147        |
| 6.1.3.    | Main axes of deformation . . . . .   | 149        |
| 6.1.4.    | Particle extensions along principal directions . . . . .                             | 151        |
| 6.1.5.    | Sample data set . . . . .  | 152        |
| 6.1.6.    | General remarks . . . . .  | 153        |
| 6.2.      | Rotation analysis . . . . .  | 154        |
| 6.2.1.    | Sample preparation . . . . .   | 155        |

---

|  |             |
|--|-------------|
| 6.2.2. Preparation of orientation anisotropic particles via selective bleaching<br>and theoretical polarization contrast . . . . . | 155         |
| 6.2.3. Experimental verification . . . . .   | 157         |
| 6.2.4. General remarks . . . . .   | 159         |
| 6.3. Conclusions . . . . .   | 159         |
| <b>7. Summary and final conclusions</b>  | <b>161</b>  |
| <b>Appendix</b>  | <b>I</b>    |
| A. Hardware architecture and Labview interface . . . . .   | I           |
| B. Rheology of polymer solutions and melts . . . . .   | VI          |
| C. Particle description . . . . .  | IX          |
| C.1. Silica core-shell particles . . . . .   | IX          |
| C.2. PMMA particles . . . . .  | IX          |
| C.3. PS-silica core-shell particles . . . . .  | IX          |
| D. Stress distribution for the indentation of a sphere in an elastic half-space . . . . .  | X           |
| <b>Bibliography</b>  | <b>XIII</b> |

# 1. Introduction and Motivation

Colloidal dispersions or for short colloids<sup>1</sup> are a special class of dispersions where the dispersed phase consists of particulate elements with sizes ranging from 10 nm to 10  $\mu\text{m}$ . Depending on the phase of matter of the dispersed and solute phase one distinguishes different types of colloids summarized in Tab. 1.1.

|              |        | dispersed phase                      |  |  |
|--------------|--------|--------------------------------------|--|--|
|              |        | gas                                  | liquid   | solid                                    |
| solute phase | gas    | not existent                         | liquid aerosol<br><i>fog, mist, clouds</i>       | solid aerosol<br><i>smoke, fine dust</i> |
|              | liquid | foam<br><i>whipped cream</i>         | emulsion<br><i>milk, mayonnaise, hand cream</i>  | sol<br><i>ink, paint, blood</i>          |
|              | solid  | solid foam<br><i>styrofoam, wood</i> | solid emulsion<br><i>gelly, swollen hydrogel</i> | solid sol<br><i>Ruby glass, alloys</i>   |

**Tab. 1.1.:** Classification of colloids with examples.

The pioneering works on colloids by Thomas Graham in the 1860s also involved polymer solutions, *i. e.* dispersions of single nanometer-sized macromolecules. However, with increasing scientific understanding and technological importance this research field soon split off. What remained was the name as the word ‘colloid’ originates from the Greek word  $\kappa\omicron\lambda\lambda\alpha$  (‘glue’) and refers to the glue-like behavior of the polymer solutions. Though, extraordinary mechanical properties are also typical for the materials listed in Tab. 1.1. Despite of a liquid solute phase foams behave elastically as they can sustain shear stresses while the response of emulsions and sols often depends on the type and rate of mechanical excitation. Mayonnaise withstands its own weight and thus retains its shape to a certain degree but yields when only small stresses are applied. In this sense they do not behave purely elastically or liquid-like but rather visco-elastically. These and other effects are well known from daily life in form of food and cosmetic products and have been heavily exploited by industry to tune the mechanical behavior of many products like *e. g.* paints and inks.

<sup>1</sup>Although there are other conventions we strictly distinguish between colloids, *i. e.* the colloidal dispersions, and the particles that are dispersed in the colloid.

The main objective of this work is to elucidate some aspects of these extraordinary mechanical properties for model colloidal sols in the arrested state. We lay special emphasis on the usage of novel combinations of experimental techniques for mechanical and structural characterization as well as intuitive and simple models to explain the dominant phenomena in these systems. As we proceed we give a brief overview on some basic concepts of colloids in general as well as their mechanical properties whereas we focus on sols. If not declared explicitly we refer to references [Hun07] and [Mac94].

## 1.1. Basic concepts and terminology

The size of the dispersed particles has a large impact on the physical description of colloids. Being of intermediate size between single molecules and macroscopic bodies a suitable model can be based on a microscopic picture of the single particles whose dynamics is determined from Newton's equations of motion. On the other side, the large number of dispersed particles in a sample also allows for a macroscopic thermodynamic description. Which approach is more suitable depends on the question that needs to be answered. Microscopic theories tend to have problems to describe average properties of colloids while in case of macroscopic theories the particulate nature of the dispersed phase might be neglected. Therefore, a combination of microscopic and macroscopic elements often is advantageous if not mandatory for a sound description of the colloid.

### 1.1.1. Diffusion and sedimentation

The importance and practicability of such an combined model already becomes apparent when discussing the question of the stability of a colloid. Considering the density difference between dispersed and solute phases it would be the inevitable fate of the particles to segregate from the solvent due to gravity. Either the particles are more dense than the solute phase and sediment to the bottom of the containing beaker or in the opposite case float to the top and thus minimize the total energy of the system.

In the microscopic picture a single dispersed particle is subject to number of forces. Beside to external forces  $\vec{F}_{\text{ext}}$  such as gravity the particle experiences a viscous drag force  $\vec{F}_{\text{drag}} = -b\vec{v}$  as it moves through the solvent at the velocity  $\vec{v}$ . A third fluctuating contribution  $\vec{\Omega}(t)$  arises from the momentum transfer in numerous collisions of the particles with the solvent molecules. These collisions are spatially uncorrelated and happen on a very short timescale which is why the average force  $\langle \vec{\Omega}(t) \rangle_t$  vanishes and the values of  $\vec{\Omega}(t)$  at different times  $t_1$  and  $t_2$  are uncorrelated:  $\langle \vec{\Omega}(t_1) \cdot \vec{\Omega}(t_2) \rangle_t = 2\Omega_0^2 \delta(t_1 - t_2)$ .<sup>3</sup> The resulting Newtonian equation of motion

<sup>2</sup> $\langle a \rangle_t$  denotes the temporal average of the quantity  $a$ :  $1/T \int_0^T a(t) dt$

<sup>3</sup>The collision frequency for a micrometer-sized particle in water is in the order of  $10^{12}$  Hz. It is reasonable to assume that any correlation is lost after about  $10^4$  collisions, equivalent to  $\tau = t_2 - t_1 = 10^{-8}$  s. This timescale is at the lower temporal resolution limit of any microscopic or scattering measurement technique.



for a particle with a mass  $m_p$

$$m_p \frac{d\vec{v}}{dt} = -b\vec{v} + \vec{F}_{\text{ext}} + \vec{\Omega}(t) \quad (1.1)$$

is also known as the Langevin equation. Its solution describes the motion of an accelerated particle in the presence of friction superimposed by a fluctuating Brownian motion that depends on the temporal evolution of  $\vec{\Omega}$ . The random nature of the fluctuations makes it impossible to derive a general, explicit expression for the velocity. However, when neglecting the external forces  $\vec{F}_{\text{ext}}$  for a moment, the time averages of  $\vec{v}$  and  $\vec{r}$  over a sufficiently large time interval  $\Delta t \gg \tau^2$  can be calculated:

$$\langle \vec{v} \rangle_t = 0 \quad \text{and} \quad \langle \vec{r} \rangle_t = \vec{r}_o \quad (1.2)$$

Here  $\vec{r}_o$  denotes the initial position of the particle. So, on average the particle stays at rest but it still undergoes a certain motion characterized by the time average of the squared quantities

$$\langle v^2 \rangle_t = \frac{3\Omega_o}{m b} \quad \text{and} \quad \langle (\vec{r} - \vec{r}_o)^2 \rangle_t = \frac{6\Omega_o}{b^2} t \quad (1.3)$$

As a matter of fact the temporal dependencies are identical to a diffusive motion like *e.g.* that of molecules in a gas. Following this analogy to the kinetic theory of gases the dispersed particle in thermal equilibrium with its environment has an average kinetic energy  $\langle E_{\text{kin}} \rangle_t$  that is related to its thermal energy according to the equipartition theorem:

$$\langle E_{\text{kin}} \rangle_t = \frac{m_p}{2} \langle v^2 \rangle_t = \frac{3}{2} k_B T \quad (1.4)$$

The corresponding diffusional constant  $D$  for a spherical particle is given by:

$$D = \frac{k_B T}{6 \pi \eta R_p} \quad (1.5)$$

with the viscosity  $\eta$  of the solvent and  $R_p$  the radius of the particle. The friction coefficient was replaced by  $b = 6 \pi \eta R_p$  for spherical particle according to Stokes. If otherwise the fluctuating motion was absent the particle would be accelerated to a maximal velocity that is given by the density difference  $\Delta\rho$  of particle and solvent:

$$\vec{v}_d = \frac{2}{9} \frac{R_p^2 \Delta\rho}{\eta} \vec{g} \quad (1.6)$$

with  $\vec{g}$  denoting the acceleration due to gravity.

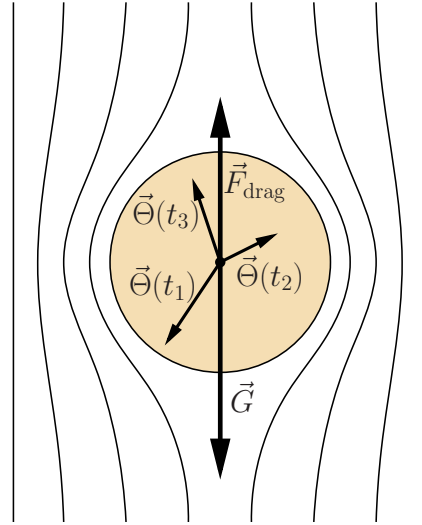


**Fig. 1.1.:** Force balance of a particle in the gravity field. The solid lines indicate the streamlines in the vicinity of the particle as it moves through the solvent.

With this knowledge the initial question of stability of colloids can be answered as follows. The undirected Brownian motion of the particles counteracts the sedimentation in the gravitation field. Hence, segregation of the dispersed particles can be prevented if the homogenization of the colloid due to Brownian motion is faster than sedimentation. The relative strength of both processes is mapped by the so called gravitation length combining equations (1.3), (1.5) and (1.6):

$$l_g = \frac{3 k_B T}{2 \pi R_p^3 \Delta \rho g} \quad (1.7)$$

The larger  $l_g$  is the more the Brownian motion dominates over sedimentation. It can be interpreted as the maximal height of the colloid in a containing beaker before sedimentation destabilizes the colloid. As can be seen from Tab. 1.2

particles in the range of 10 nanometer virtually do not sediment for typical laboratory time scales, the colloid is kinetically stabilized. On the contrary, colloids based on particles in the micrometer range always destabilize if not other mechanisms prevent sedimentation.

In summary, already the description of particle diffusion, probably the most fundamental process in a colloid, largely benefits from the combination of a deterministic microscopic model and thermodynamic principles. We want to stress the fact, that the linkage of both approaches occurs on multiple length scales. At the length scale of the individual particles the Brownian motion was related to the uncorrelated collisions of individual solvent molecules with the particles while the solvent was considered as a continuum when quantifying the viscous drag force. At a larger length scale the stabilization of colloid was argued in terms of a single particle that represents the other dispersed particles. This argument is essentially based on the assumption that the colloid is ergodic, *i. e.* statistical quantities like *e. g.* the average particle distribution in the colloid can be obtained by averaging either over the temporal evolution of a single particle or over a large ensemble of particles at a given time. Curiously enough, it is just the Brownian motion that maintains ergodicity in colloids with small dispersed particles.

### 1.1.2. Particle interactions and equilibrium phase behavior

A single particle picture obviously does not consider any particle interactions. Yet, these interactions play an important role as their balance also decides on the stability and phase behavior of the colloid. In the simplest case the particles behave like hard spheres that interact with each other solely via excluded volume and possibly hydrodynamic forces mediated by the solvent. That means that the particles are assumed to be non-deformable and therefore cannot approach closer to each other than the particle diameter  $D_p = 2 R_p$ . In reality, however, van der Waals forces cause an additional short-ranged attraction and the hard sphere case can only be realized by suitable particles surface properties that counteract this attraction.

The van der Waals forces result from electromagnetic dipole-dipole interactions between the molecules of two close-by particles and show a pronounced distance characteristics. The

| $R_p$     | diffusion<br>time over $R_p$ | $l_g$       |
|-----------|------------------------------|-------------|
| 10 nm     | 1 $\mu$ s                    | 0.2 m       |
| 100 nm    | 1 ms                         | 200 $\mu$ m |
| 1 $\mu$ m | 1 s                          | 200 nm      |

**Tab. 1.2.:** Gravitation lengths for silica particles of different sizes in water at room temperature.

underlying potential  $V_{\text{vdW}}$  for the two extreme cases of small and large distances of the particle surfaces  $D$  is approximately given by

$$V_{\text{vdW}}(D) = \begin{cases} -\frac{A_H R_p}{12 D} & \text{for } D \ll D_p \\ -\frac{16 A_H}{9} \frac{R_p^6}{D^6} & \text{for } D \gg D_p \end{cases} \quad (1.8)$$

The Hamaker constant  $A_H$  comprises the material properties of particles and solvent. The van der Waals forces get increasingly strong as the particles approach each other causing a permanent adhesion of the particles. Consequently, the particles will assemble into clusters that sediment as they are too large to be kinetically stabilized.

The destabilization of the colloid can only be prevented if counteracting repulsive interactions limit the approach of the particles. One possibility is the electrostatic repulsion of surface charges that are generated by dissociation of molecules at the particle surface. An exact determination of this repulsion force is rather complicated and must consider the formation of an electric double layer of oppositely charged mobile ions in the solvent. In the framework of the DLVO-theory (named after Derjaguin, Landau, Verwey and Overbeek) the electrostatic contribution  $V_{\text{el}}$  to the total interaction potential can be described by a screened Coulomb potential:

$$V_{\text{el}}(D) = \frac{Z^2 e^2}{4 \pi \epsilon_o \epsilon k_B T (1 + \kappa R_p)} \frac{\exp(-\kappa D)}{D_p + D} \quad (1.9)$$

with the particle surface charge  $Z$ . The Debye-Hückel length  $\kappa^{-1}$  is a measure of the range of repulsion and can be reduced by increasing the concentration of mobile ions. The difference in the distance dependencies of  $V_{\text{vdW}}$  and  $V_{\text{el}}$  leads to the formation of a potential barrier  $V_{\text{bar}}$  at intermediate distances (Fig. 1.2). The probability  $p$  of two particles to surpass this barrier and get into contact depends on the kinetic energy of the particles  $p \propto \exp[-V_{\text{bar}}/(k_B T)]$ . Hence, a sufficiently high barrier prolongs the destabilization time over experimental timescales. Large values for  $\kappa$  usually worsen the stabilizing effect. In addition a secondary minimum can appear

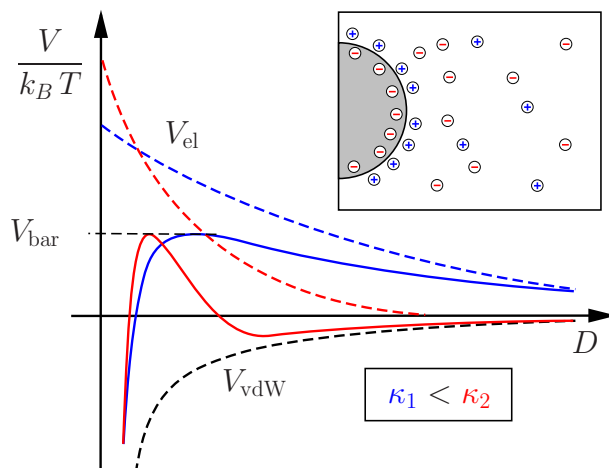


**Fig. 1.2.:** In charged colloids the stabilization results from the balance of the attractive van der Waals and the repulsive electrostatic potential that generates a potential energy barrier  $V_{\text{bar}}$ . For large values of  $\kappa$  a secondary minimum appears. The electric double layer around the charged particle is shown schematically in the inset.

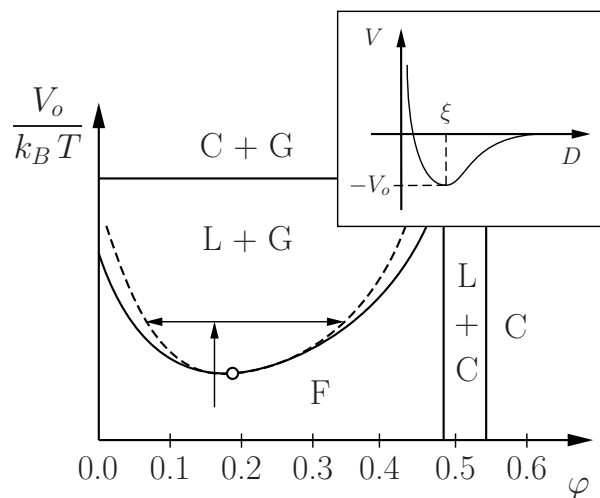


**Fig. 1.3.:** Inset: Combining all contributions the effective inter-particle potential in attractive colloids might be parametrized by the range  $\xi$  and strength  $V_o$  of the potential minimum. Main graph: For medium values of  $\xi \approx (0.3 - 0.5) R_p$  the corresponding schematic equilibrium phase diagram comprises a homogeneous fluid (F) and crystalline phase (C) as well as coexistence regions with sparsely occupied gaseous (G) and dense liquid phases (L). The phase boundary is characterized by the binodal (solid) and spinodal (dashed) lines and the critical point where both lines intersect. After reference [Aar02]

at larger distances that can also give rise to destabilization.

In apolar solvents dissociation is suppressed and the surface charge is too small to prevent destabilization of the colloid. Instead, steric stabilization methods are applied. The particles are covered with polymer chains either via chemical adsorption or covalent bonds. In good solvent conditions these polymers give rise to a strong repulsive force if two particles approach too close to each other and compress the polymer layer. Compared to the electrostatic potential the steric interaction is short-ranged as it extends only over the thickness of the polymer layer that is in the order of (2 – 20) nm.

The addition of soluble polymer to the colloidal dispersion can also cause an attractive interaction if the polymer chains are not absorbed on the particle surface but interact with particles via collisions. On average these collisions leave the particles at rest but if two particles approach close to each other there is a region between the particles that is devoid of polymer chains. The resulting momentum balance pushes the particles together and thus can be interpreted as an effective attractive force [Asa58, Vri76]. The strength  $V_o$  (parametrized like in the electrostatic case by the depth  $V_o$  of the potential minimum) and range  $\xi$  of this force scales with the concentration and size of the polymers, respectively.

The equilibrium phase behavior of colloids is determined from thermodynamic principles. The dispersed particles are treated as a canonical ensemble that interact via an effective interaction potential that combines all contributions from above. Using the particle volume fraction  $\varphi$  and the interaction strength  $V_o$  as control parameters the schematic phase diagram for a medium-ranged potential is shown in Fig. 1.3. At vanishing interaction strengths, *i. e.* in case of hard spheres, the colloid undergoes a continuous transition from a homogeneously dispersed fluid (F) to a crystalline solid as the particle volume fraction is increased from 0.494 to 0.536. This transition is driven purely by the entropic contribution to the total free energy of the system. At low volume fractions the phase space of particle positions and velocities is fully exploited as the particles are able to move freely in the solvent. The entropy of the system is maximal. With increasing particle content, however, Brownian motion of the individual

particles is restricted by the presence of the other particles and less phase space is accessible. This loss in entropy can only be regained if the particles transition to a more ordered crystalline arrangement (C) that allows for a closer packing and thus effectively increases the mobility of the particles.

At lower volume fractions and non-zero values for  $V_o$  the colloid remains in the single fluid phase (F) until it is energetically more favorable to undergo a phase separation into a sparsely populated gaseous phase (G) and a dense liquid phase (L). In the liquid phase the average distance of neighboring particles is given by the location of the potential minimum in the inset of Fig. 1.3. Depending on the initial volume fraction and the dynamical properties of the colloid the kinetics of the phase separation may be described by a nucleation-and-growth principle or spinodal decomposition. At even higher interaction strengths or lower temperatures this energy gain can even be further increased by maximizing the number of neighboring particles in the dense phase towards a closed packed crystalline conformation (G+C).

Despite the differences in energy and length scales this phase behavior of colloids very much resembles that of atomic systems. Because of that and the possibility to tune the parameters of the underlying inter-particle potentials, colloids have been widely used as model systems for atomic matter. Moreover, the larger size of colloids allow for a real-space characterization with light microscopy techniques and reduced diffusion constants slow down the phase transition dynamics to experimentally accessible time scales.

### 1.1.3. Arrested states: Aggregation, gelation and crowding

The phase diagram in Fig. 1.3 displays the phase behavior of colloids only from an energetic point of view. Hence, no detailed information about the structural and dynamic properties are available. This concerns in particular phase transition and separation processes as well as colloids with large volume fraction and interaction strengths. A microscopic approach might start from the competing influences of Brownian motion and aggregation as the fundamental processes. The term aggregation is only vaguely defined. In the present work we use a rather broad definition and refer to aggregation as any process that leads to the assembly of particles, the aggregate, bound together by attractive interactions. The ratio of attractive strength  $V_o$  and thermal energy  $k_B T$  decides on the properties of these bonds. They can be permanent on experimental timescales like for strong van der Waals adhesion ( $V_o/k_B T \ll 1$ ) or of transient nature ( $V_o/k_B T \lesssim 1$ ) if the particles are able to separate again after a characteristic bond lifetime  $\tau_B$ .

In this picture the fluid phase might be divided into different subclasses (Fig. 1.4). At low volume fractions the particles form transient aggregates ( $\alpha$ ) that dissolve again in dependence on  $\tau_B$ . With increasing volume fraction and interaction strengths the size of the aggregates rises until a large transient aggregate spans the whole system. As we will discuss below this transient percolation network ( $\beta$ ) shows remarkable mechanical features including a certain degree of elasticity. Still at long times exceeding  $\tau_B$  the sample behaves as a fluid. Though, at some point  $\tau_B$  becomes larger than the experimental observation time, according to standard conventions

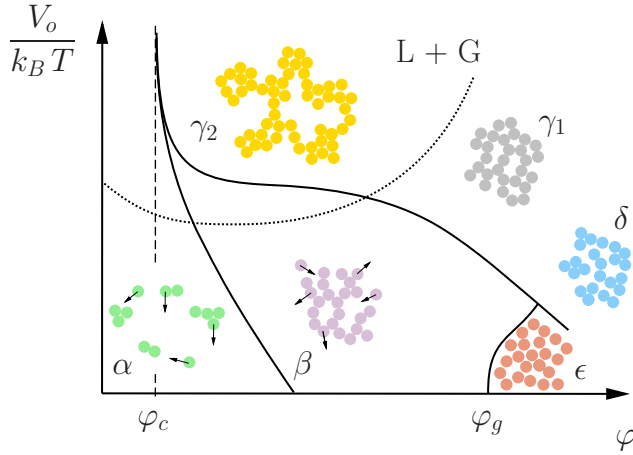


**Fig. 1.4.:** Transient and arrested states in attractive colloids: Transient separated aggregates ( $\alpha$ ), transient percolated network ( $\beta$ ), equilibrium gel ( $\gamma_1$ ), non-equilibrium gel ( $\gamma_2$ ), attractive glass ( $\delta$ ) and repulsive glass ( $\epsilon$ ). The binodal (dotted line) separating the fluid phase from the gas-liquid coexisting region is also shown (compare Fig. 1.3). The crystalline phase is not considered here.

at  $\tau = 100$  s, and the colloid passes the gelation boundary. The colloid gets kinetically arrested in its equilibrium gel state ( $\gamma_1$ ) as particle reorganizations are hindered by large energy barriers. The occurrence of the gel is accompanied by a loss of ergodicity rendering this state different from the ergodic fluid phase at the same volume fraction and interaction strength. This seeming discrepancy is purely based on the dynamic nature of the colloid and the occurrence of spatial fluctuations in the particle density that are not considered in the equilibrium thermodynamics.

At higher interaction strength the gelation boundary interferes with the liquid-gas phase separation. The kinetic pathways towards gelation in this regime is unclear and under current scientific debate. Several experiments indicate that initially spinodal decomposition leads to a microscopic phase separation into particle-rich liquid-like aggregates and particle-poor regions [Man05]. As these domains coarsen towards a macroscopic phase separation the aggregates get kinetically arrested which prevents any further phase separation. Compared to the equilibrium gel this non-equilibrium gel ( $\gamma_2$ ) has a very heterogeneous structure.

At very small volume fractions and high interaction strength the gelation and percolation boundary coincide and gel formation is described by diffusion limited cluster aggregation (DLCA). The attractive forces are so strong that as soon as two particles approach close enough to each other in course of their Brownian motion a permanent bond is formed. The particles aggregate into clusters which grow with time. If the particle volume fraction exceeds a critical value  $\varphi_c$  the clusters themselves aggregate into a system spanning fractal network. The number of particles  $N$  within the aggregate follows a power-law dependency on the extension of the aggregate  $R$ :

$$N \propto R^{d_f} \quad (1.10)$$

$d_f$  denotes the fractal dimension of the gel.

In the other limit of vanishing interaction strengths and high volume fractions the kinetic arrest is not induced by attractive inter-particle forces but by crowding of the particles. Although the particles are still mobile any long-ranged migration is hindered by the presence of

the other particles. This arrested state is called repulsive glass ( $\epsilon$ ) and will be discussed in detail in section 1.3.1 together with the attractive glass ( $\delta$ ) at slightly increased interaction strengths.

## 1.2. Rheology of the dispersed state

### 1.2.1. Constitutive relations

Rheology is the study of the flow and deformation of matter. In essence it describes the relationships between stress, deformation and deformation rate in a material as it is mechanically excited. In doing so these constitutive relations define rheological quantities, such as elastic modules or viscosities. As a matter of fact these quantities always represent macroscopic properties of the tested material. Consequently, any rheological model of colloids needs to incorporate averaging over a sufficiently large ensemble of particles whereas the behavior of the individual particles is determined microscopically. In the following we will point out how these two facets enter the rheological description of colloids. But before dealing with the more complex case of arrested colloids we will shortly introduce the notation to describe the mechanical state of matter and then review the rheology of the dispersed state.

Two of the most important constitutive relations are Hooke's law and Newton's law of viscosity that describe the behavior of an elastic solid and a Newtonian fluid, respectively. In its general three dimensional tensorial form for isotropic materials they are given by

$$\begin{array}{ll} \boldsymbol{\sigma} = K \mathbf{B} & \boldsymbol{\sigma} = 2 \eta \mathbf{D} \\ \text{Hooke} & \text{Newton} \end{array} \quad (1.11)$$

with the elastic modulus  $K$  and the viscosity  $\eta$ . The stress tensor  $\boldsymbol{\sigma}$  is a measure of the forces acting on a small volume within the sample. Its components  $(\boldsymbol{\sigma})_{ij}$  are defined by the force per unit area acting on the plane normal to  $\hat{e}_j$  in direction of  $\hat{e}_i$  [Fig. 1.5 (a)]. The Finger tensor  $\mathbf{B}$  is a measure of the deformation. It is related to the finite deformation tensor  $\mathbf{F}$  that describes the relative displacements inside the deformed specimen. With regard to Fig. 1.5 (b)

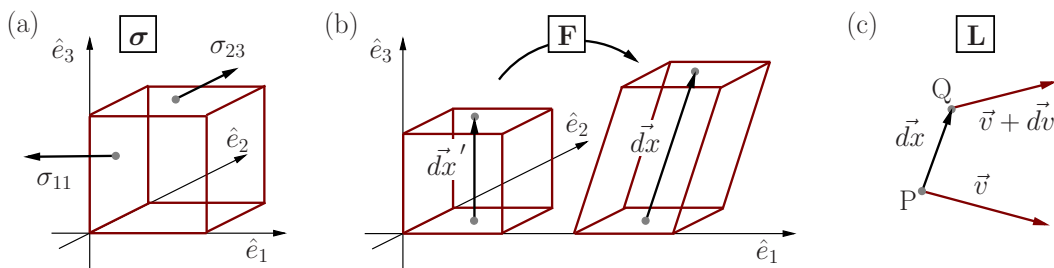


**Fig. 1.5.:** Illustration of the definitions of (a) stress, (b) finite deformation and (c) velocity gradient tensors.

their definitions are

$$\vec{dx} = \mathbf{F} \vec{dx}' \quad \mathbf{B} \equiv \mathbf{F} \mathbf{F}^T \quad (1.12)$$

or in differential form

$$(\mathbf{F})_{ij} = \frac{\partial x_i}{\partial x'_j} \quad (\mathbf{B})_{ij} = \frac{\partial x_i}{\partial x'_k} \frac{\partial x_j}{\partial x'_k} \quad (1.13)$$

$\mathbf{D}$  is called the rate of deformation tensor and is a measure of the rate at which two points in a material are displaced. It is related to the velocity gradient tensor  $L$  [Fig. 1.5 (c)] that parametrizes the spatial changes in the velocity field  $\vec{v}$ :

$$\vec{dv} = \mathbf{L} \vec{dx} \quad 2\mathbf{D} \equiv \mathbf{L} + \mathbf{L}^T \quad (1.14)$$

or in differential form

$$(\mathbf{L})_{ij} = \frac{\partial v_i}{\partial x_j} \quad 2(\mathbf{D})_{ij} = \frac{\partial v_i}{\partial x_j} + \frac{\partial v_j}{\partial x_i} \quad (1.15)$$

These definitions of  $\mathbf{B}$  and  $\mathbf{D}$  naturally guarantee that less interesting rotations of the whole sample are not included. In general  $\sigma$ ,  $\mathbf{B}$  and  $\mathbf{D}$  depend on time  $t$  and the position  $\vec{r}$  of the test volume inside the sample. However, for simple geometries like shear, extensional flow or axial deformations and under steady state conditions, *i. e.* constant deformation in case of isotropic and homogeneous solids and constant deformation rates in case of liquids, all tensors are independent of  $\vec{r}$  and  $t$ . Just like in the present work many experimental studies are done in shear geometry (Fig. 1.6) for which the formulas from above simplify to the following set of equations:

$$\mathbf{B} = \begin{pmatrix} 1 + \gamma^2 & \gamma & 0 \\ \gamma & 1 & 0 \\ 0 & 0 & 1 \end{pmatrix} \quad 2\mathbf{D} = \begin{pmatrix} 0 & \dot{\gamma} & 0 \\ \dot{\gamma} & 0 & 0 \\ 0 & 0 & 0 \end{pmatrix} \quad \begin{array}{ll} \text{Hooke:} & \sigma = G\gamma \\ G: & \text{shear modulus} \\ \text{Newton:} & \sigma = \eta \dot{\gamma} \end{array} \quad (1.16)$$

If the material is not isotropic or homogeneous  $\mathbf{B}$  and  $\mathbf{D}$  need to be defined as volume averages

$$\langle \mathbf{B} \rangle_V = \frac{1}{V} \int_V \mathbf{B}(\vec{r}) dV \quad \langle \mathbf{D} \rangle_V = \frac{1}{V} \int_V \mathbf{D}(\vec{r}) dV \quad (1.17)$$

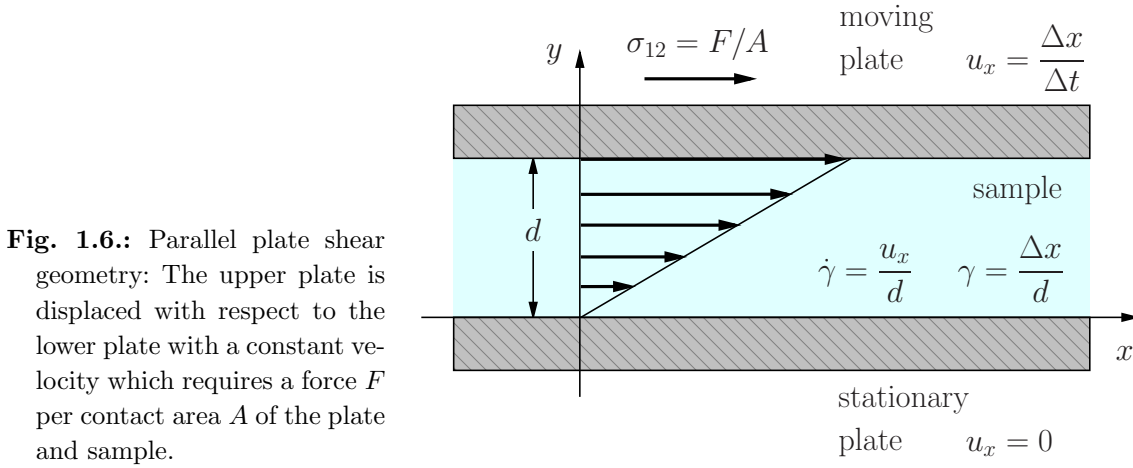
whereas the deformation and velocity fields and thus the microscopic tensors  $\mathbf{B}(\vec{r})$  and  $\mathbf{D}(\vec{r})$  are explicitly calculated from the momentum balance and the continuity equation

$$\varrho \left( \frac{\partial \vec{v}}{\partial t} + \vec{v} \cdot \vec{\nabla} \vec{v} \right) = \vec{\nabla} p + \vec{\nabla} \cdot \boldsymbol{\sigma} + \vec{F}_{\text{ext}} \quad \frac{\partial \varrho}{\partial t} = -\vec{\nabla} \cdot (\varrho \vec{v}) \quad (1.18)$$

momentum balance continuity equation

with the surrounding pressure  $p$ .





### 1.2.2. Viscosity modification

Following this methodology the constitutive relation for colloids in the dispersed state can be developed. In the diluted regime the stress tensor has two contributions, the solvent phase  $\langle \sigma_s \rangle_V$  and the particles  $\langle \sigma_p \rangle_V$ . Solving the momentum balance of the solvent around a single particles reveals a purely Newtonian behavior of the colloid

$$\langle \sigma \rangle_V = \langle \sigma_s \rangle_V + \langle \sigma_p \rangle_V = 2 \underbrace{\eta_s (1 + 2.5 \varphi)}_{\eta_{\text{coll}}} \langle \mathbf{D} \rangle_V \quad (1.19)$$

The effective viscosity of the colloid  $\eta_{\text{coll}}$  only depends on the viscosity of the neat solvent  $\eta_s$  and the volume fraction of the dispersed particles  $\varphi$  which was firstly described by Einstein [Ein06]. However, the derivation is based on a number of assumptions:

- Non-interacting, rigid, spherical particles (hard spheres) that do not sediment
- The solvent is incompressible and behaves Newtonian. Even on the lengthscale of the particles the solvent can be considered as a continuum
- The velocity perturbations due to the particles are local, *i. e.* the velocity field far away from the particles is the same as if the particles were not present

With increasing particle volume fraction  $\varphi$  hydrodynamic interaction between neighboring particles must be considered. Since these hydrodynamic forces are long-ranged a significant effect already occurs at very low values for  $\varphi$  [Fig. 1.7 (a)]. In the first approximation equation (1.19) need to be extended by an additional contribution proportional to  $\varphi^2$  [Bat77]. Yet, at sufficiently small deformation rates the colloid still behaves as a Newtonian liquid:

$$\frac{\eta_{\text{coll}}}{\eta_s} = 1 + 2.5 \varphi + 6.2 \varphi^2 + \mathcal{O}(\varphi^3) \quad (1.20)$$

At even higher volume fractions approximations are only valid for a limited parameter range. It is more suitable to fit the viscosity data to the semi-empirical Dougherty-Krieger formula

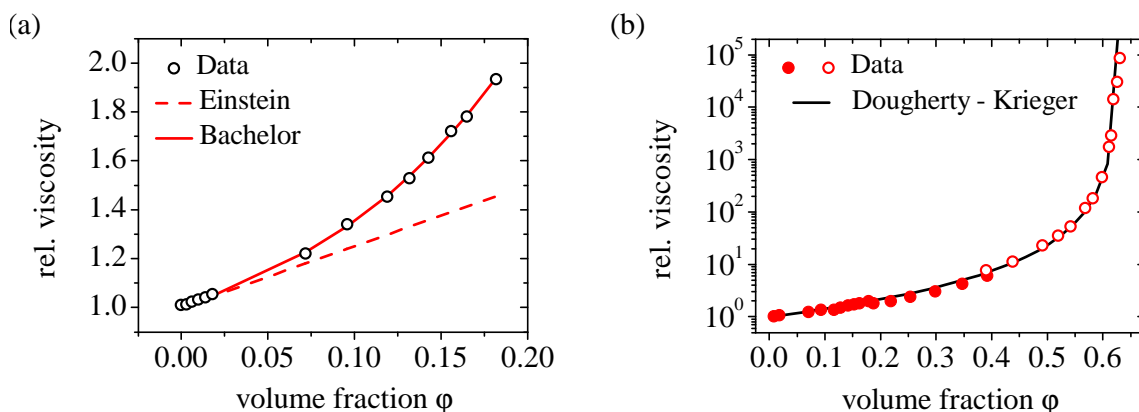


**Fig. 1.7.:** Dependency of the viscosity on particle volume fraction for a colloidal dispersion from silica particles hydrophobized with stearic alcohol ( $C_{18}H_{37}OH$ ) in cyclohexane. (a) At very low volume fractions the viscosity increases linearly according to Einstein. At medium particle contents higher order correction lead to non-linear behavior. Here the data was fitted by  $\eta_{\text{coll}}/\eta_s = 1 + 2.5\varphi + 5.0\varphi^2 + 53\varphi^3$ . (b) At even higher volume fractions the viscosity diverges with a power-law dependency which can be described by the Dougherty-Krieger formula (1.21). (data from reference [Jon91])

for the effective viscosity:

$$\frac{\eta_{\text{coll}}}{\eta_s} = \left(1 - \frac{\varphi}{p}\right)^{-\alpha p} \quad (1.21)$$

$\alpha$  is supposed to be equal to the first correction coefficient in (1.19) and  $p$  is close to the volume fraction of random close-packed spheres. Fig. 1.7 (b) shows that this relation describes experimental data very well in particular for large volume fractions. The structure of (1.21) can also be understood in the context of an effective medium approach. Under the assumption that the colloid is a continuous medium characterized by the viscosity  $\eta_{\text{coll}}$  the addition of further particle  $d\varphi$  results in a relative change of viscosity  $d\eta_{\text{coll}}$  in analogy to (1.19):

$$d\eta_{\text{coll}} = \alpha \eta_{\text{coll}} \frac{d\varphi}{1 - \varphi/p} \quad (1.22)$$

The normalization  $1 - \varphi/p$  accounts for the reduced available free solvent volume that can be replaced by the added particles. Integration of this equation directly leads to (1.21).

### 1.2.3. Non-linearity and visco-elasticity

The hydrodynamic forces also affect the spatial distribution of the particles. The particles tend to approach closer to each other effectively reducing the average stress in the colloid. Hence, the viscosity decreases, an effect that is called shear thinning. The Brownian motion of the particle counteracts this process and pursues a homogeneous particle distribution. The balance between both effects is expressed by the Peclet number

$$Pe = \frac{\eta_s \dot{\gamma} R_p^3}{k_B T} \quad \text{for shear flow} \quad (1.23)$$

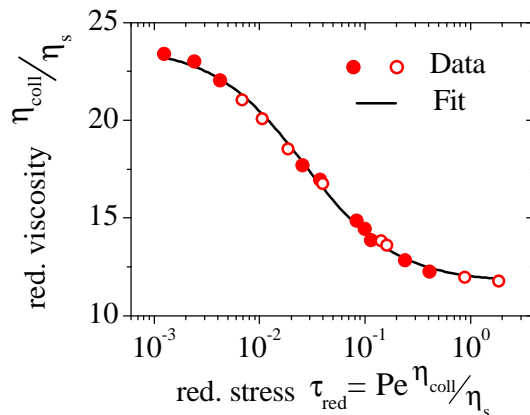


**Fig. 1.8.:** Reduced viscosity as a function of reduced shear rate for colloidal dispersions of polystyrene particles at a volume fraction of  $\varphi = 0.5$  in two different solvents. The line represents the fit after (1.24) (Data from reference [Kri72]).

If  $Pe$  is small at low shear rates  $\dot{\gamma}$  Brownian motion dominates and the distribution of the particles is homogeneous. At large values for  $Pe$  and  $\dot{\gamma}$  the apparent viscosity is reduced. According to Krieger [Kri72] this shear rate dependent transition can be well described by

$$\frac{\eta - \eta_\infty}{\eta_o - \eta_\infty} = \frac{1}{1 + \frac{Pe \eta_{coll}}{\eta_s \sigma_c}} \quad (1.24)$$

with the low and high shear rate limits  $\eta_o$  and  $\eta_\infty$  and an adjustable parameter  $\sigma_c$  denoting the critical shear stress for shear thinning (Fig. 1.8). In a similar manner anisotropic particles align in hydrodynamic flows which reflects in an anisotropic distribution of particle orientations. If the rotational Brownian motion is too slow to reorient the particles to a random distribution shear thinning is observed. These effects are just two examples of several non-linear phenomena occurring in colloids.

In the discussion so far the mechanical response of the system to an external deformation or stress was assumed to be instantaneous. This is a good approximation for purely elastic or viscous materials as the stress transmission happens at the velocity of sound. So the time required to reach a steady state is much shorter than the time for the actual experimental measurement. However, if slower reorganization or relaxation processes are involved the mechanical response will be time dependent. Now the entire deformation history influences the current state of the material and the constitutive relations (1.11) must be replaced by

$$\boldsymbol{\sigma}(t) = \int_{-\infty}^t K(t-t') 2\mathbf{D}(t') dt' \quad (1.25)$$

The relaxation modulus  $K(t-t')$  replaces the elastic modulus and the viscosity and thus characterizes the rheological behavior of such visco-elastic materials. Various types of experiments are used to measure the relaxation modulus or related mechanical quantities (see section 2.2). For now we consider the stress relaxation after a sudden shear strain. In this type of experiment the sample is subjected to a shear deformation for a short timespan  $\xi$  which generates a certain stress  $\sigma$  within in the system. Directly after shearing, at time  $t_o$ , the absolute deformation  $\gamma$  is held constant and the temporal evolution of the stress  $\sigma(t)$  is measured. If  $\xi$  is

short enough equation (1.25) can be simplified to:

$$\begin{aligned}\sigma(t) &= \int_{t_o-\xi}^{t_o} G(t-t') \gamma/\xi dt' \\ &\approx \sigma_s + \gamma G(t) \quad \text{for long times } t \gg \xi\end{aligned}\quad (1.26)$$

Hence,  $G(t)$  is proportional to the measured stress  $\sigma(t)$ . In many diluted dispersions its time dependency can be approximated by an single exponential function

$$G(t) = G_o \exp(-t/\tau_o) \quad (1.27)$$

that is characterized by the so called relaxation time  $\tau_o$ . Microscopically  $\tau_o$  can be interpreted as a characteristic time that is required by the particles to relax from the deformed state to their equilibrium conformation either by means of a dissipative Brownian motion and restoring entropic forces. In a simple mechanical analogue the Brownian motion is represented by a dash-pot that is connected in series with a spring that stands for the elastic entropic contribution. This configuration is also known as a Maxwell element.

Another common testing method is oscillatory shear rheometry where the specimen is sheared periodically at a fixed frequency  $\omega$ . After a short transient phase characterized by  $\tau_o$  the stress follows the periodic rate of deformation with the same frequency but with a certain phase difference  $\psi$ :

$$\sigma(\omega, t) = \sigma_o \sin(\omega t + \psi) \quad \dot{\gamma}(\omega, t) = \dot{\gamma}_o \sin(\omega t) \quad (1.28)$$

Mathematically  $\sigma(\omega, t)$  can be expressed as a sum of two contributions one of which  $\sigma''(\omega, t)$  is in phase with the rate of deformation and the other one  $\sigma'(\omega, t)$  out of phase. Their relative amplitudes are related with each other via the components of the complex dynamic shear viscosity  $\eta^*(\omega) = \eta'(\omega) + i\eta''(\omega)$

$$\sigma(\omega, t) = \underbrace{\eta''(\omega) \dot{\gamma}_o \sin(\omega t)}_{\sigma''(\omega, t)} + \underbrace{\eta'(\omega) \dot{\gamma}_o \cos(\omega t)}_{\sigma'(\omega, t)} \quad (1.29)$$

If the sample behaves predominantly elastic it is also useful to define the complex dynamic shear modulus  $G^*(\omega) = G'(\omega) + iG''(\omega)$  in a analogous way. It is related to the components of the complex viscosity by

$$G'(\omega) = \omega \eta''(\omega) \quad G''(\omega) = \omega \eta'(\omega) \quad (1.30)$$

$G'(\omega)$  is called the storage modulus and is a measure of the elasticity of the material while  $G''(\omega)$  is the loss modulus and is proportional to the dissipated energy per deformation cycle.  $G^*(\omega)$  is sometimes also represented by its absolute value  $|G^*(\omega)| = \sqrt{G'(\omega)^2 + G''(\omega)^2}$  and the so called loss angle  $\psi = \arctan(G''(\omega)/G'(\omega))$ . Using the explicit expression (1.27) for  $G(t)$

the components of  $G^*(\omega)$  can be calculated directly from the constitutive relation (1.25):

$$G'(\omega) = \frac{G_o \omega^2 \tau_o^2}{1 + \omega^2 \tau_o^2} \quad G''(\omega) - \eta_s \omega = \frac{G_o \omega \tau_o}{1 + \omega^2 \tau_o^2} \quad (1.31)$$

$G''(\omega)$  needed to be corrected for the contribution of the solvent phase ( $\eta_s$ ) which was not considered in the long-time approximation of equation (1.26). Just like the Peclet number in the steady shear experiments now the frequency  $\omega$  defines the timescale of the experiment. At low frequencies one approaches the steady limit of almost purely viscous Newtonian behavior as it was already discussed above. In this regime  $G'' - \eta_s \omega$  is proportional to  $\omega$  with the proportionality constant  $2.5 \varphi \eta_s$ .  $G'$  is much smaller than  $G''$  but scales with  $\omega^2$ . Hence, if tested at higher frequencies close to  $1/\tau_o$  the entropic contribution becomes increasingly important. At even higher frequencies the rate of deformation is faster than Brownian motion and thus the spatial distribution of the particles does hardly change within one deformation cycle.  $G'$  levels off while  $G'' - \eta_s \omega$  drops as  $1/\omega$ . Now only the contribution of the solvent phase  $\eta_s \omega$  determines the loss modulus  $G''$  of the colloid.

In the dispersed state at low particle concentrations a single relaxation time  $\tau_o$  is sufficient to describe the observed visco-elasticity. As  $\tau_o$  is related to the Brownian motion of the particles and visco-elastic effects become apparent at frequencies of about  $2\pi/\tau_o \geq 1$  rad/s. On the contrary, in course of the transition to an arrested state colloids are dominated by slower relaxation processes that involve cooperative motions of larger numbers of particles. In this case the onset of visco-elastic effects shift to lower frequencies and the single relaxation time is replaced by the relaxation spectrum  $H(\tau)$  that measures the relative strength of different relaxation modes:

$$G(t) = G_e + \int_{-\infty}^{\infty} H(\tau) \exp(-t/\tau) d \ln \tau \quad (1.32)$$

$G(t)$ ,  $G^*(\omega)$  (either in terms of  $G'$  and  $G''$  or  $|G(\omega)|$  and  $\psi$ ) and  $H(\tau)$  are related to each other by means of integral and differential equations that may or may not be analytically solved. Yet, each of these quantities contains the complete information about the dynamic mechanical properties of the sample in the linear visco-elastic regime.

## 1.3. Aggregated colloids in the arrested state

### 1.3.1. Glass transition and mode-coupling theory

At the highest particle volume fractions the viscosity of the colloid diverges. At the same time, the colloid sustains small applied stresses and thus shows an certain degree of elasticity. The system undergoes a liquid-solid transition. This macroscopic rheological behavior is caused by a limited mobility of the particles on a microscopic level [Wee00a]. While at lower volume fractions the whole sample volume is accessible each particle is now almost completely enclosed by its nearest neighbors. Any short-time Brownian motion ( $\beta$ -relaxation) is restricted to a

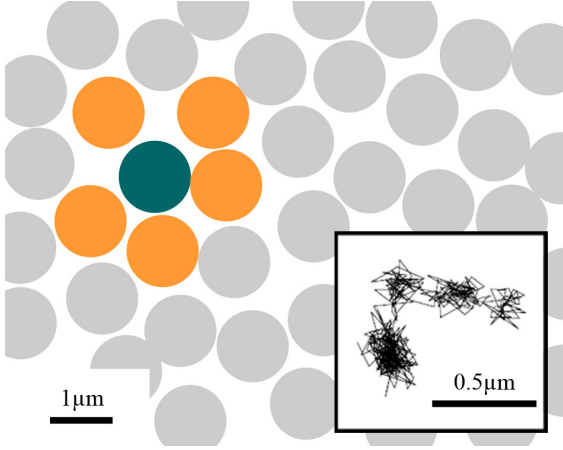


**Fig. 1.9.:** Cage effect: The motion of the cyan colored particle is restricted to a small volume, the cage, that is defined by its neighboring particles (orange). Only after long times the cage can rearrange and allow for larger displacements to be again stuck in a slightly different conformation. The inset shows the two-dimensional displacement of an individual particle obtained via confocal microscopy (section 2.1). Note the difference in the scale bars. During the cage reorganization the particle moves only by a fraction of its diameter (image from [Wee02]).

small volume, the cage, and larger displacements are only possible by cooperative movements of larger groups of particles after long times (Fig. 1.9) ( $\alpha$ -relaxation). As the sample approaches its glassy state the number of cooperatively moving particles diverges and any structural reorganization becomes impossible. The system gets kinetically arrested which is accompanied by the breakdown of ergodicity in the system.

Many studies have been devoted to the understanding of the glass transition in colloids as an ergodicity to non-ergodicity transition that is also relevant in the glass formation of atomic liquids and polymers. Ergodicity is best measured by means of the time dependence of the normalized density correlation function in the reciprocal space

$$\Phi(\vec{q}, t) = \frac{\langle \tilde{\rho}(\vec{q}, \tau + t), \tilde{\rho}(\vec{q}, \tau) \rangle_{\tau}}{\langle |\tilde{\rho}(\vec{q}, \tau)|^2 \rangle_{\tau}}. \quad (1.33)$$

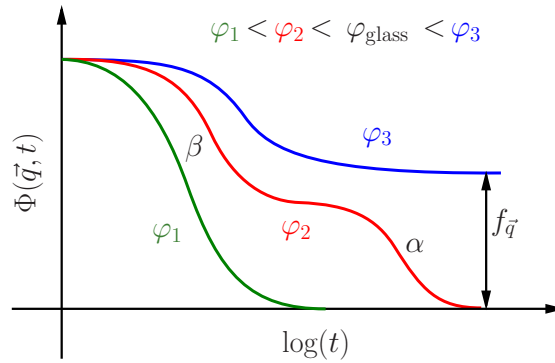
$\tilde{\rho}(\vec{q}, t)$  denotes the Fourier transform of the particle density:

$$\rho(\vec{r}, t) = \frac{1}{V} \sum_{i=1}^N \delta(\vec{r} - \vec{r}_i(t)) \quad \tilde{\rho}(\vec{q}, t) = \frac{1}{V} \sum_{i=1}^N \exp(i \vec{q} \cdot \vec{r}_i(t)) \quad (1.34)$$

In the ergodic dispersed state  $\Phi(\vec{q}, t)$  decays to zero in a finite time. As the colloid approaches the glass transition, however, only part of correlation is lost in the fast  $\beta$ -relaxation and a plateau evolves. This plateau is followed by second decay at longer times that corresponds to the  $\alpha$ -relaxation. At the glass transition the  $\alpha$ -relaxation time  $\tau_{\alpha}$  diverges and  $\Phi(\vec{q}, t)$  stays constant at the non-ergodicity parameter  $f_{\vec{q}} = \lim_{t \rightarrow \infty} \Phi(\vec{q}, t)$  (Fig. 1.10).

A mathematical description of this temporal evolution is given in the framework of the mode-coupling theory (MCT) [Cat08, Cat04b, Rei05]. Starting from the equations of motion for a single particle including viscous drag, fluctuating solvent forces and inter-particle potentials the Langevin equation for the particle density  $\rho(\vec{r}, t)$  is obtained. Due to the complexity of this equation it is easier to proceed in reciprocal space where the particle interactions are expressed as couplings between different modes  $\vec{q}$ . The result is the equation of motion for the density correlation  $\Phi(\vec{q}, t)$  that describes the temporal evolution of density fluctuations

**Fig. 1.10.:** Breakdown of ergodicity in course of the colloidal glass transition: At low particle volume fraction the colloid is ergodic and the particle density correlation  $\Phi(\vec{q}, t)$  decays to 0 at finite times. Within increasing volume fraction the correlation indicates two relaxation processes separated by a plateau. In course of the glass transition the longer  $\alpha$ -relaxation time diverges ending in a non-ergodic state for which the plateau prolong to infinite times.



at different lengthscales  $1/|\vec{q}|$ . The actual calculation is based on the static structure factor  $S(\vec{q}) = \langle \bar{\rho}(\vec{q}, \tau) \rangle_{\tau}$  that is obtained analytically from the inter-particle potential in a self-consistent way [Daw01]. This procedure only displays equilibrium behavior and thus MCT relies on the assumption that  $S(\vec{q})$  does not change significantly beyond the glass transition. Alternatively,  $S(\vec{q})$  can also be extracted from molecular dynamics simulations or directly from static light scattering experiments [Ram04].

MCT shows a large predictive potential. Beside to the temporal evolution of  $\Phi(\vec{q}, t)$  it allows for a prediction of the critical volume fraction  $\varphi_g$  at which the glass transition happens (see Fig. 1.4). Moreover,  $\Phi(\vec{q}, t)$  can be used to directly calculate the frequency dependent complex viscosity  $\eta^*(\omega)$  and shear modulus  $G^*(\omega)$  [Daw01]. Siebenbürger *et al.* compared these theoretical predictions with rheological measurements for dispersions of sterically stabilized PS-PNIPAM core-shell particles and observed a very good agreement for almost 10 decades in frequency [Sie09]. At volume fractions in the concentrated regime, yet far below the glass transition the colloid behaves like a Newtonian liquid at sufficiently low frequencies  $\omega$  and low Peclet numbers  $Pe \sim \omega$ , respectively. The loss modulus  $G''$  is proportional to  $\omega$  and largely exceeds the storage modulus  $G'$  that scales with  $\omega^2$  [Fig. 1.11 (a)]. At higher frequencies both modules approach to each other and even coincide for a limited frequency range signaling the existence of a spectrum of relaxation processes. These processes are caused by the correlated Brownian motion of the particles that can relax the generated stresses only for sufficiently low shear rates. At the highest frequencies the Newtonian behavior is regained with a reduced viscosity of the neat solvent.

With increasing volume fraction (Fig. 1.11 (b)) the viscosity rises and hence also  $G''$ . Along with the appearance of the slow  $\alpha$ -relaxation in  $\Phi(\vec{q}, t)$  (Fig. 1.10) due to the cage effect the mechanical relaxation shifts to lower frequencies. Beyond this frequency the colloid cannot relax the applied deformation via structural relaxations and a plateau in  $G'$  evolves. At the highest frequencies  $G'$  and  $G''$  behave similarly to the case of the lower volume fraction as the short-time Brownian motion within the cages is less influenced by the increased particle content.

Past the glass transition at  $\varphi_g$  (Fig. 1.11 (c)) structural reorganizations are hindered completely and the plateau extends to infinitely low frequencies. The existence of a non-vanishing storage modulus  $G'_o$  at infinitesimally small frequencies can microscopically only explained by

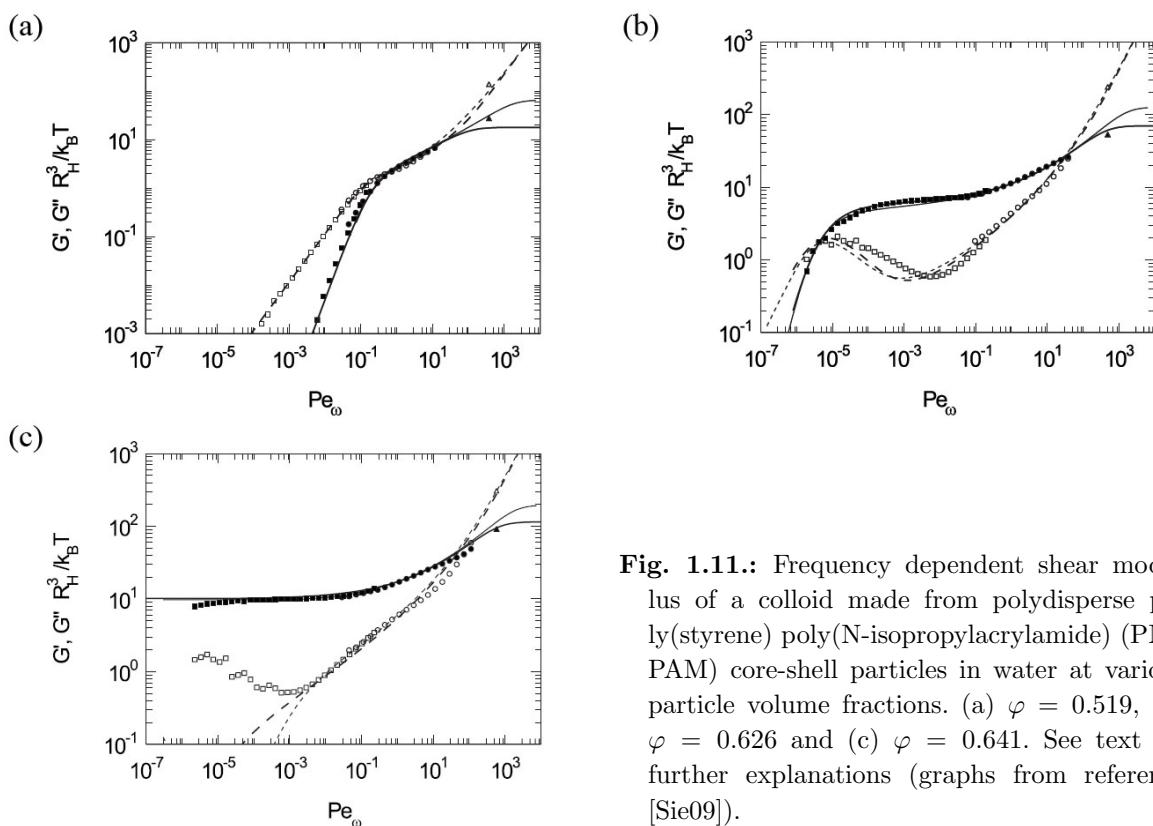


**Fig. 1.11.:** Frequency dependent shear modulus of a colloid made from polydisperse poly(styrene) poly(N-isopropylacrylamide) (PNIPAM) core-shell particles in water at various particle volume fractions. (a)  $\varphi = 0.519$ , (b)  $\varphi = 0.626$  and (c)  $\varphi = 0.641$ . See text for further explanations (graphs from reference [Sie09]).

the presence of a percolating particle network that can bear the applied stress. Indeed system spanning clusters of slow and stationary particles were observed on approaching the glass transition by means of confocal microscopy and molecular dynamics simulations [Con06]. Yet, these clusters dissemble after a characteristic, volume fraction dependent timescale corresponding to a transient plateau in  $G'$  in Fig. 1.11 (b). Only past the glass transition the percolating cluster stays permanently and thus allows for a stationary plateau at  $G'_o$ . The magnitude of  $G'_o$  strongly depends on the volume fraction as it follows a power law behavior when normalized to  $\varphi_g$  [Bra93, Kra10]

$$\lim_{\omega \rightarrow 0} G'(\omega, \varphi) = G'_o(\varphi) \sim \frac{1}{(\varphi/\varphi_g - 1)^\nu} \quad (1.35)$$

When the single particle motion is coupled to an external flow field MCT can also be used to describe colloids at strain rates in the non-linear regime [Fuc02a]. Most importantly, it correctly predicts the existence of a yield stress  $\sigma_y$  in the glassy state. For applied stresses below this critical value the colloid responds elastic while above  $\sigma_y$  the glass yields and gets liquidized, eventually followed by a shear thinning regime at higher shear rates [Cra08, Sie09]. In its simplest form such a behavior is described by the Bingham characteristics

$$\begin{cases} \sigma = G'_o \gamma & \text{for } \sigma < \sigma_y \\ \sigma = \sigma_y + \eta \dot{\gamma} & \text{for } \sigma \geq \sigma_y \end{cases} \quad (1.36)$$



Macroscopic rheometry showed that  $\sigma_y$  is closely related to the elastic modulus in the linear regime as yielding happens at a fixed strain in the order of  $\gamma_y = \sigma_y/G'_o \approx 0.1$  irrespective of the strain rate [Zau08]. Though, the microscopic picture of the yielding process in terms of possible cage breaking events is not fully understood yet [Pha06].

### 1.3.2. Attractive glass and gelation

So far the particles were assumed to be impenetrable hard spheres that interacted with each other only by means of collisions and hydrodynamic coupling mediated by the solvent. Now, we turn to arrested colloids with attractive inter-particle potentials. Despite this considerable difference in the microscopic interactions a number of analogies were observed in experiments and simulations [Pue02]:

- i As the colloid gets dynamically arrested the system undergoes an ergodic non-ergodic transition as it was described in the preceding section. In general, the non-ergodicity parameter  $f(\vec{q})$  is larger for the attractive colloids which is related to the stronger bonds between the particle.
- ii During the transition the structure of colloids, expressed by the static structure factor  $S(\vec{q})$ , does not change significantly. The precursor and final state of a arrested colloid can hardly be distinguished from just as the dispersed and the glassy state strongly resemble each other.
- iii The essential features of the rheological evolution are universal: As a critical volume fraction  $\varphi_c$  is exceeded the colloid turns from a viscous fluid to a elastic solid while passing an intermediate highly visco-elastic state. The respective particle interactions enter predominantly in  $\varphi_c$  as well as the absolute values of the rheological modules.
- iv The finite low-frequency storage modulus is caused by a permanent, system spanning particle cluster. In case of the repulsive glass the aggregation into clusters is caused by crowding while in attractive colloids aggregation happens for energetic reasons. Hence, kinetic arrest happens at much lower volume fractions.

These similarities motivated recent theoretical advances to unify the kinetic arrest in repulsive and attractive colloids in a general MCT framework. The initial formulation of the MCT was extended to account for attractive inter-particle potentials and/or low volume fractions and in particular proved to be applicable in case of concentrated weakly attractive colloids [Daw01, Cat04b]. MCT correctly predicted the existence of an ergodic liquid state at volume fractions above the glass transition of hard spheres if an attractive interaction was introduced [Daw01, Eck02] (compare Fig. 1.4). The closer binding of neighboring particles due to the attractive interaction effectively generates additional free volume for other particle which facilitates large-scale structural relaxations. With increasing attractive strengths, however, the system again gets arrested in the attractive glass. The structural properties of the attractive and repulsive glass differ notably. The structure factor of the attractive glass shows a maximum at much

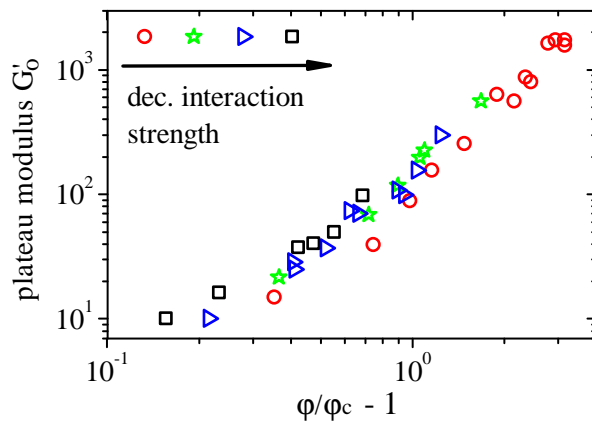
smaller wave vectors  $\vec{q}$  corresponding to a structuring of the colloid at larger length scales. This coincides with the intuitive picture that the attraction gives rise to stronger particle bonds, more dense clusters and thus a more heterogeneous structure than in the repulsive glass. In this respect the attractive glass transition is more closely related to gelation [Pue02].

While dense colloid gels ( $\varphi \geq 0.4$ ) are handled with the same basic formulation of MCT some modification are necessary in case of lower volume fractions and weak attraction for a number of reasons. Many of them come up from the fact that the MCT calculations are based on the equilibrium structure factor  $S(\vec{q})$  before the system gets arrested. This is reasonable for dense gels and glasses as structural reorganizations in course of the arrest are restricted due to the high volume fraction. In loose gels, however, finite bond lifetimes, large scale heterogeneities and structurally weak regions can cause time-dependent changes in the particle network that are not captured by MCT. Further problems arise from the dynamic nature and diversity of gelation scenarios, such as transient gelation or non-equilibrium routes via irreversible phase separation. Consequently, the equilibrium structure factor used in the MCT calculations probably deviates from actual structure. Several extensions to the standard MCT try to circumvent these problems. The cluster mode-coupling approach (CMCT) [Kro04, Cat04a] models gelation as a two-step process. In the initial step the particles aggregate to clusters that are considered as the new primary particles of the colloid. The subsequent kinetic arrest to the final gel state is described by the standard MCT using renormalized values for the volume fraction, the interaction range and strength. As another extension of MCT the PRISM method [Fuc02b] was developed to improve the calculation of the structure factor in colloids with polymer-induced depletion attraction. It takes into account the locally heterogeneous distribution of polymers and possible configuration changes of the polymers within the closed-packed particle network [Ram04].

Various hallmarks have been established to verify the applicability of this extended MCT-based framework for model colloids. These hallmarks include predictions for the gelation boundary in the phase diagram, the evolution of static and dynamic structure factors as well the mechanical properties of the colloids. Like for the repulsive and attractive glass quantitative agreement was achieved within a 10% uncertainty range for dense gels [Cat08]. At lower volume fractions, however, experimental results and theory could be compared only qualitatively in particular regarding critical volume fractions and the structure factors [Sha03]. Yet, the discrepancies were only partly related to an inappropriate MCT description. Multiple definitions of the gelation point for scattering experiment, confocal images and visual inspection by eye further complicate a proper comparison. In the same sense the occurrence of a percolating system spanning cluster does not necessarily coincide with the kinetic arrest in terms of MCT as we will discuss in more detail in section 1.3.3. Moreover, the minimal frequency  $\omega$ , for which the storage modulus  $G'(\omega)$  is assumed to be stationary, is actually chosen arbitrarily ( $\omega = 2\pi/100\text{ s} \approx 0.06\text{ 1/s}$ ) and sometimes limited by aging effects.

The bare mechanical properties in terms of the full frequency dependency of  $G'(\omega)$  and  $G''(\omega)$  or the variations in the plateau modulus  $G_o$  with the volume fraction or the interaction strength are less susceptible to ambiguous definitions. Regarding these quantities good agree-

**Fig. 1.12.:** Scaling behavior in colloidal gel made from 100 nm silica particles with steric stabilization. The interaction strength is controlled via temperature. All data collapse to an universal curve when plotted against the reduced volume fraction according to equation (1.37). Data from reference [Rue97].



ment between experiment and theory was observed in particular if the MCT calculations were aided by structure factors obtained either by experiments or molecular dynamics simulations. These results support a unified picture of arrested colloids which is most directly reflected in a scaling behavior for  $G'_o(\varphi)$  in analogy to repulsive glasses in equation (1.35)

$$\lim_{\omega \rightarrow 0} G'(\omega, \varphi) = G'_o(\varphi) = \frac{\alpha}{(\varphi/\varphi_c - 1)^\nu} \quad (1.37)$$

The characteristics of the inter-particle potential enter in the exponent  $\nu$  and the proportionality constant  $\alpha$  and thus is responsible for difference in the absolute values of  $G'_o$  (Fig. 1.12) [Pra03, Tra04]. Repulsive glasses are the weakest structures with modules in the order of 10 Pa at the glass transition. Depending on the interaction strength attractive glasses are located at about 100 Pa whereas gels can reach plateau modules up to 1000 Pa. In a simplified picture  $G'_o$  can be estimated from the free energy density  $f$  of the system and its variations  $\Delta f$  upon an externally induced deformation  $\gamma$ .

$$\Delta f = \frac{1}{2} G'_o \gamma^2 \approx \frac{1}{2} G'_o \frac{\Delta r^2}{D_p^2} \quad (1.38)$$

Here we approximated the macroscopic deformation by the microscopic displacement of the particles  $\Delta r$  that happens on the lengthscale of the particle diameter. The same particle displacement might alternatively be caused by thermally induced motions of the particles about the mean positions defined by the minimum of the inter-particle potential. In this case the energy density is approximated by

$$\Delta f = 3/2 k_B T \frac{N}{V} \quad (1.39)$$

with the number of particles  $N$  in the volume  $V$ . Comparing both equations leads to an estimate for  $G'_o$ :

$$G'_o \approx \frac{k_B T}{R_p r_{loc}^2} \varphi \quad (1.40)$$

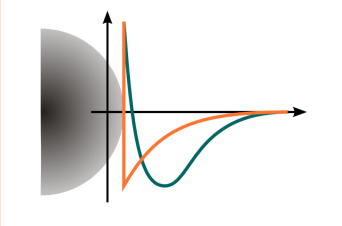
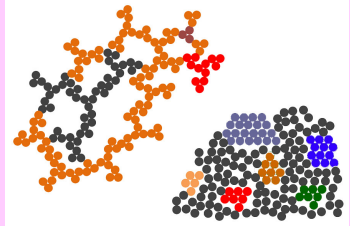
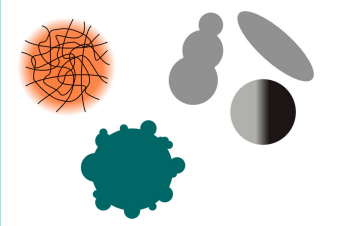
$r_{\text{loc}}$  replaces  $\Delta r$  and is called the localization length. It is a measure of binding strength of the particle to its nearest neighbor and can be obtained from the structure factor in the framework of a naive version of MCT [Sha03, Pue02, Vie08]. In agreement with the estimates for  $G'_o$  from above  $r_{\text{loc}}$  is small for colloidal gels and largest for the repulsive glass.

In summary, MCT is currently the most powerful description of colloids near and in kinetic arrest. Although quantitative predictions often achieve only an accuracy of about 10 % [Cat08] the overall agreement with experiments and its success in unifying the behavior of attractive and repulsive colloids is probably the best sign for the validity of MCT. Though, its applicability is limited to model colloids with well defined interactions at moderate and high volume fractions. For arrested colloids at low volume fractions or complex types of particle interactions more specialized and heuristic approaches can be more adequate to identify relevant processes. In the following we explore the parameter space of colloids and discuss a few examples where alternative models were successfully applied to explain the rheological behavior.

### 1.3.3. Exploring Parameters: interaction mechanisms, structure, and particle properties

So far the particles in a colloid were assumed to be impenetrable, non-deformable, and smooth spheres that interacted with each other by effective inter-particle potentials. As we discussed above this idealized scenario can be well achieved by tuning particle materials, solvents and additives. On the contrary, colloids found in industry and daily life are more complex and do not necessarily meet these simplified conditions. Consequently, unexpected rheological features might be observed. In general interaction mechanisms, structural characteristics and particle properties are the decisive factors (Tab. 1.3) but their actual impact on the mechanical behavior of the colloids depends also on their mutual interplay. We focus on three examples.

- i The existence of a percolated particle network is obviously a necessary not yet sufficient prerequisite for the observation of a macroscopic elasticity. Although all particles in the network are connected with each other it depends on the characteristics of the particle bonds, *i. e.* the inter-particle potential, whether the network can bear stresses [Tra04]. In centro-symmetric potentials the network is only stable with respect to stretching of the particle bonds while bending of particle chains does not change the energy of the system. Hence, any applied stress can be relaxed corresponding to a vanishing elasticity. Only an increased particle volume fraction and thus the addition of further particle bonds constrains these bending reorganizations. On the contrary, in non-centro-symmetric potentials any bending of particle chains by means of rotations and sliding of particles past each other is hindered by energy barriers which gives rise to an elastic response of the network. Theoretical approaches to these two types of structural and rigidity (mechanical) percolation confirms the discrepancy in the critical volume fraction and also predicts different exponents  $\nu$  in the power law of equation (1.37) [Arb93, Sah93]. Experiments with sterically stabilized particles with polymer induced depletion attraction are in accordance with these predictions [Pra03, Rue97, Gra93]. If the equilibrium separati-

| Interaction mechanisms  | Structure   | Particle properties   |
|---|---|---|
|  <ul style="list-style-type: none"> <li>• van der Waals</li> <li>• electrostatic</li> <li>• depletion</li> <li>• hydrodynamic coupling</li> <li>• solvent induced</li> </ul> |  <ul style="list-style-type: none"> <li>• fractal</li> <li>• amorphous</li> <li>• crystalline</li> </ul> |  <ul style="list-style-type: none"> <li>• compliance</li> <li>• anisotropy (shape, surface)</li> <li>• roughness</li> </ul> |

**Tab. 1.3.:** Parameters determining the mechanical properties of colloids

on distance largely exceeds the geometrical diameter of the particles by using polymers with high molecular weight chain bending cannot be avoided resulting in an exponent of  $\nu = 2.1$  [Arb93]. When using low molecular weight polymers the range of attraction is reduced and the interaction of the steric stabilization layers of bound particles limits chain bending. Consequently, the exponent is increased to  $\nu = 3.3$  [Sah93].

- ii Aqueous dispersions from temperature sensitive PNIPAM-based particles offer a unique possibility to study the colloidal glass transition [Le 08, Sch10a, Cra06]. Upon lowering the temperature the particles start to swell which leads to an increase in the effective particle volume fraction [Reu09] and finally in the dynamic arrest of the colloids. During this process the particle radius almost doubles and the particles get increasingly compliant. Yet, in the dispersed state this softness does not affect the mechanical properties of the colloid as the particle still behave as hard spheres. Only in the glassy state the swollen particle start to interact with each other via an brush-like polymer interaction which has a direct consequence on the volume fraction dependency of the elastic modulus [Sch10a]. A similar behavior was observed for the elasticity of emulsions as only in the glassy state the deformability of the emulsion droplets becomes obvious [Mas95].
- iii In colloidal dispersion made from gelatin particles aggregation was induced by a strong depletion attraction resulting in a rather fractal gel. The gel was mechanical characterized in non-linear nanoindentation experiments which revealed a pronounced aging behavior [Fil06a]. Freshly prepared gels showed a plastic yielding behavior that was connected to

a irreversible restructuring of the particle network as the indenter tip was pressed into the network. The time characteristics of the mechanical response could be related to a stick-slip frictional interaction of the particles during the restructuring [Fil06b]. Aged samples, however, showed a significant elastic recovery as the tip was retracted from the sample. This change in the mechanical response could not be related to structural changes over time which was confirmed by confocal microscopy. Instead, the increased network elasticity was attributed to the formation of strong solid particle bonds due to the special chemical composition of the colloid [Fil06a].

## 1.4. Current challenges and objectives of the present work

After this broad, yet not complete introduction to the general principles and rheology of colloids we now proceed to the basic objectives of the present work. Rather than focusing on the characterization of a specific colloid we discuss different model systems in order to draw a (selective) picture of the current challenges in the field. In our point of view this should at least cover three aspects: the diversity of colloidal dispersions, the validity of unified theories as well as alternative approaches and thirdly the development and testing of experimental methods. In the following we go through these three aspects and shortly comment on their implementation in the present work.

### 1.4.1. Diversity of colloidal dispersions

The large diversity of colloids was already subject of the preceding paragraph. Though, we want to stress the fact that the exploration of the parameter space of Tab. 1.3 and the understanding of the dynamical processes in these systems is equally of fundamental academic and industrial interest. The synthesis of new Janus particles [Wal08] such as core-shell particles [Cra06], dumbbells [Che11, Kim06] or hollow capsules [Zha09, Fen07] is subject of various publications just like techniques to adjust the particle roughness [DAc10], softness [Sch10a] and other surface properties. Beside to the obvious and rather old attempts to modify the mechanical properties of colloidal dispersions, recently considerable effort has been taken to actively enforce certain dynamical processes. The stabilizing properties in particle-stabilized emulsions can be improved by using Janus particles with adjusted chemical surface properties [Bin01] and the self-assembly of the dispersed particles into specific structural conformations is facilitated by anisotropic particle shapes or interactions, *e. g.* in liquid-crystalline solvents [Con09, Zum10]. Just to mention one example we refer to various attempts to produce colloidal crystals via self assembly.

We followed this trend and present in chapter 3 a study of the network formation in liquid-crystal based colloidal dispersions. Instead of attractive inter-particle potentials a phase transition of the solvent caused the phase separation of the colloid into a kinetically arrested network structure. The rheology of the network was investigated with piezo-rheometry which allowed for reproducible measurements in the linear visco-elastic regime by using very small strain

amplitudes. Beside to the liquid to solid transition in course of the kinetic arrest a pronounced temperature dependent visco-elasticity was observed. This visco-elasticity was successfully related to the swelling and partial dissolution of the particles as well as to the ongoing phase transition of the solvent past the network formation (chapter 4).

### 1.4.2. Unified theories and alternative approaches

Physicists always seek to describe phenomena in nature in the simplest way possible. The discovery of universal features and the development of unifying theories play a crucial role in this attempt. Due to its long history much progress has been made in case of colloidal science, *e. g.* by means of MCT. More recently, a general jamming transition was proposed to combine colloidal and granular dispersions in a universal phase diagram of jammed and fluid states [Pra03, Tra01, Liu98]. Granular dispersions differ from colloids only with respect to the size of the constituent particles that lies in the range of  $1\ \mu\text{m}$  to  $1000\ \mu\text{m}$ . Following the discussion in section 1.1.1 Brownian motion does not play a role in these systems and gravity mostly dominates van der Waals, electrostatic or depletion forces. Though, the rheological behavior of both systems partially resemble each other, *e. g.* with respect to yielding [Cou02] or the formation of shear bands [Cou02], and thus support the idea of an universal jamming behavior.

Unfortunately, a reasonable comparison between colloidal and granular dispersions can only work if the number probed particles is large enough to allow for an representative ensemble average. Otherwise, microscopic single particle effects strongly influence the overall rheological behavior. This might be one reason why studies on granular matter are often based on the motion of each individual particle. Discrete element methods has proven to be a suitable tool to conveniently include frictional interactions and single particle properties (roughness, compliance) into simulations [Cun79, Oda00]. Vice versa, finite size effects can also occur in small colloidal systems with a restricted number of particles. In these case one might ask the question whether results from simulations and experiments can be compared to macroscopic continuum models.

We addressed this question in our study of the non-linear rheology of sedimented colloidal films with the help of nanoindentation (chapter 5). Beside to structural variations in terms of amorphous and semi-crystalline samples we enforced the aggregates by rigid solid bonds between the particles. It turned out, that within the aggregate the average microscopic deformation field due to indentation could be modeled with continuum mechanics of an elasto-plastic solid. *A priori* this result was not expected as the indentation was restricted to a very limited sample volume. Yet, the validity of continuum theory for these sedimented aggregates was also indicated by reasonable average values for hardness and elastic modulus that could be related to the particle properties.

### 1.4.3. Development of experimental techniques

In its history the investigation of colloids largely benefited from utilizing novel experimental techniques, including steadily improving rheometric equipment [Cla06, Mar98, Kir02] and specialized light scattering like diffusive wave spectroscopy [Pin88, Sch01, Rom00]. In particular confocal microscopy turned out to a liable tool to get a measure of both, the dynamic and structural structure factor of colloids [Pat08, Cam05]. This information can be compared to equivalent data from simulation and theory but at the same time is partially redundant with scattering experiments. Whereas data from scattering experiments represent an average over a large sample volume obtained in reciprocal space, confocal microscopy generates a more direct quantity, *i. e.* time-dependent 3D coordinates of individual particles in real space. Besides, confocal microscopy is not only a tool for passive observation purposes but also allow for an active manipulation of the dispersed particles. Equipped with a powerful laser the setup can be used as an optical tweezer [Gri97] in order to generate well-defined particle configurations [Mus06] or to characterize inter-particle potentials via force spectroscopy [Gam09, Tak08].

Our contribution to this continuous progress in the experimental techniques is the realization and testing of new micro-rheological methods based on confocal microscopy and specialized particles in chapter 6. Compared to homogeneous solid particles hollow particles are rather compliant and deform upon external contact forces. This deformation can be detected in confocal microscope images and quantified to get an estimate of the applied forces. In a second method optically anisotropic particles are used to detect rotational motions of individual particles. Compared to other existing methods aiming for the same goal the particle must not have a shape anisotropy and standard localization procedures (chapter 2) can be applied without major restrictions.

Besides, we explored the applicability and information gain of combined experimental techniques (chapter 2). In the study on the liquid-crystal based colloidal dispersions piezo-rheometry was complemented by simultaneous confocal microscopy which had not been done before. The combined mechanical and structural data did not only ascertain that the linear rheology of the system was tested but also gave further insights into the network formation dynamics (chapter 3). In the nanoindentation experiments of the colloidal films only the structural information from confocal microscopy allowed for a proper utilization of existing data evaluation procedures. Furthermore, confocal microscopy was used for a micro-rheological analysis of the indentation process that complemented the mechanical nanoindentation data (chapter 5).



## 2. Experimental methods

The experimental methods split up into three parts. The first two parts deal with the two central measurement techniques in the present work, confocal microscopy and rheometry in terms of piezo-rheometry and nanoindentation. We give a short overview about the working principles and describe the used setups. The bigger part of these setups were home-made and thus very versatile which allowed for an easier combination of the methods. In section 2.1 we further give a comprehensive introduction into particle localization and tracking algorithms. The chapter is closed by a short description of other experimental methods used for additional characterization of particles and dispersions.

### 2.1. Laser scanning confocal fluorescence microscope

#### 2.1.1. General working principle

In 1957 Marvin Minsky introduced the first setup of a confocal microscope in order to overcome the limited depth resolution and contrast of wide-field microscopes [Min88]. While for the latter one the specimen is fully illuminated in confocal microscopes the light source is focused by an objective to illuminate only a small point in the sample. The reflected/scattered/emitted light is collected by the same objective and imaged on a pinhole before it is quantified by a detector. The pinhole is positioned at the plane that is optically conjugated to the illumination focal spot. In this configuration light that does not originate from the focal spot is rejected by the pinhole (see Fig. 2.4). This so called confocal condition does not only involve lateral directions but also the direction along the optical axis and thus allows for a true 3D-imaging by moving the focus relative to the sample.

The maximal spatial resolution of a confocal microscope is restricted by the diffraction limitation of light [Paw06]. It accounts for the fact that the laser focus is not infinitesimally small but has a finite size. The spatial intensity distribution in the laser focus  $I_{\text{foc}}(x, y, z)$  can be calculated from the Kirchhoff diffraction integral in the Fraunhofer approximation:

$$I_{\text{foc}}(x, y, z) = I_o \left| \iint_{\text{aperture}} \exp \left[ \frac{k}{L+z} (x x' + y y') \right] dx' dy' \right|^2 \quad (2.1)$$

The integral extends over the open aperture of the objective.  $k$  denotes the wavenumber of the used light and  $L$  the distance from the aperture to the focus defined by geometrical optics.

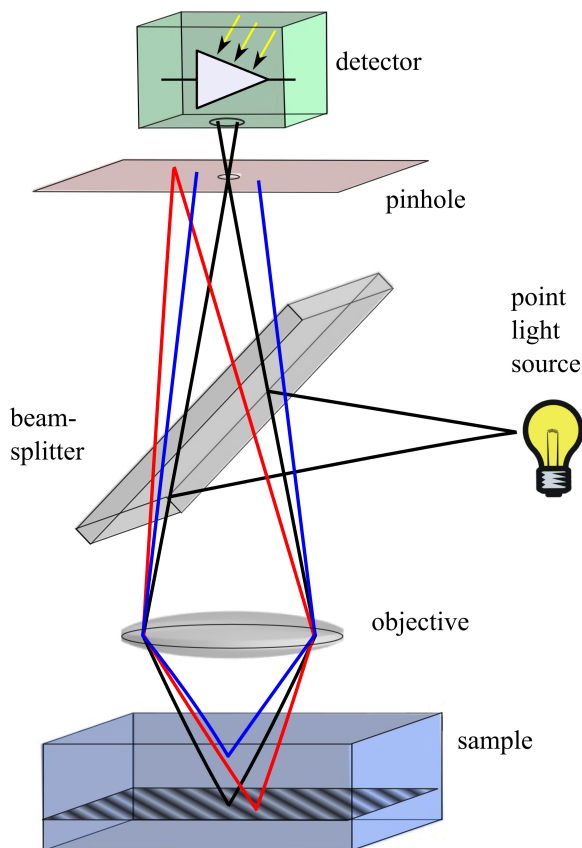


**Fig. 2.1.:** Schematic optical setup of an confocal microscope showing the confocal condition. The illumination point and the pinhole before the detector are at optically conjugated planes and thus efficiently eliminate out-of-focus light.

For a circular aperture with a radius  $R$  the integral results in the Airy function

$$I_{\text{foc}}(x, y, z) = I_o \left( \frac{2 J_1[k R \sin(\theta)]}{k R \sin(\theta)} \right)^2 \quad (2.2)$$

with  $\sin(\theta) = \sqrt{x^2 + y^2} / \sqrt{(L + z)^2 + x^2 + y^2}$  and  $J_1$  denoting the first order Bessel function.

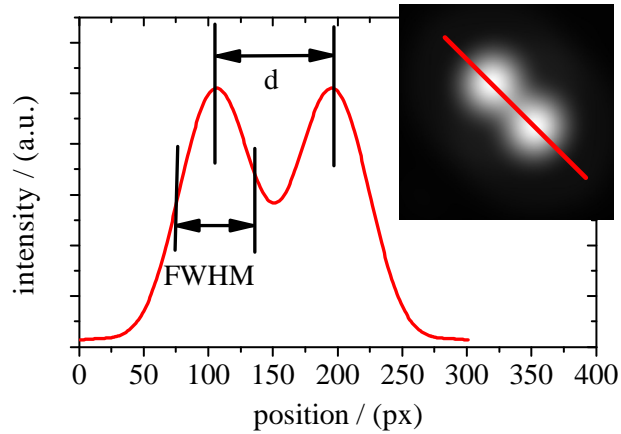
The same formalism can be applied for the detection of the reflected/scattered light. The pinhole is mathematically back-projected into the sample resulting in an equivalent Airy function  $I_{\text{pin}}$ . As the pinhole and the laser focus in the sample are optically conjugated both Airy functions can be convolved to give the total transfer function or so called point spread function  $g_{\text{PSF}}$  of the confocal microscope: to give the total transfer function or so called point spread function  $g_{\text{PSF}}$  of the confocal microscope:

$$g_{\text{PSF}}(x, y, z) = \iiint_V g_{\text{foc}}(x - x', y - y', z - z') g_{\text{pin}}(x', y', z') dx' dy' dz' \quad (2.3)$$

$g_{\text{PSF}}$  can be interpret as a weighting function that converts the spatial distribution of the optical response of the sample (reflectance, scattering strength, fluorescence) at the illuminated point into the actually measured light intensity.

Assuming a specimen consisting of two infinitesimal small scattering centers at a distance  $d$  the resulting image is shown in the inset Fig.2.4. As a general criteria in microscopy both

**Fig. 2.2.:** Simulated microscopic image of two individual point-like object (inset). Both objects can be distinguished if the extension of intensity distributions is smaller than the distance  $d$  between the points. As can be seen from the profile this criteria is fulfilled here.



points can be distinguished if  $d$  is larger than the full width at half maximum (FWHM) of the intensity maxima. This results in a spatial resolution in lateral x,y-directions of

$$d_{\text{lateral}} \approx 0.4 \frac{\lambda}{\text{NA}} \quad (2.4)$$

with  $\lambda$  and NA denoting the wavelength of the used light and NA the numerical aperture of the objective [Paw06]. A lateral resolution of  $0.25 \mu\text{m}$  is a typical value for high numerical aperture objectives ( $\text{NA} > 1.3$ ). Along the optical axis the resolution is decreased by a factor of 2-3 and can be approximated by

$$d_{\text{axial}} \approx 1.4 \frac{\lambda n}{\text{NA}^2} \quad (2.5)$$

Here  $n$  gives the refractive index of the surrounding medium.

### 2.1.2. Characteristics of the home-made setup

Commercially available state-of-the-art confocal microscopes use either fast scanning units like *e. g.* resonating mirrors or acusto-optical deflectors to scan the laser focus through the sample or a multi-beam illumination by means of Nipkow-spinning disks for a simultaneous imaging at different foci. As a result these systems record 2D images at video-frame rates of 60 Hz and higher depending on the scanning parameters. Most systems work in reflection or fluorescence mode<sup>4</sup> incorporating several combinations of excitation and detection wavelengths which can be operated simultaneously [Sem05]. Different objectives and pinhole sizes are available to adjust spatial resolution and the depth of field. Despite these comforts we constructed a home-made confocal microscope for the following reasons:

- The confocal microscope needed to be combined with various other experimental setups such as the piezo-rheometer together with the temperature control unit (section 2.2.1) or

<sup>4</sup>The detected intensity results from an fluorescence process within the sample. Either the sample is labeled on purpose with fluorescent dyes or the specimen shows auto-fluorescence which is often the case in biological samples. By variation of the wavelengths of the illumination light and optical filters in the detection path of the microscope special several dyes can be individually addressed.

the indentation module (section 2.2.2). These devices demand for a increased flexibility of the confocal setup already starting with varying space requirements on the sample stage. Furthermore special care has to be taken on the vibration isolation of the sample stage since in particular the piezo-rheometer will react with an enhanced noise level to any additional source of vibration. These specifications are usually not met by commercial microscopes.

- Certain methods like *e. g.* the rotation analysis (section 6.2) ask for a special preparation of the incident beam. This is most conveniently accomplished if the optical beam path is accessible.
- Other options like the possibility to change the laser wavelength or the objective during the experiments are not required. Diameters of the used particles lie in the range of  $1 - 2 \mu\text{m}$ . Hence, only objectives with numerical apertures of 1.3 and higher give rise to a sufficient spatial resolution in order to extract reliable 3D coordinate. Such a high NA can only be reached with an oil immersion objective at a magnification of  $100\times$ . In this case the 2D field of view is automatically limited to  $(150 \mu\text{m})^2$ .

### Instrumentation

The schematic setup with all relevant optical elements is shown in Fig. 2.3. The probing laser (Cobolt Samba™532 nm with a maximum power of  $P_{max} = 25 \text{ mW}$ , Cobolt AB, Sweden) beam is coupled into the optical path via a polarization maintaining single mode fiber. After a change to circular polarization (Glan-Thomson polarizer, Bernhard Lange Nachf. GmbH, Germany, and  $\lambda/4$  quartz retardation plate, Linos, Germany, at relative angle of the principle axes  $45^\circ$ ) and attenuation to a intensity level of  $(0.001-1) \%$  it is expanded to a beam diameter of 8 mm. A small amount of the beam intensity is cut for beam diagnosis via a CCD camera module while the bigger part is separated in two halves, one being used to measure the beam intensity (PM100D compact power meter, Thorlabs GmbH, Germany) and the other to illuminate the sample. After passing the dichroic mirror (Laser-beamsplitter z 532 RDC, 90% transmission above 545 nm, AFH Analysetechnik AG, Germany) a galvanomotor based scanning unit (SCANcube®7, SCANLAB AG, Germany) scans the focus across the fixed sample in x,y-directions. A telescope is used to project the pivot point of the scanning unit into the entrance aperture of the focusing objective (UPlanApo PH3,  $100\times$  oil immersion, NA=1.35, working distance  $170 \mu\text{m}$ , Olympus Deutschland GmbH, Germany). The z-position of the objective is controlled with a piezo-positioning system (nanoX 200 S, ENV 40 SG nanoX, Piezosysteme Jena GmbH, Germany). The collected fluorescent light (Rhodamin B or Nile Red) is separated from the excitation laser light firstly by the dichroic mirror and directly before the detector by a optical high pass filter (laser clean-up filter z 532/10, AFH Analysetechnik AG, Germany). A single lens focuses the transmitted light on an avalanche photo diode (id100, idquantique, Switzerland) with an active area of  $(50 \mu\text{m})^2$  in size directly acting as the confocal pinhole. Photons are detected with a high quantum efficiency of about 25 % at a maximum count rate of 17 MHz. As single photons are counted (NI PCI-6602 Counter/Timer, National Instruments

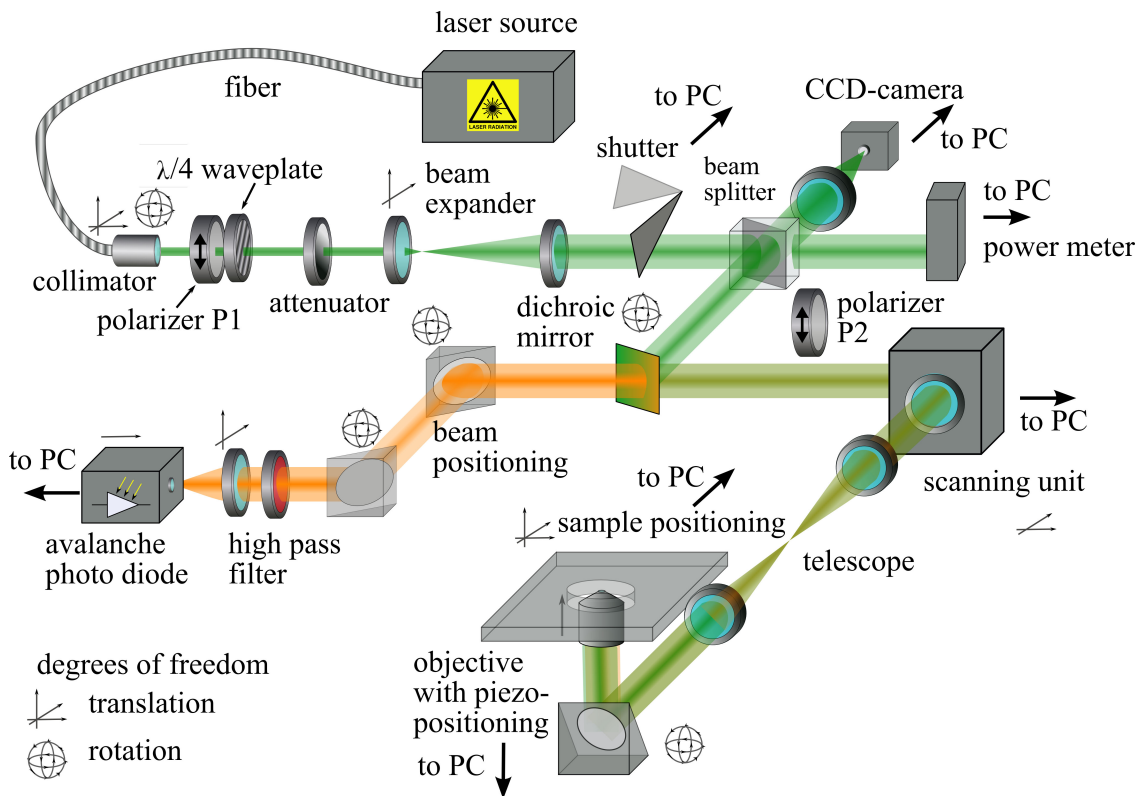


**Fig. 2.3.:** Schematic optical setup of the home-made laser scanning confocal microscope. For the analysis of rotational particle movements, we added the polarizer P2 between the dichroic mirror and the scanning unit.

Germany GmbH, Germany) only small input intensities of down to 50 nW are needed (depending on the type and amount of dye). For the polarization dependent bleaching of particles (section 6.2) a thin film polarizer (VIS 4 K, Linos Photonics GmbH & Co. KG, suppression ratio 1:4000, Germany) is placed between the dichroic mirror and the scanning unit.

The sample is placed on a sample stage (xyz, xy-range 50 mm, z-range 30 mm) equipped with stepping motors (miCos GmbH, Germany, and HVM 100 from OWIS GmbH, Germany, controlled with a LSTEP-PCI module, Lang GmbH & Co.KG, Germany) for a coarse positioning. Most of the electronic elements are controlled by a personal computer via a graphical user interface programmed in LabVIEW™ (Version 8.5, National Instruments Germany GmbH, Germany). The scanning unit and the piezo-positioning of the objective are operated indirectly via synchronized waveform generators (33220A, Agilent Technologies Deutschland GmbH, Germany). Detailed information about the interplay of all components together with the software architecture can be found in appendix A.

### Operation parameters

In the standard operation mode the fluorescence intensity is recorded discretely as a photon count at fixed 3D pixel (px) positions while the beam is scanned across the sample. The pixels are evenly distributed on an 3D orthogonal grid at a spatial sampling rate in the range of

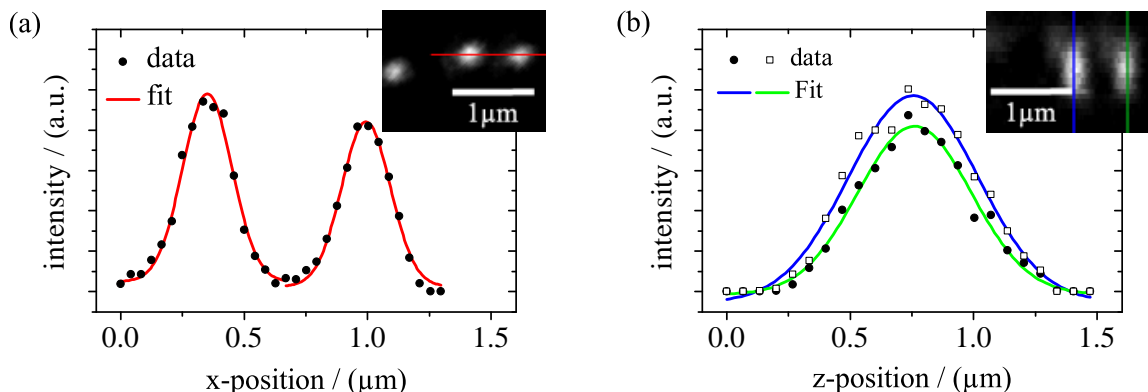


**Fig. 2.4.:** Small  $\text{SiO}_2$  particles were imaged to estimate the resolution of the confocal microscope in lateral  $x,y$ -directions (a) and axial  $z$ -direction (b). The line profiles from  $xy$ - and  $xz$ -cuts (insets) were fitted by a Gaussian function.

$[3.4 - 10]$   $\text{px}/\mu\text{m}$  in lateral  $x,y$ -directions and  $[2 - 5]$   $\text{px}/\mu\text{m}$  in axial  $z$ -direction. Using a  $100\times$  objective the field of view is limited to about  $150\ \mu\text{m}$  in each direction. At larger extensions the spherical aberration causes a reduction of the detected fluorescence intensity and blurring of the image. The maximal scanning speed of the galvanometers is  $1000\ \text{Hz}$  resulting in imaging times of about  $0.5\ \text{s}$  for a 2D-frame and  $5\ \text{min}$  for a 3D data set at a reasonable image size of  $(512 \times 512 \times 256)\ \text{px}^3$ .

In the following we shortly discuss the spatial resolution of the present setup. The inset in Fig. 2.4 shows  $xy$ - and  $xz$ -cuts of a 3D confocal data set of fluorescent labeled particles with a diameter of about  $100\ \text{nm}$ . As these particles were smaller than the theoretical resolution of the microscope, effectively the extension of the point spread function  $g_{\text{PSF}}$  was tested as we already discussed above. The line profiles could be fitted by an Gaussian function with a FWHM of  $(235 \pm 5)\ \text{nm}$  in  $xy$ -direction and  $(570 \pm 30)\ \text{nm}$  in  $z$ -direction. These values are in reasonable agreement with the expected resolution in equations (2.4) and (2.5).

### 2.1.3. Localization of particles

In first place confocal microscopy serves the same purposes like wide-field microscopy, *i. e.* real space imaging of the specimen under study. The information gain from the improved spatial resolution especially in axial direction opens up routes for 3D structural characterization which we will exploit in chapter 3.

In colloidal systems the confocal data can be further used to extract 3D coordinates  $\vec{r}_n$  of the constituent particles. Before we go into detail about the used algorithm we shortly derive the mathematical expression of the detected intensity distribution. Assuming fluorescent labeled particles at the positions  $\vec{r}_n$  with a distribution of dye molecules  $g_{\text{dye}}(\vec{r})$  inside the particles the fluorescent light  $I_f$  emitted from point  $\vec{r} = (x, y, z)$  is proportional to

$$I_f(\vec{r}) \sim \sum_n g_{\text{dye}}(\vec{r} - \vec{r}_n) \quad (2.6)$$

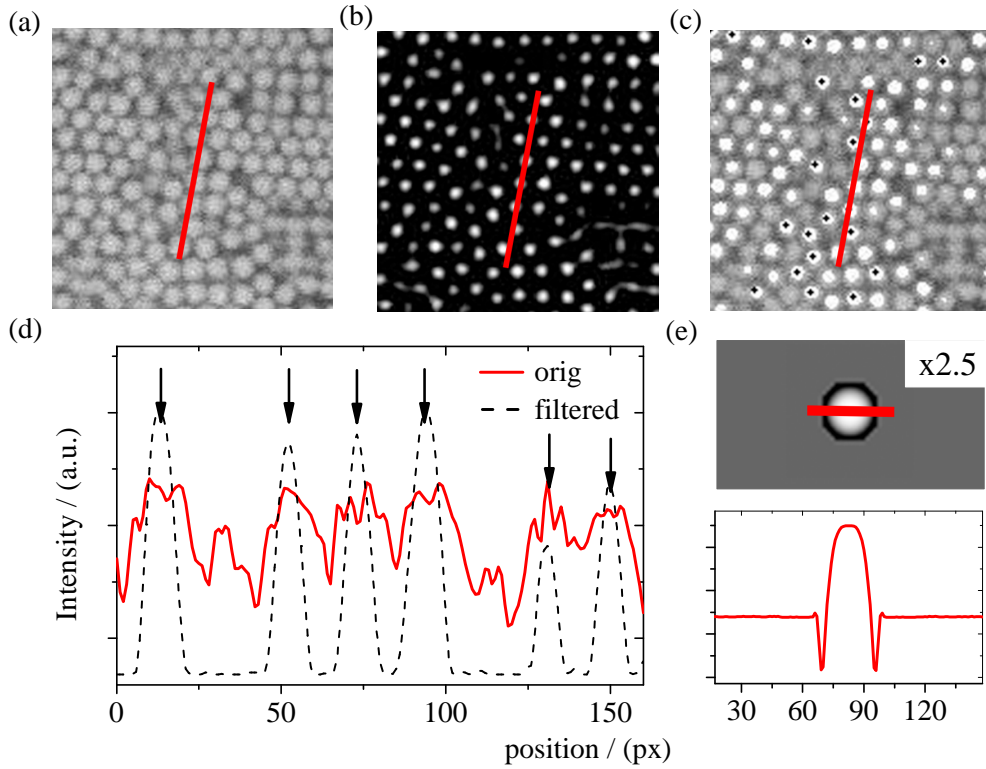


**Fig. 2.5.:** Localization algorithm after Crocker, Grier and Weeks shown for xy-cuts through the 3D fluorescence intensity data: (a) Although the individual particles can be identified in the original intensity distribution (top) the line profile (d) is rather noisy which hinders an automated localization. (b) After filtering the convolved intensity shows pronounced, smooth maxima. (c) After refinement of the maximum positions the localization of the particles is complete. Particles with mean z-positions close to and within the shown xy-cut are indicated by white circles and white circles with black dots, respectively. (e) The shape and extension of the mask distribution is identical to that of the particle in the original image. Compared the former ones the image is magnified by a factor of 2.5 for better visualization.

$\sum_n$  denotes the sum over all particles in the observation volume. Due to the finite resolution of the optical imaging  $I_f$  needs to be convolved with the PSF  $g_{\text{psf}}$  to give the detected intensity:

$$I_d(\mathbf{r}) \sim \int_V g_{\text{PSF}}(\mathbf{r} - \mathbf{r}') \left( \sum_n g_{\text{dye}}(\mathbf{r}' - \mathbf{r}_n) \right) d^3 r' \quad (2.7)$$

Iterative deconvolution methods [McN99] can be used to solve equation (2.7) for the particle positions  $\mathbf{r}_n$  if the distributions  $g_{\text{dye}}$  and  $g_{\text{PSF}}$  are known. While  $g_{\text{PSF}}$  can be obtained theoretically and in experiments [Nas07] (Fig. 2.4),  $g_{\text{dye}}$  is accessible via reasonable assumptions. However, these algorithms suffer from long computation times.

The problem is simplified for big and/or well separated particles since the apparent distribution function

$$g_{\text{app}}(\mathbf{r} - \mathbf{r}_n) = \int_V g_{\text{PSF}}(\mathbf{r} - \mathbf{r}') g_{\text{dye}}(\mathbf{r}' - \mathbf{r}_n) d^3 r' \quad (2.8)$$

does not overlap significantly for neighboring particles. The particles are represented by more or less well separated intensity maxima. In this case a time-expensive deconvolution procedure is unnecessary and replaced by a more practical approach. The algorithm introduced by Crocker and Grier [Cro96] and extended by Weeks [Wee00a] involves three steps: a local filtering to improve the image quality, a coarse determination of the particle coordinates and a subsequent refinement to subpixel accuracy. The filtering is done via an additional 3D-convolution of the experimental data set with a mask  $g_{\text{mask}}(i, j, k)$ :

$$C(l, m, n) = \sum_{i,j,k} g_{\text{mask}}(l - i, m - j, n - k) \cdot I_d(i, j, k) \quad (2.9)$$

Here we switched from continuous coordinates  $\vec{r}$  to the experimentally relevant case of indexed coordinates  $(x_i, y_j, z_k)$  and the discrete 3D intensity data  $I_d(i, j, k)$ . If the mask distribution  $g_{\text{mask}}$  is modeled to match the apparent distribution  $g_{\text{app}}$  [Fig. 2.5 (e)] the 3D convolved intensity  $C$  is maximal in the center of the particle. Here the measured intensity and the mask distribution overlap completely. With increasing separation of mask and particle the convolved intensity decreases. This procedure does not only sharpen the original intensity maxima but also reduces data scatter by replacing  $I_d$  with the locally averaged quantity  $C$ . In the initial computational implementation of this algorithm by Crocker, Grier and Weeks<sup>5</sup> a centered Gaussian profile with an extension  $\sigma_{x,y,z}$  similar to the particle size was used as mask distribution:

$$g_{\text{mask}}(i, j, k) = \frac{1}{\sqrt{2\pi(\sigma_x^2 + \sigma_y^2 + \sigma_z^2)}} \exp \left[ - \left( \frac{x_i}{2\sigma_x^2} + \frac{y_j}{2\sigma_y^2} + \frac{z_k}{2\sigma_z^2} \right) \right] \quad (2.10)$$

Exemplary data are shown in Fig. 2.5 (a,d) as a xy-slice through the complete 3D confocal image and as a line profile. A poor signal-to-noise ratio prevents an automatized localization of the particles from these raw images. The filtering, however, generates well separated maxima in the convolved intensity  $C$  with a high signal-to-noise ratio Fig. 2.5 (b,d) which can be easily localized. Misidentification is avoided by setting a threshold value for the intensity  $C$  as well as a minimal distance between two maxima given by the diameter of the particles. Though, the extracted maximum positions are referenced by the set of indexes  $(i, j, k)_{\text{max}}$  and therefore only accurate within one pixel. Further sub-pixel accuracy is obtained if the mean maximum position, intensity weighted with the local convolved intensity around the maximum, are calculated:

$$(x, y, z)_{\text{max}} = \sum_{C(i,j,k) > C_{\text{th}}} (x_i, y_j, z_k) C(i, j, k) \quad (2.11)$$

Again a suitable threshold  $C_{\text{th}}$  is applied to prevent any coupling to nearby maxima and background scatter. In general an additional local background subtraction simplifies the localization process. This can already be incorporated into  $g_{\text{mask}}$  by subtracting the reciprocal of

<sup>5</sup><http://www.physics.emory.edu/weeks/idl/>, E. Weeks, 06/2010/06



its total sum:

$$\tilde{g}_{\text{mask}}(i, j, k) = g_{\text{mask}}(i, j, k) - 1 / \left( \sum_{lmn} g_{\text{mask}}(l, m, n) \right) \quad (2.12)$$

The result of the localization procedure is shown in Fig. 2.5 (d).

The algorithm can be used for particles with arbitrary spherical symmetric profiles if the mask distribution  $g_{\text{mask}}$  is modeled appropriately. In chapter 6.1 we will discuss the special case of hollow particles in connection with a analysis of the deformation state when forces are applied to the particles. On the contrary anisotropically shaped particles without intrinsic mirror symmetries cannot be localized reliably.

#### 2.1.4. Tracking of particles

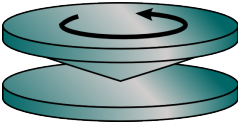
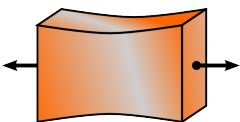
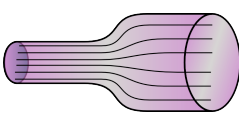
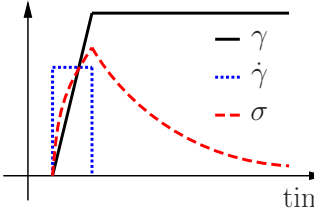
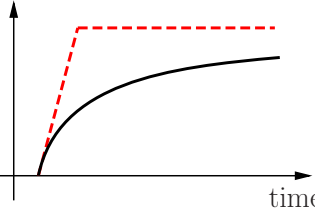
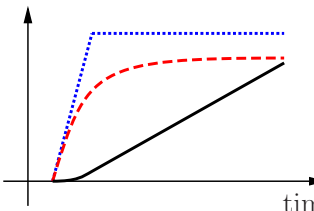
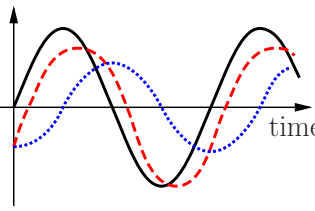
If the sample volume is imaged continuously tracking algorithms can be used to connect the 3D coordinates to 3D trajectories of the individual particles [Cro96, Wee, Lu07]. The assignment of the particles to their equivalent in the subsequent confocal image is based on the assumption that the total displacement of all particles within each step is minimal. Obviously, this definition leads to wrong results if the particles move too far from their initial position within a single step. Moreover, the number of possible trajectories rises strongly with the number of particles  $N$  and confocal images  $m$  according to  $\mathcal{O}(N^m)$ . Therefore, it is necessary to limit the maximal displacement of each particle which is accomplished by a sufficiently small waiting time between two consecutive confocal images. Consequently, fast Brownian motion of small particles and large shear rates generally require high scanning speeds [Zau08]. The processes studied in the present work, however, are rather slow and the scanning speed of the home-made setup does not impose limitation to the experiments. We used a freely available implementation of the tracking algorithm by Crocker, Grier and Weeks.<sup>6</sup>

## 2.2. Rheometry

The term rheometry comprises all experimental measurement techniques designed to determine the bulk mechanical properties of a material. In principle, any method that is capable of controlling and/or quantifying stresses and deformations in a specimen can be used. This definition appears to be quite extensive and indeed, in course of its long history a large variety of rheometers have been developed. A classification is possible in terms of the geometry and amplitude of the deformation, its temporal execution characteristics as well as the consistency of the material that can be handled. Some options for these parameters are illustrated in Tab. 2.1.

One of the most frequently used setups are oscillatory shear rheometers with a plate-plate geometry. Here the sample is placed between two parallel plates one of which is used to apply a periodic deformation  $\gamma(\omega, t)$  (compare section 1.2.1 and Fig. 1.6). The second plate is connec-

<sup>6</sup><http://www.physics.emory.edu/weeks/idl/tracking.html>, E. Weeks, 06/2010/06

|   |  |   |   |
|---|--|---|---|
| <b>Geometry</b>                           | <br>cone-plate  | <br>uniaxial extension                            | <br>capillary flow |
| <b>Amplitude</b>                          | <p>The magnitude of the deformation <math>\mathbf{B}</math> (solid-like) or rate of deformation <math>2\mathbf{D}</math> (liquid-like) decides whether the linear or non-linear visco-elasticity of the material is tested. The most important non-linear phenomena are yielding, fracture, shear-thinning and shear-thickening.</p> |   |   |
| <b>Temporal execution characteristics</b> | <br>Progressive: Stress relaxation after sudden shear strain  | <br>Progressive: Creep after sudden shear stress |   |
|   | <br>Steady state: Continuous shear  | <br>Periodic: oscillatory shear strain         |   |
| <b>Consistency of the sample</b>          | <p>One distinguishes methods for liquid, viscoelastic and solid materials.</p>   |   |   |

**Tab. 2.1.:** Parameters for classification of rheometers. See section 1.2.1 for the definition of  $\gamma$ ,  $\dot{\gamma}$  and  $\sigma$ .

ted to a transducer that measures the shear stress  $\sigma(\omega, t)$  transmitted through the sample. From these two quantities the complex shear viscosity  $\eta^*(\omega)$  and the complex shear modulus  $G^*(\omega)$  can be calculated according to the constitutive relation (1.29). These rheometers are frequently used in shearing mode because of their easy operation, choice of plate geometries (parallel plates, cone-plate, couette) and direct interpretation of the data. There are no special demands on the sample, *i. e.* elastic, viscoelastic and fluid materials can be tested. Moreover, the frequency of the applied deformation can be set easily which is why this method is also referred to as dynamic mechanical analysis. Due to their long history and mature machinery we refer to such kind of traditional setups as classical rheometers. For a more detailed description, in particular of experimental realizations in terms of driving motors, transducer

working mechanisms and mounting of the plates, we refer to standard introductory literature on rheology [Mac94, Fer80a].

More recently, other measurement principles utilizing particles have been introduced in order to serve special purposes. In particle image velocimetry small particles are used to investigate how an liquid flows in complicated geometric environments. As the particles are dragged along with the liquid, three-dimensional flow profiles can be extracted from stereographic images of the particle movements. By contrast, some micro-rheological methods utilizes the Brownian motion of small particles to determine the viscosity of a quiescent liquid. As the particle displacement is limited to a small volume it is possible to test the sample very locally.

In the present work we apply *piezo-rheometry*, nanoindentation and specialized micro-rheometry using confocal microscopy for mechanical characterization. In the following we go through the peculiarities and advantages of the first two methods while the latter one will be discussed in detail in chapters 5 and 6.

### 2.2.1. Piezo-Rheometer

The schematic setup of piezo-rheometers strongly resemble that of classical oscillatory rheometers. Though, excitation and detection is not realized with the help of electromotors and optical/capacitive transducers but rather with piezoelectric actuators by means of the piezo-electric and inverse piezo-electric effect. This has several advantages when dealing with colloids. While used strain amplitudes for classical rheometers typically lie in the range of  $10^{-2}$ , piezo-rheometers work at about  $10^{-4}$ . At these small strains yielding is prevented even for soft and fragile materials which makes piezo-rheometers in particular suitable for measurements in the linear regime. Moreover, the use of piezoelectric actuators allows for a compact design. Sample volumes can be reduced to  $10\mu l$  and reduced inertia moments shift the upper frequency limit to 1 kHz beyond which resonance effects prevent an accurate determination of the shear modulus. At last the compactness of the rheometer also allows for a combination of rheometry with other methods like confocal microscopy as we will discuss below (section 2.2.1)

The first piezo-rheometer was introduced by Durand and coworkers [Bar77, Cag80] in their study on smectic liquid crystalline phases. Here small strains were essential since deformation energies required for the formation of unwanted defects were low. Beside the above mentioned shearing mode also squeeze flow geometries were applied. Yamamoto et al. [Yam86, Yam90] and Martinoty et al. [Mar98, Aue06, Col03] continued the development of the piezo-rheometer but stick to the original design that is also used in the present work. In the last decade several other rheometers were constructed using piezo-elements to extend their applicability. Flexure based rheometers [Cla06] can measure smaller shear moduli as well as normal forces and torsional resonant rheometers further extend the frequency range to few 100 MHz [Wil07].

#### Detailed description of the home-made setup

The central elements of our piezo-rheometer are shown in the schematic setup of Fig. 2.6: two piezo-ceramic-stacks (PICA<sup>TM</sup>-Shear Piezo Actuators; PICeramic, Lederhose, Germany) were

glued to a glass substrate on one side and a massive glass holder on the other side. Both glass holders were fixed together with screws defining a gap between the two glass substrate, that was filled with the sample. The gap size  $D$  could be varied between  $10\ \mu\text{m}$  and  $1\ \text{mm}$  with three fine thread screws at an absolute accuracy of better than  $3\ \mu\text{m}$ . The following alignment procedure was applied. After fixing the two glass holders the gap size was reduced until the glass substrates touched each other. Then all three fine thread screws were screwed in successively in order to stepwise increase the gap between the substrate glasses. Up to gap sizes of  $50\ \mu\text{m}$  plate parallelism was checked with Newton rings generated by multiple reflection from the substrate glass-air-interfaces. The quality of parallelism was estimated to be better than  $0.01^\circ$ . The absolute gap size was determined from the total distance of the glass holders at the center minus the corresponding distance when the glass substrates touched each other. At larger gap sizes parallelism of the plates was checked by measuring the distance of the glass holders at the edges. This procedure slightly depressed the accuracy in the parallelism which yet was good enough to exclude any significant influence on the extracted values of the shear modulus. The dimensions of the glass substrates and the whole cell were  $(12 \times 20 \times 2)\text{mm}^3$  and  $(55 \times 58 \times 100)\text{mm}^3$ , respectively. As can be seen in Fig. 2.6 the glass substrates were larger than the piezo-actuators and mounted asymmetrically. This allowed for microscopic imaging of the sample inside the rheometer at a low magnifications. We used a CCD-camera (Evolution<sup>tm</sup> MP Color; Media Cybernetics) and imaging optics (ZOOM 70XL; Opto Sonderbedarf GmbH) of up to  $6\times$ -magnification.

The excitation piezo actuator was electronically connected to a frequency generator (33220A, Agilent) to apply a sinusoidal voltage  $V_E(t)$  to the ceramics.

$$V_E(t) = V_{Eo} \cdot \sin(\omega \cdot t) \quad (2.13)$$

In our case the frequency  $f = \omega/2\pi$  was varied in the range of  $0.1\ \text{Hz}$  to  $1000\ \text{Hz}$  and the amplitude  $V_{Eo}$  was set in the range of  $0.2\ V_{pp}$  to  $18\ V_{pp}$ . According to the inverse piezo-electric effect and the specific polarization of the ceramics this voltage is transferred to a shear

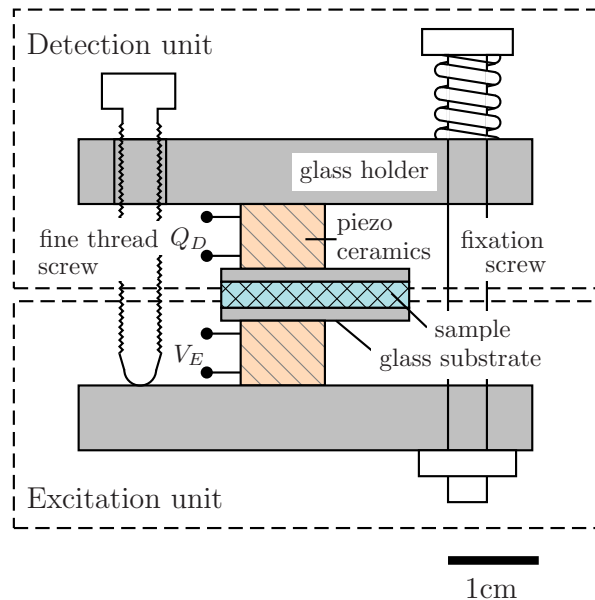


**Fig. 2.6.:** Schematic view of a symmetric shear piezo-rheometer. Used symbols are explained in the text.

deformation  $s(t)$  of the sample at the glass substrate according to:

$$s(t) = d_{15} \cdot V_E(t) \quad (2.14)$$

The proportionality constant amounted to  $d_{15} = (3.4 \pm 0.1) \cdot 10^{-8}$  m/V giving absolute deformations from  $s_{\min} = 7$  nm up to  $s_{\max} = 600$  nm.

The deformation propagated through the sample via the frequency dependent complex shear modulus  $G^*(\omega)$ . The resulting stress  $\sigma(t)$  at the upper glass substrate gave rise to the generation of free charges  $Q_D(t)$  in the piezo actuator of the detection unit by means of the piezo-electric effect:

$$Q_D(t) = d_{15} \cdot \sigma(t) = d_{15} \cdot G^*(\omega) \cdot \frac{s(t)}{D} \quad (2.15)$$

These generated charges were collected with a charge sensitive amplifier (Type 2635, Brühl & Kjaer ) and converted into a voltage  $V_D(t)$ .  $V_D(t)$  was recorded simultaneously with the excitation voltage by an oscilloscope (DSO6044, Agilent). As the stress was directly proportional to the voltage  $V_D(t)$ , the amplitude ratio and the phase difference of  $V_E(t)$  and  $V_D(t)$  was a direct measure of the complex shear modulus of the sample.

In the case of low signal levels the deformation of the detection piezo could be as small as 0.2 pm and generated charges amounted to about 0.1 pC equivalent to a stress of  $\sigma_{\min} = 1$  Pa. In combination with the sample thickness  $D$  this amounts to a minimal resolvable shear modulus of

$$|G_{\min}^*| = \frac{\sigma_{\min}}{s_{\min}} \cdot D \approx 5 \text{ Pa}/\mu\text{m} \cdot D \cdot A \quad (2.16)$$

The empirical scaling factor  $A$  was influenced by the actual data recording and processing. Typically we recorded  $V_E(t)$  and  $V_D(t)$  over ten periods ( $T = 2\pi/\omega$ ) at a sampling rate of at least  $10^5$  points per period. The complete data set was processed via fast fourier transformation in order to define averaged values for the shear modules. For above mentioned parameters  $A$  amounted to approximately 0.05.

Vibrational isolation was achieved by an active anti-vibration table (T140, Table Stable Ltd., Switzerland) while electro-magnetic isolation, intrinsic to the piezo-ceramics, was relied upon. Our ceramics consisted of stacks of single sheets with alternating crystal orientations and electric contacts which effectively canceled long-wavelength electro-magnetic radiation. Additionally, cable connections to the actuators were enclosed by a metal shielding, not shown in Fig. 2.6.

### Gauging measurements

To obtain absolute values for the complex shear modulus we calibrated the rheometer with two certified calibration fluids (DKD - Deutscher Kalibrierdienst, Germany). These fluids were supposed to behave purely as Newtonian liquids in a broad frequency range. The dynamical viscosities  $\eta$  at 25 °C were stated at about 2 Pa.s (2000AW, DKD) and 100 Pa.s (100000BW, DKD). Exemplary measurements of the frequency dependency of the loss modulus  $G''$  for 100000BW at three different temperatures are shown in Fig. 2.7 (a). In the double-logarithmic

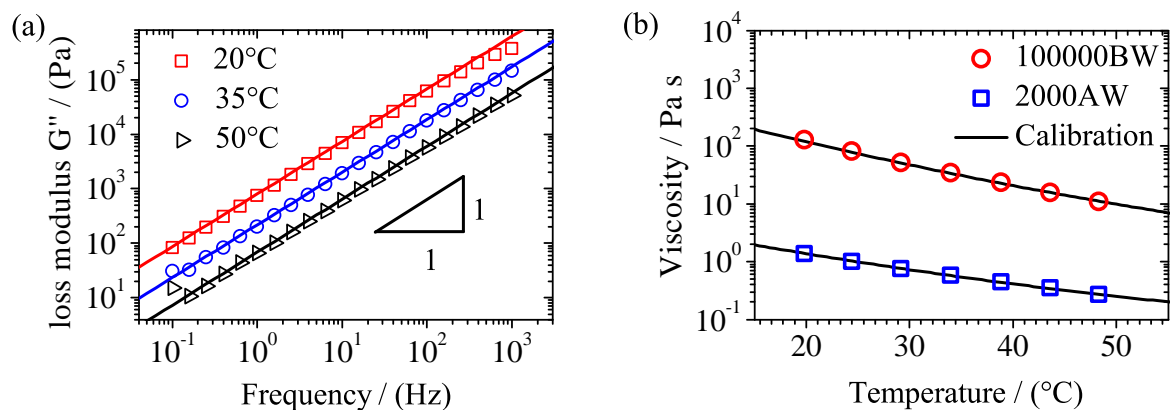


**Fig. 2.7.:** Calibration measurements of Newtonian liquids 2000AW and 100000BW. Graph (a) shows the frequency dependency of the loss modulus  $G''$  of 100000BW at three different temperatures together with the fit according to  $G'' = 2\pi f\eta$  with  $\eta$  as the dynamic viscosity (straight lines with a slope of 1 Pa s). In the left graph (b) the viscosity  $\eta$  is plotted against the temperature for both compounds together with the calibration curves (solid lines) provided by the Deutscher Kalibrierdienst GmbH.

plot a straight line was fitted to the loss modulus according to  $G'' = 2\pi f\eta$ . The dynamical viscosity  $\eta$  was extracted as the only fitting parameter. Measurements were repeated and completed for other temperatures in order to compare the extracted temperature dependency to the calibration data [Fig. 2.7 (b)]. Agreement was observed for the whole temperature range with an uncertainty of less than 3%.

For high frequencies and low temperatures the loss modulus,  $G''$ , deviated from the straight line of the fit. This behavior was related to internal relaxation processes due to the polymeric nature of the gauging liquid [Fer80a] (see also appendix B).

### Temperature control

The gauging measurements as well as the study of the liquid crystal-colloid suspensions in chapter 3 the sample temperature demanded for a temperature control of the sample. Convictional heating and cooling could not be used since any ventilation would lead to an increased noise level in the rheological data. Thermal conduction is not an option either because it implies large temperature gradients and a complex installation. Therefore the whole rheometer was placed inside a massive ( $100 \times 100 \times 120$ ) mm<sup>3</sup> brass cube in order to heat and cool the rheometer along with the

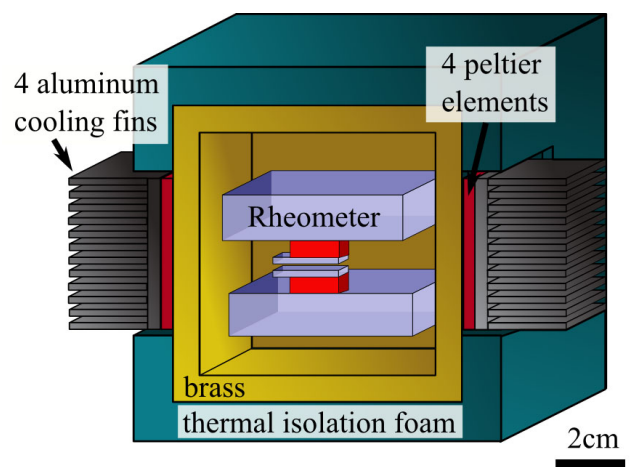


**Fig. 2.8.:** Temperature control of the piezo-rheometer. See text for details.

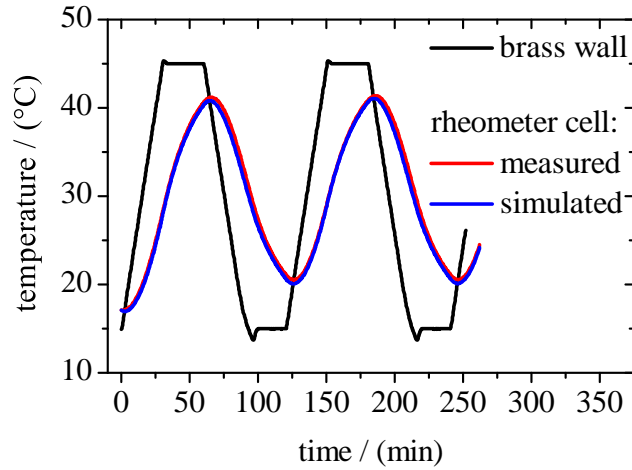


**Fig. 2.9.:** Simulation of the rheometer-cell temperature for a given temporal temperature profile  $T_w(t)$  of the wall according to (2.17). A proportionality constant of  $\alpha \sigma C_c = 3.5 \cdot 10^{-10} \text{ 1/K}^3 \text{ s}$  was used.

sample via radiation. The temperature of the brass cube itself was adjusted by four peltier elements that were mounted to the outer walls (Fig. 2.8). Additional thermal isolation prevented extensive heat exchange with the environment.

According to the Stefan-Boltzmann law for black body radiation any temperature difference between the rheometer cell  $T_c$  and the metal walls  $T_w$  led to a net radiation power  $P_c$  that was exchanged between the metal walls and the cell:

$$P_c = \alpha \sigma_{SB} (T_w^4 - T_c^4)$$

Here  $\sigma_{SB}$  was Stefan-Boltzmann constant and  $\alpha$  a proportionality constant that accounted for the specific geometry of the cell inside the walls. The heat transmitted to the cell within a short time interval  $\Delta t$  gave rise to a change in the cell temperature depending on the heat capacity of the cell  $C_c$ :

$$\begin{aligned} \Delta T_c &= \alpha \sigma_{SB} C_c (T_w^4 - T_c^4) \Delta t \\ &\approx 4 \alpha \sigma_{SB} C_c (T_w - T_c) T_c^3 \Delta t \end{aligned} \quad (2.17)$$

The temperature  $T_w$  of the metal wall was assumed constant. Starting from equilibrium with identical known temperatures, (2.17) could be numerically integrated for any temporal evolution of the wall temperature  $T_w(t)$  to obtain the cell temperature  $T_c(t)$  once the effective proportional constant  $\alpha \sigma_{SB} C_c$  was found. Although substantial simplifications with respect to black body radiation and the complex geometrical configuration of cell and brass cube were made in this derivation, a calibration was possible (Fig. 2.9).

According to the electric control of the setup the temperature stability of the walls and in thermal equilibrium also that of the rheometer cell was better than 0.05 K. As the thermal mass of the rheometer cell was large and  $P_c$  only varied linearly with the temperature difference  $T_w - T_c$ , we further estimated the homogeneity of the temperature across the sample to be better than 0.01 K. For the same reasons however maximum cooling and heating rates are limited to  $\pm 0.5 \text{ K/min}$ . The accessible temperature range of  $20^\circ \text{C}$  to  $60^\circ \text{C}$  was sufficient for

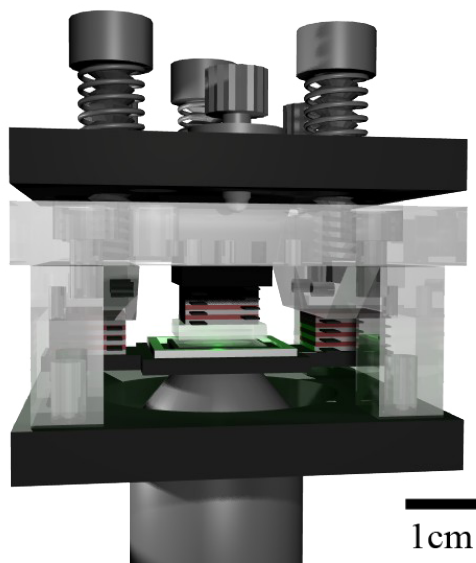


**Fig. 2.10.:** Computer rendered realistic view of an asymmetric shear piezo-rheometer that can be combined with the confocal microscope. The lower glass substrate is directly accessible with the objective (also shown) from below. For better visualization part of the supporting metal base was set transparent. The scale bar indicate approximate size dimensions.

our experiments.

### Combination with the confocal microscope

As it was already mentioned in preceding sections confocal microscopy and piezo-rheology were combined in order to get simultaneous mechanical and structural information. This is only possible for an asymmetric setup where the lower glass substrate is accessible with the objective. A computer rendered realistic view on the rheometer cell together with the objective is shown in Fig. 2.10. The original design in Fig. 2.6 was modified as follows. Most importantly, the single piezo-actuator in the lower excitation unit was replaced by two actuators that were connected in parallel to the waveform generator. Thereby, we generated free space to reverse the excitation unit and bring it closer to the detection unit which left the two glass substrates exposed at the bottom. In addition, confocal imaging with a  $100\times$ -oil immersion objective required a thickness of the lower excitation glass substrate of only  $170\ \mu\text{m}$ . In order to maintain a certain degree of stability the substrate was enforced by a metal plate that left only a small area accessible for the objective. Moreover, the glass from the supporting frame was replaced by steel which allowed for an easier manufacturing and a more open architecture of the rheometer. Invar<sup>®</sup> steel (Goodfellow GmbH, Germany) turned out to be a good choice as it had a similarly low thermal expansion coefficient like glass.

### 2.2.2. Nanoindentation

In contrast to piezo-rheometry indentation experiments are especially useful for measurements in the non-linear viscoelastic regime. Instead of the shear modulus  $G'(\omega)$  and  $G''(\omega)$ , hardness  $H$  and Young's modulus  $E$  are the quantities reflecting the mechanical properties of the tested material. While the Young's modulus solely accounts for the elasticity, the hardness is more difficult to define. In a nutshell it measures the mechanical resistance of the specimen against



any deformation with an even harder material. As such the hardness has contributions of elastic and plastic deformations. Eventually local fracture also plays a role. These varying influences demand for further classification of the hardness in terms of the used testing procedures. One distinguishes between scratch hardness, rebound hardness and indentation hardness. Originally scratch hardness is a relative measure, *i. e.* one material A is said to be harder than another material B, if A can scratch B without being destroyed itself. Although this method was known in ancient times, Only in 1812 Mohs introduced a reference scale of ten ‘standard’ materials, including various minerals and gemstones, in order to define an approximate absolute measure of scratch hardness [Tab54]. In rebound experiment the hardness of a material is derived from the loss in kinetic energy of a test body as it impacts on and rebounds from the test specimen. The energy loss is measure of the plastic deformation induced by the impact and thus a material is considered as hard if the energy loss is small. Obviously these methods are very specific and rather vaguely defined.

Here we focus on the indentation hardness which measures the resistance of a material against indentation with a much harder tip. The most common methods after Brinell, Vickers, Rockwell or Martens differ with respect to the geometry of the tip and the specific testing procedure. The first two methods are very similar as in both cases the tip is indented into the specimen until a predefined force acting on the tip is reached. After retraction of the tip the remnant indent is analyzed in order to get a measure of the contact area between tip and specimen. The hardness is defined as the applied force normalized by this contact area. The choice of different tip geometries, *i. e.* sphere (Brinell) and four-sided pyramid (Vickers), influences the results as the distribution of stresses within the specimen depends on the tip geometry. In case of a spherical indenter (Brinell) the stress is more uniformly distributed compared to the four-sided pyramid used in the method after Vickers. Consequently, yielding happens at lower applied forces which makes the method after Vickers more suitable for hard metals. The method after Rockwell involves a sequence of indentation steps with different loads and a well-defined timing. This temporal control of the indentation process allows for an adjustment of the method to the visco-elasticity of sample making the method also suitable for polymeric samples. Finally, in the method after Martens the applied loads and indentation depths are measured continuously during the indentation process. Such an approach yields detailed information about the plastic and elastic deformation works at the expense of an increased experimental effort.

What is common to all these methods is that the macroscopic properties of the sample are tested. Deformation amplitude are large as the remnant indents can be inspected by eye. In contrast nanoindentation experiments tests the material only very locally. Indentation depths lie in the range of tens of nanometer to a few micrometers and thus allow for a local mechanical characterization on a micrometer scale[Kon07]. Though, it has been shown, that the results from above mentioned testings and nanoindentation experiments are well comparable in case of atomic matter such as metals, dielectrics, ceramics or polymers [Hay09].

For our nanoindentation experiments on colloidal films we used a TriboIndenter<sup>®</sup> TI 900 (Hysitron Inc, USA) equipped with a Berkovich diamond tip. The tip was mounted to a three

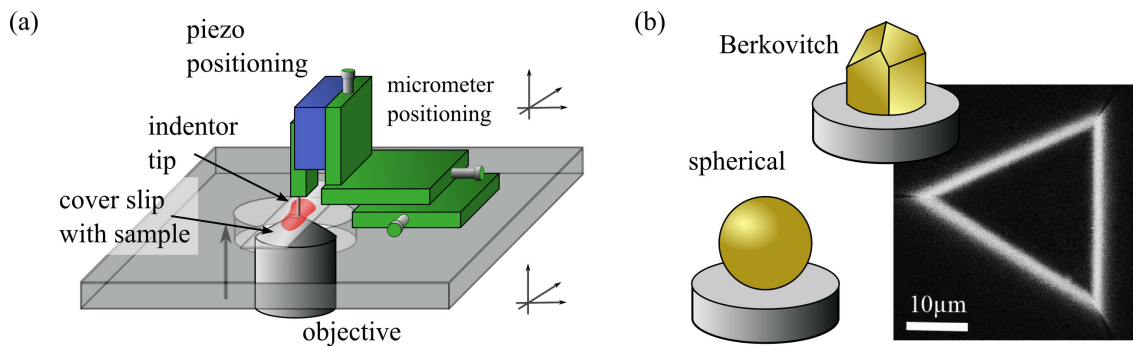


**Fig. 2.11.:** (a) Schematic setup for the combination of confocal microscopy and nanoindentation. The xyz-position of the indenter tip relative to the objective is adjusted by a micrometer translation stage equipped with fine-thread screws. The actual indentation is controlled via the piezo-actuator. (b) The position of the indenter can be checked by confocal imaging of the tip in reflection mode. Depending on the tip geometry, Berkovitch or spherical, the tip appears as a triangle (shown) or circle, respectively.

plate capacitive transducer TriboScanner™ (Hysitron Inc, USA). The displacement of the tip is measured by a change in capacitance at a noise level of 0.2 nm while the force is applied electrostatically with a resolution of 100 nN. We chose a displacement controlled operation for which the tip is pressed into the sample at a constant indentation rate. The depth of the tip inside the sample as well as the normal force on the tip is recorded continuously during the indentation and the subsequent retraction of the tip. The resulting force-depth curves are interpreted following the method of Oliver and Pharr [Oli04] in order to determine hardness and Young's modulus of the specimen.

These measurements were complemented by so called 'live indentation' experiments in which the indentation process was imaged with the confocal microscope described in section 2.1. Unfortunately, a combination of the confocal microscope with the TriboIndenter® TI 900 and thus a truly simultaneous structural and mechanical analysis was not possible. Instead, only the indenter tip was mounted to a piezo-translation stage (Actuator PXY 200SG, Controller ENV40, piezosystems jena GmbH, Germany) that was placed on the sample stage of the confocal microscope. Beside to the Berkovitch indenter also a spherical indenter made from silica (diameter: 25 μm) was used (Fig. 2.11).

### Theory of Oliver and Pharr

The force-depth curves were analyzed according to the theory by Oliver and Pharr [Oli04]. This method has successfully been used to extract hardness and Young's modulus in case of atomic systems like ceramics, metals or polymers. In the following we shortly summarize the basic steps in this analysis.

A typical force-depth curve of a complete indentation-retraction cycle is shown in Fig. 2.12. In analogy to the indentation methods from above the hardness  $H$  of a material is defined as the force  $P_{\max}$  needed to indent the tip to the maximal depth  $h_{\max}$  normalized by the

projected contact area  $A_c$  of tip and sample.

$$H = \frac{P_{\max}}{A_c} \quad (2.18)$$

During the retraction process the elastic deformation is recovered resulting in a force pushing the indenter out of the specimen. This elastic recovery is free of plastic contributions and therefore can be used to extract the Young's modulus. The derivation is based on the theory of elastic contacts. Using the constitutive relations in section 1.2.1 the three dimensional distribution of deformation and stresses in an elastic half space upon indentation with a rigid indenter tip can be calculated. On the basis of these deformation and stress fields Oliver and Pharr showed, that the reduced Young's Modulus  $E_r$  is related to the contact area and the contact stiffness  $S$  in a simple manner [Oli92]:

$$E_r = \frac{\sqrt{\pi} S}{2 \sqrt{A_c}} \quad (2.19)$$

The contact stiffness is given by the slope of the force-depth curve at the beginning of the retraction process. Usually it is determined by fitting a power-law behavior to the retraction curve and analytically calculating the derivative at  $h_{\max}$ :

$$P_{\text{ret}} = \alpha \cdot (h - h_f)^m \quad (2.20)$$

$$S = \left. \frac{dP_{\text{ret}}}{dh} \right|_{h=h_{\max}} \quad (2.21)$$

Equation (2.19) was verified for various tip geometries, including spheres and flat punches [Tim70] as well as more generally for any axisymmetric punches with an arbitrary profile [Sne65]. Simulations showed the same relation is also appropriate for slight variations from the axisymmetric geometry and in particular for pyramidal shapes like the Berkovich indenter [Kin87]. Moreover, Cheng *et al.* proved that also plastic yielding and strain hardening did not

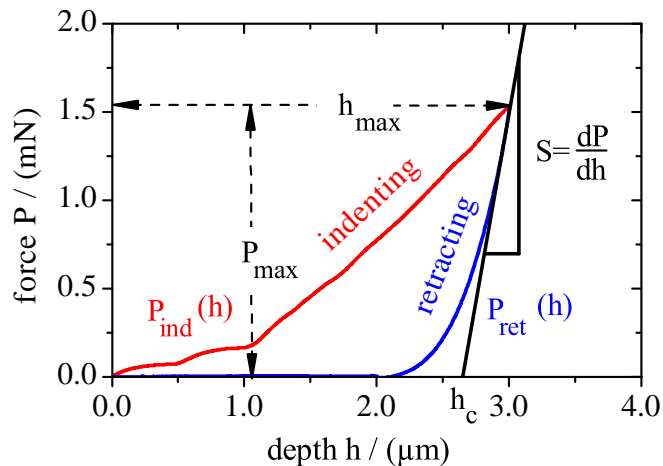


**Fig. 2.12.:** Exemplary force-depth curve: See the text for explanations of used variables. After Oliver and Pharr [Oli04].

corrupt equation (2.19) either [Che97]. Finally, the actual Young's modulus of the tested material is obtained by eliminating the influence of elastic deformations of the tip ( $E_i$ ,  $\mu_i$ ):

$$E = (1 - \nu^2) / \left( \frac{1}{E_r} - \frac{1 - \mu_i^2}{E_i} \right) \quad (2.22)$$

Here  $\mu$  and  $\mu_i$  denotes the Poisson ratios of sample and indenter, respectively.

Except for the contact area  $A_c$  all quantities required for the evaluation of hardness  $H$  and Young's modulus  $E$  can be extracted from the force-depths curve. In practice two routes are applied to get a measure for  $A$ , microscopic imaging of the residual indent or further utilization of the indentation curve. However, for both approaches difficulties can occur and the method of choice depends strongly on the experimental details. The microscopic inspection is often done with an atomic force microscope (AFM) [Cho04, Jee10]. This method can not only accurately quantify the contact area but also reveal sink-in or pile-up behavior [Smi03]. However, the AFM image depicts the indent after the whole indentation experiment and therefore does not account for the elastic recovery of the material which leads to an underestimation of  $A_c$ . The mathematical determination of  $A_c$  assumes a linear dependency of the restoring force on the indentation depth. Therefore, the effective depth  $h_c$  of the tip in the sample is given by

$$h_c = h_{\max} - \epsilon \frac{P_{\max}}{S} \quad (2.23)$$

with a geometrical factor  $\epsilon$ . Once  $h_c$  is known  $A_c$  can be calculated from geometrical consideration [Hay09]. In our study a Berkovitch indenter was used:

$$A = 24.56 h_c^2 \quad (2.24)$$

This approach is especially suitable for smooth samples, where the indentation depth is well described. For rough surfaces the onset of the indentation process can be altered resulting in large errors in  $h_{\max}$ . This is especially the case for our colloidal films. In section 5.4.2 we will come back to this difficulty in the determination of the contact area  $A_c$ .

Beside to the hardness and Young's modulus the total, elastic and plastic deformation works can be used to characterize the mechanical properties of the material [Bar10, Mal02]. They are defined by the integrals of the indentation  $P_{\text{ind}}$  and retraction curves  $P_{\text{ret}}$  as follows:

$$W_{\text{tot}} = \int_0^{h_{\max}} P_{\text{ind}}(h) dh \quad (2.25)$$

$$W_{\text{ela}} = \int_0^{h_{\max}} P_{\text{ret}}(h) dh \quad (2.26)$$

$$W_{\text{pla}} = W_{\text{tot}} - W_{\text{ela}} \quad (2.27)$$

## 2.3. Other methods

Various other methods were used for a basic characterization of particles and dispersions. As most of them are standardized we largely refer to literature and only describe the basic working principle, analysis procedures and used experimental instrumentation.

### 2.3.1. Dielectric spectroscopy [Kre03a]

Dielectric spectroscopy (DS) measures the complex dielectric function  $\epsilon^*$  that relates the electric field strength  $\vec{E}$  to the electric displacement  $\vec{D}$  via

$$\vec{D} = \epsilon^* \epsilon_o \vec{E} \quad (2.28)$$

with the vacuum dielectric permittivity  $\epsilon_o$ . It accounts for the presence of matter that can be electrically polarized or conduct electric currents. The associated static macroscopic polarization

$$\vec{P} = \epsilon_o (\epsilon^* - 1) \vec{E} \quad (2.29)$$

is microscopically composed of partial alignment of permanent dipoles, various types of induced polarization, and motions of free charge carriers like ions or defect charges. These processes do not only determine the static polarization  $\vec{P}$  but also its temporal response on an time dependent external electric field  $\vec{E}(t)$ . In case of weak electric fields below  $10^6$  V/m the linear response theory is applied to calculate  $\vec{P}(t)$ :

$$\vec{P}(t) = \epsilon_o \int_{-\infty}^t \epsilon(t-t') \frac{dE(t')}{dt'} dt' \quad (2.30)$$

This approach maintains causality as the polarization at time  $t$  is defined by changes of the electric field and the dielectric function of the past  $\epsilon(t-t')$  with  $t' \leq t$ . In case of a stationary sinusoidal disturbance  $\vec{E}(\omega, t) = \vec{E}_o \exp(-i\omega t)$  with an angular frequency  $\omega$  the solution to (2.30) is given by a simple extension of (2.29):

$$\vec{P}(\omega, t) = \epsilon_o (\epsilon^*(\omega) - 1) \vec{E}(\omega, t) \quad (2.31)$$

Technically the frequency dependent complex dielectric function  $\epsilon^*(\omega) = \epsilon'(\omega) - i\epsilon''(\omega)$  is obtained from  $\epsilon(t)$  via a one-sided Fourier transform. The real part is proportional to the energy reversibly stored in the system in each period whereas the imaginary part represents the dissipated energy.

According to the fluctuation-dissipation theorem the dissipation  $\epsilon''(\omega)$  is connected to the thermally induced fluctuation of the polarization

$$\Delta\mathcal{P}^2(\omega) = \frac{1}{k_B T} \frac{\epsilon''(\omega) - 1}{\pi \omega} \quad (2.32)$$

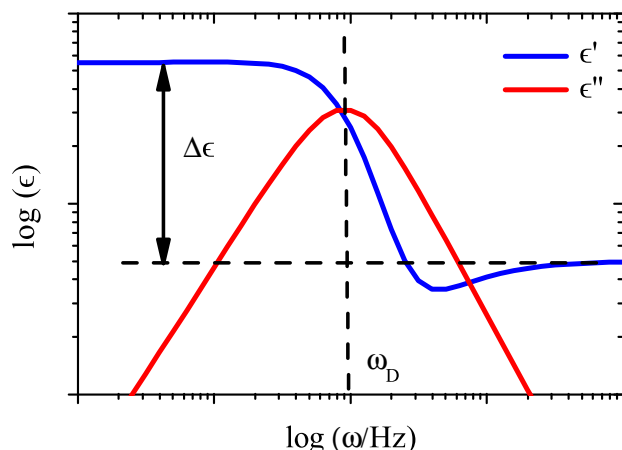


**Fig. 2.13.:** Real  $\epsilon'$  and imaginary part  $\epsilon''$  of the complex dielectric function vs. angular frequency for a Debye relaxation process.

$\Delta\mathcal{P}^2(\omega)$  denotes the spectral density of the polarization fluctuations  $\Delta\vec{\mathcal{P}}(t) = \vec{\mathcal{P}}(t) - \langle\vec{\mathcal{P}}\rangle_N$  about the mean value  $\langle\vec{\mathcal{P}}\rangle_N$ <sup>7</sup>. In the Debye approximation a single relaxation time  $\tau_D$  defines the temporal characteristics of  $\Delta\vec{\mathcal{P}}(t)$ . On shorter timescales compared to  $\tau_D$  the induced fluctuations maintain while at larger times they decay. In terms of  $\Delta\mathcal{P}^2(\omega)$  this relaxation behavior is represented by the characteristic frequency  $\omega_D = 2\pi/\tau_D$  that defines the rate at which thermally induced fluctuations grow and decay. For lower and higher frequencies  $\mathcal{P}^2(\omega)$  decays to zero. The same characteristics also apply to externally induced polarizations and  $\epsilon^*(\omega)$ . For slow variations of the electric field the molecular dipoles can align to the external field and contribute to the polarization according to their density and dipole moment. At high frequencies above  $\omega_D$  this alignment is no longer possible as the dipoles cannot follow the changes in the electric field. Therefore, the average polarization due to these dipoles vanishes and the macroscopic polarization is reduced. At the characteristic frequency  $\omega_D$  field induced alignment happens at the same rate as the thermal fluctuations leading to a maximized energy dissipation. Using the Kramers-Kronig relation

$$\epsilon'(\omega) = \frac{1}{\pi} \lim_{a \rightarrow 0} \left[ \int_{-\infty}^{\omega-a} \frac{\epsilon''(\xi)}{\xi - \omega} d\xi + \int_{\omega+a}^{\infty} \frac{\epsilon''(\xi)}{\xi - \omega} d\xi \right] \quad (2.33)$$

the complex dielectric function can be mathematically expressed by

$$\epsilon^*(\omega) = \epsilon_\infty + \frac{\Delta\epsilon}{1 + i\omega\tau_D} \quad (2.34)$$

In reality this functionality, however, is only rarely observed but can be generalized to the Havriliak and Negami function to fit the experimental data:

$$\epsilon^*(\omega) = \epsilon_\infty + \frac{\Delta\epsilon}{[1 + (i\omega\tau_D)^\beta]^\gamma} \quad (2.35)$$

<sup>7</sup>The notation  $\langle A \rangle_N$  represents the ensemble average of the quantity  $A$ .

of the relaxation process (see Fig. 2.13).

Conduction effects show a different frequency behavior. For pure electronic conduction like in metals the complex conductivity  $\sigma(\omega) = \sigma' + i\sigma'' = i\omega\epsilon_o\epsilon(\omega)$  is purely real and given by the DC conductivity  $\sigma_o$ . Hence, there is no contribution to  $\epsilon'(\omega)$  and  $\epsilon''(\omega)$  decreases linearly with increasing frequencies. In amorphous materials conductivity is often modeled by hopping processes of mobile charge carriers with their local polarization cloud. If the charge moves to a new site the polarization cloud must follow this movement. Otherwise the charge is dragged back to its original position and the current density is reduced. So not only the mobility of the charge is relevant but also the dynamic properties of the polarization cloud. Its relaxation again is connected to the thermal fluctuations and thus defines a characteristic time  $\tau_C$ . For frequencies much smaller than  $\omega_C = 1/\tau_C$   $\sigma'(\omega)$  levels off defining  $\sigma_o$ . At high frequencies  $\sigma'(\omega)$  and  $\sigma''(\omega)$  increase with decreasing frequencies.  $\sigma_o$  and  $\tau_C$  is determined by a fit of  $\sigma'(\omega)$  after Jonscher[Jon77]:

$$\sigma'(\omega) = \sigma_o [1 + (\omega\tau_C)^s] \quad (2.36)$$

with an exponent  $s \in [0, 1]$ .

Inhomogeneous materials like *e. g.* colloidal suspensions, phase separated systems or certain liquid crystalline phases show additional polarization effects that are based on partial charge separation at mesoscopic internal dielectric interfaces. This effect is called Maxwell-Wagner-Sillars polarization. If the system is partially conductive the effect on the polarization can be quite large. In a simple model the structure is described as an double layer arrangement with individual permittivities  $\epsilon'_{1/2}$  and conductivities  $\sigma'_{1/2}$ . The equivalent electric circuit can be simplified to an effective dielectric function

$$\tilde{\epsilon}^*(\omega) = \tilde{\epsilon}_\infty + \frac{\Delta\tilde{\epsilon}}{1 + i\omega\tau_{MW}} \quad (2.37)$$

with

$$\tilde{\epsilon}_\infty = \frac{\epsilon'_1\epsilon'_2}{\epsilon'_1 + \epsilon'_2}, \quad \Delta\tilde{\epsilon} = \frac{\epsilon'_2\sigma'_1 + \epsilon'_1\sigma'_2}{(\sigma'_1 + \sigma'_2)^2(\epsilon'_1 + \epsilon'_2)} \quad \text{and} \quad \tau_{MW} = \epsilon_o \frac{\epsilon'_1 + \epsilon'_2}{\sigma'_1 + \sigma'_2} \quad (2.38)$$

Various methods have been developed to measure the complex dielectric function over a broad frequency range of 20 decades. In the range from  $10^{-2}$  Hz to  $10^6$  Hz used in this work typically the Fourier correlation analysis is applied. A simple setup is schematically shown in Fig. 2.14. A capacitor of known vacuum capacitance  $C_o$  is filled with the material under study and thus modifies its capacitance according to

$$C^*(\omega) = \epsilon^*(\omega) C_o$$

The capacitance is connected to the complex impedance of the capacitor via  $Z^*(\omega) = i\omega C_o^*(\omega)$ . Hence the dielectric function can be calculated from the frequency Fourier components  $U_s^*(\omega)$  and  $I_s^*(\omega)$  of the time dependent voltage and current across the capacitor if a sinusoidal voltage

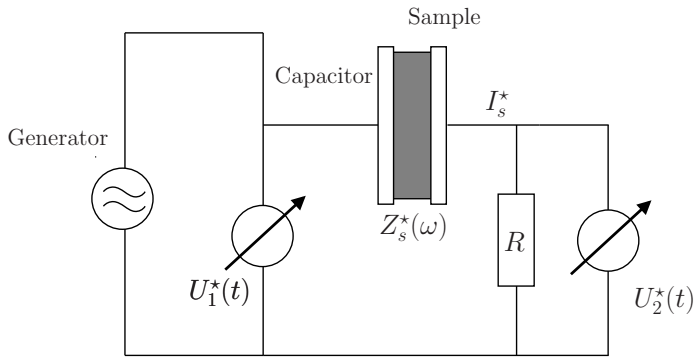


**Fig. 2.14.:** experimental setup for measurements of the complex dielectric function. After reference [Kre03b]

$U_1(\omega)$  is applied. Technically the voltage drop  $U_2(\omega)$  over a ohmic resistor  $R$  in series with the capacitor is used to measure the current in the circuit:

$$Z^*(\omega) = \frac{U_s^*(\omega)}{I_s^*(\omega)} = R \frac{U_1^*(\omega)}{U_2^*(\omega)}$$

### 2.3.2. Differential scanning calorimetry

Differential scanning calorimetry (DSC) measures the heat that is transferred to or extracted from the sample in order to change its temperature in comparison to a reference sample. This data is used to determine the relative specific heat capacity  $c_{p,rel}$  under constant pressure or latent heats involved in phase transition processes like crystallization.

The used DSC device (DSC 822, Mettler Toledo) works in the heat flux mode. Both, reference and test sample, are placed in an oven and thermally connected to two individual temperature sensors. While the temperature in this oven is changed at a fixed rate the temperature of both samples is measured. From the temperature difference between both samples differences in the heat flux can be calculated and thus allows for an determination of the relative heat capacity.

### 2.3.3. Dynamical light scattering of diluted colloidal suspensions [Pec85]

Dynamical light scattering (DLS) measures the time characteristics of Brownian motion in order to determine the size and polydispersity of particles in a highly diluted suspension. A laser beam is focused into the suspension where it is scattered at the contained particles. At large distances from the sample the coherently scattered light is superposed and creates an irregular interference pattern. This so called speckle pattern is strongly dependent on the relative particle positions. As the suspended particles undergo Brownian motion the speckle pattern changes continuously with time and so does the absolute scattered intensity  $I(q, t)$ . Here  $q = 4\pi \cos(\Theta)/\lambda$  denotes the absolute value of the scattering vector that is a function of the scattering angle  $\Theta$ . These temporal changes are measured in terms of the second order autocorrelation function:

$$g^{(2)}(q, \tau) = \frac{\langle I(t) I(t + \tau) \rangle_t}{\langle I(t) \rangle_t^2}$$



The angle brackets  $\langle \rangle_t$  denote averaging over all times  $t$ . The first order autocorrelation function  $g^{(1)}(q, \tau)$  refers to the electric fields instead of the measured intensities  $I \propto \vec{E}^2$  and is related to  $g^{(2)}(q, \tau)$  via the Siegert equation:

$$g^{(2)}(q, \tau) = B + \beta \left[ g^{(1)}(q, \tau) \right]^2$$

For monodisperse particles and low particle concentrations  $g^{(1)}(q, \tau)$  is modeled by an exponential decay

$$g^{(1)}(q, \tau) = \exp(-\Gamma \tau) \quad \text{with} \quad \Gamma = q^2 D_t \quad (2.39)$$

$D_t$  is interpreted as the translational diffusion constant of the particles that is linked to the particle radius  $R_p$  according to equation (1.5) If the particles are moderately polydisperse (2.39) is extended to account for a distribution of decay rates  $G(\Gamma)$ :

$$g^{(1)}(q, \tau) = \int G(\Gamma) \exp(-\Gamma t) d\Gamma$$

Several methods exist to solve this equation for  $G(\Gamma)$ . According to the cumulant analysis[Kop72, Fri01]  $g^{(2)}(q, \tau)$  can be developed into a series of the moments  $\mu_m$  of  $G(\Gamma)$  and the average decay rate  $\bar{\Gamma}$ :

$$g^{(2)}(q, \tau) = B + \beta \exp(-2\bar{\Gamma} t) \left( 1 + \frac{\mu_2}{2} \tau^2 + \frac{\mu_3}{6} \tau^3 + \dots \right)^2$$

with  $\mu_m = \int_0^{\infty} G(\Gamma) (\Gamma - \bar{\Gamma})^m d\Gamma$

While the average particle diameter is determined by  $\bar{\Gamma}$  in analogy to (2.39) and (1.5),  $\sigma = \mu_2/\bar{\Gamma}^2$  is the normalized variance of  $G(\Gamma)$  and thus also a measure of the particle polydispersity.

The used home-made setup works at a wavelength of 532 nm and an intensity of up to 250 mW depending on particle size and concentration as well as the dielectric contrast of particles and dispersion liquid. The temperature was adjusted via a toluene bath (temperature control by means of refrigerated and heating circulator FP30, JULABO Labortechnik GmbH, Germany). The refractive index of toluene is well matched to the glass cuvettes containing the suspension reducing optical artifacts due to reflection and scattering at the toluene-cuvette interfaces. The intensity was detected with an avalanche photo diode (ALV-Laser Vertriebsgesellschaft, Germany) and the correlation data was calculated and recorded with an ALV-5000/60X0 Multiple Tau Digital Correlator and ALV-Correlator software for scattering angles between 30° and 150°C.

### 2.3.4. Scanning electron microscope

Scanning electron microscopes (SEM) are widely used for microscopic imaging at high spatial resolutions down to 1 nm and below. The working principle is similar to that of a LSCM.

An focused electron beam is scanned across the sample and interacts with its atoms via a manifold of processes. This interaction gives rise to scattering of the electron or the emission of other electrons or photons which are quantified in order to define an equivalent “intensity” associated to the illuminated region. Rastered on a regular grid these intensity values can be interpreted as an 2D image of the sample. The most common imaging mode utilizes secondary electrons that are ejected from the outer shells of the atom via inelastic scattering with the beam electrons. As their energy is rather low ( $<40$  eV) these electrons tend to be reabsorbed before they can leave the sample. Only electrons emitted near the sample surface are detected and thus map the surface topography.

The beam electrons are generated by a heated electron gun mostly made from tungsten. After acceleration in an electric field in the range of (0.1–50) keV they are collimated and focused by a set of electromagnetic lenses. The corresponding de-Broglie wavelengths  $\lambda$  are (5 – 100) pm. Following Abbe’s criterion for the distinction of two individual points  $d = \lambda/(2NA)$  the above mentioned spatial resolution can be easily obtained. In reality the focusing elements limit the size of the beam focus. Yet small numerical apertures  $NA$  are sufficient to maintain a decent resolution of few nanometers. At the same time the depth of field is low which allows for imaging of rough surfaces without changing the sample height. Beside to the local electron density the image contrast is largely defined by the relative orientation of the sample surface normal and the direction of the electron beam. As a result SEM images appear three-dimensional although the sample is scanned only in two dimensions.

Other imaging modes are based on elastically backscattered electrons or x-rays that are emitted if electrons from the inner shells are liberated and the vacancy is filled by electrons from the outer shells (energy dispersive x-ray spectroscopy). These modes are sensitive to the specific atoms and can be used to determine the chemical composition of the sample.

SEM images in the present work were recorded on a LEO Gemini 1530 with a In-Lens SE detection system (Carl Zeiss NTS GmbH, Germany) at an electron energy of 0.5 – 5 keV. In case of PMMA (Poly-methyl methacrylate) particles the electron energy was reduced to 0.1 keV in order to prevent excessive beam damage.

### 2.3.5. Polarization optical microscopy

Polarization optical microscopy (POM) works in transmission geometry and utilizes polarized light in order to identify and image optically anisotropic materials. Compared to conventional wide-field microscopes two polarizers are introduced into the light path. One polarizer is positioned before the condenser, the second one which is also called analyzer is placed before the camera/ocular. If the principle axis of both polarizers are perpendicular to each other, light that passed through an isotropic sample does not change its polarization and thus cannot pass the analyzer. On the other hand, if the sample is optically anisotropic the polarization of the light passing the sample is rotated and partially transmitted through the analyzer. The rotation angle  $\Delta\varphi$  of the beam polarization depends on the degree of anisotropy in the refractive index

$n_{\parallel} - n_{\perp}$ , the thickness  $d$  of the sample and the wavelength  $\lambda$  of the used light.

$$\Delta\varphi = 2\pi \frac{n_{\parallel} - n_{\perp}}{\lambda} d$$

We used a Olympus BX51 (Olympus Deutschland GmbH, Germany) equipped with LM-PlanFl objectives at magnifications/NA of  $50\times/0.5$ ,  $20\times/0.4$  and  $10\times/0.25$  (Olympus Deutschland GmbH, Germany). A THMS600 heating stage and TMS94 controller (Linkam Scientific Instruments Ltd, United Kingdom) with an additional liquid nitrogen cooling system LNP93 was integrated to dynamically control the sample temperature in the range from  $-30^{\circ}\text{C}$  to  $100^{\circ}\text{C}$  with maximal heating and cooling rates of  $20\text{ K/min}$ .



## 3. Liquid crystal based colloidal suspensions

In liquid crystal-based colloids particle-solvent interactions lead to a phase separation as the sample is cooled below the isotropic-nematic transition temperature of the liquid crystal. Due to the elastic interaction of the particles with the nematic director the particles are expelled from nucleating nematic droplets and concentrate in the remaining isotropic phase. The viscosity of the isotropic phase diverges, the particles get crowded and for a sufficiently high initial particle content the system gets kinetically arrested into a system spanning network structure. The kinetic arrest is accompanied by a liquid to solid transition with remarkably high elastic modules. Moreover, the visco-elastic evolution of the sample with further cooling continues even after the network is formed. The origin of this network rheology is currently under debate.

In this chapter we present an extensive rheological study of the network formation using piezo-rheology and simultaneous confocal microscopy. We start with an introduction into solvent-mediated particle aggregation with the special emphasis on liquid crystal-related effects. After that we give an overview over previous works which relate the network rheology with the interaction of the particles with the liquid crystalline solvent. Our results, however, disagree with the predictions of these theories. We present a new model that ascribes the visco-elasticity of the network to a temperature dependent plastification of the used polymeric particles by the liquid crystal.

The greater greater part of this chapter is published in the paper ‘**Viscoelastic rheology of colloid-liquid crystal composites**’ [Rot10].

### 3.1. Solvent mediated mechanisms of particle aggregation

Many studies on aggregation in colloidal systems utilize depletion interactions in order to induce attractive inter-particle forces. The strength and shape of the effective potential can be tuned by choosing appropriate depletion agents. Moreover, electrostatic and van der Waals forces need to be taken into account. In these systems the dispersion liquid is neutral with respect to the particle interactions. Though, it can be used to serve other purposes. In solvent mixtures the mixing ratio can be chosen such that densities or indexes of refraction of solvent and particles are matched. Besides, there is a class of so called solvent-mediated (SM) interactions for which the appearance of the interaction lies in the wettability of the particles with the dispersion liquid. The simplest case of such a mechanism happens in colloids with steric stabilization. If the stabilization layer on the particle surface is no longer solvated, like *e. g.* for octadecyl-stabilized silica particles in decahydronaphthalene (DEC) below a critical

temperature [Rue98, Hel81], van der Waals forces causes aggregation of the particles.

### 3.1.1. Particles in binary mixtures of liquids

In binary mixtures of partially miscible liquids the difference in wettability of the individual components give rise to a variety of effects. One example is the critical Casimir effect, an equivalent to the quantum mechanical Casimir effect [Cas48]: At compositions and temperatures close to the critical point of the mixture long-ranged composition fluctuations occur in the single phase region. The preferred wetting of the particle by one component imposes boundary conditions to these fluctuations that result in an attraction if two identical particles approach each other and a repulsion if two particles of different wettabilities come close [Gam09, Sch03b, Bon09]. Far off the critical point fluctuations are small and Casimir forces can be neglected. Yet, close to the two-phase region of the mixture preferred wetting of one component can lead to a local phase separation around the particles. If two particles come close to each other these wetting layers can merge and form a capillary bridge. Due to the surface tension between the liquid bridge and the surrounding phase the particles again experience an attractive force [Bey99, Guo08, Arc05, Bau00].

Despite of completely different origins all interactions mentioned so far can be expressed by attractive inter-particle potentials that depend primarily on the distance between two particle. As we already discussed in chapter 1 the aggregation dynamics is mainly determined by the strength and range of the interaction compared to the thermal energy  $k_B T$  of the particles. Strong, short-ranged interactions lead to diffusion-limited cluster aggregation and the formation of fractal particle aggregates [Lin90b, Wit83, Mea83]. In the opposite case of weak, long-ranged interactions attraction-limited cluster aggregation takes place and the forming clusters are more compact [Lin90a, Pue04]. The exact shape of the potential has a minor influence and existing models for phenomenology and rheology of the aggregation process may also be suitable for the interactions mentioned above.

Other particle-solvent interactions do not necessarily induce attractive forces between particles but nevertheless lead to aggregation of the particles and a kinetic arrest of the colloid. In the phase separated state of a binary mixture nano- or micrometer-sized particles can behave similarly to surfactant molecules and stabilize the interface between both phase [Pic07, Bin02]. If particles attach to the liquid-liquid interfaces the effective surface tension between both liquids is reduced. The corresponding gain in free energy per particle

$$\Delta G = \pi R_p^2 \gamma_s (1 - |\cos(\theta)|)^2$$

scales with the surface tension  $\gamma_s$  between both liquids,  $R_p$  the radius of the particle and  $\theta$  the three phase liquid-liquid-colloid contact angle [Cle07, But06a]. Even for partially miscible liquids with weak surface tensions  $\Delta G$  largely exceeds the thermal energy of the particles and permanently bind the particle to the liquid-liquid interface.

At carefully chosen relative amounts of particles and liquids and appropriate mixing procedures all internal interfaces are occupied by the particles. In most cases one phase forms

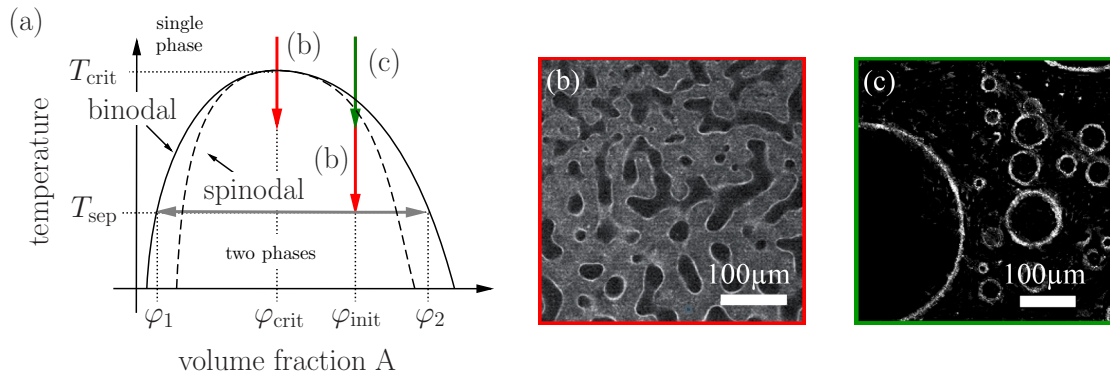


**Fig. 3.1.:** (a) Exemplary phase diagram of a binary mixture of liquids A and B with added solid particles. (b) Upon cooling at the critical volume fraction  $\varphi_{\text{crit}}$  of liquid A or for deep quenches below the spinodal for an asymmetric composition  $\varphi_{\text{init}}$  a spinodal decomposition takes place. Image taken from ref. [Her07] (c) At slower cooling rates droplets of with a majority phase of A or B nucleate and grow while passing through the coexistence region in (a). Images taken from ref. [Cle07]

droplets that are dispersed in the other continuous phase [Zen06]. This so called Pickering emulsion is stable against macroscopic demixing on long timescales [Pic07, Sac07] which makes them valuable for a large variety of industrial applications and products such as crude oil extraction or cosmetic products. The stability of the emulsion is closely related to its mechanical properties. As the particles are bound to the interface, they hinder coalescence of the droplets [Tam94]. Several parameters affect the probability for coalescence. Besides to material properties such as particle radii, contact angles and viscosities of either phase, structural parameters like the coverage of the droplets with particles and the size of the droplets are relevant [Tor07, Tar04, Bin00]. Of course, interactions between the particles also play a role [Zen06].

Various preparation routes for such stabilized emulsions have been tested. Beside to crude mixing via stirring or ultrasonication temperature induced phase separation from the single phase region is also a viable option [Thi10, Cle07, Her07]. Assuming an upper critical solution temperature (UCST) like in Fig. 3.1 (a) the initial composition  $\varphi_{\text{init}}$  and cooling procedures determine the kinetics and structural evolution of the phase separation. Moderate cooling at the critical composition  $\varphi_{\text{crit}}$  or deep quenches below the spinodal *e. g.* to the temperature  $T_{\text{sep}}$  result in a diffusion driven homogeneous phase separation of both liquid. During this so called spinodal decomposition density fluctuations lead to small domains of separated phases that undergo a self-similar coarsening in course of time. The dispersed particles, however, attach to the forming interfaces preventing a complete phase separation due to a kinetic arrest of the particles at the interface and the increasing viscosity of the particle-laden phase [Cle07, Her07]. The resulting structure is reminiscent of a continuous irregular network [Fig. 3.1 (b)]. On the other side, more shallow temperature quenches below the binodal give rise to a nucleation of spherical droplets and a structure similar to pickering emulsions like in Fig. 3.1 (c) [Thi10, Cle07].

The dynamics of these phase separation scenarios cannot be described purely by hydro-

dynamic flow as it is the case in binary mixtures without particles. Tanaka et al. [Tan00] proposed a new model of visco-elastic phase separation in dynamically asymmetric mixtures. The particle-free and particle-rich phases as well as the interface have vastly different relaxation rates and their delicate interplay defines the morphological and rheological evolution of the system. Hence, such kind of phase separating systems open up new possibilities for the study of the correlation between structure and rheology of arrested colloids. Though, most studies were devoted solely to the structural properties, partially because of unwanted side effects. The phase separated domains have different densities and buoyancy can lead to a gradual coarsening and macroscopic phase separation of the system. Furthermore, gradual changes in the chemical composition in course of the phase separation and therewith varying wetting properties complicate the modeling.

We chose to study an experimentally more convenient model system. In liquid crystal based colloidal suspensions a similar phase separation process occurs. When the liquid crystal transitions from the isotropic phase to the nematic phase, the particles remain in the isotropic phase while the nematic phase is virtually free of particles [Mee00, Ull09]. Since both phases are chemically identical, surface tension and differences in density and wettability of the particles are small compared to binary mixtures and the above mentioned drawbacks are neutralized. For the same reason other interactions are responsible for the preferred dispersion of the particles in the isotropic phase.

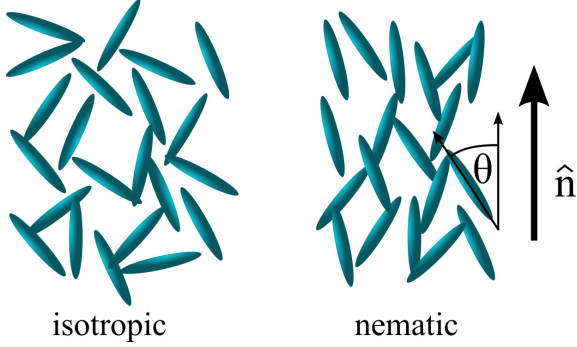
### 3.1.2. Particle interactions in liquid crystals

Before going into detail about the special case of interactions with particles we give a short general introduction into liquid crystals (LC). As already indicated by the contradictory naming, LCs denote a special class of phases that are intermediate to liquid and crystalline phase. Molecules that form LCs, also called mesogenes, neither are fully disordered like in liquid nor do they show the full orientational and three dimensional translational ordering of crystals. They rather exhibit selected ordering phenomena. Various combinations of ordering properties are possible and define a large family of liquid crystalline phases that are often also called mesophases. Transitions between different mesophases occur either by variation of temperature (thermotropic LCs) or a combination of temperature and composition (lyotropic LCs). Before going into detail about the special case of interactions with particles we give a short general introduction into liquid crystals (LC). As already indicated by the contradictory naming, LCs denote a special class of phases that are intermediate to liquid and crystalline phase. Molecules in LCs, also called mesogenes, neither are not fully disordered like in liquid nor do they show the full orientational and three dimensional translational ordering of crystals. They rather exhibit selected ordering phenomena. Various combinations of ordering properties are possible and define a large family of liquid crystalline phases that are often also called mesophases. Transitions between different LCs occur either by variation of temperature (thermotropic LC) or a combination of temperature and composition (lyotropic LC).

In the present work we focus on the thermotropic nematic phase that is often formed by



rod-like mesogenes. Nematic LCs have no translational order but show an average alignment along a preferred axis (Fig. 3.2). This axis is denoted as the nematic director  $\hat{n}$  and the degree of alignment is given by



$$S = \frac{1}{2} \langle 3 \cos^2(\theta) - 1 \rangle_N \quad (3.1)$$

The angle brackets  $\langle \rangle_N$  denote the ensemble average and  $\theta$  is the angle enclosed by of the long axis of the mesogenes and the nematic director. The transition from the isotropic phase ( $S = 0$ ) to the nematic phase ( $S \neq 0$ ) is induced by cooling the system below the transition temperature  $T^*$ . Above this temperature entropy forces the mesogenes to equally occupy all orientational states. With decreasing temperatures, however,

the entropic contribution decreases with respect to the molecular interactions and it becomes energetically favorable to transition into the ordered state. This transition is of weak first order as it involves a latent heat which is, however, much smaller compared to common phase transitions such as crystallization.

Due to the missing translational order nematic LCs have similar flow properties like ordinary liquids. However, the presence of orientational order induces a certain degree of elasticity. Any splay, twist or bending deformation will cost energy. In a first order approximation this energy can be estimated by

$$\begin{aligned} \mathcal{E} = & \frac{1}{2} K_1 \left( \vec{\nabla} \cdot \hat{n} \right)^2 + \frac{1}{2} K_2 \left[ \hat{n} \cdot \left( \vec{\nabla} \times \hat{n} \right) \right]^2 \\ & + \frac{1}{2} K_3 \left[ \hat{n} \times \left( \vec{\nabla} \times \hat{n} \right) \right]^2 \end{aligned} \quad (3.2)$$

$K_1$ ,  $K_2$  and  $K_3$  are called Frank elastic constants and are often combined to a single parameter  $K_F$ . Due to the translational disorder the mesogenes can rearrange in order to relax the induced stress. Though, such a relaxation process is not possible if the mesogenes are anchored at solid boundaries in the system. Anchoring means that depending on relative topological and chemical compatibility the mesogenes have a preferred orientation at solid surfaces. This orientation can be planar or homeotropic (perpendicular to the surface) and its strength is quantified by the so called anchoring energy  $W$  [Fig. 3.3 (a)].

These two energetic contributions of Frank elasticity and surface anchoring give rise to new interaction mechanisms in colloids with a solvent phase that features mesophases [Sta01, Pou97]. In the presence of a particle with radius  $R_p$  the anchoring energy scales with the particle surface  $\mathcal{E}_{\text{anc}} \propto W R_p^2$  and the elastic energy is given by  $\mathcal{E}_{\text{ela}} \propto K_F R_p$ . Hence, the quantity  $W R_p / K_F$  measures the relative strength of both energies and can be used to distinguish between the following cases. In the case of strong anchoring  $W R / K_F \gg 1$  the particle stron-

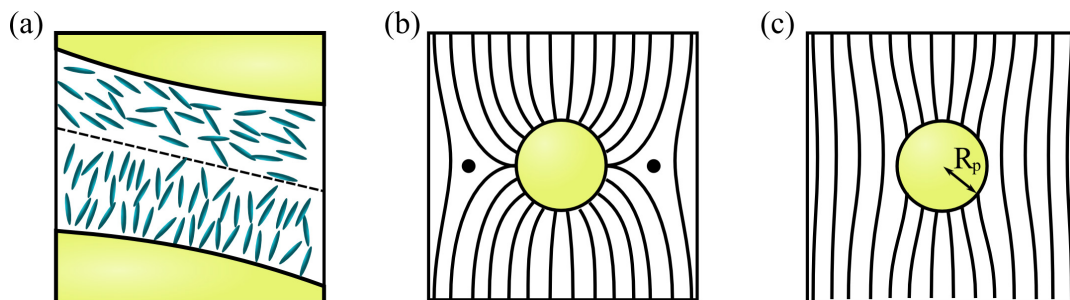


**Fig. 3.3.:** (a) Planar (top) and homeotropic (bottom) anchoring of mesogenes at a solid surface. In the nematic phase the ordering extends further into the volume. (b) The lines denote the local orientation of the nematic director in the vicinity of a particle of radius  $R_p$ . In case of strong homeotropic surface anchoring dipole or satellite defects (the latter is shown in the image) are formed. (c) Weak anchoring does not induce defects but rather leads to a long-ranged distortion of the nematic director field. Images after reference [Sta01]

gly influences the orientation of adjacent mesogenic molecules. If the bulk phase is isotropic the particle locally aligns the molecules which can lead to the formation of a nematic bridge if two particles approach close to each other. This bridge in turn generates an attractive force between the particles [Sta04]. This phenomenon is purely based on the elastic properties of the director field. A capillary interaction is suppressed as the interfacial tension between the nematic and isotropic phases is  $\gamma_{s,NI} = 10^{-5}$  N/m that is  $10^3$  to  $10^2$  times smaller than for other liquid-liquid interfaces.

In a nematic matrix particles with strong anchoring generate topological defects as the nematic director around the particle is incompatible with the director at larger distances [Fig. 3.3 (b)]. These defects effectively increase the energy of the system. The contribution of each particle can be approximated by

$$\mathcal{E}_{\text{elas}}^{\text{strong}} \approx 10 K_F R \quad [\text{And00a}]. \quad (3.3)$$

It is energetically favorable if particles 'share' defects. Therefore such particles tend to form strings and even stable 2D and 3D crystalline arrangements have been observed [Jea00, Mus06].

In the case of weak anchoring  $W R/K_F \ll 1$  no effects are expected in the isotropic phase. In the nematic phase the surface anchoring is too weak to generate defects but the nematic director is distorted even far away from the particles [Fig. 3.3 (c)]. The stored energy in this deformation amounts to

$$\mathcal{E}_{\text{elas}}^{\text{weak}} \approx 0.2 W^2 R^3 / K_F \quad [\text{And00a}]. \quad (3.4)$$

The system reaches an energetically favorable state if the particles can be expelled from the nematic phase.

When going through the isotropic-nematic phase transition this interaction leads to a particle enrichment in the isotropic phase (Fig. 3.4). The phenomenology of this process resembles that of the nucleation and growth-type phase separation in binary liquids like in Fig. 3.1 (c).

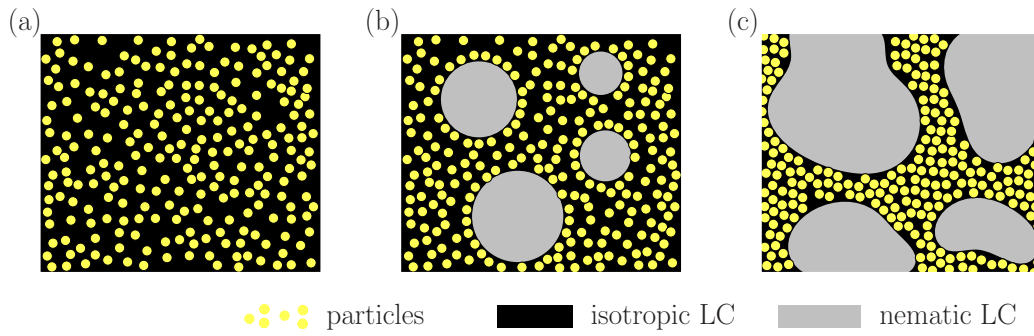


**Fig. 3.4.:** Schematic representation of the phase separation in LC-colloidal suspensions. Upon cooling from the mixed isotropic state (a) through the isotropic nematic transition nematic droplets nucleate and expel the particles from their volume (b). As the droplets grow the particles are concentrated in the remaining isotropic phase forming a network structure (c). After reference [Mee00].

In the initial state the particles form a stable suspension in the isotropic phase. As soon as the isotropic-nematic transition takes place nematic droplets nucleate and expel the particles from their volume. Upon further cooling these droplets grow and the particle concentration in the isotropic phase increases until the particles are highly compacted forming the walls of a cellular network.

This kind of network formation was first described by Meeker *et al.* [Mee00] in a suspension of sterically stabilized PMMA particles (Appendix C) in 4 pentyl-4'-cyanobiphenyl (5CB). Beside to the characteristic network structure they found strong changes in the mechanical properties of the sample. Starting with a liquid suspension in the isotropic state the forming network turned colloid from a visco-elastic material to an almost purely elastic solid at 20 °C. The shear modules were in the order of  $10^5$  Pa and the structure easily supported its own weight.

## 3.2. Previous Works

Poon, Terentjev and coworkers [Mee00, And00b] were the first to propose a theoretical model of the phase separation in colloidal-LC suspensions. Based on the experimental observation that the isotropic-nematic transition temperature in the suspension was reduced compared to the pure LC the free energy of the system was formulated. The phase diagram was calculated and the driving forces of the phase separation were identified. Furthermore they developed a rheological model that relied on the nematic frustration of the LC in the network walls due to the closed packing of the particles [And00a]. In the following several studies by Vollmer, Hinze and Poon complemented the experimental picture with confocal microscopy, DSC and nuclear magnetic resonance (NMR) [Cle04b, Cle04a]. The results suggested that a third low molecular component was present in the system which affects the phase separation kinetics and more importantly challenged the prior rheological description [Vol04, Vol05]. In the following we go through the essential steps and findings of these previous works and formulate open questions.

### 3.2.1. Theoretical modeling and phase diagram

The starting point of the theoretical modeling was the experimental observation, that the isotropic-nematic transition temperature  $T_{\text{NI}}$  of the LC-colloidal suspension was reduced compared to  $T^*$  for the pure LC:

$$T_{\text{NI}} = T^* (1 - \alpha \varphi) \approx T^* \left( 1 - \frac{\xi^2}{R^2} \varphi \right) . \quad (3.5)$$

Terentjev and coworkers [Mee00, And00b] ascribed this effect to the bare presence of the particles and their anchoring interaction with the mesogenic molecules. Accordingly, they identified the fitting parameter  $\alpha$  with the particle radius  $R_p$  and the correlation length  $\xi$  of the nematic director<sup>8</sup>. In the next step  $T_{\text{NI}}$  was used to replace the transition temperature  $T^*$  of the pure LC in the phenomenological Landau-type formulation of the nematic contribution to the free energy of the system:

$$F_n = \frac{1}{2} A_o [T - T_{\text{NI}}(\varphi)] S^2 - \frac{1}{3} B S^3 + \frac{1}{4} C S^4 \quad (3.6)$$

As described above  $S$  denotes the scalar nematic order parameter and  $A_o$ ,  $B$ , and  $C$  are LC specific material constants. Minimizing expression (3.6) with respect to  $S$  yielded the equilibrium order parameter of the mixed nematic phase in dependency on the particle volume fraction  $\varphi$ :

$$S = \frac{B}{2C} \left( 1 + \sqrt{1 + \frac{4A_o T^* C}{B^2} (1 - T/T^* - \alpha \varphi)} \right) \quad (3.7)$$

Finally the free energy  $F$  of the system was completed by the universal mixing free energy of particles with hard sphere behavior according to Carnahan and Starling [Car69]

$$F_s = \frac{k_B T}{4/3 \pi R^3} \begin{cases} \varphi \ln(\varphi) + \varphi^2 \frac{4 - 3\varphi}{(1 - \varphi)^2} & \varphi \leq 0.52, \text{ liquid} \\ 1.79 \varphi + 3 \varphi \ln \left( \frac{\varphi}{1 - \varphi/0.52} \right) & \varphi > 0.52, \text{ solid} \end{cases} . \quad (3.8)$$

The total free energy  $F = F_n + F_s$  is depicted in Fig. 3.5 (a) as a function of  $\varphi$  for various temperatures. Above a temperature of

$$T = T^* \left( 1 + \frac{B^2}{4 A_o T^* C} \right) \approx 1.003 T^* \quad (3.9)$$

the suspension is isotropic at  $Q = 0$  and  $F_n$  vanishes for any particle concentration. Due to the fully convex shape of the  $F_s(\varphi)$  no phase separation can occur as expected for particles with pure hard sphere interaction. With decreasing temperatures  $F_n$  becomes increasingly important and dominates the free energy at the lower concentrations. The absolute values of  $F_n$  in Fig. 3.5 needed to be depressed by a factor of  $10^{-3}$  in order to be able to resolve

<sup>8</sup>The correlation length measures the extension of the long-range orientational order in the nematic phase.

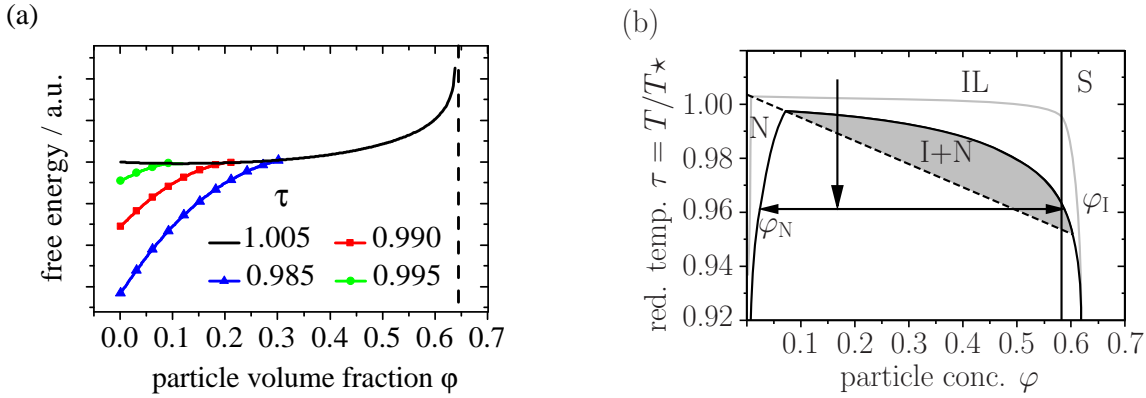


**Fig. 3.5.:** (a) Free energy  $F$  of the LC-colloidal suspension in dependency of particle volume fraction  $\phi$  for various reduced temperatures  $\tau_{\text{red}} = T/T^*$  according to equations (3.6) to (3.8): The contribution  $F_n$  is depressed by a factor of  $10^{-3}$  for better visualization. (b) Upon cooling the suspension at a fixed composition below the spinodal line (dashed line), phase separation to the equilibrium volume fractions  $\phi_I$  and  $\phi_N$  takes place. For sufficiently deep cooling the particle-rich isotropic phase solidifies while passing from the isotropic liquid state (IL) to the isotropic solid state (IS). Reproduced from reference [And00b]. See text for further explanations.

$F_s$  and  $F_n$  in the same graph. The convex shape of the nematic contribution  $F_n$  causes an instability of the system and favors phase separation into a particle-poor nematic phase (N) and a particle-rich isotropic phase (I).

The complete phase diagram [Fig. 3.5 (b)] was calculated from the total free energy using the standard criteria for phase stability. The binodals (solid lines in the graph) describe the phase boundaries between the single phases and the coexistence regions of isotropic and nematic phases (I+N). At a given temperature the chemical potentials of solvent and particles must be equal for both phases resulting in equilibrium particle volume fractions  $\phi_I$  and  $\phi_N$

$$\mu_{\text{LC}}(\phi_I) = \mu_{\text{LC}}(\phi_N) \quad (3.10a)$$

$$\mu_{\text{coll}}(\phi_I) = \mu_{\text{coll}}(\phi_N) \quad (3.10b)$$

The chemical potential is defined by

$$\mu_\zeta = \frac{\partial F}{\partial N_\zeta} \quad (3.11)$$

with  $\zeta$  denoting one of the constituent species and  $N_\zeta$  their respective occurrence.<sup>9</sup> In the coexistence region the suspension is in a metastable state. The phase separated state is energetically favorable but an energy barrier has to be overcome. Below the spinodal (dashed line) the suspension is absolutely unstable and phase separation into two phases with the volume fractions  $\phi_I$  and  $\phi_N$  takes place. Its location  $(\phi_s, T_s)$  in the phase diagram is given by the

<sup>9</sup>The definition of the chemical potential via the free energy requires a fixed sample volume. For the small temperature intervals involved in the phase separation process and thus rather small thermal expansion of the sample this is a reasonable approximation.

condition

$$\left. \frac{\partial^2 F}{\partial \varphi^2} \right|_{\substack{T=T_o \\ \varphi=\varphi_o}} = 0 \quad (3.12)$$

In the phase diagram of Fig. 3.5 (b) the same scaling factor for the nematic contribution was applied like for the illustration for the total free energy. If the correct scaling was used the nematic phase N would narrow and could not be resolved. At the same time the binodal to the coexistence region would look much more box-like with a much more shallow slope for the lower volume fractions and a steeper drop towards the high volume fractions (light gray lines). Hence,  $\varphi_N$  is almost zero, *i. e.* the nematic phase is virtually free of particles while the isotropic phase reaches high particle densities already for shallow cooling below the isotropic-nematic transition. As already discussed in the introduction the maximal volume fraction in the isotropic phase is limited, either by a crystallization process or kinetic arrest in the glassy state. Both scenarios are possible and we do not distinguish between both phase but uniformly denote them by (S) for solid.

### 3.2.2. Phase separation process

The phase separation process and network formation were investigated via confocal microscopy [And00b, Cle04b, Vol05] and is exemplary shown in Fig. 3.6 for a cooling process at a particle concentration of 13%. Upon cooling the suspension below the isotropic-nematic transition temperature spherical nematic droplets nucleated in the free volume and dragged the particles along with the nematic-isotropic interface. The heterogeneous distribution of the droplets gave rise to a large spatial variation in the local particle concentration which is reflected in different fluorescence intensity levels in the confocal images. With decreasing temperatures the volume fraction of the nematic phase increased and neighboring droplets eventually coalesced. The enrichment of particles in the isotropic liquid phase (IL) led to a strong increase in viscosity that finally ended in the kinetic arrest of the particles (IS) [Fig. 3.5 (b)]. It is remarkable that this whole process took place within a temperature range of only 0.5 K.

Although a complete phase separation was energetically favorable, structural relaxations were strongly suppressed and the system remained in the metastable network state. Further cooling resulted only in slight changes of the structure. However, these processes were hard to identify as the birefringence of the nematic droplets and the general mismatch in refractive indexes limited the resolution of the confocal images. For the same reason no detailed information about the conformation of the particles in the walls could be obtained even if larger particles were used like in image (III) Fig. 3.9 (b).

### 3.2.3. Rheological properties

As already mentioned above, the network exhibited remarkable mechanical properties. Being of wax-like consistency at 20 °C it easily supported its own weight. At these temperatures the sample behaved purely elastic in the linear rheological regime and yielded at stresses

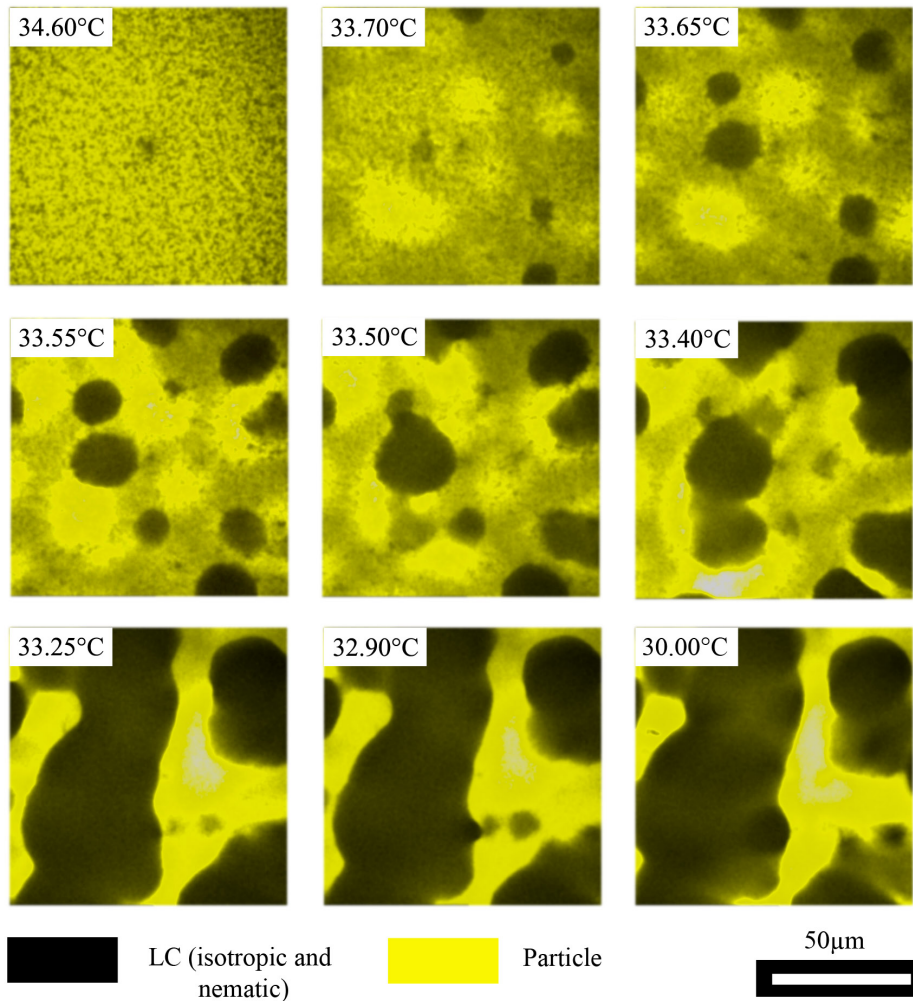


**Fig. 3.6.:** Confocal xy-images of the phase separation process in a colloidal suspension of PMMA particles at a concentration of 13 wt% in 5CB (Sample PHSA2-13 in Tab.3.1). The particles were labeled with a fluorescent dye and are colored yellow while the isotropic and nematic LC phases do not contribute to the fluorescence signal. The images were obtained  $30 \mu\text{m}$  above the cover glass with the home-made confocal microscopy described in section 2.1. The results are in good agreement with previous publications [And00b, Cle04b, Vol05].

in the order of 1 kPa with a square root dependency on the initial particle concentration [Mee00, And00a].

The complete temperature dependent mechanical response in terms of shear modules at a sampling frequency of 50 Hz is shown in Fig. 3.7. In the isotropic phase ① the suspension behaved liquid-like with the loss modulus  $G''$  largely exceeding  $G'$ . Passing the isotropic-nematic transition at about  $33.5^\circ\text{C}$  both modules increased by more than two orders of magnitude within the first 1 K. Upon further cooling beyond this regime ② the evolution of the mechanical properties with temperature leveled off, but did not end.  $G'$  and  $G''$  developed simultaneously rendering the highly visco-elastic regime ③ until both modules split apart and the mechanical evolution gradually ceased. In this low temperature regime ④ the sample became highly elastic with a storage modulus  $G'$  of up to  $10^6$  Pa at  $20^\circ\text{C}$ . The interplay between  $G'$  and  $G''$  is also

displayed by the loss angle  $\psi = \arctan(G''/G')$ . The general trend from a viscous fluid to an elastic solid in course of cooling is reflected in the decrease of the loss angle from more than  $80^\circ$  to about  $10^\circ$ . The above mentioned visco-elastic regime ③ was expressed by a shallow maximum at intermediate temperatures. For this particular example the loss maximum does not reach  $45^\circ$ , *i. e.* there are no real crossing points of  $G'$  and  $G''$  in this regime ③. Yet, we will show other samples with a more pronounced visco-elasticity and a maximum loss angle of up to  $55^\circ$ .

Terentjev et al. argued that the interaction of the particles with the mesogenic molecules determines the mechanical properties of the network as soon as it was formed, *i. e.* 1 K below  $T_{NI}$  [Mee00, And00a]. However, it is not the elastic distortion of the nematic director due to the presence of the particles that cause such high modules. Following equation (3.3), even in the most disadvantageous situation of homogeneously distributed particles with strong surface anchoring the energy density only amounted to

$$\mathcal{E}_{\text{elas}}^{\text{sys}} = \frac{\phi}{4/3 \pi R_p^3} \cdot 10 K_F R_p \approx 60 \text{ Pa} . \quad (3.13)$$

Any grouping of particles would further reduce this energy. Instead they proposed that mesogenic molecules located in the network walls experiences strong constraints induced by their anchoring to the particle surface. They can not transition to the nematic phase but instead are forced to the isotropic phase on expense of an increase of the energy density in the order of:

$$\Delta f_n \approx \frac{(A_o T^*)^2}{4C} \frac{1 - \tau_{\text{red}}}{\tau_{\text{red}}} \approx 10^7 (1 - \tau_{\text{red}}) \text{ J/m}^3 \quad (3.14)$$

Indeed NMR-measurements showed that there is a large amount of isotropic material located in the network wall even 15 K below  $T_{NI}$  [Vol04, Vol05]. Assuming an average thickness  $d_{\text{net}}$  of the network wall the expression  $\gamma_s \approx d_{\text{net}} \Delta f_n$  can be interpreted as an interfacial tension of the wall and the nematic droplets. Any deformation of the network structure enlarges the interface and thus also the energy of the system. If the deformation is small the energy can be

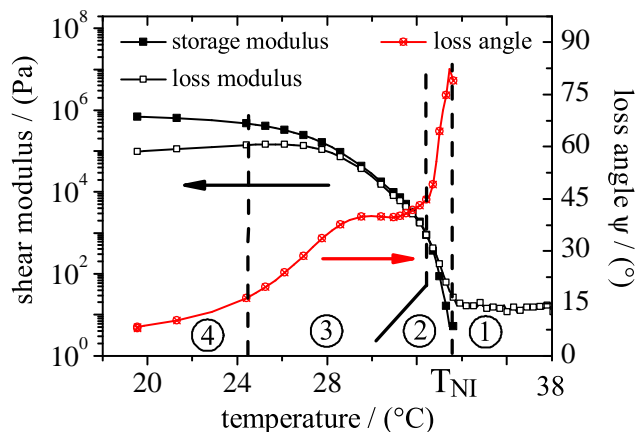


**Fig. 3.7.:** Temperature dependence of storage  $G'$  and loss modulus  $G''$  (left axis) at 50 Hz in course of the network formation. The right axis gives the scaling for the loss angle  $\psi = \arctan(G''/G')$ . Due to resolution limits the values for  $G'$  and  $\psi$  above  $33.5^\circ\text{C}$  cannot be resolved. The rheological data is taken from the identical sample as the confocal images shown in Fig. 3.6.



recovered giving rise to a temperature dependent contribution to the shear storage modulus.

A second effect was also taken into account. If two particles are in contact they create a so called depletion gap that is devoid of mesogenic molecules. In the densely packed network walls the number of particle contacts is high and so the surface area covered with the mesogenic liquid is reduced compared to the homogeneous mixture. However, when the network is deformed the number of particle contacts drops down again. The surface coverage increases and so does the surface energy that is proportional to the surface tension  $\gamma_{s,o}$  between particle surface and mesogenic liquid. This effect also generates a restoring force. Following reference [And00a] both contributions to the storage modulus amount to:

$$\begin{aligned} G' &\approx (1 - \phi_c) \frac{(A_o T^*)^2 (1 - \tau_{\text{red}})}{4 C \tau_{\text{red}}} \phi + \frac{\beta \gamma_{s,o} a \phi_c}{R_p^2} \\ &\approx [10^6 (1 - \tau_{\text{red}}) \phi + 10^5] \text{ Pa} \end{aligned} \quad (3.15)$$

Here  $\phi_c = 0.64$  denotes the particle concentration at random closed packing and  $a \approx 1$  nm the size of the mesogenic molecule. This theoretical estimate is not far off the experimental values.

### 3.2.4. Testing of the model and open problems

Although the essential features of the phase separation could be explained more recent experimental observations challenged this first model description. The particle radius critically influences the anchoring strength of the mesogenic molecules and thus enters in all formulas of the model, either directly like in equation (3.5) for  $T_{\text{NI}}$  and the depletion gap interaction in (3.15) or indirectly in the energy cost of the locally melted nematic phase in the network walls. Here one has to consider that the interstice between the closed-packed particles in the network walls widens with increasing  $R_p$ . Eventually this space becomes larger than the nematic correlation length  $\xi$  and a transition into the nematic state is no longer hindered. Assuming a typical correlation length of 10 nm [And00b] this requirement is already fulfilled for rather small particles:

$$\begin{aligned} d_{\text{Int}} = 2 \left( \frac{2}{3} \sqrt{4 R_p^2 - R_p^2} - R_p \right) &\geq \xi \\ \Rightarrow R_p &\geq 32 \text{ nm} \end{aligned}$$

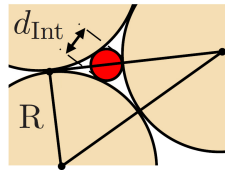


**Fig. 3.8.:** Size of the interstice in closed-packed spheres

In any case increasing particle radii cause a reduction in  $G'$ . Different experimental results either supported this prediction [Pet01] or challenged it [Vol05] showing no clear dependency at all. In the latter study no influence of the particle radius on the  $T_{\text{NI}}$  was found either. In general, for a given particle volume fraction of 10%<sub>vol</sub> the observed transition temperatures for particle radii in the range of 120 nm and 780 nm were consistently 2 K smaller than that for pure 5CB. Using the approximation in equation (3.5) the corresponding values for  $\xi$  doubtfully lie in the broad range of 10 nm and 62 nm. Hence, it is questionable whether the particles themselves are responsible for the reduction in  $T_{\text{NI}}$ .

Further questions arise if the observed phase separation kinetics is compared to the predic-

tions of the phase diagram. The theoretical model states that the isotropic-nematic transitions happens below the spinodal in Fig. 3.5 (b). However, the typical continuous phase separation like in Fig. 3.1 (b) was not observed even for the highest cooling rates of 30 K/min. Vice versa, a nucleation and growth-like phenomenology suggests that the phase separations sets in when passing the binodal line. Balancing the energy gain for the formation of a nematic nucleus and the energy cost for increasing its surface during the growth the minimal size of the nucleus is given by

$$r_{\min} = -\frac{2\gamma_{s,NI}}{\Delta F_n} \quad (3.16)$$

Taking into account that the interfacial tension  $\gamma_{s,NI}$  is very small and there is lots of free space between the particles in the initial isotropic suspension this criterion should not hinder the phase transition [Vol04]. So the phase diagram in Fig. 3.1 (b) rather predicts the nucleation of nematic droplets at temperatures close to that of the pure LC as it is also observed in the experiments.

Poon et al. [Cle04a] and Vollmer et al. [Vol05] suggested that in addition to colloids and LC a third low molecular impurity is present in the sample. Mixtures of LC and various types of solutes such as alkanes [Owe80] or more spherical molecules [Mar76] have been extensively investigated and behaved according to the phase diagram shown in Fig. 3.9 (a). With addition of the solutes the weakly first order isotropic-nematic transition of the pure LC converts into an extended coexistence region of isotropic and nematic phases that widens with increasing amount of solutes. Cooling the system at a fixed solute concentration into this coexistence region immediately causes the nucleation of small nematic droplets that are in coexistence with the isotropic phase and only grow with further cooling [red arrow ① in Fig. 3.9 (a)]. The phenomenology of this phase separation strongly resembles that of the LC-colloidal mixtures [Cle04a]. Though, the molecular solutes are more efficient as the required volume fraction for a fixed reduction of  $T_{NI}$  is about 10 times lower than for the particles [Vol05]. Possible candidates for such an impurity are short alkane chains like hexane or heptane that enter the particles during synthesis and storage [Kle03]. Although the particles are dried intensively before suspending them in 5CB, a small amount of alkane can remain in the particles and is slowly released into the suspension [Ceb83].

Clearly, an exact theoretical modeling of three component system of LC, particles and alkanes is even more complicated and we want to restrict ourselves to the phenomenological picture of the phase separation. Fortunately, the schematic phase diagram in Fig. 3.9 (a) has a certain degree of universality and applies for initial compositions up to 10 % [Mar76]. The occurrence of a nucleation and growth-like phase separation is not only properly predicted for the discussed cooling process ① but also during the evaporation of the low molecular solutes in course of time indicated by the blue arrow ②. This process is depicted in the confocal images of Fig. 3.9 (b) for a suspension of PS-SiO<sub>2</sub> core-shell particles [Appendix C] in N-(p-methoxybenzylidene)-p-butylaniline (MBBA 98 %, Sigma-Aldrich Chemie GmbH, Germany) with small amounts of tetrachlorethylene (TCE 99 + %, Sigma-Aldrich Chemie GmbH, Ger-

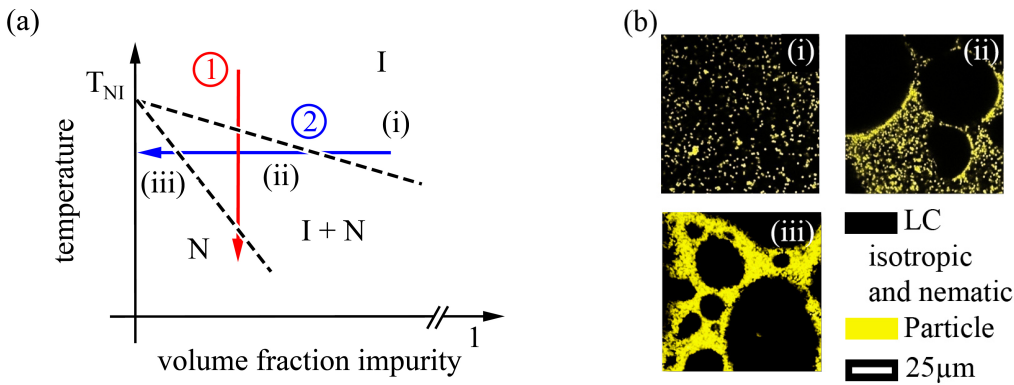


**Fig. 3.9.:** (a) Schematic phase diagram of a mixture of LC with additional small amounts of miscible contaminant. For the pure LC the isotropic-nematic transition is a weakly first order transition that happens at a single temperature  $T_{NI}$ . In the presence of low molecular solutes a coexistence region of isotropic and nematic phases opens enclosed by two binodal up that widens with increasing volume fraction of the solute. b) Confocal images of the phase separation induced by evaporation of the low molecular solute at a constant temperature represented by arrow ② in the phase diagram of part (a). The images (i), (ii) and (iii) correspond to the isotropic, isotropic-nematic coexistence and phase separated domains. The process resembles that of Fig. 3.6 that was induced by an experimentally easier controllable cooling the sample (red arrow ①).

many). As TCE evaporated over time the transition temperature  $T_{NI}$  of the mixture rose and the system entered the coexistence region. Just like for the cooling process nematic droplets nucleated and pushed the particles in the isotropic phase. In the end of the phase transition the suspension was phase separated into a cellular network [Fig. 3.9 (b)].

Beside to the phenomenology of the phase separation the coexistence region has also a large impact on the actual motion of the particles. Although a phase separation is energetically favorable the particles need to be moved by the isotropic-nematic interface. Taking into account surface anchoring, viscous drag and surface tension, the interface velocity must be smaller than a critical value of  $v_{crit} \approx 1 \text{ mm/s}$  [Vol04, Wes02]. Though, the nematic front in pure 5CB can move with velocities as high as  $v_{NI}^{pure \text{ 5CB}} \approx 1 \text{ cm/s}$  [Cle04a], a value that is largely defined by supercooling  $T - T^*$  of the isotropic phase. In the colloidal suspension with additional alkanes the coexistence of isotropic and nematic phases is thermodynamically stable and therefore rather the cooling rate defines the velocity of the interface. In this case even the highest rates of  $30 \text{ K/min}$  correspond to velocities of less than  $10 \mu\text{m/s}$ . Therefore, the phase separation process is very efficient and no particles get caught in the nematic phase.

In summary, the phase behavior and the phenomenology of the network formation is reasonably well understood whereas the rheology of the network still poses lots of questions. Are the interactions of the mesogenic molecules with the particles in the network responsible for the large shear modules? In how far do particle properties and the network morphology influence the mechanical properties? What is the origin of the highly visco-elastic behavior at intermediate temperatures?

Beside to the formulation of an appropriate mechanical model problems with the experimental measurements need to be solved. Vollmer et al. reported artifacts and low reproducibility

| Sample name | Content PMMA (% wt) | Stabilizer   | Radius (nm) | Density (g/cm <sup>3</sup> ) |
|-------------|---------------------|--|-------------|------------------------------|
| PHSA1-05    | 5                   | poly<br>(12-hydroxy)<br>-stearic acid<br>[Bos02]       | 460         | 1.189<br>±0.001              |
| PHSA1-10    | 10                  |  | ±15         |                              |
| PHSA2-13    | 13                  |  | 190 ± 10    |                              |
| PHSA3-10    | 10                  |  | 220 ± 5     |                              |
| PHSA4-10    | 10                  |  | 90 ± 10     |                              |
| PDMS-05     | 5                   | Methacryl-<br>oxypropyl-<br>terminated<br>PDMS [Kle03] | 380         | 1.187                        |
| PDMS-10     | 10                  |  | ±20         | ±0.001                       |

**Tab. 3.1.:** Particle parameters: Radii and standard deviations were determined by SEM on the basis of 50 particles. Both, radii and densities were comparable for the two types of colloids.

of the temperature dependent shear modules when the applied shear strain or frequency was too high [Vol05]. During its formation the network is prone to structural changes that may alter the mechanical response at lower temperatures. In the present work these difficulties were avoided by using the piezo-rheometer instead of a classical rheometer. As described in section 2.2.1 the applied strains were much smaller to assure that the mechanical testing was done in the linear visco-elastic regime. The accurate temperature control and homogeneous temperature profile across the sample further guaranteed reproducibility. Moreover, we extended our measurements to the full frequency response in order to get further insight into the visco-elastic nature of the network.

We proceed as follows: After a short note on the preparation techniques and used sample in sections 3.3 we continue with an detailed rheological analysis of the network formation and its evolution in terms of the regimes ② to ④ in Fig. 3.7 (sections 3.4 to 3.6). In particular we focus on the correlation of structural and mechanical characteristics during the network formation, the influence of various parameters like cooling rates as well as the time and frequency dependency of the mechanical properties. Section 3.7 emphasizes on the influence of the particle properties. We show that swelling and partial dissolution of the particles needs to be considered. Finally we reiterate experimental key results and give an interpretation in the framework of a new mechanical model (section 3.8).

### 3.3. Preparation techniques

Two types of PMMA particles were used in this work (appendix C). The main difference lay in the steric stabilization that was either chemically grafted poly(12-hydroxy-stearic acid) (PHSA) [Bos02] or methacryloxypropyl-terminated poly(dimethylsiloxane) (PDMS,  $M_W = 50$  kg/mol)[Kle03]. In order to study solely the influence of the stabilization agent, particles

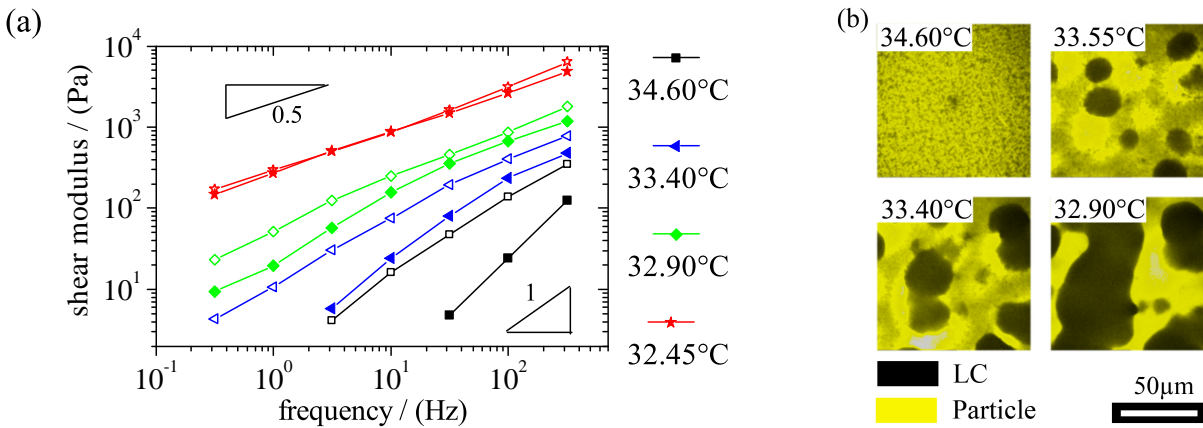


**Fig. 3.10.:** Correlation of mechanical and structural properties during network formation: a) The steady increase of both shear modulus ( $G'$ : filled symbols,  $G''$ : open symbols) and the changes in visco-elastic behavior are reflected in the confocal images of b). For easier comparison a selection of the confocal images from Fig. 3.6 were reproduced. See text for a detailed discussion.

of comparable radius were used. Besides, we varied the radii of the PHSA-stabilized particles to test the unclear previous results. Radii were determined by SEM images and the densities were measured using a density gradient column [Lin37] (Tab. 3.1).

The preparation procedure for the suspensions was adapted from the previous studies. After drying the particles in a vacuum oven at 50 °C and 1 mbar for several days, mixtures with 5CB (Chemos GmbH, Germany) were prepared at the desired PMMA weight fraction. The suspensions were stored in the isotropic phase and continuously stirred for at least one week before use in rheometric measurements.

The suspension was filled into the gap of the rheometer cell via capillary forces. The gap was varied in a range of 50  $\mu\text{m}$  to 1000  $\mu\text{m}$ . In order to prevent any phase separation during this filling procedure the rheometer cell was preheated to a temperature of 45 °C. After equilibration for 15 min in the temperature control box (section 2.2.1) the cooling process was started.

## 3.4. Phase separation: From a fluid suspension to an arrested state - Regime ②

### 3.4.1. Correlation of the structural and mechanical evolution

Up to now the mechanical and structural evolution was recorded in separate experiments. Different preparation techniques, uncertainties in the absolute temperatures and problems with reproducibility in the rheological measurements hindered an accurate correlation of both characteristics during the initial phase of the network formation. We circumvented these issues and complemented the mechanical analysis with simultaneous confocal microscopy using the combined setup described in section 2.2.1.

Frequency dependent storage and loss shear modulus are depicted in Fig. 3.10 for various

temperatures<sup>10</sup> together with the corresponding confocal images from Fig. 3.6. Starting in the isotropic phase at a temperature of 34.60 °C the suspension was homogeneous consisting of freely moving particles as well as some fragile particle clusters. Consequently, the mechanical response was viscous with  $G''$  exceeding  $G'$  in the whole accessible frequency range. The resolution limit of the piezo-rheometer was in the order of 5 Pa. So, for the spectra at the highest temperatures the natural frequency range of [0.3, 300] Hz was cut at the low frequencies. Nevertheless the Maxwell-like behavior of  $G'' \sim \omega$  is clearly visible.  $G'$  was considerably steeper but its slope in the double logarithmic plot did not reach the theoretical value. The extracted viscosity of 300 mPa.s was significantly larger than expected for a particle induced increase of the bare solvent viscosity ( $\eta_{5CB} = 25$  mPa.s [Pes06]) after Batchelor [Bat77].

$$\eta = \eta_{5CB} (1 + 2.5 \varphi + 6.2 \varphi^2) = 35 \text{ mPa.s} . \quad (3.17)$$

One possible explanation of this discrepancy is the partial clustering of the particles. At high frequencies  $G'$  and  $G''$  approached to each other indicating an relaxation process at slightly higher frequencies.

With the onset of the phase transition below 33.70 °C both modules rose over the whole frequency range and the relaxation shifted to lower frequencies. Although the crossing of  $G'$  and  $G''$  still lay outside the frequency range at 33.40 °C the deviations from the purely Maxwell-like behavior became obvious. At low frequencies *i. e.* on longer timescales, however,  $G''$  still exceeded  $G'$  and the sample behaved liquid-like. Local strains induced by to the nucleating and growing nematic droplets were dissipated by Brownian motion of single particles

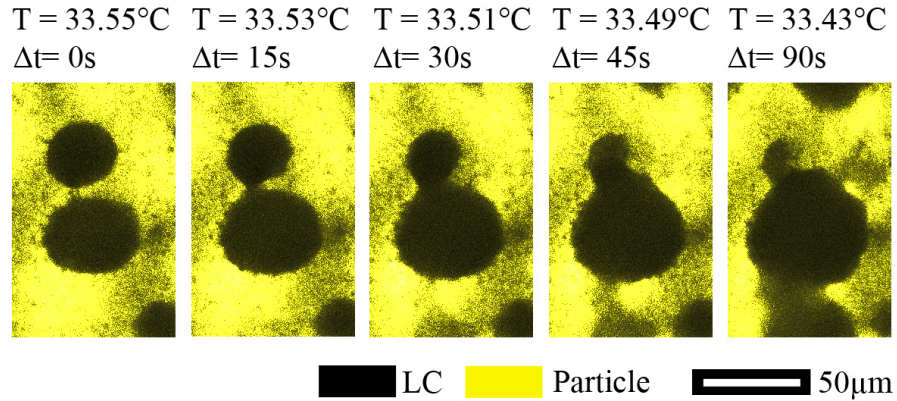


**Fig. 3.11.:** Coalescence dynamics of two neighboring nematic droplets: Differences in Laplace pressures cause the larger droplet to grow at the expense of the smaller one. The dynamics of the process depends on the interplay of surface tension and visco-elastic behavior of the isotropic colloidal phase.

<sup>10</sup>For every data point in the temperature data of Fig. 3.7 a complete frequency sweep with 16 points in the range from 0.3 Hz to 300 Hz was recorded. In every sweep single frequencies  $f$  were set successively and the mechanical response was averaged over 10 Periods. So, the actual measurement per each frequency took approximately  $10/f$  and for the complete frequency sweep about six minutes. At constant cooling rate of 0.1 K/min this resulted in a temperature difference between the first and last data point in the frequency sweep of about 0.6 K. To correct for this discrepancy the shear modules at a fixed temperature and frequency were interpolated from three consecutive frequency sweeps.

and irreversible reorganizations of particle clusters. Though, high viscosities of about 1 Pa s prevented a fast homogenization of the local particle concentration.

The mechanical properties of the sample are also mirrored in the shape and coalescence dynamics of the nematic droplets. Fig. 3.11 shows two neighboring droplets that were separated by a thin layer of particles. The droplets were not completely spherical because of the low surface tension and the inhomogeneous particle distribution. The generally high viscosity additionally slowed down the relaxation to a spherical shape. As soon as the separating particle layer ruptured and the droplets started to coalesce, the larger droplet grew at the expense of the collapsing smaller droplet due to the difference in Laplace pressures [But06b]. Yet, the merged droplet did not relax completely as indications of the small droplet remained. At the lowest temperature in Fig. 3.11 another even larger coalescence event happened but structural relaxations were limited to the contact area resulting in droplet interfaces that were no longer purely convex.

This transition to a more elastic behavior is reflected in the mechanical spectra and the evolution of a low frequency plateau in  $G'$  whose indications are firstly visible at a temperature of 32.90 °C. However, the plateau is not easily accessible because of the resolution limit of the rheometer and the increased recording time at low frequencies of 0.3 Hz. The cooling rate needed to be lowered significantly to maintain a roughly constant temperature during the measurements. This is experimentally challenging and the evolution of the plateau could be masked by aging effects.

### 3.4.2. Relaxation time spectrum

Although the structural evolution had almost ceased at a temperature of 32.90 °C the changes in rheology upon further cooling were considerable (Fig. 3.10). The network response became highly visco-elastic: The relaxation was still visible and shifted further to lower temperatures.  $G'$  and  $G''$  approached closer to each other showing a similar power law dependency on frequency. The loss angle  $\psi$  was almost constant at a value of 45°. The same features were also observed for other particle concentrations and surface modifications (Fig. 3.12). Yet, the absolute shear modulus  $|G^*|$  were much smaller for the PDMS stabilized particles.

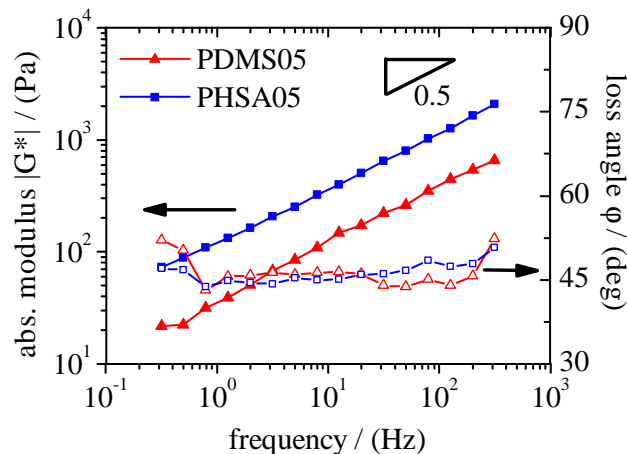


**Fig. 3.12.:** Self similarity was found to be universal irrespective of particle surface modification and concentration. The absolute shear modulus (filled symbols) follows a power law behavior with an exponent of 0.5. Accordingly the loss angle  $\psi$  (open symbols) is constant at a value of about 45°.

Such a power-law behavior corresponds to a so called self-similar distribution  $H(\tau)$  of relaxation times  $\tau$ .

$$H(\tau) \propto \frac{1}{\Gamma(n)} \tau^{-n} \quad \text{for } \tau_o < \tau < \tau_{\max} \text{ and } n > 0.$$

Such a behavior is characteristic for sol-gel transitions in various types of polymer solutions and melts when the constituent polymer chains start to form bonds between each other [Ada95, Win97, Nij97]. The nature of these bonds can be manifold. Physical bonds like entanglements, crystalline clusters or double helix formation are not permanent and form with time or a change in sample temperature. On the other side chemical bonds induced by covalent crosslinks between the polymer chains are permanent. The interconnected chains build up fractal clusters that grow until a single cluster spans the whole system at the gel point. The mechanical coupling between the polymer chains gives rise to new relaxation modes with a broad range of relaxation times. The smallest relaxation time  $\tau_o$  corresponds to the segmental relaxation of a single polymer chain that was already present before the transition. The largest relaxation time  $\tau_{\max}$  is linked to the motion of the largest clusters. As the cluster size and therewith  $\tau_{\max}$  diverges the self-similar distribution  $H(\tau)$  extends over several decades, and  $G'$  and  $G''$  follow a power law within the frequency range  $2\pi [1/\tau_{\max}, 1/\tau_o]$ .

In the given case of a gelling colloids the polymer chains are replaced by aggregating particles.  $\tau_o$  is related to the relaxation of the particles itself via Brownian motion, *i. e.* timescales in the order of seconds compared to milliseconds in case of polymers. This severely limits the range of frequencies where the self-similarity is observable. In particular it should be hardly visible in our spectra that extend to larger frequencies if not other unknown processes beside Brownian motion shift the spectrum to higher frequencies. The applicability of gelation theories could also be tested by means of the zero shear viscosity  $\eta_o$  in the fluid regime or the plateau modulus  $G'_o$ . In the vicinity of the gel point the divergent behavior of  $\lambda_{\max}$  is expressed in simple scaling laws for these two quantities [Win97]. Unfortunately, a reasonable determination of  $\eta_o$  and  $G'_o$  is not possible because of the limited frequency and modulus ranges. Hence, a gelation model cannot be used to describe the visco-elasticity of the network.

Besides, self similarity of  $H(\tau)$  is also observed in diluted polymer solutions if the polymer concentration or the molecular weight of the chains is too low for entanglement coupling (see appendix B). Dependent on whether hydrodynamic interactions between the monomers and the solvent are relevant (Zimm Model) or can be ignored (Rouse Model) storage and loss modules follow a power-law dependency with exponents of  $2/3$  and  $1/2$ , respectively. Although a slope of about  $1/2$  was observed for the colloidal network in Fig. 3.12 a connection to the relaxation of diluted polymers is not clear at this point.

### 3.4.3. Dependency on cooling rate

Before we proceed with the mechanical evolution at intermediate temperatures we shortly discuss the dependency of the droplet size distribution on the cooling rate. For the range of accessible cooling rates microscopic images of the network structure (PHSA1-10) are shown in



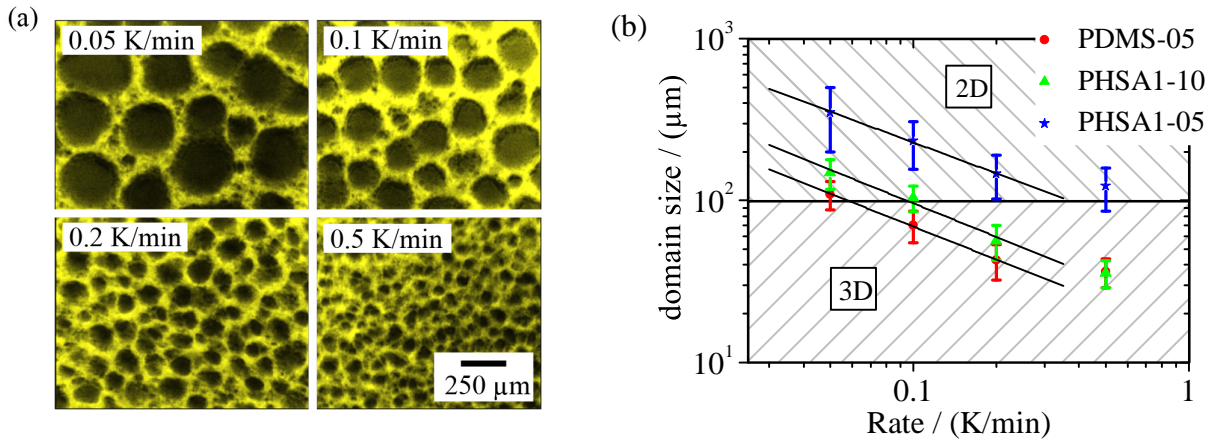


**Fig. 3.13.:** (a) Microscopic images of the network structure (yellow) of sample PHSA1-10 at a sample thickness of 100 μm and various cooling rates. With increasing cooling rate the size of the nematic droplets (black) decreased. (b) Image analysis: For each data point the average droplet size and its variance is calculated on the base of more than 50 droplets. All data follow a power law-like dependency (indicated by the straight lines). Areas with different hatching separates parameter constellations for which the droplet size exceeds the sample thickness and vice versa.

Fig. 3.13 (a). The images were made with the low magnification objective described in section 2.2.1. Like in the confocal images bright parts represent the network walls while darker areas correspond to the nematic domains inside the network cells. The extension of the nematic domains decreased steadily with increasing cooling rates which can be ascribed to two effects: At first the nucleation rate is increased for higher cooling rates. As the sample is cooled deeper into the coexistence region the energy gain and with this also the probability for the nucleation of nematic droplets is increased in the initial phase of the network formation. Secondly, the coalescence dynamics depends on the growth rate of the nematic droplets. As  $G''(\omega)$  increases with frequency larger stresses are required to disrupt the particle layers between adjacent nematic droplets in case of fast cooling. In addition the coalescence of droplets is a rather slow process. Hence, in case of low cooling rates nucleating nematic droplets are given more time to coalesce until the network freezes in its final structure [Vol05, Cle04a].

For a quantitative analysis we determined the size of at least 50 droplets per image with image processing software (ImageJ). The statistical analysis delivered an average droplet size and an estimate of the width of the underlying distribution. In the case of non-spherical droplet shapes, ellipses were approximated and both main axes were averaged. The double-logarithmic presentation of the droplet size in Fig. 3.13 (b) reveals a power law-like behavior for the lower cooling rates with similar slopes for all measured samples but largely different absolute values. In case of the samples PDMS-05 and PHSA1-10 the average droplet size dropped below the sample thickness within the given range of cooling rates which may be interpreted as a transition from a two-dimensional (2D) to a three-dimensional (3D) structure.

### 3.5. Rheology at intermediate temperatures: Relation between frequency and temperature - Regime ③

#### 3.5.1. Time-temperature-superposition and master curve

We further exploited the information gain from the combined frequency and temperature dependent measurements in order to study the visco-elastic regime ③ in Fig. 3.7. The overall rise of the shear modules with decreasing sample temperature is evident for the whole frequency range in Fig. 3.14. The spectra differ substantially with respect to the ratio of  $G'$  and  $G''$  reflecting distinct changes in the visco-elasticity of the sample. This evolution is more pronounced for the PDMS-stabilized particles and apparently correlate with the reduction in temperature.

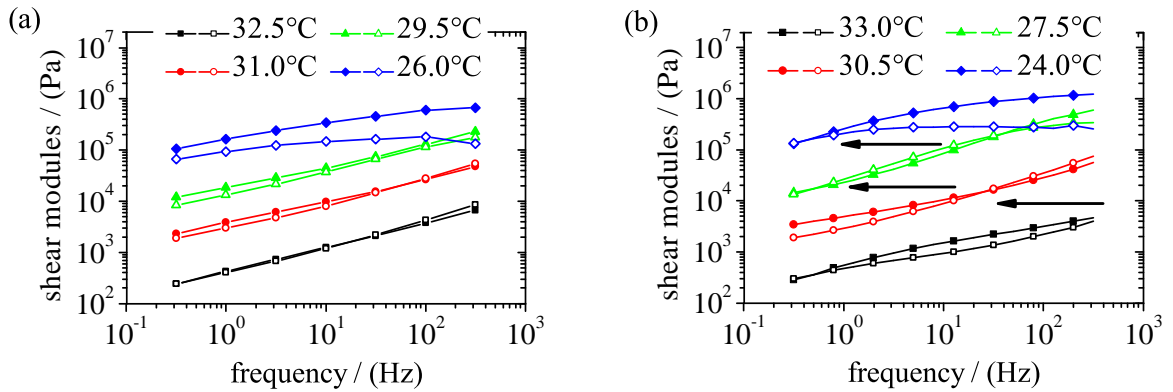


**Fig. 3.14.:** Frequency dependence of the shear modules for four different temperatures in case of sample PHSA1-13 (a) and PDMS-10 (b). Filled symbols represent  $G'$  and open symbols  $G''$  respectively. Especially for PDMS-stabilized particles characteristic features such as crossing points of  $G'$  and  $G''$  are common to all spectra. The spectra can be superimposed if they are shifted along the frequency axis. These shifts are indicated by the arrows in (b). For PHSA13 the spectra are less similar and a superposition behavior can only be based on the general increase in both modules.

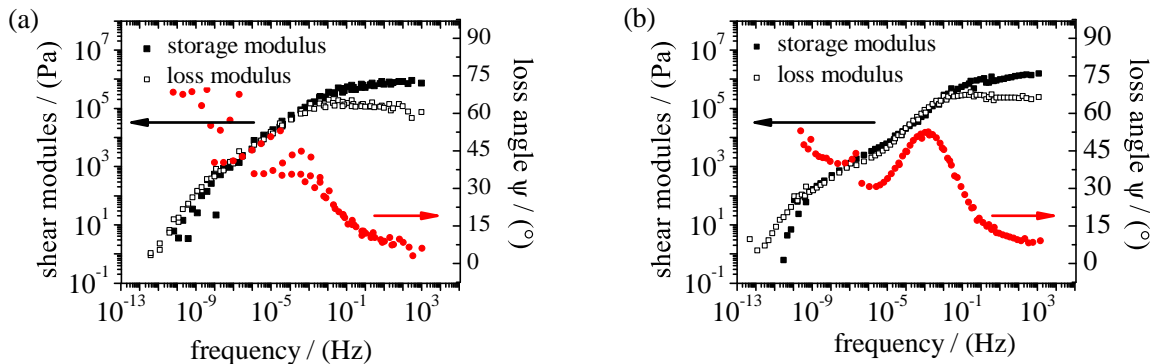


**Fig. 3.15.:** Master curves were obtained from a superimposed of the spectra from Fig. 3.14 for samples PHSA1-13 [a] and PDMS-10 [b]. Except for the initial network formation for frequencies below  $10^{-6}$  Hz the superposition worked reasonable well for PDMS-10. In particular the loss angle  $\varphi$  describes a smooth curve. The reduced congruence of the frequency spectra of PHSA1-13 led a poor superposition in particular for the loss angle. Only at high frequencies an continuous spectrum is obtained.

The individual spectra partially overlap when shifted along the frequency axis as indicated by the arrows in Fig. 3.14 (b). The resulting master curves of shear modulus and loss angle are depicted in Fig. 3.15 (b). The superposition works best for the temperature range of regime ③. At frequencies below  $10^{-6}$  Hz there are larger discrepancies in the master curves that are connected to the initial network formation. In general, the superposition appears much better for the PDMS-stabilized particles because of the pronounced maximum in the loss angle. In case of the PHSA-stabilized particles and the spectra in Fig. 3.14 (a) the superposition was based purely on the absolute shear modulus [Fig. 3.15 (b)]. The loss angle  $\psi$  remained discontinuous.

Such a behavior is well known in the rheology of polymers and is referred to as time-temperature-superposition (tTS) [Tob45, Tob56]. However, it has never been observed for colloidal suspensions before. Moreover, it was discussed that tTS cannot be applied to samples involving phase separations [Fer80a, Cav87]. Finally, time or frequency ranges involved in polymer rheology span ten decades while temperature changes typically by more than 100 K. In the given case of phase separating LC-colloidal suspensions the visco-elastic evolution of the network takes place in a temperature range of roughly 15 K. Therefore, the bare temperature dependency of the PMMA, that the particles were made of, cannot account for the observed temperature dependency. Nevertheless a superposition is feasible in particular for PDMS-10 and the resulting master curve very much resembles that of a polymer spectrum. We will come back to this point in section 3.8.

### 3.5.2. Reversibility and aging phenomena

The dynamics of the visco-elastic changes were tested in subsequent heating-cooling cycles in the temperature range [19.5, 29.5] °C, staying always well below  $T_{NI}$ . The temperature dependent storage modulus for the first nine cycles are shown in Fig. 3.16 (a). Within their experimental errors all data collapse onto a single curve for the whole frequency range. Yet, the curves reveal a pronounced hysteresis. For a rate of 0.5 K/min the weakening of the network due to heating was delayed by approximately 1 K compared to the stiffening under cooling. The hysteresis loop was significantly narrowed for lower rates and nearly vanished for quasi-stationary temperature control [inset in Fig. 3.16 (a)].

During the following cycles  $G'(\omega)$  at 20 °C dropped slightly [Fig. 3.16 (b)]. This tendency was reversed if the upper cycle temperature was increased to 34.5 °C, well above  $T_{NI}$ . The network was enforced after each cycle. In previous studies [Vol05] confocal microscopy showed that the network does not disintegrate completely under heating. Local variations of colloid concentrations persist long time in the isotropic state and lead to a network structure resembling that of the first cooling process. With every cooling the network formation becomes more ‘efficient’ accompanied by further compaction of the network walls.

The time dependent equilibration processes that cause the hysteresis must also be visible at a constant temperature. In addition, aging effects are expected as the network structure is meta-stable. The system can reduce its energy by compaction towards a macroscopic phase separation [Cat08]. The latter effect is called syneresis. For a temperature of 20 °C we observed

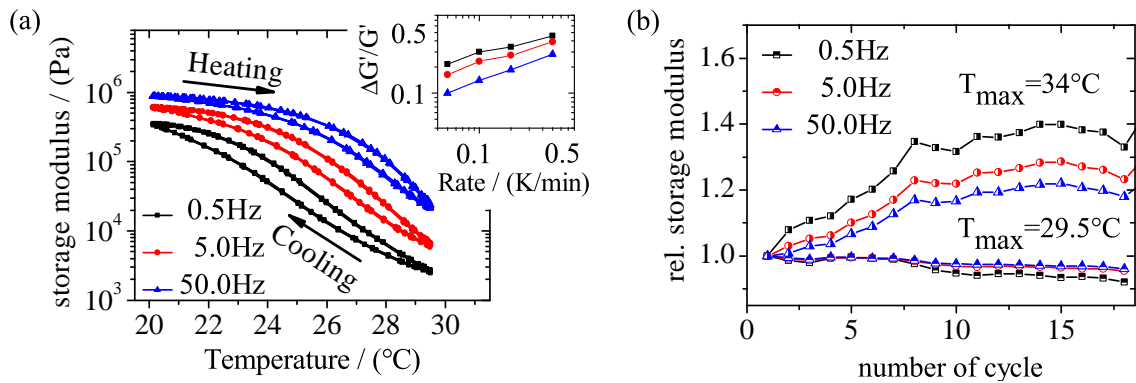


**Fig. 3.16.:** The sample PDMS-05 was kept inside the rheometer for successive heating-cooling-cycles. (a) The temperature dependent storage modulus  $G'$  is plotted for three different frequencies and for the first nine subsequent cycles. A pronounced hysteresis with respect to cooling and heating is revealed. The maximal cooling rate between the turning points was 0.5 K/min. The inset shows the dependency of the normalized maximal separation between the two hysteresis branches  $\Delta G'/G'$  on the cooling rate. (b) Differently shaded symbols represent the storage modulus normalized by the modulus at 20 °C for maximal temperatures was 29.5 °C and 34.5 °C respectively in course of 20 cycles. The temperatures were hold constant for 50 min before each measurement.

minor changes of the relative shear modules within the first hour after the end of the cooling (Fig. 3.17). In the following  $G'$  and  $G''$  clearly split apart reaching relative changes of up to 10%. This aging effect is most probably related to the compaction of the network to reach a macroscopic phase separation. On the timescale of two months at 22 °C we observed a macroscopic reduction of the network volume by about 25%.

When the cooling was halted at 32 °C both shear modules immediately dropped with a shallow shoulder at 1 h. This shoulder might result from the superposition of two independent processes. The first process is the delayed equilibration that is also expressed in the hysteresis. Corresponding to a vanishing hysteresis for rates much smaller than 0.05 K/min the mechanical evolution of the network is slowed down within the first hour after the cooling. On the other side the ongoing reduction of the modules is caused by the same aging processes like for the lower stopping temperature. The differences in the relative changes of the modules are most probably related to the altered visco-elastic state of the network. In case of the lower

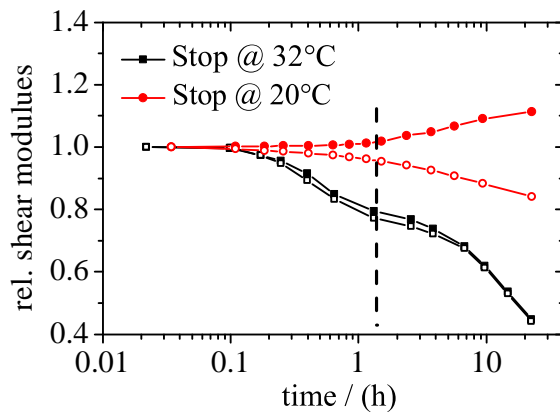


**Fig. 3.17.:** Aging behavior of PDMS-10 in the network state exemplary shown for stopping temperatures of about 32 °C and 20 °C. The filled and open symbols represent the storage and loss modulus, respectively. The data was normalized to the initial modules.

temperature the network is very stiff and elastic which imposes high energy barriers for a collapse. At higher temperatures plastic deformations of the network are more likely since  $G'$  and  $G''$  are nearly equal at a much lower level of about  $10^4$  Pa.

## 3.6. Rheology at low temperatures: Parameter study and morphology - Regime (4)

### 3.6.1. Dependency on colloid parameters

At this point we come back to the controversially discussed origin of the large shear modules of the network. If elastic energies between colloids and nematic LC were responsible for the network stability different surface modifications and therewith altered surface anchoring energies,  $W$ , should have a significant effect. Indeed we found quite substantial differences in the superposition behavior (Fig. 3.14) and visco-elasticity of the network for the PDMS and PHSA stabilized particles. This is most obvious in the maximum in the loss angle that is very shallow for the PHSA stabilized particles while it is strongly pronounced for the PDMS stabilized particles. Though, the fundamental features of the master curves in Fig. 3.15 were observed for either stabilizer. In particular at the lowest temperatures of  $20^\circ$  the frequency response of  $G'$  in Fig. 3.18 did only depend on the particle concentration. The loss modules  $G''$  were almost one order of magnitude smaller and less sensitive to the particle concentration.

The general increase of the network stiffness with increasing particle content is supported by previous works where a linear proportionality of the low frequency storage modulus  $G'(\omega = 1 \text{ 1/s})$  and the particle concentration was fitted to the data [And00a]. However, here we did not find a constant scaling factor for the whole frequency range and more importantly  $G'$  did not level off at low frequencies but rather at high frequencies.

In previous studies the influence of the particle radius remained ambiguous. With our measurements we confirm the results by Vollmer et al. [Vol05] which did not show any significant dependency. Suspensions were prepared from particles with radii covering a range of [90 – 460] nm (Tab. 3.1). We did not observe any changes in the frequency dependent shear modules either.

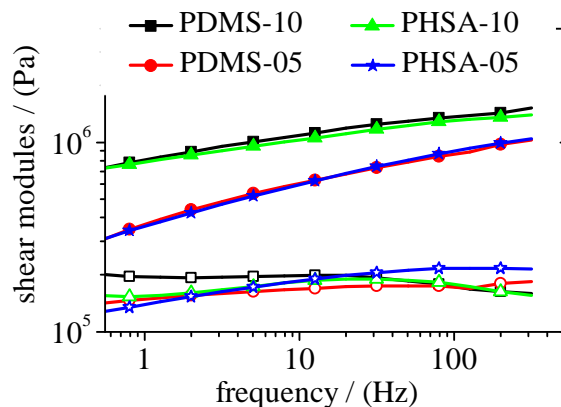


**Fig. 3.18.:** Frequency spectra for PHSA1-05, PHSA1-10, PDMS1-05 and PDMS1-10 at  $20^\circ\text{C}$ . The mixtures were cooled at  $0.1 \text{ K/min}$  and kept constant at the sampling temperature for 30 minutes before measuring. Filled symbols represent  $G'$  and open symbols  $G''$ .

### 3.6.2. Dependency on network morphology

Beside to material properties the network structure itself can have an impact on its mechanical properties. At first we tested the influence of the droplet size on the mechanical properties. We have shown in section 3.4.3 that the cooling rate during the network formation can be used as a control parameter for the droplet size. Moreover, a transition between a 2D and 3D network can be induced with a proper choice of sample thicknesses as well as particle materials and concentrations.

Fig. 3.19 shows the shear modules of sample PHSA1-10 at 20 °C corresponding to the network morphologies of Fig. 3.13 (a). As the cooling rate was increased,  $G'$  slightly dropped down over the whole frequency range and converged to cooling rate independent spectra at a rate of 0.5 K/min. This convergence of the mechanical spectra coincided with the mentioned transition from a 2D to a 3D network structure. Although the same effect was also observed for other samples the rheological differences between 2D and 3D structures were rather small. Moreover, if an analogous 2D-3D transition was induced by varying the sample thickness at a constant cooling rate the network rheology did not alter significantly.

In a more general approach the colloidal network may be regarded as a cellular solid [Gib97a, Ash83]. Examples for this class of materials are sponges, corals or foams. One distinguishes between open cell-structures where the material is built up from single solid strands with interconnected voids and closed cell-structures where the voids are separated by additional membranes. Following these definitions the colloidal network should be regarded as a mixed type as only a fraction of voids are separated (Fig. 3.20) .

The mechanical properties of cellular solids are described by simple scaling arguments that does not rely on the exact geometry of the cells. If a shearing force is applied to the sample two types of deformations occur; the bending of the cell edges and the stretching of the membranes. If  $\zeta$  is the fraction of open cell faces and  $\rho$  the average mass density of the cellular material

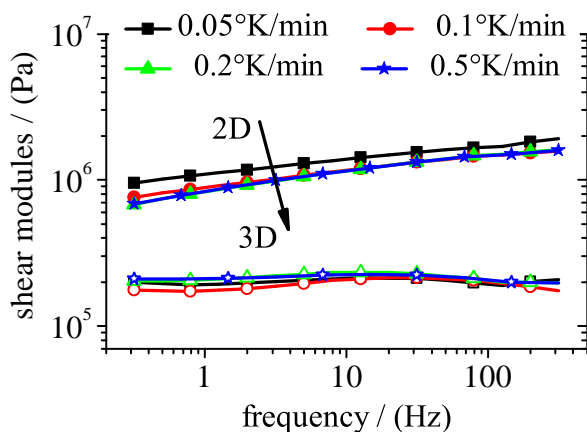
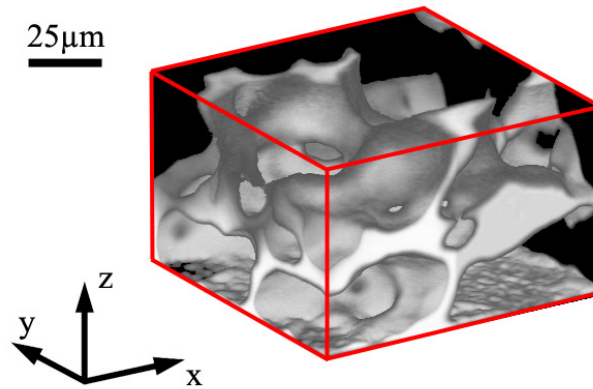


**Fig. 3.19.:** Dependency of the shear modules on the cooling rate for sample PHSA1-10. The spectra converge for increasing cooling rates until they collapse over the whole frequency range for the highest rates 0.2 K/min and 0.5 K/min.

**Fig. 3.20.:** The computer rendered reconstruction of the network from Fig. 3.6 shows the cellular morphology with partially separated voids. The image was generated with ImageJ software from a 3D data confocal set. The shaded area is an iso-fluorescence intensity surface representing the border between the nematic droplets and the colloidal walls.



the shear modulus  $G$  is given by [Gib97b]:

$$\frac{G}{E_s} \approx \frac{3}{8} \left[ \underbrace{\zeta^2 \left( \frac{\rho}{\rho_s} \right)^2}_{\text{edges}} + \underbrace{(1 - \zeta) \frac{\rho}{\rho_s}}_{\text{faces}} \right] \quad (3.18)$$

Here  $\rho_s$  and  $E_s$  denote the mass density and Young's modulus of the material the solid walls are made of. However, this model fails in case of the colloidal network. Assuming a constant packing density of colloids in the walls the relative density  $\rho/\rho_s$  is proportional to the initial particle volume fraction  $\varphi$ . Previous studies[And00a] found a linear dependency on  $\varphi$  which suggest  $\zeta = 0$ . This result, however, overestimates the contribution of the cell membranes.

In summary, we did not find a major effect of the morphology on the rheology of the LC-colloidal network. Neither the absolute shear modules nor the visco-elasticity could be related to the network structure.

### 3.7. Swelling and dissolution: Influence of sample age

Up to now the discussion of the results was based on the assumption that the PMMA particles behave as hard spheres and only the thin stabilizer layer induces a certain degree of softness. Previous studies, however, neglected that 5CB is a weak solvent for PMMA. Consequently, dissolution of the particles or at least swelling, in case the particles are crosslinked, must be taken into consideration. These processes definitely were present as they caused changes in the optical appearance of the suspension. Directly after dispersing the particles in 5CB the suspension was completely opaque as the micro- and nanometer-sized particle strongly scatter light. Though, with time and continuous stirring in the isotropic phase the suspensions became increasingly transparent.

Two processes can explain this change in the optical appearance. If the particles shrank due to dissolution their scattering efficiency  $\sim R^6$  was reduced and therefore the opacity of the suspension was reduced. On the other hand if the particles were swollen, the refractive index of particles and solvent aligned and thusly reduced the scattering. As these optical changes happened on the timescale of months we assume that the compatibility of PMMA and 5CB is

rather weak compared to good solvents like tetrahydrofuran (THF) or toluene. Moreover, at temperatures far below the glass transition of the PMMA ( $T_g \approx 110^\circ\text{C}$ ) the polymer chains are rather immobile and cannot be easily swollen or even freed by the 5CB molecules.

The dissolution and swelling dynamics were also influenced by the surface modification of the particles. While the suspension containing the PDMS stabilized particles became completely transparent after about six months the suspension with the PHSA stabilized particles remained slightly opaque for the time span of the whole study. This resistance against dissolution was most probably caused by a layer of crosslinked PHSA (Appendix C) at the surface of the particles that hindered dissolution.

In this section we discuss how dissolution and swelling of the particles were quantified and in how far the phase separation and the rheology of the network were affected.

### 3.7.1. Dynamics light scattering study

There are several methods to investigate the dissolution and swelling of the particles. For example, the changes in opacity can be directly utilized in measurements of the extinction coefficient of the suspension. A quantitative analysis, however, would require a complex model that accounts for partially swollen particles, *i. e.* a spatially varying dielectric contrast as well as the effect of dissolved PMMA. As the particle concentration must be sufficiently high to detect a significant effect, multiple scattering might also come into play as well as increased scattering by particle clusters. Another possibility is to measure the zero-shear viscosity of the suspensions. Dissolved PMMA as well as an increase of the particle volume fraction due to swelling equally affects the viscosity of the suspension. Again it is challenging to distinguish between both effects in particular when particle clusters influence the outcome of rheological measurements.

We followed a third approach and determined the hydrodynamic radius  $R_{\text{hydr}}$  of the particles via dynamic light scattering (section 2.3.3). As the measurements were performed in the diluted regime with volume fractions in the order of  $10^{-4}$  clustering of particles was negligible. In addition to 5CB we chose cis-DEC ( $\geq 98\%$ , Merck Schuchardt OHG, Germany) and THF

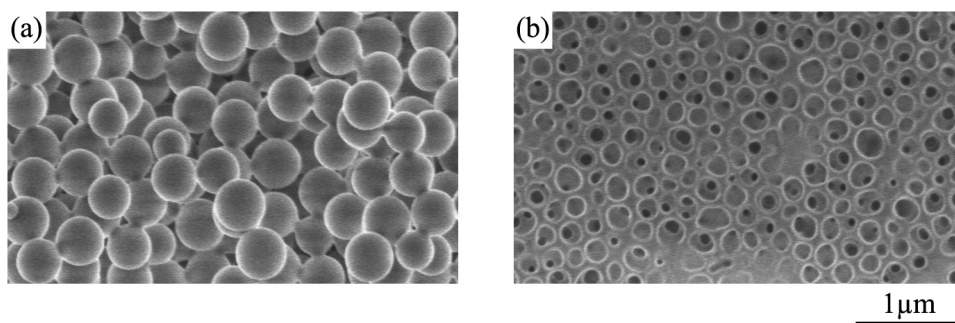


**Fig. 3.21.:** (a) The particle used for the DLS study were dried from a suspension in hexane. (b) The particles were dispersed in THF for several days to dissolve the non-crosslinked parts. After evaporation of the THF the remaining empty shells were embedded in the solidified PMMA matrix.



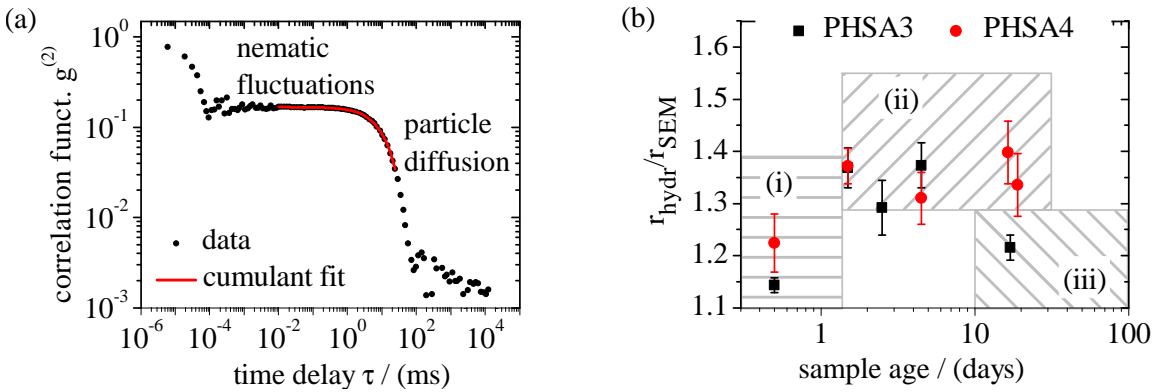


**Fig. 3.22.:** (a) Correlation function  $g^{(2)}$  for a suspension of 220 nm sized PHSA stabilized PMMA particles in 5CB at a temperature of 45 °C and a scattering angle of 30 °. The nematic fluctuations in the isotropic phase of 5CB cause a decay in the correlation at the lowest delay times  $\tau$ . The decay at  $\tau_{\text{diff}} \approx 40$  ms is caused by the Brownian motion of the particles. (b) The ratio of the hydrodynamic radius and the radius from SEM images shows a distinct evolution with time. Different regimes can be associated with the swelling of the stabilizer layer (i) and the whole particle (ii) respectively as well as the progressive dissolution of the particles (iii).

(99 %, Sigma-Aldrich Chemie GmbH, Germany) as reference dispersion liquids. The PHSA stabilized test particles had an average radius of  $220 \pm 3$  nm and a polydispersity of about 8 % determined by SEM images [Fig. 3.21 (a)]. In cis-DEC, which is commonly used to disperse organophilic PMMA particles, the hydrodynamic radius was measured to be  $(226 \pm 2)$  nm. The slight increase in the hydrodynamic radius compared to the SEM data is related to the PHSA layer that was swollen in the suspension and collapsed in the dried state. When the particle were dispersed in THF which is a good solvent for PHSA and PMMA the particles swelled fast within a one day after preparation. The hydrodynamic radius rose to  $(280 \pm 10)$  nm. After a few days the non-crosslinked compound was dissolved and the remaining shell gave a reduced hydrodynamic radius of  $(190 \pm 10)$  nm. After evaporation of the THF the empty shells shrank further to a radius of about  $(125 \pm 20)$  nm in the SEM image of Fig. 3.21 (b).

The DLS experiments with 5CB as dispersion liquid were more challenging. Obviously a measurement is not possible in the birefringent nematic phase. Though, in the isotropic phase the autocorrelation function  $g^{(2)}(t)$ , exemplary shown in Fig. 3.22 (a) at a scattering angle of 30 °, was distorted, too. Beside to the decay at  $\tau_{\text{brown}} \approx 40$  ms that was caused by the Brownian motion of the particles an additional decay became apparent. The origin of this decay were most likely pre-nematic fluctuations. As the isotropic-nematic transition in LCs is of weak first order these fluctuations occur even far above  $T^*$ . Their average lifetime and strength critically depend on temperature. Upon approaching the critical temperature  $T_c$ <sup>11</sup> both quantities diverge. As we performed the measurements at a temperature of 45 °C, *i. e.* about 10 K above  $T^*$  the fluctuations relaxed fast with a decay rate of about 42 MHz [Dro02]. Due to the poor statistics at the lowest delay times in Fig. 3.22 (a) the extracted decay rate of about  $1/\tau_{\text{fluc}} = 1/1.3 \cdot 10^{-8} \text{ s} \approx 80 \text{ MHz}$  is in reasonable agreement with these earlier results.

<sup>11</sup>For 5CB  $T_c$  is about 1 K above  $T^*$

Both decays did not interfere in the correlation function and could be fitted individually. However, part of the correlation was lost in the pre-nematic fluctuations which effectively reduced the signal-noise ratio for the detection of the decay due to Brownian motion. Moreover, the preparation method of the DLS sample apparently influenced the time span associated with the swelling and dissolution processes. One preparation route was to prepare a stock dispersion that was kept homogeneous in the isotropic phase under continuous stirring. For each DLS measurement a new sample was prepared from this dispersion. A second method was to prepare a single sample that was used for all DLS measurements. In between the measurements the cuvette with the dispersion was tumbled to prevent sedimentation of the particles. In case of the first method swelling and dissolution occurred earlier most probably due to the mechanical agitation by the stirrer. In previous studies ultrasonication was used for dispersing the particle which might accelerate the swelling and dissolution even more.

Despite these difficulties we found in 5CB a similar swelling and dissolution behavior like for the dispersion with THF. The freshly prepared suspension revealed a hydrodynamical radius of  $(236 \pm 4)$  nm consistent with the cis-DEC based suspension. Though, within a few days  $R_{\text{hydr}}$  rose significantly to a level of roughly 280 nm that was well in accordance with the first stage of the THF suspension and thus indicated a swelling of the particles with 5CB molecules. Within a few weeks the radius dropped down again due to partial dissolution of the particles [Fig. 3.22 (b)]. Although the time span of the different stages changed from one synthesis batch to the other the same features were universally observed.

The PDMS-stabilized particles showed a much more pronounced initial swelling of the stabilizer layer since the surface was not crosslinked and thus did not provide any mechanical hindrance to dissolution. For the same reason significant dissolution effects set in already after a few days but slowed down with further aging of the suspension.

### 3.7.2. Effect on the network properties

For the given set of cooling rates and sample thicknesses the swelling and dissolution of the particles affected the phase separation behavior only with respect to the observed transition temperature.  $T_{\text{NI}}$  gradually decreased from 35 °C which was very close to that of pure 5CB to about 32 °C for a sample age of more than 100 days. The structural properties were only marginally influenced. The domain size stayed roughly constant at level of 100  $\mu\text{m}$ .

The mechanical evolution of the sample, however, altered completely reflecting the transition from hard spheres to swollen particles. Within the first day after preparation of the suspension only the steric stabilization layer was swollen [cmp. Fig. 3.22 (b)]. The corresponding shear modules revealed an almost linear increase with decreasing temperature. The storage modulus was in the order of magnitude predicted by equation (3.15) in the model by Terentjev et al. [Fig. 3.23 (a)]. As soon as the network was formed the storage modulus exceeded the loss modulus over the whole temperature range at a nearly constant loss angle also supporting the hard sphere model [Fig. 3.23 (b)]. There was a rather weak frequency dependency exemplary shown in Fig. 3.23 (c) and Fig. 3.23 (d) at the lowest temperature  $T - T_{\text{NI}} = -15$  K.

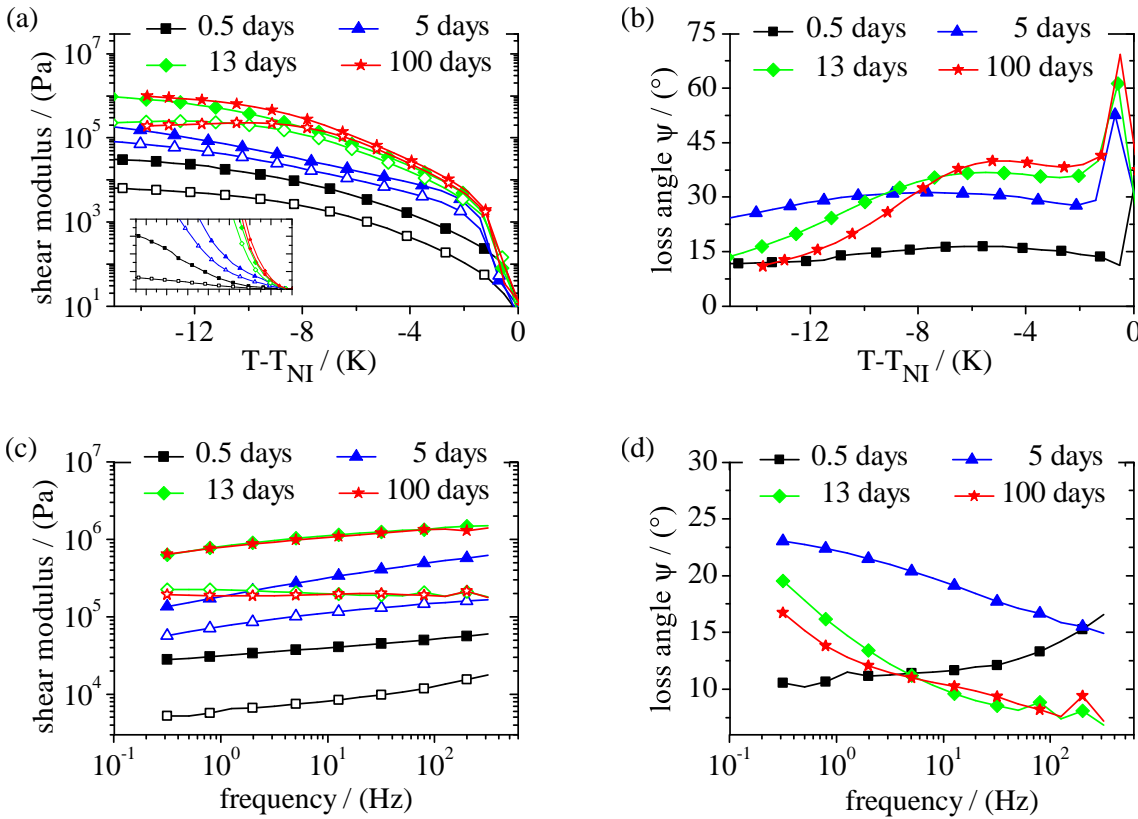


**Fig. 3.23.:** Evolution of the mechanical properties during the network formation and stiffening in dependency of sample age for PHSA stabilized particles with an initial diameter of 220 nm: (a) and (b) shows the temperature dependency of the shear modulus and the loss angle respectively at a excitation frequency of 5 Hz. The onset of the temperature axis was shifted to account for the different values of  $T_{NI}$ . The inset in (a) shows the same data as the large graph but in linear scale for the modulus. The frequency spectra in (c) and (d) were taken at a temperature of  $T - T_{NI} = -13$  K. See text for a detailed analysis.

Already a few days later the rise in  $G'$  and  $G''$  was much steeper reaching low temperature values nearly one order of magnitude larger than those of the fresh sample. Moreover, both modules approached closer to each other and in the temperature dependent loss angle a shallow maximum evolved. This maximum became clearer with further aging of the suspension and gradually shifted to higher temperatures while at lower temperatures the familiar splitting of  $G'$  and  $G''$  was observed. After 13 days a steady state was almost reached as the temperature and frequency dependent modules almost equaled those of the 100 days-old sample.

The same evolution was found for all PHSA stabilized particles whereas the aging time necessary for a convergence to the universal spectra was prolonged for larger particles. This is in accordance with the results from the DLS study that did not reveal a drop in the hydrodynamic radius of the larger particles in the observed time span. On the contrary the PDMS-stabilized particles showed a faster swelling and dissolution which coincided with the mechanical evolution. Already after 3 days the characteristic long-time visco-elasticity of the network was observed.

### 3.8. A detailed look on the network composition

#### 3.8.1. Discussion: Extension of the previous model

The model by Terentjev et al. is only valid for non-swollen particles. Therefore, we start the discussion of the results by setting up an extension of the model to account for the swelling and dissolution of the particles. The focus lies on the qualitative understanding of the mechanical properties rather than a quantitative description of the phase separation process in terms of a phase diagram. We have already discussed that the reduction in  $T_{NI}$  can have several reasons. In addition to low molecular impurities dissolved polymer chains have to be considered, too, and will be dominant with progressive dissolution of the particles. Yet, the general appearance of the phase separation process is not altered significantly as we shortly mentioned in section 3.7.2. The microscopic structure of the network walls, however, needs to be revised.

Upon entering the isotropic-nematic coexistence region both, the swollen particles and dissolved polymer, are expelled from the nematic droplets and concentrate in the remaining isotropic phase [Fig. 3.24 (a)]. The network wall resembles an inhomogeneous mixture of PMMA and mesogenic molecules at a broad distribution of local concentrations. In the core of the particles the concentration of mesogenic molecules is very low while they build the majority compound in the swollen shells and the interstices between the particle. As the phase sepa-

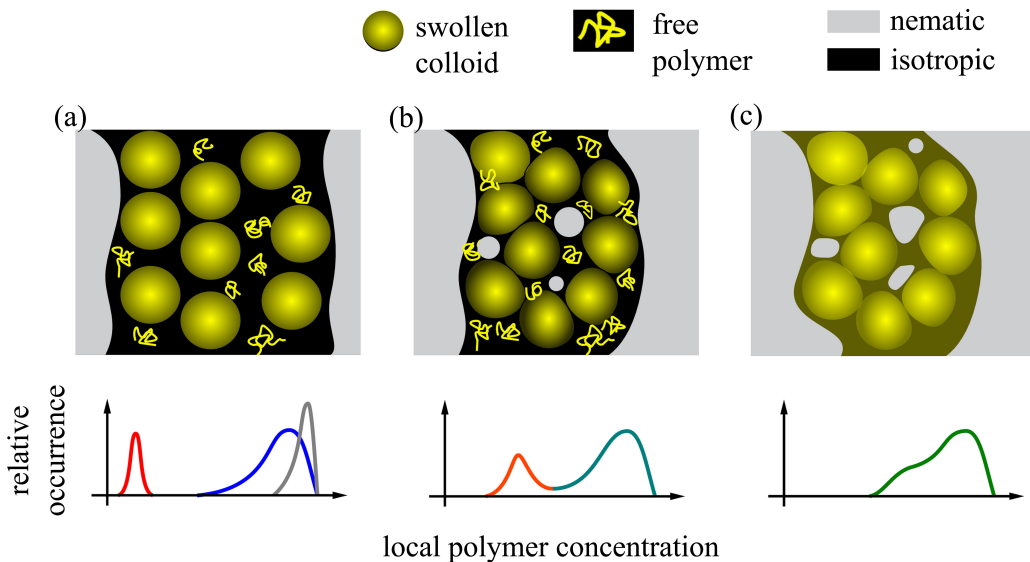


**Fig. 3.24.:** The microscopic composition of the network walls changes with temperature: (a) Just after the network formation the swollen particles are embedded a low concentrated polymer solution. The distribution of local polymer concentrations is split into two separate contributions (red and blue). The non-swollen particle have a narrower distribution (gray) (b) Mesogenic molecules diffuse to the large nematic domains and eventually nucleate to form small nematic droplets in the network walls. As the isotropic volume shrinks the swollen particles get deformed and the concentration of dissolved polymer in the interstices between the particles rises. The distributions of local polymer concentration start to merge (orange and cyan). (c) The ongoing phase separation equalizes the local composition of the network, *i. e.* the local polymer concentration becomes more uniform (green).

ration progresses, mesogenic molecules in the network walls join the large nematic droplets or nucleate smaller ones within the walls. The molecules stem mainly from the highly diluted regions of the network as here  $T_{NI}$  is largest. Consequently, the distribution of local polymer concentrations narrows. [Fig. 3.24 (b)]. At this point the network is fully developed and any large scale structural reorganization are hindered due to the stiffness of the network. However, upon further temperature reduction mesogenic molecules can still diffuse to the nematic droplet. In this way the local concentrations further align and the network composition becomes more uniform [Fig. 3.24 (c)].

### 3.8.2. Network rheology revised

Up to this point there are no immediate evidences that could affirm our view of the network wall. Microscopic imaging techniques turned out to be less effective to study the structure of the network walls due to a corrupted image quality. DSC and NMR measurements did not give further insight either. Only the rheological data can be used to prove the swelling of the network wall and its steady composition changes. Here we follow an simplified way to describe the rheology of the system as if it was composed of individual components with specific mechanical properties. The geometrical arrangement and mechanical coupling of these components define the effective mechanical response of the sample.

In the network state the systems shows two levels of structuring. On the large scale the nematic droplets as well as the colloidal network build a bi-continuous system with both components spanning the space between the substrate plates of the rheometer. The mechanical properties of both materials deviate strongly. While the nematic phase is a liquid of low viscosity  $\eta_{nem}$ , the network is a rather stiff visco-elastic material characterized by the complex shear modulus  $G^*(\omega)$ . Any displacement of one substrate is transmitted deeply into the network while its range in the nematic phase is short. Hence, the response of the nematic phase can be neglected and the rheology of the sample is dominated by the network phase  $G^*(\omega)$ .

We repeat this argument in the framework of an equivalent mechanical circuit. The nematic and network phase are connected in parallel, so the strain  $\gamma$  and strain rate  $\dot{\gamma}$  equally apply to both phases. The stress transferred to the detection plate of the rheometer is a sum of the stresses transmitted through the nematic phase  $\sigma_{nem}$  and the network phase  $\sigma_{net}$ . For a sinusoidal excitation the complex effective modulus  $\tilde{G}_{para}^*(\omega)$  is then given by:

$$\sigma(\omega, t) = \sigma_{nem}(\omega, t) + \sigma_{net}(\omega, t) = \underbrace{[c_{nem} i \eta_{nem} \omega + c_{net} G_{net}^*(\omega)]}_{\tilde{G}_{para}^*(\omega)} \gamma(\omega, t) \quad (3.19)$$

$c_{nem}$  and  $c_{net}$  denote the relative amplitude of both contributions which can be approximated by the corresponding relative volume or mass fractions. Even for the highest frequencies  $\omega = 2\pi f \approx 2000$  1/s the contribution  $\eta_{nem} \omega$  only amounts to 40 Pa which is much smaller than the measured modules.

At the second level of structuring the network wall itself is build up of a swollen polymer matrix with a broad distribution of the relative amounts of PMMA and 5CB as described

above. To be more precise during and directly after the network formation the particles are embedded in a diluted polymer melt. The particles itself consist of a hard core that is surrounded by the swollen shell. So, only the mechanically weak diluted polymer is continuous. The equivalent mechanical circuit of the network consists of a complex combination of serial lines of viscoelastic, diluted polymer  $G'_{\text{visc}}$ ,  $G''_{\text{visc}}$  and hard, elastic particle cores  $G'_{\text{ela}}$ . In each of these serial lines the total strain is distributed over both components while the applied stress is constant:

$$\gamma(\omega, t) = \gamma_{\text{visc}}(\omega, t) + \gamma_{\text{ela}}(\omega, t) = \underbrace{\left[ \frac{c_{\text{visc}}}{G'_{\text{visc}}(\omega) + i G''_{\text{visc}}(\omega)} + \frac{c_{\text{ela}}}{G'_{\text{ela}}(\omega)} \right]}_{1/\tilde{G}_{\text{net}}^*(\omega)} \sigma(\omega, t) \quad (3.20)$$

The complex effective modulus  $\tilde{G}_{\text{ser}}(\omega)$  is dominated by the component with the smaller modulus  $G'_{\text{visc}}$  and  $G''_{\text{visc}}$ .

Clearly there is no sharp but a rather continuous transition between the particle core, the swollen shell and the free dissolved polymer. In this sense the above argument states that the rheological measurements test predominantly the weakest continuous component of the network walls. That is the dissolved polymer in the initial state of the network formation and the swollen polymer matrix in the final network. As the phase separation continues inside the network walls the 5CB concentration in the swollen polymer decreases and the network becomes more homogeneous. Now the contribution of the hard particle cores  $G'_{\text{ela}}$  rises and the network response becomes more elastic.

### 3.8.3. Evidences for polymer dynamics

If the presented rheological model is correct the measured shear modules reflect the viscoelastic behavior of a polymer solution at various degrees of dilution. In the following we go back to the experimental results and correlate the rheological properties of the sample with its composition.

In the isotropic phase the behavior of a Newtonian fluid was observed together with the indication of a relaxation process at frequencies slightly higher than experimentally accessible [Fig. 3.10 (a)]. The dynamics of the mesogenic molecules is too fast to account for this relaxation while the dynamics of the particles characterized by a diffusion time of  $\tau = 6 \pi \eta R^3 / k_B T \approx 1$  s are too slow. Only the dynamics of the dissolved polymer fits to the observed frequency range. Depending on the concentration of the polymer either the Zimm or Rouse model can be applied. Unfortunately, the exact concentration is not known and there are no information about  $G'$ ,  $G''$  for frequencies beyond the relaxation. Therefore, we can only monitor the evolution of the relaxation as the concentration of the polymer in the isotropic phase increases in course of the phase separation. At a temperature of 32.9 °C the relaxation shifted to lower frequencies of roughly 30 Hz. No crossing of  $G'$  and  $G''$  was observed which promotes the application of the Zimm model. However, the expected power law behavior of  $G'$  and  $G''$  with frequency at an exponent of 2/3 could not be unambiguously verified because of the limited accessible frequency

range. The Zimm model is applicable in the low concentration regime where hydrodynamic interactions play a role. At higher concentration a gradual transition to a Rouse-like behavior should take place. Indeed the expected power law behavior with a slope of  $1/2$  was found at lower temperatures consistently for all samples.

As the phase separation continues and the 5CB concentration in the polymer matrix decreases, entanglement of the polymer chains sets in. The corresponding rubbery plateau is clearly visible in the master curve Fig. 3.14 (b) of the PDMS-stabilized particles. The dissolved polymer chains and the swollen part of the particle generate an entanglement network that spans the whole system. The situation is different for the PHSA-stabilized particles that show less dissolution effects. Only the free dangling ends of the crosslinked chains in the particle shell can contribute to the entanglement network. Though, it is questionable if the necessary entanglement length is reached at all. Consequently, the rubbery plateau is very weakly evolved in Fig. 3.14 (a).

The entanglement region is followed by the transition zone at the lowest temperature. As the local polymer concentration further increases the viscosity of the network diverges. The network enters the glassy state and its mechanical response becomes highly elastic.

As the composition of the sample gradually changes with temperature the transitions between the different dilution regimes are smooth. The frequency spectra of Fig. 3.14 can be superimposed and the resulting master curve resembles that of a polymer melt. The LC acts as a plasticizer and shifts the polymer chain dynamics to higher frequencies just like a change in temperature does [Fer80b]. The heterogeneity of the local polymer concentration and its asymmetric changes with decreasing temperatures corrupts the quality of the superposition. Due to stronger dissolution and swelling the polymer distribution is more homogeneous for the PDMS-stabilized particles and the superposition works reasonably well. In case of the PHSA-stabilized particles the distribution of local concentrations is very broad leading to a poor superposition behavior.

#### 3.8.4. Thermodynamic equilibrium

In the following we discuss whether the system is in a thermodynamic equilibrium during the phase separation. Strictly speaking, this question needs to be negated. The aging experiments at low temperatures already proved that the cellular network itself is a metastable state of the system. The interface between the network wall and nematic droplets can be reduced by a macroscopic phase separation which lowers the total energy of the system. However, the corresponding energy gain is rather small and the stiffness of the network hinders any relaxation. In the isotropic state at high temperatures the ongoing swelling and dissolution process indicate that thermal equilibrium is not reached either. Yet, the involved processes are slow and we can assume the system to be stable on the timescale of the experiment.

Neglecting these issues, only the network formation and stiffening upon cooling remain questionable. According to our model the composition changes are the result of the ongoing phase separation due to an isotropic-nematic transition of the mesogenic molecules. That transition

happens at the concentration dependent temperature  $T_{NI}(\varphi)$  and thus the composition of the network is purely a function of temperature. If the network is in a quasi-static equilibrium its composition changes under cooling must be reversible if the sample is heated again.

Indeed we found that the mechanical response of the network is reversible in consecutive heating-cooling cycles. The observed hysteresis seemed to vanish for a quasi-static temperature control. Following our model of the network we suppose that once the network is formed diffusion of mesogenic molecules is the dominant process in the phase separation. Due to the high viscosity of the polymeric matrix and the correspondingly low diffusion constant of 5CB in the polymer matrix this process is slow and causes the dependency of the hysteresis splitting on the cooling rate.

Although all experimental observations can be qualitatively explained our argumentation is based on the direct correlation of the network composition and its rheology. Yet, the pronounced spatial heterogeneity of the network makes it virtually impossible to set up a detailed mechanical model as an extension of the equations (3.19) and (3.20). We pursued a different route and used the fact that 5CB is a solvent for PMMA in the isotropic phase. Instead of dispersing particles with unclear chemical and mechanical properties we prepared homogeneous mixtures of linear PMMA and 5CB at the full range of concentrations. In doing so we can relate the phase behavior of these composites with their temperature dependent mechanical behavior. But before going into detail on this approach in the following chapter we come back to the motivation of the presented study and state our conclusions.

## 3.9. Conclusions and Outlook

### 3.9.1. Mechanical properties of aggregated soft colloids

We shortly summarize the insights into the network formation in LC-colloidal composites with respect to our vaguely formulated problem in the beginning of the chapter. How do structural and mechanical properties correlate during the aggregation of the particles into the network and what are the influences of the present interactions as well as the particle properties. In the given case the aggregation mechanism is a phase separation process that is driven by the isotropic-nematic transition of the mesogenic molecules and the repulsive interaction of the particles with the nematic phase. Though, a complete macroscopic phase separation is hindered because of the enrichment of the particles in the isotropic phase and the accompanying kinetic arrest. Instead, the system remains in a metastable network structure.

Several parameters like the initial particle concentration or the cooling rate contribute to the actual appearance of the network but cannot explain its characteristic temperature dependent visco-elasticity and the high absolute values of the shear modules. Instead it is essentially the mechanical properties of the particle that define the mechanical behavior of the network. A freshly prepared suspension consists of hard spheres and the network rheology is highly elastic for the complete temperature range. It remains unclear whether the model by Terentjev et al. can be applied to explain this behavior. With time, however, the mesogenic molecules



swell and partially dissolve the particles. When these soft particles aggregate during the phase separation it is the softness that determines the mechanical properties of the network. We were able to affirm this statement by relating the temperature dependence of the mechanical network response to the dynamics of the constituent polymer chains that varies with dilution.

At this point we clarify the ambiguous use of the terminology "softness". For colloidal systems it is usually used to describe long-ranged repulsive inter-particle potentials caused *e.g.* by electrostatic interactions. The particle itself is made of a hard glassy polymer or silica. On the contrary a hard sphere-type potential has a short range and therefore is largely confined to the direct vicinity of the particle. Only a thin steric stabilizing layer prevents aggregation due to van der Waals forces.

In our case softness is rather related to the real mechanical weakening of the particle due to swelling which does not necessarily result in a long-ranged soft potential. The energy stored in the compression of a swollen particles still can be much larger than the thermal energy. In this case the particles actually behave like hard spheres if suspended as single particle. However, if strong forces cause aggregation of the particles it is a delicate interplay of the physical mechanical stiffness of the particles and the aggregating forces that determines the mechanical behavior of the whole aggregate.

In most cases either contribution dominates; In the beginning of chapter 1 we discussed systems for which any deformation of the particles can be ignored (polystyrene particles in water or silica particles in organophilic solvents). On the other side the LC-colloidal suspensions were dominated by the mechanics of the swollen particles. The same is true for the polymer brush-like rheology of water-based suspensions of PNIPAM-particles beyond the glass transitions (item ii in section 1.3.3). Though, in systems where both contributions are balanced out an unexpected mechanical behavior might be observed. The stick-slip motion of the aggregated gelatin particles that was discussed in item iii of section 1.3.3 might be considered as an example for this case.

### 3.9.2. Benefits of piezo-rheometry and simultaneous confocal microscopy

The present study clearly demonstrates the benefits of piezo-rheometry when dealing with fragile soft matter like the forming colloidal network. Low excitation amplitudes provided a high degree of reproducibility, small sample volumes and the compactness of the piezo-rheometer allowed for a homogeneous temperature profile across the sample and the shifted frequency range gave deeper insight into the visco-elasticity of the sample at reasonable recording times.

Furthermore, we showed for the first time that piezo-rheometry in shear mode with simultaneous imaging via confocal microscopy is possible. The oscillatory excitation of the rheometer did not deteriorate the spatial resolution of the confocal images. Vice versa, the placement of the rheometer cell on top of the microscope objective did not influence the mechanical testing except for a slightly increased noise level. The combination of both methods delivered more than bare mechanical and structural characteristics and their relationship. It also gave evidence that the mechanical excitation induced by the rheometer did not alter the sample

and thus guaranteed that the results displays the sample rheology in the linear visco-elastic regime.

### **3.9.3. Future prospects**

Despite of numerous advantages the finite resolution in the shear modulus of a few pascal limits the applicability of the shear piezo-rheometer to more compact aggregates and viscous fluids. Other piezo-based rheometers working in squeeze-flow mode might induce non-linear effects at lower strain rates but have a better resolution [Cra05]. Due to the usage of compact piezo-actuators as active elements a combination with confocal microscopy should be feasible, too.

After a long debate the present work explains the principle features of the rheology of 5CB-colloidal PMMA suspensions. Due to swelling and dissolution the particles cannot be dealt as hard spheres which leaves the initial theory by Terentjev et al. without experimental verification. Though, further investigations would be valuable and only requires a different type of particles. These particles must be dispersible in the LC but only show marginal swelling. Unfortunately, it turned out in several attempts that this condition is not easily fulfilled. PS particles swell even faster than PMMA while silica particles show flocculation already in the isotropic phase. So the search for suitable particle materials and steric stabilizers is still open.

## 4. Polymer dispersed liquid crystals

In the preceding chapter we set up a microscopic model of the network that is formed during the phase separation in colloidal-PMMA 5CB composites upon cooling through the isotropic nematic phase. In this model the network walls consist of PMMA and 5CB with a broad bandwidth of relative proportions that varies spatially as a function of temperature. These composition changes are supposed to be based on the phase diagram and demixing behavior of 5CB and PMMA. We already tested some implications like *e. g.* the reversibility of the mechanical properties in consecutive heating and cooling cycles (section 3.5.2) or the dependency on the swelling state of the particle before the network formation (section 3.7.2). However, there were some experimental limitations that attenuate the significance of our findings. Microscopic imaging was not capable of resolving the ongoing phase separation inside the network walls at low temperatures and the rheological data could not be used to determine the composition of network wall because of its intrinsic heterogeneity.

Instead of facing these shortcomings directly by means of further measurements with other experimental methods we followed an evasive strategy and compared the particle-based system with composites of linear PMMA chains and 5CB at various concentrations. Compared to the case of swollen and partially dissolved particles, PMMA and 5CB are now homogeneously mixed on a molecular level throughout the sample (in the isotropic single phase region of the mixture). As the majority materials, *i. e.* PMMA and 5CB still are the same, chemical interactions do not change and the thermodynamic description is similar to the colloidal suspension. In particular we expect an analogous phase separation into a PMMA-rich network phase and almost pure nematic 5CB droplets upon cooling through the isotropic nematic transition. Though, the forming network walls are more homogeneous than in the colloidal case facilitating a quantitative analysis of the rheological data. Still, we add dielectric spectroscopy (DS) as a new experimental technique to microscopy and rheology. Due to the large dielectric susceptibility of the 5CB molecules [Pes06] compared to PMMA DS is especially sensitive to the dynamics of the 5CB. Therefore, DS perfectly complement the rheological measurements which test predominantly the segmental dynamics of the polymer chains [Nob08].

The DS measurements and data analysis were performed by **Christos Grigoriadis** and **Professor Dr. George Floudas** from the **Foundation for Research and Technology-Hellas (FORTH)** at the **Biomedical Research Institute (BRI)**, Ioannina (Greece). We will present these data in section 4.4. Wide angle x-ray scattering experiments were also part of this collaboration which however will not be discussed in detail.

Before we start with the actual treatise on the PMMA-5CB composites we will give a short general introduction to phase separated composites of polymer and mesogenic molecules. Such

systems are often referred to as polymer dispersed liquid crystals (PDLC) and have been investigated intensively focusing predominantly on possible technological applications.

## 4.1. Introduction

A PDLC film [Coa95, Wes90] consists of micrometer-sized droplets of nematic liquid crystal that are embedded in a polymer matrix. The nematic director within the droplets has a well-defined configuration that is defined by the elastic properties of the LC and the anchoring of the mesogenes to the surrounding polymer matrix. This configuration is similar for all particles but its actual orientation with respect to an outer laboratory system is not subject to any constraints and thus differs from one droplet to the other. Consequently, the anisotropy in the dielectric constants ( $\epsilon_{\perp}$ ,  $\epsilon_{\parallel}$  for the components perpendicular and parallel to the nematic director) induces strong spatial variations in the refractive index of the film which gives rise to pronounced scattering [see Fig. 4.1 (a)]. The film appears opaque (“OFF”-state).

The situation is different if a homogeneous electric field is applied. At a sufficiently high field strength the mesogenic molecules align with the external field along their long axis ( $\epsilon_{\parallel}$ ) and the refractive indexes of the droplets converge to  $n_{\perp} = \sqrt{\epsilon_{\perp}}$ . In case the refractive index of the polymer  $n_p$  also equals  $n_{\perp}$  scattering is largely reduced and the film becomes transparent [see Fig. 4.1 (b)]. The PDLC film is in its “ON”-state.

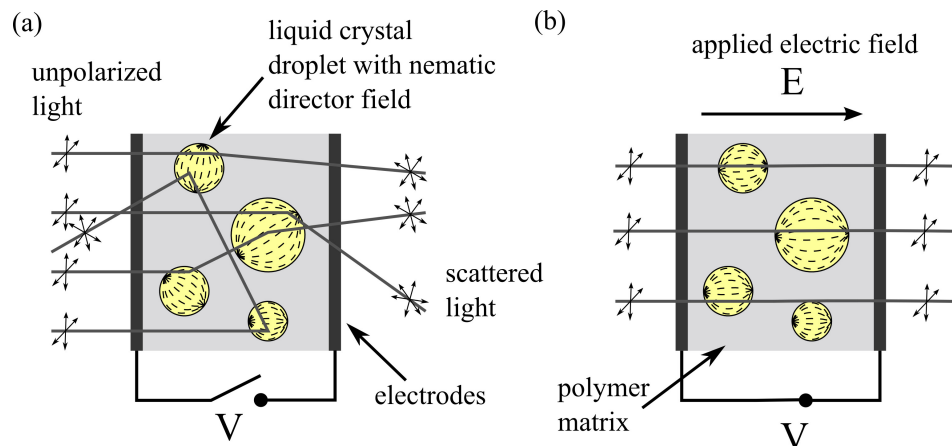


**Fig. 4.1.:** (a) OFF-state: Without an applied electric field the orientation of the nematic director of the LC droplets is uncorrelated. Large spatial variations of the refractive index give rise to scattering. (b) ON-state: If the nematic director field of the droplets is aligned due to an external electric field the scattering is strongly reduced. After reference [Coa95].

This functionality of switching the transparency of the film via an electric field opens up many applications in the field of displays, monitors and especially windows [Drz86]. As most of the incident light is scattered in forward directions and only a small fraction is actually absorbed the transmittance in the OFF-state is rather high [Coa95]. Therefore PDLC films are often used as coatings for front windows to prevent direct exposure to sunlight without darkening the interior. Another application are so called privacy windows that are used in offices to block insight in certain areas whenever needed.

The construction principle of PDLCs is comparatively easy. In contrast to the better known twisted nematic displays and other liquid crystal-based displays (LCD) no polarizers are required and the continuous polymer matrix provides means to tune the mechanical properties of the film. Devices can be made either flexible or rigid, and at the same time large areas can be covered which additionally emphasizes their usability for windows.

Several preparation methods were developed. In the early days the LC was emulsified in an aqueous polymer solution with the help of surfactants. During the subsequent evaporation of the water the already existing nematic droplets were enclosed in the solidifying polymer matrix. Due to the curved orientation of the nematic director in the droplets the phrase “nematic curvilinear aligned phase” (NCAP) was propagated [Kim98]. More recent methods start from a single isotropic phase and generate the droplet morphology via phase separation processes. The phase separation is either induced by evaporation of a common solvent for the polymer and the LC (SIPS - solvent induced phase separation) or by polymerization of an immiscible polymer from monomers that are miscible with the LC induced by ultraviolet light [Rou00] or heat (PIPS - polymerization induced phase separation). In this sense the phase separation in the PMMA-5CB composites upon cooling is related to SIPS.

The biggest part of scientific studies has been devoted to the understanding of the phase diagram [Gog01, Gog03, Bou01, Kyu96, Kar02, Che07, Cha95], the phase separation kinetics [Kyu93] as well as their influence on the optical performance [Mas02, Kal99] of the PDLC films. In particular the switching dynamics between the ON and OFF state and the optimization of contrast and transmittance were of interest. As key parameters the droplet size and shape [Ono05] as well as the configuration of the nematic director [Bla05] were identified. Next to the standard experiments for the optical characterization of the films DS was applied to study the dynamical properties of the LC molecules as well as their interaction with the polymer matrix. We come back to these studies when discussing our DS measurements of the PMMA-5CB composites. Less effort has been taken in the mechanical analysis of the PDLC films. Especially the rheology of the phase separation process lacks of a detailed description. Instead, problems related to the mechanical properties of the films were solved empirically.

By now PDLC films are fully commercialized and their development is largely taken over by industry. Hence, we will not draw any explicit conclusions related to PDLCs, but rather focus on the initial motivation of our study.

## 4.2. Sample preparation and general characterization

### 4.2.1. Preparation methods

Two methods were used to prepare the PMMA-5CB mixture at the full range of compositions. For samples with a PMMA volume fraction below 50%<sub>vol</sub>, 5CB (Chemos GmbH, Germany) and PMMA ( $M_w = 63$  kg/mol,  $PDI = 1.1$ ) were mechanically mixed in a closed glass flask and heated to a temperature of 100 °C. With the help of occasional mechanical homogenization with a spatula the PMMA dissolved within one day resulting in a transparent colorless liquid

of rather high viscosity. In order to prevent a phase separation the samples were stored in its homogeneous isotropic state at a temperature of 45 °C.

For the compounds with larger PMMA volume fraction the PMMA was first dissolved in THF and then mixed with 5CB. After a clear mixture was obtained the bigger part of THF was evaporated under ambient conditions. During this procedure the compound solidified and thus hindered any further evaporation of THF. Therefore, the mixture was exposed to a vacuum of 0.01 mbar for three days to remove the remaining THF. Cooling the sample with liquid nitrogen to  $-195\text{ °C}$  prevented extensive evaporation of the 5CB. The resulting relative amounts of 5CB and PMMA were determined via  $\text{H}^1\text{-NMR}$ . These samples were stable at room temperature and did not change over time.

#### 4.2.2. Phase behavior

The phase behavior of the mixtures was investigated with DSC and POM. Despite of a large number of experimental and theoretical studies on the phase diagram of various polymer-LC mixtures only very few dealt with the special case of PMMA-5CB composites. Unfortunately, only slight variations of the used materials can have tremendous effects on the phase behavior. For example, an additional isotropic-isotropic transition happens at temperatures above the isotropic nematic transition when replacing 5CB by E7 that is a mixture of four different mesogenic liquids with 5CB as the majority component [Kyu93, Cha95]. Yet, a complete description of the phase behavior of the 5CB-PMMA compound is out of the scope of this study and not essential for the further understanding. Instead, we draw a more general picture and refer to literature if necessary.

#### Glass transition of the compounds

Starting with pure PMMA a glass transition was observed in the DSC spectra at  $(110 \pm 2)\text{ °C}$  in agreement with other reported values. With increasing volume fraction of 5CB the glass transition temperature  $T_g$  dropped rapidly due to the plasticizing behavior of 5CB in PMMA [see Fig. 4.2 (a)] [Fer80b]. The experimental data could be described by the Fox equation [Fox56]

$$\frac{1}{T_g} = \frac{w_{\text{PMMA}}}{T_{g,\text{PMMA}}} + \frac{w_{\text{5CB}}}{T_{g,\text{5CB}}} \quad (4.1)$$

without any adjustable parameters.  $w_{\text{PMMA}}$  and  $w_{\text{5CB}}$  denote the mass fractions of 5CB and PMMA, respectively. For the glass transition temperature of pure 5CB a value of  $-68\text{ °C}$  was used. Together with the decrease in  $T_g$  the temperature range of the glass transition gradually increased indicated by the error bars in Fig. 4.2 (a). In principle, the Fox equation is based on the physical picture that the compound undergoes a single glass transition. Yet, the observed broadening can also be interpret as two individual glass transitions that are splitting apart with increasing 5CB content. One corresponds to PMMA and the other one to 5CB. The change in the specific heat  $\Delta c_p$  associated with the glass transition in Fig. 4.2 (b) cannot give

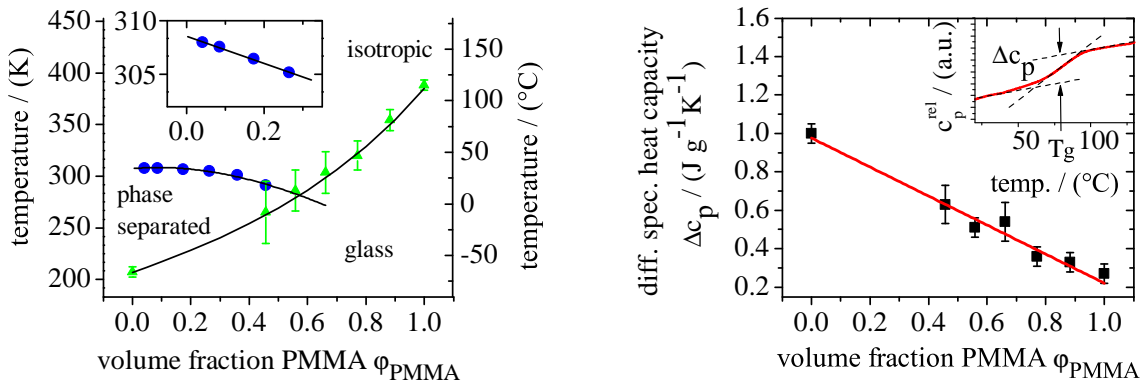


**Fig. 4.2.:** (a) High temperature phase behavior of the 5CB-PMMA composites: For high volume fractions of PMMA the system undergoes a glass transition that shifts to lower temperatures with increasing amount of 5CB. The error bars indicate the temperature range in which the transition occurs. At low volume fractions the glass transition temperature drops below the isotropic-nematic transition. The onset of the isotropic-nematic transition shifts to lower temperatures for increasing PMMA contents. (b) The difference in the specific heat associated with the glass transition follows a linear dependency on composition of the system. The inset shows a typical DSC curve and the tangents used to extract the characteristic quantities of the glass transition.

further insight into this question. Its linear decrease with increasing volume fraction of PMMA is in accordance with a single transition as well as two merged individual transitions.

A similar behavior was observed for other polymer solutions [Pla79, Flo93b, Flo92]. In particular, mixtures of polystyrene (PS) and toluene were investigated in detail. Dielectric spectroscopy, depolarized Rayleigh scattering and NMR-spectroscopy [Flo93a, Ada13, Rss85] proved that there are indeed two glass transitions. One transition happens at a temperature slightly above those predicted by the fox-equation and corresponds to a cooperative motion of PS and toluene. However, not all toluene is involved in this transition. Additional “free” toluene molecules shows a glass transition at a temperature slightly higher compared to pure toluene. This scenario requires the existence of concentration heterogeneities in form of PS-rich and toluene-rich domains at length scales in the order of  $20 \text{ \AA}$  [Flo93a, Don82]. In how far this picture is applicable to the PMMA-5CB compounds cannot be answered from the given data set. The presence of the phase separation prevents necessary experiments with highly diluted PMMA at low temperatures.

### Phase separation

Below a PMMA volume fraction of  $\varphi_{\text{PMMA}} = 0.40$  no glass transition was observed as the sample was already phase separated. The morphology of the separation process was very similar to that of the colloidal suspensions. With the onset of the isotropic-nematic transition nematic droplets nucleated homogeneously throughout the volume and grew with decreasing temperatures [see Fig. 4.3 (a)]. Droplets that got into contact eventually coalesced until any large-scale structural relaxation was hindered due to the stiffness of the polymer-rich network wall in Fig. 4.3 (b). The isotropic-nematic transition was also visible in the DSC thermographs

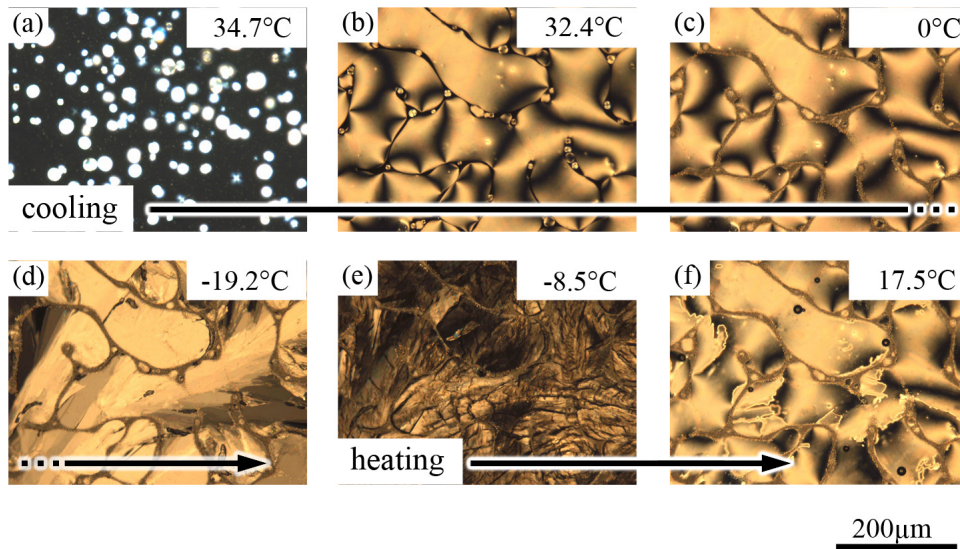


**Fig. 4.3.:** Microscopic images of the PMMA-5CB composite at various temperatures during a cooling-heating cycle taken under crossed polarizers. The phase separation, the Schlieren texture in the nematic phase and the crystalline structure compare well with the phase diagram of Fig. 4.2 and the DSC spectra of Fig. 4.4.

in Fig. 4.4 (b) but accurate temperatures could only be determined from the POM images. The data in Fig. 4.2 (a) represent the onset temperature of the phase transition *i. e.* the first occurrence of birefringent nematic droplets. At low PMMA volume fraction the transition temperature followed a linear dependency that was also observed for other impurities like alkanes [Owe80]. With increasing volume fractions, however, the decrease in the transition temperature became steeper. It is questionable if this behavior displays thermodynamic equilibrium. The sharp rise of the viscosity of the mixture from about 20 mPas to 1 MPas at a volume fraction of 0.46 %<sub>vol</sub> severely limited the nucleation and growth rates of the nematic droplets. Even the rather low cooling rate of 0.05 K/min used in the POM experiments might have been sufficient to supercool the sample. While this question could not be answered the higher cooling rates in the DSC measurements were definitely large enough to supercool the sample. Only the supercooling allowed for a determination of the glass transition temperature at this composition. In reference [Che07] even the initial linear regime for small PMMA contents was corrupted as the cooling rate was set to 1 K/min.

For other polymer-LC mixtures the experimentally obtained phase diagram was compared to thermodynamical calculations. The free energy of the system was modeled as the sum of the Flory-Huggins free energy of mixing and the nematic contribution according to the Maier-Saupe-Model [Che07, Kar02, Kyu96]. Although the agreement between the experimental and theoretical data was quite good the motivation for the used Flory-Huggins interaction parameter  $\chi(T)$  was not convincing. In many cases  $\chi(T)$  was determined by fitting model functions to the experimental data instead of independent considerations. Since already slight variations of  $\chi(T)$  can account for the above mentioned reduction in the transition temperatures such



an approach is not suitable in the present case.

From the experimental point of view any information about the relative compositions was lost in the phase separated state. So one could only distinguish between the polymer-rich network phase and the polymer-poor LC droplets. Until a temperature of about  $0^\circ\text{C}$  the network phase underwent further phase separation forming additional small nematic droplets inside the polymer-rich phase. These droplets were not directly resolved in the POM image but their existence can be inferred from the birefringent appearance of the network walls in Fig. 4.3 (c). This ongoing reduction of 5CB in the PMMA matrix should give rise to a glass transition of the PMMA. However, it was not observed in the DSC spectra. As both the change in specific heat as well as the relative content of PMMA were small the glass transition signal might have been masked by the isotropic-nematic transition. In PMMA-E7 composites the glass transition in the network was visible since the major part of the phase separation happened already at about  $60^\circ\text{C}$  [Cha95].

### Glass transition and crystallization of the nematic droplets

Before proceeding with the phase behavior at temperatures below  $0^\circ\text{C}$  we shortly discuss the phase behavior of pure 5CB based on Fig. 4.4 (a). Just like for the PMMA-5CB composites the observed phase boundaries of 5CB critically depend on the used temperature rates. If cooled very fast<sup>12</sup> the nematic phase was supercooled and 5CB transitioned into the glassy state (GLC). In the subsequent heating the glass transition was located at a temperature of  $-66^\circ\text{C}$ . At  $-40^\circ\text{C}$  5CB recrystallized from the supercooled nematic state to a metastable

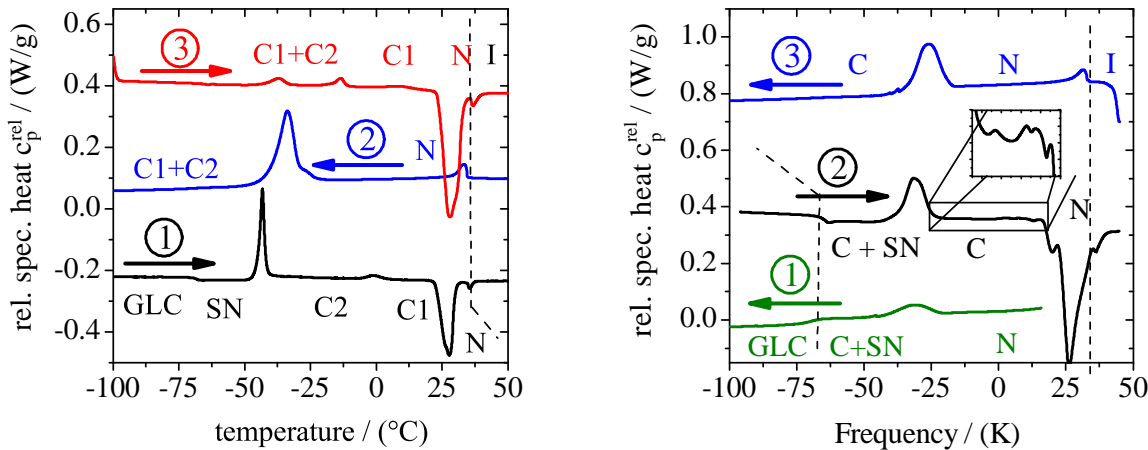


**Fig. 4.4.:** (a) DSC thermograms of pure 5CB: Prior to the first heating the sample was cooled at a rate of  $20\text{ K/min}$  to the starting temperature of  $-150^\circ\text{C}$  without measuring. Afterwards the heat flow was recorded for a set of heating [①, ③] and cooling ② cycles. (b) In case of the PMMA-5CB composites ( $\varphi_{\text{PMMA}} = 9\%_{\text{vol}}$ ) the first cooling ① started at room temperature followed by a heating ② and another cooling ③ cycle. All spectra were taken at a absolute temperature rate of  $5\text{ K/min}$ .

<sup>12</sup>The cooling rate for which supercooling is observed depends strongly on the purity level of the 5CB. Even small amounts can alter the behavior significantly. In our case a rate of  $> 20\text{ K/min}$  was sufficient to supercool the majority of the sample.

| Phase transition            | 5CB   |                                 |                                     | PMMA-5CB<br>( $\varphi_{\text{PMMA}} = 9\%_{\text{vol}}$ ) |                                 |                                     |
|-----------------------------|-------|---------------------------------|-------------------------------------|--|---------------------------------|-------------------------------------|
|                             | cycle | temp. $T$<br>$^{\circ}\text{C}$ | enthalpy $\Delta H$<br>$\text{J/g}$ | cycle  | temp. $T$<br>$^{\circ}\text{C}$ | enthalpy $\Delta H$<br>$\text{J/g}$ |
| I $\leftrightarrow$ N       | ②, ③  | 35                              | 2.4                                 | ①, ②, ③  | 32                              | 2.5                                 |
| N $\rightarrow$ C           | ②     | -33                             | 32                                  | ①<br>③   | -31<br>-26                      | 4<br>23                             |
| GLC $\leftrightarrow$<br>SN | ①     | -68                             | $\Delta c_p =$<br>0.55 J/g K        | ①  | -69                             | $\Delta c_p =$<br>0.23 J/g K        |
| SN $\rightarrow$ C          | ①     | -42                             | 38                                  | ②  | -32                             | 17                                  |
| C1 $\rightarrow$ N          | ①, ③  | 27                              | 65                                  |  |                                 |                                     |
| C $\rightarrow$ N           |       |                                 |                                     | ②  | 25                              | 52                                  |

**Tab. 4.1.:** Absolute values of the transition enthalpies of 5CB corresponding to the DSC thermograms in Fig. 4.4. The enthalpies for the composite were rescaled to account for the reduced amount of 5CB per total sample weight.

crystalline phase C2.<sup>13</sup> From this state a second recrystallization into the stable crystalline phase C1 took place at about 0 °C until the melting into the nematic phase happened at about 25 °C.

At moderate and slow temperature rates 5CB crystallized already during the cooling cycle into a mixed crystalline state of C1 and C2. Though, the transition was delayed by over 50 °C compared to heating cycle. During the following heating process various recrystallization events were observed ending again in the stable crystalline state C1. The final melting to the nematic phase did not change either. The associated transition temperatures and enthalpies in Tab. 4.1 were in fair agreement with the literature values [Man02].

In case of the PMMA-5CB composites only part of the 5CB could crystallize even at a moderate cooling rate of 5 K/min. A significant amount of 5CB transitioned into the glassy state. Upon heating a recrystallization event occurred at -30 °C in analogy to pure 5CB as well as several subtle events with low enthalpies that are magnified in the inset of Fig. 4.4 (b). The relative amounts of crystalline and glassy 5CB was largely affected by the morphology of the network. If the droplet size was small the amount of glassy 5CB was increased. Prior to the DSC measurements the sample was cooled fast through the isotropic nematic transition to room temperature resulting in nematic droplets with diameters in the range of a few micrometers. In the second cooling ③ in Fig. 4.4 (b) the droplet size was significantly larger<sup>14</sup> and all 5CB in the nematic droplets crystallized as it was the case for the sample shown in the POM

<sup>13</sup>Here crystallinity does imply full orientation and translational symmetry in all three space dimensions in contrast to nematic or smectic phases.

<sup>14</sup>The sample was given an equilibration time of only 30 minutes in the isotropic phase. This is not sufficient to fully homogenize the sample via diffusion. Therefore, the already existing phase separation into polymer-rich and polymer-poor regions aided the isotropic-nematic driven phase separation leading to a more efficient phase separation and larger nematic droplets.

images of Fig. 4.3. A possible explanation of this behavior is that the surface of the network walls imposes constraints to the 5CB and thus hinders crystallization. The same effect was observed for nematic 5CB in porous silica gels [Cra97]. However, in this study the cavities were much smaller in the range of tens of nanometers.

The transition enthalpies in Tab. 4.1 were not in agreement with the values for pure 5CB when normalized to the total amount of 5CB in the sample. In combination with the occurrence of multiple recrystallization processes this suggests the existence of other crystalline structures besides C1 and C2. Indeed, X-ray scattering spectra of the composite were not consistent with those of pure 5CB either.

We do not go into detail on this question and do not designate the individual crystalline phases in Fig. 4.4 (b). We rather emphasize that at sufficiently slow cooling the nematic 5CB droplets completely transition into the crystalline state. This is in particular the case for the rheological and dielectric measurements that we will describe in the following sections.

## 4.3. Rheological properties

### 4.3.1. Time-concentration-superposition in the isotropic phase

We proceed with the rheology of the linear PMMA-5CB composites starting with the isotropic phase at high temperatures. As we already mentioned before the reduction of the glass transition temperature of a polymer like PMMA due to mixing with a low-molecular diluent is known as plasticization. It is often used in industrial products in order to tailor the mechanical properties of polymeric parts. However, the plasticizing effect can only be controlled if the low-molecular component is miscible with the polymer on a molecular level. The validity of the fox equation is a first indication that this prerequisite is fulfilled [Fer80b, Kim93, Sch03a]. Further insight can be gained via rheological measurements as not only the glass transition temperature is influenced by the addition of the diluent but also the complete frequency dependent mechanical response which is described in the framework of the so called time-concentration superposition (tcS). We start with a theoretical introduction into this concept.

#### Theoretical background [Fer80b]

Going deeper into the microscopic picture of diluted polymers, the reduction of the glass transition is interpreted as a speed-up of the dynamics of the polymer chains. The addition of small mobile molecules locally generates additional free volume for the polymer chain and thus allows for further conformational changes. Hence, if the chain is stressed by a macroscopic deformation of the whole sample the chain relaxes faster to an equilibrated conformation compared to the non-plasticized polymer. The changes in free volume can be equally induced by plasticization or a change in temperature. Just as the  $\alpha$  relaxation times  $\tau_\alpha$  of the polymer is shifted to shorter times when the temperature is increased (appendix B), incorporation of

a low-molecular diluent  $\varphi_{\text{dil}}$  has the same effect.

$$\tau_{\alpha}(T_o, \varphi_{\text{dil}}) = a_C(T_o, \varphi_{\text{dil}}) \tau_{\alpha}(T_o, 0) \quad (4.2)$$

In this sense the concept of time-temperature superposition (tTS) [Fer80c, Wil55, Gur] can be transferred to a time-concentration-superposition (tcS) with temperature shift factors  $a_T$  replaced by concentration shift factors  $a_c$ .

In the theoretical derivation these concentration shift factors are related to the volume fraction of the diluent  $\varphi_{\text{dil}}$  and the free volume of the polymer  $f_{\text{poly}}$  via

$$\log[a_c(T_o, \varphi_{\text{dil}})] = \frac{\varphi_{\text{dil}}}{\ln(10)} \left( \frac{f_{\text{poly}}^2(T_o)}{\beta(T_o)} + \varphi_{\text{dil}} f_{\text{poly}}(T_o) \right)^{-1} \quad (4.3)$$

The shift factors  $a_c$  only indirectly depend on the reference temperature  $T_o$  via the free volume of the polymer and the diluent

$$f(T_o, \varphi_{\text{dil}}) = f_{\text{poly}}(T_o) + \beta(T_o) \varphi_{\text{dil}} \quad (4.4)$$

and

$$\beta(T_o) = \alpha_{\text{dil}} (T_o - T_{g,\text{dil}}) - \alpha_{\text{poly}} (T_o - T_{g,\text{PMMA}}) \quad (4.5)$$

with the thermal expansion coefficients  $\alpha_{\text{poly}}$ ,  $\alpha_{\text{dil}}$  and the glass transition temperatures  $T_{g,\text{dil}}$ ,  $T_{g,\text{PMMA}}$  of both components. The absolute modules scale linearly with the volume fraction of the polymer:

$$G_{\text{trans}}(t, \varphi_{\text{dil}}) = \varphi_{\text{poly}} G_{\text{trans}}[t/a_c(\varphi_{\text{dil}}), 0] \quad (4.6)$$

This formalism is not only valid for the transition zone of the master curve. It can also be used in the plateau and terminal zone with slight modifications in the scaling behaviors as long as one does not leave the regime of highly concentrated polymer solutions. In the plateau zone the presence of the diluent leads to an increase in the entanglement spacing. As a result, the height of the rubbery plateau shows a stronger reduction than the modules in the transition zone. Furthermore, the escape dynamics of the polymer chain from its current entangled configuration is accelerated:

$$G_{\text{rub}}(t, \varphi_{\text{dil}}) = \varphi_{\text{poly}}^2 G[\varphi_{\text{poly}}^{-2} t/a_c(\varphi_{\text{dil}}), 0] \quad (4.7)$$

In the terminal zone the same scaling for the modules apply but the terminal relaxation time scales differently:

$$G_{\text{term}}(t, \varphi_{\text{dil}}) = \varphi_{\text{poly}}^2 G[\varphi_{\text{poly}}^{-b} t/a_c(\varphi_{\text{dil}}), 0] \quad (4.8)$$

Depending on the model the exponent  $b$  lies between 1 and 1.5 whereas empirical results stated

$b = 1.4$ .

tcS was successfully applied to various systems [Fer80b] such as mixtures of PS with dodecane [Kim93], dioctyl sebacate and dioctyl phthalate [Sch03a] or ethylbenzene [Bau96].

### Application to the PMMA-5CB composites

In the following we verify the tcS concept for the PMMA-5CB mixtures. According to their definition in (4.2) the determination of the shift factors  $a_c$  require knowledge only about the relaxation times  $\tau_i$  or frequencies  $f_i = 1/\tau_i$  that can be obtained from frequency dependent rheological measurements. In principle these measurements have to be done at the same temperature as the scaling laws (4.6) to (4.8) are only valid for a fixed reference temperature  $T_o$ . However, the shift factors  $a_c$  typically span more than ten decades for the full range of compositions which is by far larger than the natural frequency range of the rheometer [see Fig. 4.5 (b)]. Fortunately, the relaxation process can be shifted to the accessible frequency range by changing the sample temperature. This change in temperature in turn is accounted for with the help of the tTS principle. Still, this strategy is not applicable for the  $\alpha$  relaxation as the phase separation at low PMMA volume fraction intercepts the determination of the relaxation time. Instead, we focused on the terminal relaxation that happens at higher temperatures for which the samples still is in the isotropic phase.

In practice the following procedure was applied. For each composition the frequency dependent shear modulus was recorded for various temperatures in course of a cooling process. Because of the upper temperature and shear modulus limit of the piezo-rheometer the measurements for PMMA contents larger than  $\varphi_{\text{PMMA}} = 0.1\%_{\text{vol}}$  were done with a classical rheometer setup (RMS-800, TA Instruments, USA) in oscillatory rotational shear with a parallel plate configuration. The sample temperature was reduced stepwise giving the sample

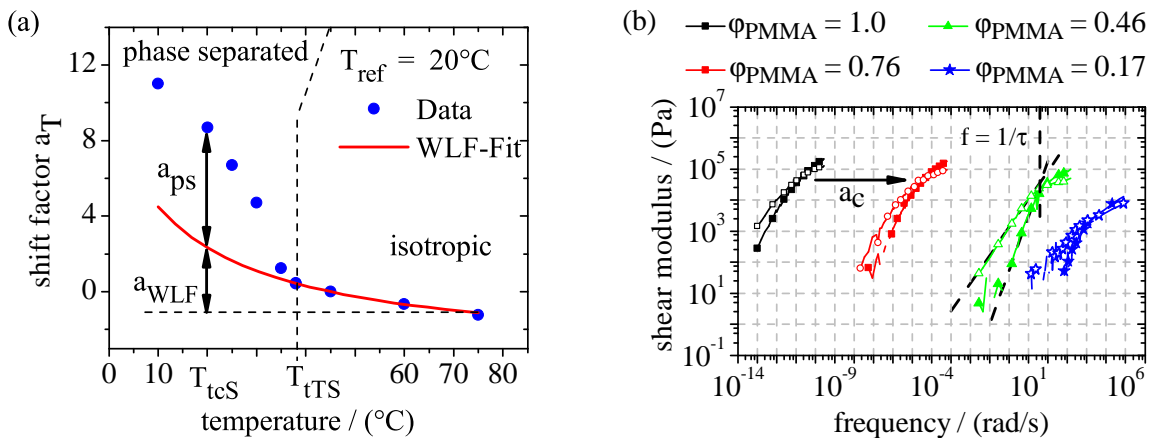


**Fig. 4.5.:** (a) If a phase separation process occurs, the temperature shift factors can be fitted to a WLF behavior [equation (B.9)] only for the high temperatures where the sample is isotropic. The discrepancy of the shift factor and the WLF fit at low temperatures are related to the compositions changes due to the phase separation. (b) The concentration shift factors were determined from the flow relaxation in the isotropic phase. The spectra refer to a single reference temperature  $T_{\text{tCS}} = 100^\circ\text{C}$  and span more than 15 decades in frequency.

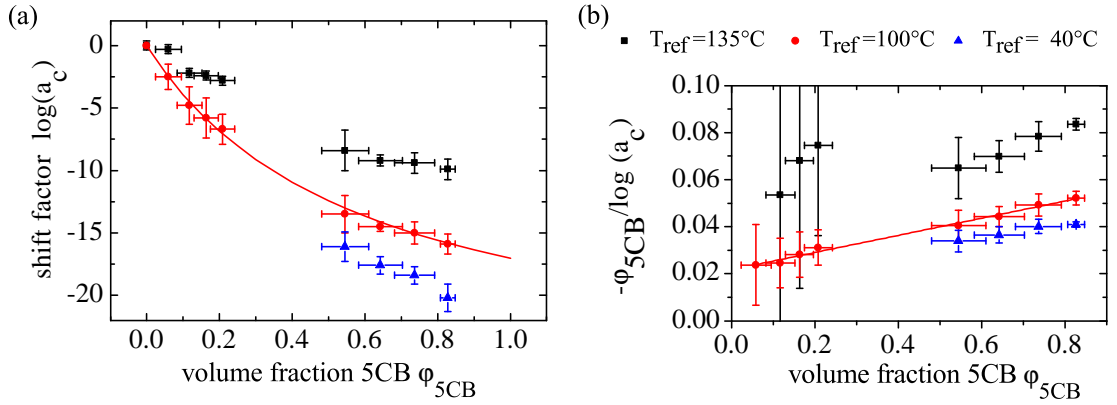


**Fig. 4.6.:** (a) Correlation of the concentration shift factors and 5CB volume fraction at different reference temperature  $T_{tcS}$ . The concentration shift factors span several decades depending on the temperatures. (b) According to equation (4.3) a linear dependency is expected in the plot of  $\phi_{5CB}/\log(a_c)$  versus  $\phi_{5CB}$ . Due to largely increased errors at low volume fractions of 5CB a reasonable fit is only possible for a reference temperature of  $T_{ref} = 100^\circ\text{C}$ . See text for further explanations.

10 minutes for equilibration before the start of the measurement. The master curve at the reference temperature  $T_{o,tTS}$  as well as the temperature shift factors  $a_T$  were obtained from the superposition procedure in analogy to section 3.5. For the temperature range where the sample was isotropic and no phase separation occurred the temperature shift factors  $a_T$  were fitted to a WLF-behavior (B.9) like in Fig. 4.5 (a) (appendix B). From this fit the WLF related shift factors  $a_{WLF}$  could be extrapolated for any desired reference temperature  $T_{o,tcS}$  and in particular separated from the shift factors  $a_{PS}$  in the phase separated state. The shift factors  $a_{WLF}$  were used to shift the master curves for each initial PMMA volume fraction  $\varphi_{PMMA}$  along the frequency axis to account for the change in the reference temperature from  $T_{o,tTS}$  to  $T_{o,tcS}$ . The terminal zones of the shifted master curves at various compositions are shown in Fig. 4.5 (b). For each spectrum the terminal relaxation time  $\tau_{term}(T_{o,tcS}, \varphi_{dil})$  was determined from the crossing point of asymptotic lines to  $G'$  and  $G''$  in the double logarithmic plot. Finally equation (4.2) was applied to calculate the concentration shift factors  $a_c$  for different reference temperatures  $T_{o,tcS}$  [Fig. 4.6 (a)].

This procedure is limited to reference temperatures  $T_{o,tcS}$  that are covered or close by the range of sample temperatures that are used to generate the master curves. Especially, if the reference temperature lies far below the glass transition temperature the extrapolation from the WLF fit shows large uncertainties. Therefore, no concentration shift factors could be obtained for small 5CB volume fraction in case of the lowest reference temperature of  $40^\circ\text{C}$  in Fig. 4.6. Furthermore, at high reference temperature like for  $T_{tcS} = 135^\circ\text{C}$  the errors in the shift factors for samples with high contents of 5CB increased rapidly. For an intermediate temperature of  $100^\circ\text{C}$ , however, the fit to (4.3) is reasonable. Both fit parameters,  $f_{PMMA}^{fit}(100^\circ\text{C}) = (0.016 \pm 0.003)$  as well as  $\beta^{fit}(100^\circ\text{C}) = (0.027 \pm 0.013)$ , compare well with the literature value of  $f_{g,PMMA} = 0.013$  [Fer80c] and  $\beta = 0.03$  obtained from equation (4.5) using thermal expansion coefficients of  $\alpha_{g,PMMA} = 1.6 \cdot 10^{-4} 1/\text{K}$ ,  $\alpha_{5CB} = 1.9 \cdot 10^{-4} 1/\text{K}$  and the glass transition temperatures in Fig. 4.2.

The validity of the Fox equation and tcS confirms that the PMMA-5CB compounds are homogeneously mixed on a molecular level in the isotropic state. At the same time tcS also supplies means to correlate mechanical properties and composition of the sample. Following this idea the shift factors  $a_{PS}$  in Fig. 4.5 (a) can be interpreted as concentration shift factors that are related to the composition changes during the phase separation. With the help of the parameters found in the previous paragraph these composition changes can be quantified and the temperature dependent concentration of PMMA in the network walls can be estimated. Before we continue with this idea we have a closer look on the superposition behavior during the phase separation.

### 4.3.2. Superposition behavior during phase separation

Fig. 4.7 shows the master curves and shift factors for various initial compositions of PMMA and 5CB for which the phase diagram in Fig. 4.2 (a) predicts a phase separation. As the reference temperature was set to 20 °C all master curves shifted to the same frequency range. Their general appearance resembles that of pure PMMA which is also shown for a reference temperature of 135 °C. Terminal zone, rubbery plateau and transition zone can be clearly

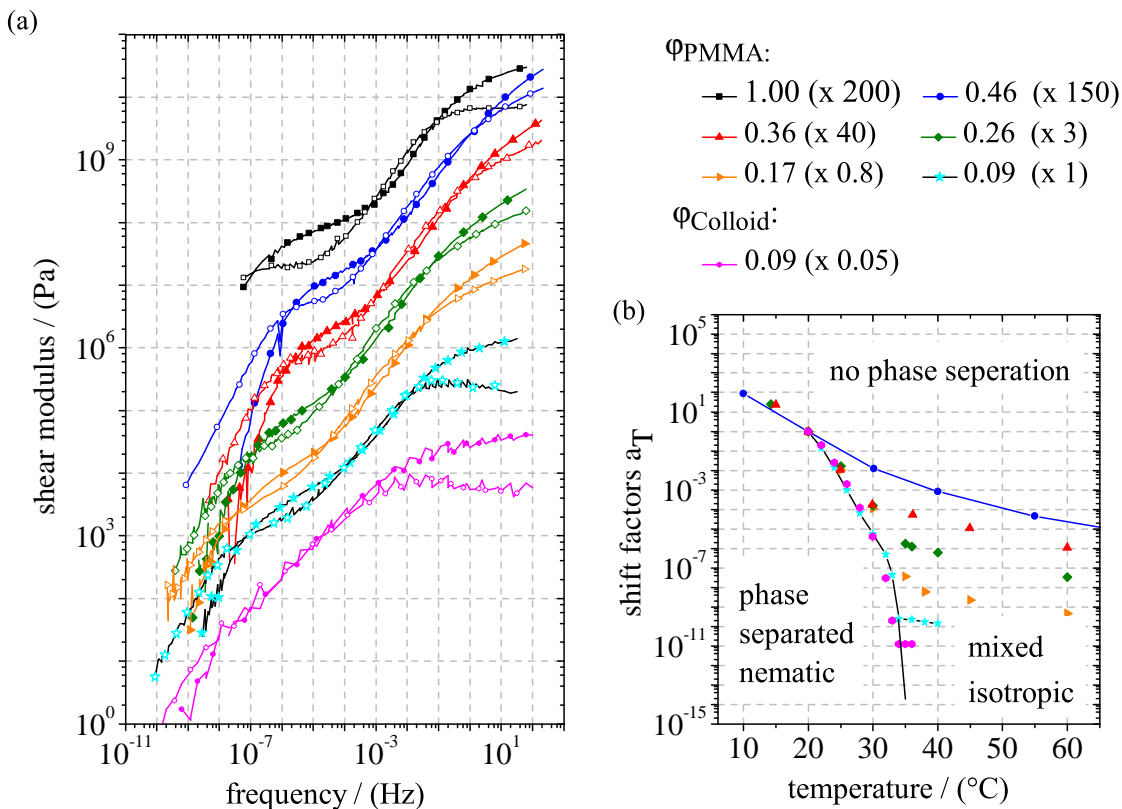


**Fig. 4.7.:** Master curves (a) and temperature shift factors (b) for PMMA-5CB composites at various contents of PMMA. Filled and open symbols denote  $G'$  and  $G''$ , respectively. The reference temperature is set to  $T_{o,tcS} = 20$  °C for all samples except for pure PMMA for which a temperature of  $T_{o,tcS} = 135$  °C was chosen. The moduli of the master curves were rescaled to minimize the overlap between the curves.

identified and do not show any obvious sign for phase separation. The terminal zone of pure PMMA was not accessible in the experiments as the sample foamed up at temperatures above  $180^\circ$ . This foaming was most likely caused by the evaporation of residual impurities in the PMMA. Similar, yet less pronounced effects were observed for the composites, too. Nevertheless, the superposition of the spectra was possible but the absolute values were corrupted and therefore will not be discussed.

The shift factors in Fig. 4.2 (b) exhibit a clear signature of the phase separation (except for  $\varphi = 0.46\%_{\text{vol}}$ ) as we already discussed above for an initial PMMA content of  $\varphi_{\text{PMMA}} = 9\%_{\text{vol}}$  in course of Fig. 4.5 (a). Following a shallow WLF behavior in the isotropic phase the shift factors rose sharply with the onset of phase separation. Moreover, all shift factors corresponding to samples and temperatures in the phase separated state collapsed to a single curve when referenced to a temperature of  $20^\circ\text{C}$  or below. This behavior indicates that the composition of the network walls was identical for all samples and only dependent on the temperature according to the phase boundary line in Fig. 4.2 (a). At a composition of  $\varphi = 0.46\%_{\text{vol}}$  the shift factors gave no evidence for a phase separation as the whole temperature range could be described by the WLF equation. This result is also in accordance with the phase diagram as the diverging sample viscosity delays the phase separation or hinders it completely if the sample is cooled too fast.

### 4.3.3. Concentration gauging

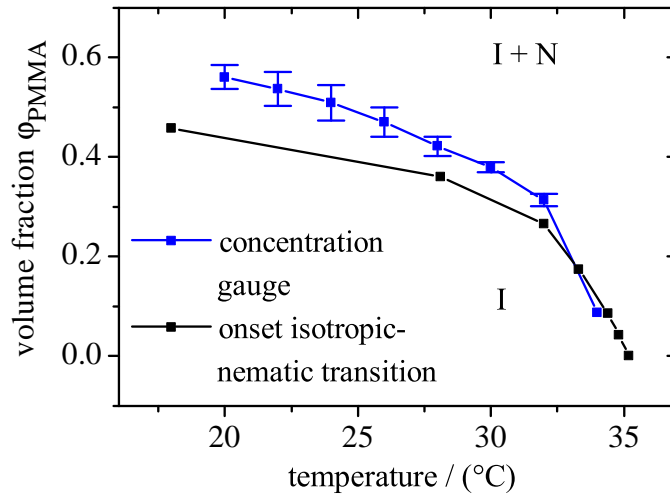
Up to now the connection between the shift factors and the phase diagram is based on a comparison of sample with different initial compositions. In other words, a direct quantitative interpretation of the shift factors for each sample on its own is still missing. Therefore, we come back to the idea from above and use the shift factors to determine the composition changes in the PMMA-rich network during the phase separation process.

The following stepwise numerical algorithm was applied: Starting at the onset temperature for phase separation with a known initial composition changes in the composition due to phase separation were calculated in small temperature decrements. In each temperature step the corresponding shift factor  $a_T$  was separated into its two contributions  $a_{\text{WLF}}$  and  $a_{\text{PS}}$ .  $a_{\text{WLF}}$  was calculated from the WLF-equation with the parameters extracted from the rheological data in the isotropic phase. Here it was essential that the WLF calculation was not based on the initial composition of the sample but the actual composition of the network at the current temperature. The remaining part  $a_{\text{PS}}$  was attributed to a change in composition  $\Delta\varphi$  according to equation (4.3). Knowing the new composition of the network the whole calculation was repeated for the next temperature until the lowest temperature is reached.

The results of this calculation are shown in Fig. 4.8 in terms of the temperature dependent volume fraction of PMMA inside the network walls averaged over different initial polymer concentrations. The error bars give a measure of the standard deviation of all tested samples. The overall agreement with the phase diagram is fair. In particular the non-linear drop of the onset temperature for phase separation with increasing volume fraction is correctly reproduced.



**Fig. 4.8.:** Local PMMA concentration in the network walls as a function of temperature estimated from the concentration and temperature shift behavior of PMMA-5CB mixtures. The data is compared to the observed onset temperature for phase separation in Fig. 4.2 (a).



However, there are larger deviations at the lower temperatures which can have several reasons. Since the algorithm works consecutively initially small errors increase steadily with the number of iterations and thus become largest for the lowest temperatures. The deviations can also be of physical origin. The phase diagram data were obtained from POM measurements at a cooling rate of 0.05 K/min which was slower than for the rheological measurements [(0.1 – 1) K/min]. Therefore it can be assumed that the average size of the nematic domains in the rheological measurements was smaller (compare chapter 3) and the network walls were thinner. If now the phase separation was dominated by diffusion of 5CB molecules in PMMA thinner walls allowed for a faster phase separation. In this case the kinetic hindrance, that led to the depression of the onset temperature in the POM measurements, was reduced for the rheology measurements. Consequently, the calculated polymer concentrations are higher than those predicted by the phase diagram.

## 4.4. A complementary approach: Dielectric spectroscopy

### 4.4.1. General measurement idea

The concentration gauging relies on the assumption that tcS works not only for the isotropic high temperature phase of the PMMA-5CB compounds but also for the network walls in the phase separated state. As we discussed above this requires a homogeneous mixing of PMMA and 5CB on a molecular scale. Dielectric spectroscopy (DS) is a technique that can give further insight into this question as it tests the rotational dynamics and relaxation behavior of molecular dipoles, *i. e.* 5CB molecules and the monomeric units of the PMMA. However, the dipole moment of 5CB  $\mu_{5\text{CB}} \approx 5$  Debye [Pes06] is larger than that of a PMMA unit  $\mu_{\text{PMMA}} \approx 1.4$  Debye [Shi94]. So, the dielectric response of the sample is dominated by 5CB. In this respect DS is complementary to the rheological measurements that gives information about the dynamics of the PMMA chains [Nob08].

In particular we are interested in the 5CB that is located in the network walls in the

phase separated state. Unfortunately, the corresponding dielectric response is masked by the signal of the nematic droplets that contain the bigger part of all 5CB in the system. Both contributions cannot be separated in the nematic state but as soon as the 5CB molecules in the nematic droplets crystallize their mobility is strongly restricted and the dielectric strength is largely diminished. Now the dielectric response is dominated by isotropic 5CB molecules in the PMMA matrix as well as supercooled nematic 5CB molecules that cannot crystallize due to confinement.

In the experimental realization the sample was cooled stepwise from the isotropic phase to a temperature of  $-65^\circ\text{C}$ . At each temperature the complex dielectric function  $\epsilon^*(\omega)$  is recorded for the full frequency range from  $10^{-3}$  Hz to  $10^7$  Hz. Since the measurement at each temperature took about one hour the effective cooling rate was sufficiently small to prevent supercooling of the nematic droplets (compare section 4.2.2). Obviously such a procedure is not suitable for pure 5CB as the whole sample crystallizes. Instead, the sample was cooled very fast below the glass transition temperature of  $-68^\circ\text{C}$ . During the subsequent heating the complex dielectric function  $\epsilon^*(\omega)$  of the supercooled nematic 5CB could be measured up to the recrystallization temperature.

#### 4.4.2. Rotation relaxation spectrum

We start with the discussion of the dielectric relaxation of pure 5CB [Kre03c]. Due to its chemical structure the 5CB molecule has a large dipole moment of  $\mu_{5\text{CB}} \approx 5$  Debye [Pes06] that is oriented approximately parallel to the long axis of the molecule. In the isotropic phase the molecules show no preferential orientation and the dielectric function  $\epsilon^*(\omega)$  is isotropic and can be described by a scalar value. On the molecular level there is only a single relaxation process that involves rotations of the 5CB molecule.

In the nematic phase, however, the average orientation of the molecules along the nematic director causes an anisotropy in  $\epsilon^*(\omega)$  that must now be described by a tensor. The two main components  $\epsilon_{\parallel}^*(\omega)$  and  $\epsilon_{\perp}^*(\omega)$  refer to parallel and perpendicular directions with respect to the nematic director. These components can be identified with two different relaxation processes of the molecule. The slower  $\delta$ -process is associated with  $180^\circ$  rotations of the molecule around its short axis. The other process combines three tumbling motions of the molecule around its long axis with similar dynamics and is referred to as the  $\alpha$ -relaxation [Roz96, Cra97].

Both processes can be clearly identified in Fig. 4.9 that shows the imaginary part  $\epsilon''(\omega)$  of the measured dielectric function in the supercooled nematic phase. The spectrum was fitted to the Havriliak-Negami function in equation (2.35) in order to determine the dielectric strengths  $\Delta\epsilon_{\alpha/\delta}$  as well as the relaxation times  $\tau_{\alpha/\delta}$ . These data are depicted in Fig. 4.10 for various temperatures. Both processes follow the phenomenological Vogel-Fulcher-Tammann (VFT) equation:

$$\tau = \tau_o \exp\left(\frac{D}{T - T_{inf}}\right) \quad (4.9)$$

A Vogel-Fulcher-Tammann behavior usually indicates the presence of a glass transition [Zel82, Bra07]. As a general convention in dielectric spectroscopy the corresponding glass transition temperature is taken at the point where the relaxation time equals  $\tau = 10^{-2}$  s. The extracted values are almost identical for both processes with a value of about  $-67^\circ\text{C}$  that coincides with the glass transition temperature obtained from DSC.

At higher temperatures in the isotropic and nematic phase a contribution of mobile ions was identified. The corresponding conductivity decayed exponentially with the inverse temperature indicating a Arrhenius-like behavior

$$\tau = A \exp\left(-\frac{E_A}{RT}\right)$$

with an activation energy of  $E_A = (2.7 \pm 0.1)$  kJ/mol.

In case of the PMMA-5CB compounds the ion conductivity was significantly increased in the isotropic phase. Upon the onset of phase separation, however, the conductivity approached the data of pure 5CB as the nematic droplets are almost free of PMMA. At a temperature of about  $0^\circ\text{C}$  the difference completely vanished.

The  $\delta$ -relaxation time is slightly decreased compared to pure 5CB but more importantly its dielectric strength dropped down by one order of magnitude compared to pure 5CB. This decrease cannot be explained by the replacement of 5CB by PMMA in the composites as the PMMA volume fraction was only 9%<sub>vol</sub>. Instead x-ray diffraction experiments (not shown) revealed that part of the 5CB molecules paired together and formed dimers. These dimers had a largely reduced dielectric susceptibility compared to two single molecules and thus reduced the dielectric strength. As the 5CB in the nematic droplets crystallized the  $\delta$ -relaxation time  $\tau_\delta$  further reduced and the dielectric strength was lowered to a level of 3% of the initial value in the nematic phase. The non-crystallizing molecules contributing to this signal were located in the glassy PMMA matrix of the network wall. If we assume that the effective

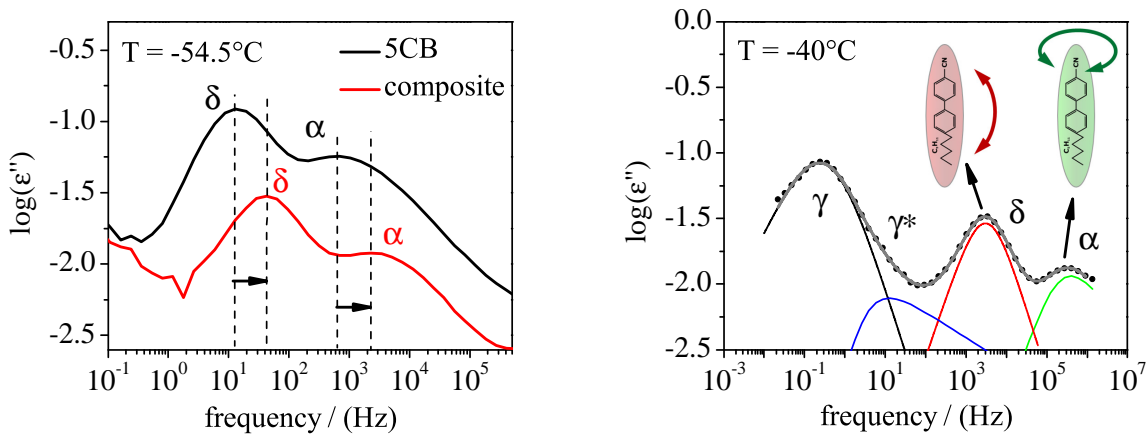


**Fig. 4.9.:** (a) Exemplary dielectric spectra of the PMMA-5CB composite at a PMMA volume fraction of  $\varphi_{\text{PMMA}} = 9\%_{\text{vol}}$  in comparison to pure 5CB. Due to the presence of the polymer the dynamics of the  $\alpha$  and  $\delta$  relaxation shifted to higher frequencies (indicated by the arrows). (b) In addition two other relaxation modes  $\gamma$  and  $\gamma^*$  appeared for the composites that were not present in pure 5CB.

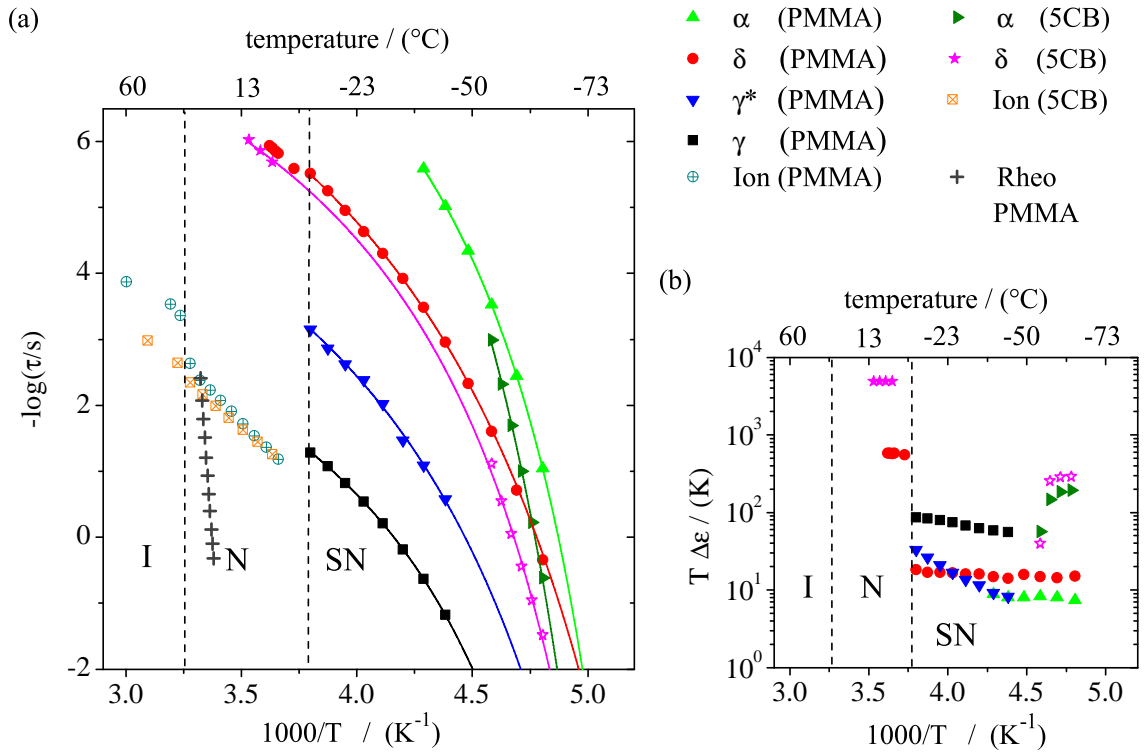


**Fig. 4.10.:** Dielectric relaxation times and ion mobilities (a) as well as the corresponding dielectric strengths (b) for pure 5CB in comparison to the 5CB in the PMMA based composites.

dielectric strength  $T \cdot \Delta\epsilon$  was proportional to the number of contributing 5CB molecules the PMMA volume fraction in the network walls amounted to 76 %<sub>vol</sub>. The discrepancy between this value and the result of the concentration gauging ( $\varphi_{\text{PMMA}} \approx 55$  %<sub>vol</sub>) is quite substantial. Though, both values refer to different temperatures, *i. e.*  $-10^{\circ}\text{C}$  in case of DS and  $20^{\circ}\text{C}$  for the rheological data. Taking into account that the 5CB molecules in the glassy PMMA matrix were still mobile, phase separation could happen via diffusion even below the glass transition of PMMA. Hence further composition changes in the network walls below  $20^{\circ}\text{C}$  were possible and could explain the discrepancies.

Two additional relaxation processes  $\gamma$  and  $\gamma^*$  can be identified in  $\epsilon''(\omega)$  [see Fig. 4.9 (b)]. The corresponding relaxation times are larger than for the  $\alpha$  and  $\delta$  relaxation and their temperature behavior follows the VFT model. Similar relaxations were also observed for other polymer-LC compounds and their origins were controversially discussed without a decisive conclusion [Hor04, Zho03, Bra06]. The large interfacial area in the network state gives rise to pronounced interface effects. The well known Maxwell/Wagner/Sillars polarization that is related to the motion of mobile ions at the interface, however, has a slower dynamics and is expected at longer relaxation times [Zho03, Bra06]. Partial immobilization of 5CB molecules in an interface layer can also be responsible. These molecules form bonds with the polymeric wall but frequently exchange with free molecules which contributes to  $\epsilon^*(\omega)$  as a relaxation process. Such an effect was identified in porous materials with large internal interfaces [Cra97] but can only account for one of the processes  $\gamma$  and  $\gamma^*$ .

### 4.4.3. Restricted motion of 5CB in the PMMA matrix

Coming back to the initial question of the distribution of 5CB in the PMMA matrix we focus on the  $\alpha$  and  $\delta$  relaxation modes of the 3% fraction of 5CB molecules in the network walls. The speed-up of the rotational dynamics of these molecules compared to the supercooled pure 5CB again seems to be a general feature of PDLC as it was observed for other systems, too [Bra06, Hor04, Zho03]. Though, a detailed discussion is missing. Assuming a homogeneous mixing of PMMA and 5CB this effect can be explained by the restricted rotational diffusion model (RRD) [Wan80, Oli85].

#### Theoretical model [Wan80]

A freely moving rod-like molecule such as 5CB does not experience any constraints regarding its rotational motion. Hence, the probability density  $P(\hat{u}, t)$  of the molecule to be oriented along the direction  $\hat{u}$  at time  $t$  is constant over the whole unit sphere parametrized by polar  $\vartheta$  and azimuthal angles  $\varphi$ . If, however, the 5CB molecule is confined by the much stiffer PMMA matrix its rotational motion is restricted to the subset of rotational states that lie in a cone with an opening angle of  $\vartheta_o$  [see inset in Fig. 4.11 (b)]. Furthermore  $P(\hat{u}, t)$  is not uniform as it must decay continuously to zero at the edge of the cone:

$$\left. \frac{\partial P(\hat{u}, t)}{\partial \vartheta} \right|_{\vartheta=\vartheta_o} = 0 \quad (4.10)$$

In the mathematical description of this problem  $P(\hat{u}, t)$  is found by solving the three dimensional diffusion equation with the boundary condition (4.10). Based on this probability density the rotational diffusion constant  $D_{\text{RRD}}$  in the constraint case is related to the diffusion constant  $D_o$  of the freely moving molecules via

$$D_{\text{RRD}} = \nu(\nu + 1) D_o \quad (4.11)$$

$\nu$  is a positive constant exceeding 1 that varies inversely with  $\vartheta_o$  [Wan80]. Hence, the smaller the opening angle  $\vartheta_o$  is, the faster the diffusion is compared to the free molecule, and the relaxation time decreases.

This result can be directly understood in a more general physical context. In equilibrium the molecule occupies a well defined region in the phase space of rotation angles and angular momentum. The volume of this phase space tends to be maximal and is only bound to the Heisenberg uncertainty relation. Therefore, any restriction of accessible rotation angles involves an increase of the angular momentum of the molecule. The rotational motion becomes faster.

#### Application to the PMMA-5CB composites

If we apply the RRD-model to the relaxation time data in Fig. 4.10 (a) the cone angle was found to be constant at about  $55^\circ$  down to a temperature of about  $-35^\circ\text{C}$  [Fig. 4.11 (b)]. Upon further cooling there was a rather sharp transition to a regime where  $\vartheta_o$  decrease linearly to

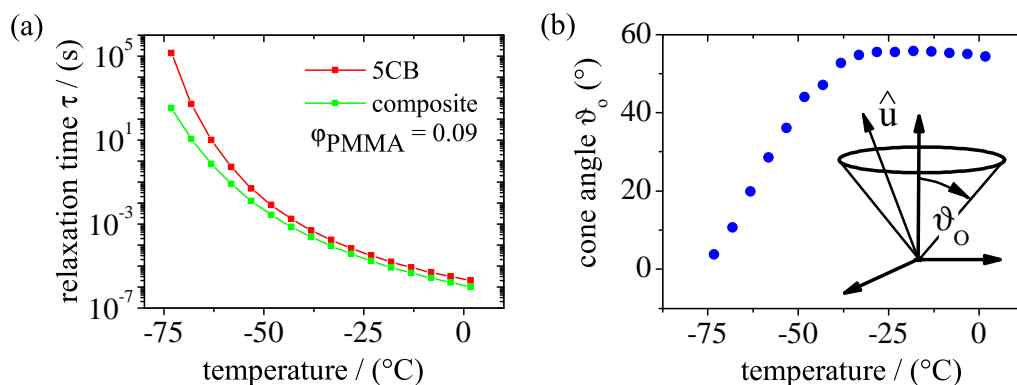


**Fig. 4.11.:** The speed-up of the relaxation modes for the PMMA-5CB composites compared to the pure 5CB can be explained in terms of a restricted diffusional motion. The space available for the mesogenic molecules to freely relax is reduced because of the presence of the polymer.

almost  $0^\circ$  at  $-75^\circ\text{C}$ .

There is no obvious reason for this crossover. As the exact mechanisms causing the constraint is not specified in the RRD-model one possible explanation is the presence of two contributing processes: At higher temperatures the PMMA matrix restricts the motion of the 5CB molecule. According to the fox equation the PMMA related glass transition for a  $\varphi_{\text{PMMA}} = 76\%_{\text{vol}}$  mixture happens at  $44^\circ\text{C}$ . Hence, the PMMA is already in its glassy state defining a rigid temperature independent environment for the 5CB leading to a constant cone angle. The 5CB molecule might experience an additional constraint by neighboring 5CB molecules. Above  $-35^\circ\text{C}$  this effect is negligible but becomes increasingly important as the general dynamics of the 5CB molecules is slowed down when approaching the glass transition. Clearly we are not able to ascertain this picture the given set of experimental data. NMR-measurements can give further insight when following an analogous strategy like for PS-toluene compounds in reference [Rss85]. Moreover, the influence of the beta-relaxation of PMMA [Rib85, Sch94] on the dynamics of the 5CB molecules needs to be examined.

Although a definite interpretation of the results in terms of the RRD-model is not possible at this point the differences in the relaxation times of pure 5CB and the composite gives further indications for a homogeneous mixing of PMMA and 5CB in the composites. If the sample was phase separated on lengthscales smaller than the resolution of the optical microscope no difference in the relaxation times would had been observed.

## 4.5. Conclusions and Outlook

We presented a study of the phase behavior and rheological properties of PMMA-5CB composites for the full range of compositions. At high temperatures both components are mixed homogeneously forming a single phase that undergoes a glass transition for high polymer concentrations. In case of small PMMA contents there is an isotropic-nematic phase transition that leads to a phase separation into a network-like structure of virtually PMMA-free droplets of nematic 5CB and polymer-rich network walls. Both, the glass transition temperature as

well as the onset temperature of phase separation are lowered when approaching their crossing point at medium concentrations of about 50 %<sub>vol</sub>.

The rheology is dominated by the polymer dynamics of the PMMA that is accelerated in the presence of 5CB. In the isotropic phase the principles of time-temperature-superposition (tTS) and time-concentration-superposition (tcS) were successfully applied to quantify the influence of temperature and composition changes. It turned out that these descriptions are also valid for the network walls in the phase separated state. As a result the network composition during the phase separation could be determined and showed reasonable agreement with the phase diagram.

The whole analysis is based on the assumption that 5CB is homogeneously dispersed in the PMMA matrix of the network walls. Dielectric spectroscopy indicated that this is indeed the case. The measurements did not only reproduce the expected proportions of 5CB and PMMA in the network walls but also revealed a speed-up of the rotational relaxation of 5CB molecules due to the confinement by the glassy PMMA matrix.

In the following we relate these observations to other systems focusing on two aspects: In how far is tcS applicable to phase separating polymer melts and solutions in general? And, how do the results of the PMMA-5CB composites relate to the network formation in LC-colloidal suspensions?

#### 4.5.1. Generality of time-concentration-superposition

The tTS and tcS principles rely on the assumption that all relaxation times in the system have the same dependency on temperature and composition, respectively. In case of tTS this requirement is often fulfilled with numerous examples in literature [Fer80c, Wil55, Gur]. Though, there are several reasons that can cause a breakdown of the superposition principle. Phase transitions such as crystallization fundamentally change the nature of the relaxation processes and does not allow for a simple superposition [Tob55]. Structural changes can also occur in isotropic polymer melts in course of cooling or shearing and thus prevent proper superposition [Cav87]. In multicomponent systems micro phase separation [Han93] or temperature dependent interaction between the components [Col89] can corrupt the superposition behavior.

Seeing all these complications it is quite remarkable that tcS works in our case at all and in particular can be applied to systems involving phase separation. The lack of experimental studies on other systems apart from the PMMA-5CB composites supports this statement. Though, it is questionable whether a proper superposition behavior is hindered in other phase separating systems because of fundamental changes in the relaxation behavior or because of more practical reasons. Obviously the morphology has a strong influence on the rheological measurements as the polymer-rich phase must form a percolating network. Any phase separation process that leads to isolated polymer rich droplets cannot be investigated with classical rheometry. Furthermore, the composition of the phases needs to be well defined. A broad distribution of relative concentrations leads to a broadening of the relaxation time spectrum and tcS will fail. These conditions of percolation and homogeneity are fulfilled for the PMMA-5CB

composites as the PMMA-rich network is system spanning even for polymer concentration down to 5%<sub>vol</sub> and the composition of the network walls is well defined by the underlying phase diagram of PMMA and 5CB.

A careful revision of the superposition behavior of other systems might give further evidence of a generality of tcS. Beside to other PDLC systems aqueous solutions of xanthan [Cuv86] are worth a closer look as the temperature dependent shift factors exhibit two different temperature regimes [Cho10] similar to those in Fig. 4.7 (b). Unlike the isotropic-nematic transition for the PMMA-5CB composites a conformational change of the xanthan molecules [Tak93] separates both domains.

#### 4.5.2. Comparison with colloidal-LC composites

The initial motivation of this study was to verify the model of the network walls in the colloidal LC suspension from section 3.8. We shortly recapitulate the essential concept: Due to partial swelling and dissolution of the used PMMA particles the local composition of the newly formed network walls varies strongly. Upon cooling PMMA and 5CB further phase separates within the walls starting with most diluted regions according to the PMMA-5CB phase diagram. Via this process the local composition aligns across the complete network walls until the PMMA is in its glassy state.

If this model is correct the temperature dependent mechanical response of the colloidal network must be similar to the network formed from the polymer solution. Fig. 4.7 shows that this is indeed the case. The temperature shift factors coincide for the whole temperature range except for the initial network formation at about 35 °C. Yet, the master curves exhibit striking differences. Although the general shape and extension along the frequency and modulus axes are identical the rubbery plateau is not evolved for the colloidal sample and the transition into the glass happens at lower frequencies. However, these deviations are related to a broad distribution of relaxation times caused by the heterogeneous consistency of the colloidal network walls and thus actually support the proposed model. So, our strategy to get further information on the network composition in LC-based colloids by means of an analogue investigation of the composites with linear PMMA chains worked out as planned.



## 5. Nanoindentation of aggregated particles

Nanoindentation has been widely used to characterize atomic matter such as metals, ceramics and polymers. Although the specimen is tested only very locally the extracted mechanical quantities like hardness and Young's modulus are in good agreement with those obtained from classical macroscopic testings [Hay09]. This might be related to the fact that despite of indentation depths down to  $0.25\ \mu\text{m}$  sufficiently large ensembles of atoms or molecules are tested to treat the specimen as a continuous material and obtain average material properties [Cat06]. This is not necessarily the case for colloidal systems. *A priori*, the aggregate must be regarded as a composite rather than a continuous material. Therefore, it is questionable if standardized methods for the analysis of nanoindentation data can be used for colloidal systems. Even if the indentation depths were increased the number of involved particles in colloidal systems is effectively  $10^5$  times smaller than for atomic systems due to enlarged inter-particle spacings. The question of applicability is intensified if obvious differences in the interaction mechanisms between the constituent elements are taken into account. Though, colloids have been intensively used to model atomic systems [Sur06]. Increased lengthscales enable for optical observation with light microscopes and lead to slowed down kinetics compared to atomic systems. Capillary waves could be visualized in real space [Aar04] and colloidal glasses helped to understand the phenomena of a glass transition [Bes07, Wee00a]. In former studies on the indentation of extended colloidal crystals the nucleation of defects could be explained in the theoretical framework usually used for atomic crystals [Sur06, Sch05].

In the present study we test the validity of the widely used analysis by Oliver and Pharr [Hay09, Oli04, Doe86] for nanoindentation data of colloidal aggregates. The aggregate structure is rather dense and stiff as the particle interactions are dominated by adhesion and solid bonds. Special emphasis lies on the influence of structural characteristics of the aggregate as well as particle bonds. We complement the nanoindentation experiments with real-space imaging using confocal microscopy. With the help of particle localization and tracking algorithms the particulate structure of the aggregate as well as displacements of all particles during indentation are obtained in all three dimensions. These displacements enable for a calculation of the local strain tensor that can be related to predictions from continuum theories. If this comparison turns out to be positive there is a good chance that resulting mechanical quantities display average material properties of the colloidal aggregate. Though, for the moment it is delicate to properly define a Young's modulus or a Poisson ratio on the tested mesoscopic scale. Therefore, we refrain from using these terms and their definition in equation (2.22) and rather use the effective elastic modulus  $E_{\text{eff}}$  in analogy to (2.19).

In the following we give a short motivation for the study of the mechanical properties of

stiff colloidal aggregates from an industrial point of view. Thereafter we introduce the methods for preparation and structural analysis of the aggregates (section 5.2). In the first part of the indentation experiments we focus on the microscopic distribution of displacements and strains as well as reorganization effects for amorphous and semi-crystalline structures (section 5.3). We compare our results with the predictions of a continuum model as well as with former studies on the indentation of atomic matter. In section 5.4 the analysis of nanoindentation data in analogy to the theory of Oliver and Pharr is presented and the extracted mechanical properties of hardness and effective elastic modulus are related to the microscopic reorganization effects.

Half of the indentation experiments were done as part of a collaboration with **Carsten Schilde** and **Professor Dr. Arno Kwade** at the Institute for Particle Technology (iPat) at the University of Braunschweig. The greater greater part of this chapter is published in the paper ‘**Colloidal aggregates tested via nanoindentation and simultaneous 3D imaging**’ [Rot11b].

## 5.1. Industrial motivation

Micro- and nanometer-sized particles are frequently used as filler material in various industrial products of daily life. Depending on the application certain requirements related to morphology, abrasion resistance, specific surface and tendency to agglomeration must be met. These properties depend on the physio-chemical properties of the used materials as well as the technical control of the production process. Yet, in many cases the particles are not produced as single primary particles but rather as aggregates consisting of several primary particles. Additional mechanical treatments are required in order to obtain isolated primary particles or certain aggregate sizes. Different grinding and dispersing processes might serve this purpose [Sch07, Sch10b] but what method is most efficient depends on the structural and material properties of the aggregates [Zac09]. Therefore, especially the breakage energy as well as hardness and elasticity of nanostructured aggregates have to be considered [Sch09a, Sch09b].

Ordered and disordered assemblies of colloids also attracted interest because of their advantageous preparation in large scales and via self-assembly techniques. Examples are photonic colloidal crystals that show a great potential as optical elements [Zum10, Vla01] or surfaces that can be made super-hydrophobic by coating them with hydrophobic raspberry-like particles [DAc10]. Beside to their primary function again the mechanical properties play a key role as these colloidal aggregates must render a certain mechanical stability for a convenient usage in daily life.

Indentation experiments have been used before for the mechanical characterization of colloidal aggregates. Basic research on the deformation and fracture behavior of aggregates under loading were done by Kendall and Weihs [Ken92] and Raichman et al. [Rai06]. Kendall and Weihs observed elastic and plastic deformations of aggregates during compression tests. In their experiments, the total macroscopic behavior of aggregates was characterized but only little information about the dominant processes inside the aggregates could be obtained [Ken92]. Especially particulate reorganizations, the overall stress distribution inside the ag-

gregate and the nature of plasticity remained unclear. Raichman et al. [Rai06] characterized the mechanical strength of individual small silver agglomerates via nanoindentation. However, the interpretation of the results was complicated due to large statistical scatter, varying structural properties and a difficult fixation of the aggregates on the substrate.

## 5.2. Materials and methods

### 5.2.1. Sample Preparation

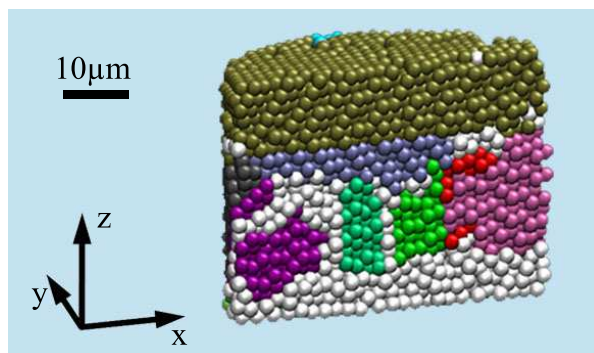
PMMA particles were prepared via dispersion polymerization in presence of the fluorescence dye Nile Red. The principle synthesis route is described in Appendix C. The particles had a mean diameter of  $1.65\ \mu\text{m}$  and a polydispersity of 5% determined from SEM images on the basis of 100 particles.

Colloidal aggregates were prepared as thin films with thicknesses ranging from few layers up to  $40\ \mu\text{m}$ . Such extended films are advantageous compared to isolated aggregates as the mechanical properties are not affected by finite size-effects and results from different indentation spots are well comparable. Local surface height variations did not exceed  $2\ \mu\text{m}$  over  $10\ \mu\text{m}$  in lateral dimensions. The preparation of all colloidal films used in this study started with a suspension of the base particles in a suitable dispersion liquid that was eventually enriched with additives and finally dried on a glass substrate. Originating from the same synthesis batch, differences in the particle properties were avoided. Hence, preparation methods only varied with respect to the choice of liquids for the initial suspension, additives and evaporation rates.

For the first set of films neat hexane (98%, Sigma-Aldrich Chemie GmbH, Germany) was used to disperse the particles. One film was prepared by drying the suspension at an elevated temperature of  $50\ ^\circ\text{C}$  on a heating plate without any further environmental control. Due to the fast evaporation and presumably strong convection during evaporation of the hexane no crystals nucleated and the resulting structure turned out to be completely amorphous.

In a second experiment the hexane was dried very slowly in course of a whole day in an almost saturated hexane environment giving the particles time to sediment. Due to the small polydispersity [Pus86, Pus09] of the particles and sufficiently fast diffusion compared to sedimentation velocities [Dul06, Kur10] a semi-crystalline sediment was formed with crystal

**Fig. 5.1.:** Computer reconstruction of a half-cylindrical shaped section of a semi-crystalline film obtained from LSCM images. The structure is cut in half to reveal the different crystal domains that are distinguished by different colors. Particles belonging to the amorphous part are white. The algorithms to determine 3D particle coordinates and to identify crystal domains are described below.



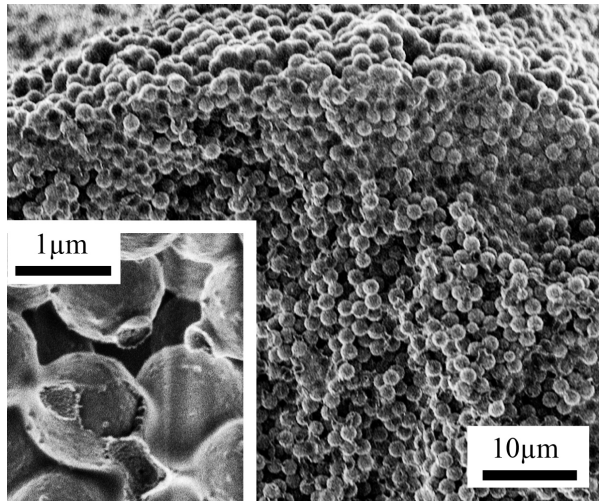


**Fig. 5.2.:** Scanning electron microscope images of a film made of PMMA particles with additional PS (1%<sub>vol</sub> with respect to the amount of PMMA). The homogeneous distribution of PS throughout the whole film is visualized in the large image. The PS coverage of the PMMA particles and the solid bridges are revealed if a particle is broken out of the film (see inset).

domains of up to  $(25\ \mu\text{m})^3$  in size embedded in variable amounts of amorphous regions. The structure was mechanically stable even in the final stage of evaporation and almost no cracks evolved. A representative structure is shown in Fig. 5.1 as a computer aided reconstruction.

For a second set of samples a mixture of cyclohexyl bromide (CHB 98%, Sigma-Aldrich Chemie GmbH, Germany) and (DEC) was used to suspend the PMMA particles at a volume fraction of 10%<sub>vol</sub>. Various amounts of polystyrene (PS,  $M_w = 64\ \text{kg/mol}$ ,  $PDI = 1.03$ ) were dissolved in the suspension to incorporate a tunable amount of solid bridges between the particles in the dried film. The mixing ratio of CHB and DEC was set to 4:1 for practical reasons: Pure CHB swells and partially dissolve the particles while films casted from pure DEC were not stable and peeled off the glass substrate after evaporation. Moreover, the film surface was very smooth which might be related to the approximate density matching of the solvent mixture and PMMA.

In the liquid state the dissolved PS acted as a depletion agent and induced attractive forces between the particles. As a result the particles aggregated to extended clusters [Lu06]. Yet, these attractive forces were small compared to the hydrodynamic forces acting on the particles during drying at 50 °C. In the late stage of the drying process the remaining amount of CHB and DEC allocated on the surface of the particles<sup>15</sup> forming capillary bridges between them. The PS was strongly enriched in these regions forming solid bridges of glassy PS<sup>16</sup> when the solvent was completely evaporated.

These bridges as well as the homogeneous average distribution of PS through the whole sample can be seen in the scanning electron microscope images in Fig. 5.2. Due the presence of the PS the effective particle density was slightly reduced compared to the films without PS (see table 5.1) and the initially formed particles clusters induced a slight heterogeneity in the local particle concentration.

All preparation methods, chemical composition as well as their structural properties are summarized in table 5.1

<sup>15</sup>Apparently the mixture of CHB DEC wets the particles as the macroscopic contact angle was almost 0 °.

<sup>16</sup>The glass transition temperature of PS is about 95 °C

| Initial suspension   | Preparation method   | Structure   | Particle vol. fraction (% <sub>vol</sub> ) |
|--|----------------------|---|--|
| 2 % <sub>vol</sub> PMMA in Hexane  | slow drying at 50 °C | amorphous   | (63 ± 2)                                   |
| 2 % <sub>vol</sub> PMMA in Hexane  | fast drying at 50 °C | semi-crystalline<br>$N_{\text{cryst}}/N_{\text{total}} =$<br>(0 – 90) %<br>(see text) | (67 ± 2)                                   |
| 10 % <sub>vol</sub> PMMA and (0.02 – 0.1) % <sub>vol</sub> PS in 4:1(vol) mixture of DEC and CHB | fast drying at 50 °C | amorphous   | (67 ± 2)                                   |

**Tab. 5.1.:** Preparation methods and structural parameters of the colloidal films. The errors give a measure of the variations for different indentation positions on the sample (see section 5.2.3). The methods used for the structural characterization are described below.

### 5.2.2. Structural characterization

The structural characterization of the films was based exclusively on the confocal microscope images. The starting point of the analysis was the extraction of the 3D coordinates of all particles by using the algorithm by Crocker, Grier [Cro96] and Weeks [Wee00a] introduced in section 2.1.3. In the following these 3D coordinates were further processed to obtain characteristic structural quantities such as the number of nearest neighbors, the local ordering of the particles and the crystallinity of the film.

#### Nearest neighbors

There is no unambiguous definition of the term nearest neighbors. In systems where particles interact predominantly via frictional sliding or deformation of solid bridges it is most appropriate to call two particles nearest neighbors if they are in physical contact. However, in practice a distinction to particles that are just close by each other is difficult because of the finite resolution of the confocal images and localization algorithm as well as the polydispersity of the particles. Therefore, we declared two particles to be nearest neighbors if their separation distance fell below a predefined value  $D_o$ . This limiting distance was obtained from the distribution of inter-particle distances in the film, the so called radial distribution function (RDF) [Oht08]. The RDFs for an amorphous, a semi-crystalline and a simulated, fully crystalline structure are depicted in Fig. 5.3. All graphs display a maximum at a normalized distance  $D/2 R_p = 1$  with  $R_p$  denoting the average radius of the particles. The maximum embraces all particles in close vicinity (first shell) to the reference particle, *i. e.* the nearest neighbours. In contrast to the simulated data the maxima corresponding to the real structure have a finite extension and the subsequent minimum discriminates the nearest neighbors from the farther particles. The minimum is located at approximately  $D/2 R_p = 1.2$  which we chose as radial

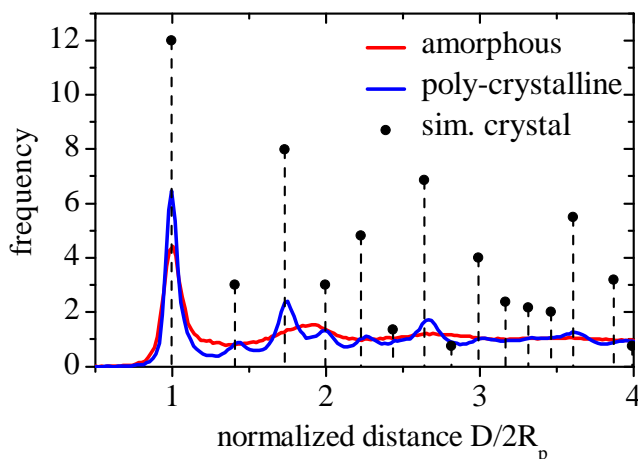


**Fig. 5.3.:** Radial distribution functions for an amorphous and a poly-crystalline sample. The first maximum embraces the nearest neighbors and is used to define  $D_o$ . In case of the polycrystalline sample also the other individual maxima can be clearly identified with the theoretical singular peaks for a face centered cubic lattice.

distance for the discrimination of the nearest neighbors. For this value the average number of nearest neighbors  $N_n$  in hexagonally closed packed crystalline regions equaled 12 as expected.

Beside to the number of nearest neighbors the RDF also gives a first estimate about the overall crystallinity. In case of a highly crystalline structure the RDF consists of well-defined maxima with absolute heights and radial positions that are characteristic for the crystal lattice. In the present case the maxima of the semi-crystalline film coincided with the simulated face centered cubic lattice.

### Local order parameter

In addition to the number of nearest neighbors  $N_n$  also the local ordering of the particles is of interest. It is a direct measure of local crystallinity [Lec08]. We used the algorithm introduced by Steinhardt et al. [Ste83] to calculate the bond order parameter  $\bar{q}_l(i)$  for each particle  $i$  as a multiple weighted average of spherical harmonics  $Y(lm)(\vec{u}^{(ij)})$  of the bond vector  $\vec{u}^{(ij)}$  over all nearest neighbors  $j$  as well as over all allowed values for  $m \in [-l, \dots, l]$  [Ste83].

$$q_{lm}(i) = \frac{1}{N_n} \sum_{j=1}^{N_n} Y_{lm}(\vec{u}^{(ij)}) \quad (5.1)$$

$$\bar{q}_{lm}(i) = \frac{1}{N_n} \sum_{j=0}^{N_n} q_{lm}(j) \quad (5.2)$$

$$\bar{q}_l(i) = \left[ \frac{4\pi}{2l+1} \sum_{m=-l}^l |\bar{q}_{lm}(i)|^2 \right]^{1/2} \quad (5.3)$$

The different starting indexes  $j = 1$  and  $j = 0$  in the first two sums denote that the particle  $i$  itself is excluded and included, respectively. Since most crystal lattices of densely packed spherical particles (face centered cubic, hexagonal closed packed, random hexagonal closed packed) involve 4,6 and 8-fold symmetries,  $l = 4, 6, 8$  are common choices. Although different crystal lattices can be distinguished with the help of a combined discrimination analysis of the corresponding  $\bar{q}_l$  [Lec08], adjacent crystal domains with the same lattice but different

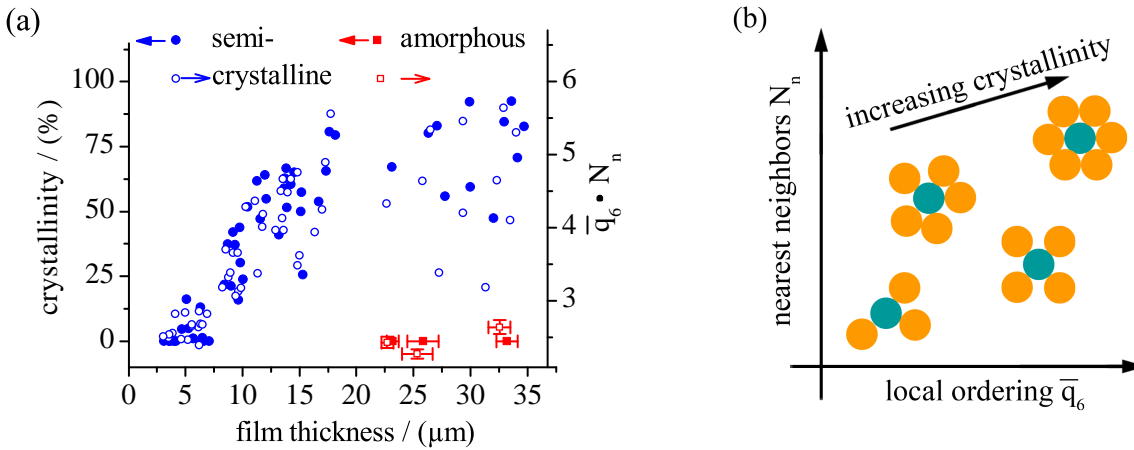


**Fig. 5.4.:** (a) Crystallinity (left axis, filled symbols) and  $\bar{q}_6 \cdot N_n$  (right axis, open symbols) for semi-crystalline (data from single indent positions, see section 5.2.3) and amorphous samples (averaged over all indents on each sample). In case of the semi-crystalline structure both quantities were strongly correlated with the sample thickness in particular for low and medium degrees of crystallinity. In case of the thickest semi-crystalline sample the data scatter was rather large. The amorphous films was characterized by constant values for crystallinity and  $\bar{q}_6 \cdot N_n$  irrespective of film thickness. (b) Proposed correlation between crystallinity, number of nearest neighbors  $N_n$  and order parameter  $\bar{q}_6$ . Although we do not discuss any scaling laws the approach to a more crystalline particle assembly with increasing order and local particle density is obvious.

orientations might not be separated. However, such kind of stacking faults can be crucial for the transmission of stresses in crystalline structures. [Li02]

## Crystallinity

We developed a different algorithm to find and separate crystal domains that mimics the nucleation and growth-principle: At first a nucleus, *i. e.* a small group of neighboring particles with a defined crystal lattice structure and orientation, must be identified. Once such a nucleus is found, further neighboring particles are tested successively for their conformity with the crystal lattice and if positive are added to build up the whole domain. The domain is complete if no further neighboring particles can be added. Then the nucleus of a new domain is defined until all crystalline domains are identified and only amorphous regions are left.

The search for a new nucleus starts with a particle and its at least 10 nearest neighbors that are found to be in a highly ordered local environment, *i. e.* with high values of  $\bar{q}_6$ . Though, this group of particles do not necessarily form a crystalline nucleus. Crystallography tells that the vector connecting two arbitrary particles of a crystal lattice can be described by a characteristic linear combination of three linear independent base vectors. Consequently two bond vectors, *i. e.* the connecting vector between two neighboring particles, enclose angles that are characteristic for the crystal lattice, *e. g.*  $120^\circ$  for a hexagonal lattice or  $90^\circ$  for a cubic. In general, such two bond vectors are sufficient to define the lattice base vectors and all other bond vectors if the crystal lattice type is known. So, one chooses pairs of experimentally

determined bond vectors with specific bond angles to calculate the third base vector as well as all bond vectors of the central particle to each of its nearest neighbors. If these calculated bond vectors coincide with the experimentally determined vectors for a special crystal lattice a nucleus and a new set of base vectors are found. Experimental errors in the bond vectors are compensated by suitable tolerances that depend on the given data set and sample system.<sup>17</sup>

The nucleus is the first precursor of the complete crystal domain. During its growth adjacent particles are incorporated into the domain if the corresponding bond vectors can be described by the lattice base vectors. Unfortunately, this requirement alone eventually result in a chain-like morphology of the domain which is unrealistic. Therefore, a particle can only join a crystal domain, if a certain number of its nearest neighbors already belongs to the domain. This condition ensures a globular shape of the domain. In practice a minimum number of two crystalline neighbors is reasonable.

The results of this analysis are exemplary shown in the computer aided reconstruction of a semi-crystalline film in Fig. 5.1. Particles not belonging to a crystal domain appear white while the remaining particles are colored according to their membership to different crystal domains. The clear distinction between crystalline domains and amorphous regions allowed for an easy definition of the local crystallinity in terms of the total fraction of crystalline particles within a limited volume. In our case we defined this volume by means of the range of deformation in the indentation experiments which was in the order of  $(30 \mu\text{m})^3$ . Since the extension of the crystalline domains was in the same order of magnitude as this averaging volume the extracted values for the number of crystalline domains and the total crystallinity showed large spatial variations. In addition the crystallinity depended on the overall thickness of the film. Thinner films had lower degree of crystallinity as can be seen from Fig. 5.4 (a). The crystallinity and the product of the order parameter  $\bar{q}_6$  and the number of nearest neighbors  $N_n$  was correlated. Given the fact that  $N_n$  and  $\bar{q}_6$  are measures of the local particle density and ordering respectively this correlation comes out naturally [Fig. 5.4 (b)].

### 5.2.3. Indentation modes

The colloidal films were tested in two different indentation modes. The first one is a nanoindentation experiment as it was already discussed in the experimental section 2.2.2. The film was indented with a commercial device - TriboIndenter<sup>®</sup> TI 900 from Hysitron Inc equipped with a Berkovich diamond tip - featuring a measurement of the force acting on the indenter at a given depth inside the sample. The indentation speed and maximal indentation depth was set constant to  $0.5 \mu\text{m/s}$  and  $3 \mu\text{m}$ , respectively. In order to increase the measurement statistics each sample was indented at multiple locations. After indentation the films were imaged with the confocal microscope firstly to determine the local structure in terms of the above introduced parameters. Second, standard image analysis was used to get an estimate of the extension on the indent as we will discuss in section 5.4.2. Clearly in this indentation mode any

<sup>17</sup>Dried structures where particles are direct contact show less uncertainties than crystal domains in suspension with next neighbors distances exceeding the particle diameter.



information about the deformation field inside the film as well as particulate rearrangements during the indentation was missing.

Therefore, another experiment was set up to image the colloidal film quasi-continuously during the complete indentation process. Using the setup, that was presented in section 2.2.2 and Fig. 2.11, the indenter was pressed into the film in steps of  $(0.5 - 1) \mu\text{m}$  up to a maximal indentation depth of  $3 \mu\text{m}$ . After each step the indenter was halted and the whole film structure was imaged. With the help of tracking algorithms (section 2.1.4) identical particles could be linked through all measured 3D frames to give vectorial displacements for each particle in the film for the complete indentation process. We will refer to this method with the term ‘live indentation’. However, in this mode the load applied by the indenter was unknown. The primary purpose of the live indentation experiments was a comparison of the experimentally determined particle displacements and strain fields with theoretical continuum models. As this task was accomplished much easier for a cylindrically symmetric indentation geometry we focus on results using a spherical indenter tip. However, essentially the same observations were made for the Berkovitch tip geometry.

Some drawbacks have to be mentioned at this point. The films needed to be infiltrated with a liquid matching the refractive index of PMMA to allow for imaging with the confocal microscope. This can be a low viscosity PDMS oil or so called laser liquids with specified refractive index which are commercially available (Cargille Laboratories, USA). The films were neither re-dispersed nor were the solid bridges affected and the shape of the indent was not altered. However, in the live indentation experiments the kinetics of the particle movement under indentation might be changed due to the increased viscosity of the immersion liquid compared to air. The effects of a possible hydrodynamic drag was minimized by low indentation speeds ( $\approx 0.01 \mu\text{m/s}$ ). Though, different indentation speeds may lead to an altered mechanical response for visco-elastic materials. However, experiments using the commercial device at varying indentation speeds did not reveal pronounced differences.

### 5.3. Microscopic deformation analysis

Tracking of all particles in the film in course of the indentation process offers the unique opportunity to get a measure of the induced deformation. There are various ways to quantify these deformations. Though, the starting point of any analysis is the calculation of the individual vectorial displacement  $\vec{d}^{(i)}$  of particle  $i$  as a function of the indentation depth  $h$  with respect to a reference state at a depth  $h_o$  (see Fig. 5.5 for the definition of the indentation geometry and identification of the used variables).

$$\vec{d}^{(i)}(h, h_o) = \vec{r}^{(i)}(h) - \vec{r}^{(i)}(h_o) \quad (5.4)$$

We mostly use the cumulative displacement  $\vec{d}^{(i)}(h, 0 \mu\text{m}) \equiv \vec{d}^{(i)}(h)$  and its absolute value  $d^{(i)}(h, 0 \mu\text{m}) \equiv d^{(i)}(h)$  for which the state of the film before indentation is used as reference. These displacements are exemplary shown in Fig. 5.6 (a) for a particle and its nearest neigh-

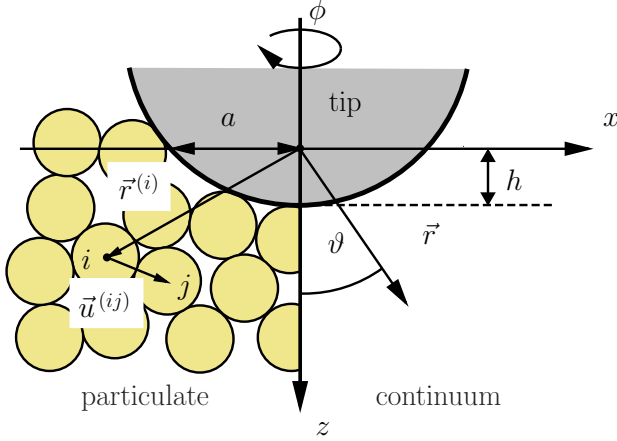


**Fig. 5.5.:** Indentation geometry: The indenter tip is indented in positive  $z$ -direction with  $h$  denoting the depth of the tip inside the sample. Due to the cylindrical symmetry of the setup only the  $xz$ -plane is shown. We refer to the colloidal film either in the native particulate picture  $\vec{r}^{(i)}$  (left) or via continuous position vectors  $\vec{r}$  (right). Next to Cartesian coordinates also cylindrical coordinates  $\vartheta, \phi, z$  are introduced.

bors at the largest indentation depth of  $h = 3 \mu\text{m}$ . The particles are located directly below the indenter at a depth of about  $8 \mu\text{m}$ . Obviously, the displacement vectors are collectively dominated by their large  $z$  component. Though, this overall displacement in indentation direction is superposed by small relative displacements that can be interpreted as a deformation of the local particle arrangement. This deformation is mapped by the strain tensor  $\epsilon^{(i)}$  [Che10, Sch05] that is determined by minimizing the expression

$$\mathcal{F}^{(i)}(h) = \left| \sum_{j=1}^{N_n} \Delta \vec{u}^{(ij)}(h) - \epsilon^{(i)}(h) \vec{u}^{(ij)}(0 \mu\text{m}) \right|^2 \quad (5.5)$$

Here  $\Delta \vec{u}^{(ij)}$  denotes the change in the bond vector  $\vec{u}^{(ij)}$  between particles  $i$  and  $j$ :

$$\Delta \vec{u}^{(ij)}(h) = \vec{u}^{(ij)}(h) - \vec{u}^{(ij)}(0 \mu\text{m}) \quad (5.6)$$

If the minimal value for  $\mathcal{F}^{(i)}(h)$  does not equal zero, the relation between bond vectors and its changes under indentation is non-affine and  $\epsilon^{(i)}$  only approximates the actual deformation state. Moreover,  $\epsilon^{(i)}$  does not contain any information about the exact reorganization mechanisms. Elastic deformations of the particle bonds compete with more complex reorganizations like rolling and sliding if the particle bonds break. Moreover, deformations of the particles itself must be taken into account if the bonds are strong or local rearrangements are hindered in closed-packed crystalline regions.

In the example of Fig. 5.6 the results of this data treatment for the central particle gives

$$E^{(i)}(h) = 4.5 \cdot 10^{-2} \quad \left( \epsilon^{(i)} \right)_{\alpha\beta} \equiv \epsilon_{\alpha\beta} = \begin{bmatrix} 9.1 & 2.3 & 1.7 \\ 2.3 & 0.9 & -3.6 \\ 1.7 & -3.6 & -8.3 \end{bmatrix} 10^{-2} \quad (5.7)$$

The absolute values of the strain components lie in the range of  $(1 - 10) \%$  and are so small that the new particle arrangement in Fig. 5.6 (a) is hardly distinguishable from the initial configuration.  $\epsilon^{(i)}$  is better visualized by the deformation of a test cube in Fig. 5.6 (b).

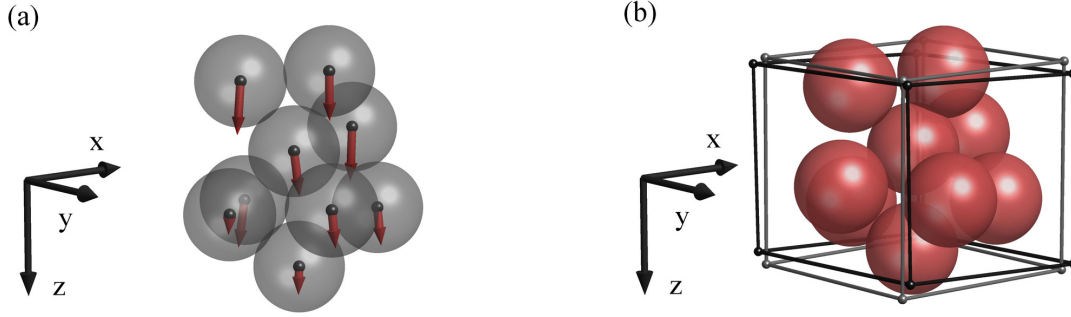


**Fig. 5.6.:** (a) Cumulative displacements  $\vec{d}^{(i)}(h)$  at the deepest indentation position for an exemplary set of neighboring particles that are located directly below the indenter at a depth of about  $8 \mu\text{m}$ . The particles are depicted at their initial positions before the indentation. The overall displacement of all particles in positive z-direction (indentation direction) is superposed by smaller changes in the relative particle positions. (b) The new configuration resembles the old one as the absolute strain components are rather small and in the order of  $(1 - 10)\%$ . The magnitude of deformation is visualized by the wire frames of the initial configuration (gray cube) and after the deformation (black frame).

Uncertainties in  $\vec{d}^{(i)}$  and the components of  $\varepsilon^{(i)}$  result from the experimental uncertainties in the particle positions. Depending on the quality of the confocal images, the spatial sampling frequency, the size and dynamics of the particles, the position uncertainty amounts to about 10% of the particle diameter, *i. e.*  $\sigma_d = 0.02 \mu\text{m}$ . As  $\vec{d}^{(i)}$  is given by the difference of particle position vectors the uncertainty is increased by a factor of  $\sqrt{2}$ . The issue of uncertainty propagation is much more complicated for the  $\varepsilon^{(i)}$  because of the correlation of its six independent strain components. Moreover,  $\varepsilon^{(i)}$  is calculated from a set of relative particle position vectors  $\vec{u}^{(ij)}(h)$  which show increased uncertainties compared to  $\vec{d}^{(i)}$ . This is clearly visible in the computer reconstructions of the film in Fig. 5.7.  $d^{(i)}$  shows minor local variations and after averaging over the nearest neighbors strongly resembles the distribution of the raw data. Consequently, the standard deviations from this averaging are almost one decade smaller than the mean values. On the contrary the strain components - exemplary shown in terms of  $\varepsilon_{xx}^{(i)}$  - reveal large spatial heterogeneities and the patterning in regions of negative compressive and positive extensional strains is much more pronounced in the averaged data. Therefore, the standard deviations are in the order of magnitude of the mean values.

As it is rather difficult to get a reliable quantitative estimate of the uncertainties in the strain components we cannot definitely account the data scatter to statistical fluctuations. The heterogeneities in the strain components might also be of physical origin. The acting stresses in the particulate film are localized to the contact points of the particles and thus can result in heterogeneities in the deformations. Since the origin of the fluctuations cannot be clarified unambiguously from the given data set we restrict ourselves to the discussion of locally averaged magnitudes. Though, we do not perform the average over the nearest neighbors but over all particles in a  $(3 \times 3 \times 3) \mu\text{m}^3$  subvolume. In doing so we define quasi-continuous

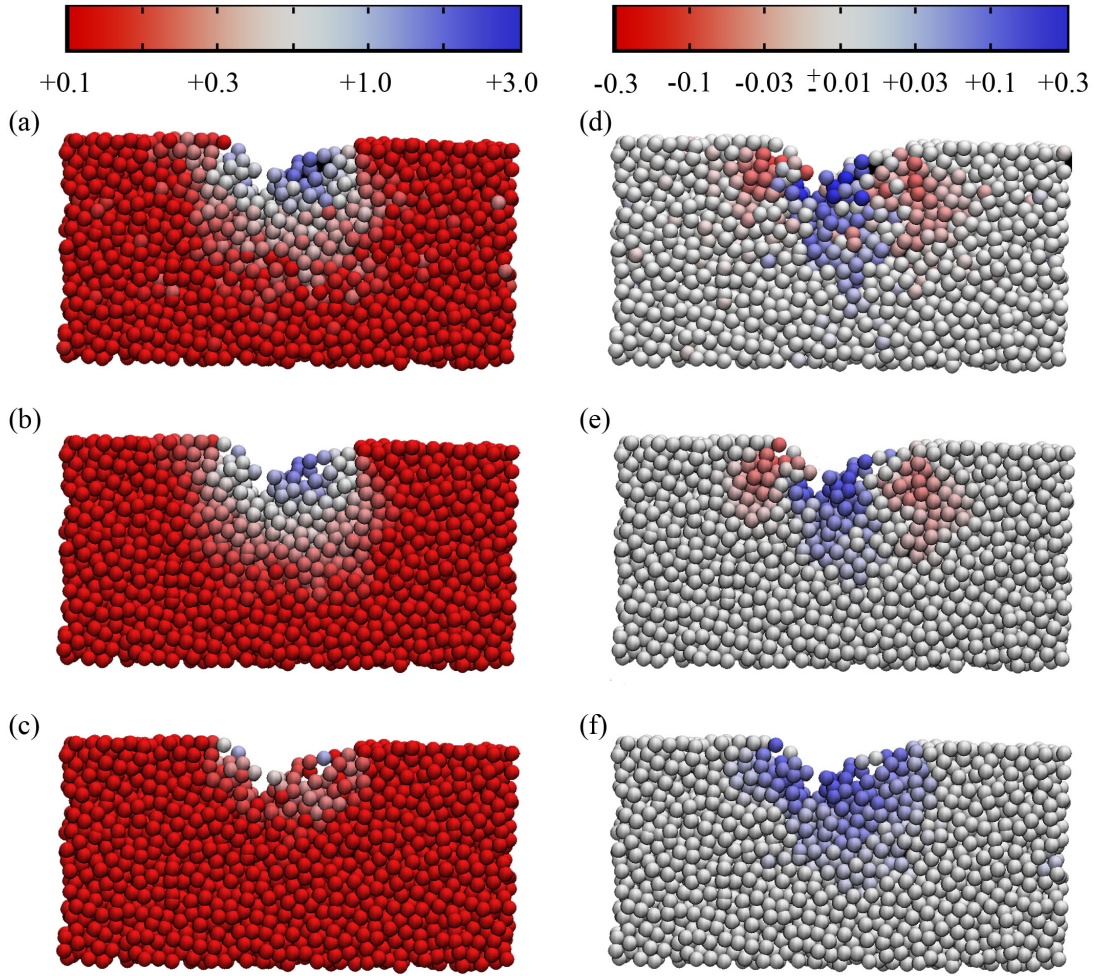


**Fig. 5.7.:** (a) Raw absolute displacement  $d^{(i)}(h)$  for each particle without further data treatment. (b) The data scatter between neighboring particles is moderate and the distribution of displacements after averaging over the nearest neighbors is similar to the raw data. (c) Consequently, standard deviations corresponding to this averaging are significantly smaller than the raw data. (d) The raw strain components ( $\varepsilon_{xx}$ ) shows larger scatter and (e) the characteristic distribution (see text) is better recognizable after averaging. (f) The standard deviations from averaging is in the order of magnitude of the average values.

magnitudes  $\vec{d}(\vec{r})$  and  $d(\vec{r})$  as well as  $\varepsilon(\vec{r})$  and  $\mathcal{F}(\vec{r})$  at the position  $\vec{r}$  that can be more easily compared to predictions of continuum models than in the particle based representation.

### 5.3.1. Displacement and strain field of the amorphous structure

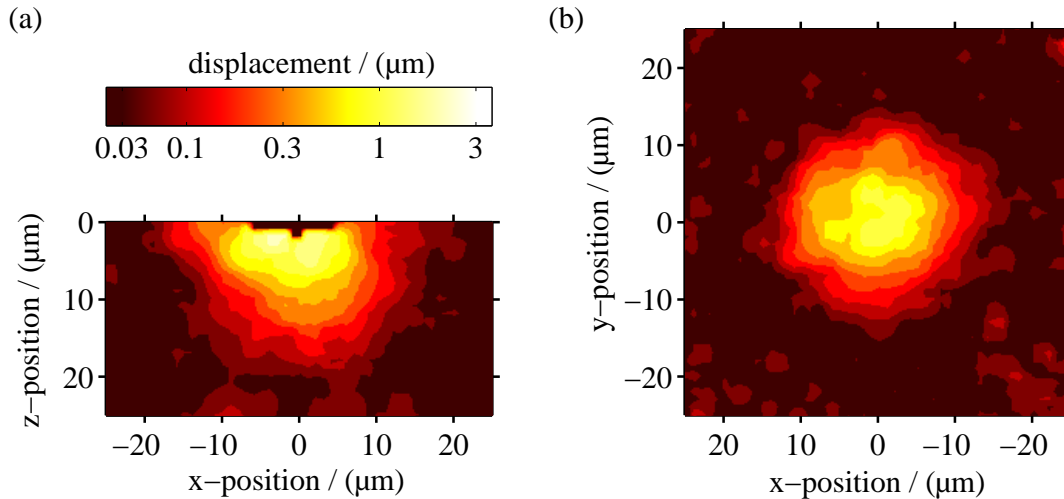
We start the discussion of the result with the live indentation of the amorphous structure that was not enforced by additional PS. As listed in table 5.1 the volume density was close to the value of 63 % that agrees well with the expectation of a random close-packing of monodisperse spheres. The average number of nearest neighbors was  $9.4 \pm 0.1$  and no single crystalline nucleus was found in the observation volume.

Fig. 5.8 shows the absolute cumulative displacement field  $d(\vec{r})$  as a xz-cut and a xy-cut

through the film at a depth of  $3\ \mu\text{m}$ . The indenter was located at its deepest position of  $h = 3\ \mu\text{m}$  inside the film. As expected for a spherical indenter tip and an amorphous structure the distribution was symmetric along the  $z$ -axis. In this averaged representation no major spatial heterogeneities were apparent and the total displacement decayed monotonically with increasing distance to the indenter tip. Further averaging over all azimuth angles  $\phi \in [0^\circ, 360^\circ]$  and intervals of  $15^\circ$  in polar angles  $\vartheta$  revealed an exponential decay (Fig. 5.9) with no significant dependency on  $\vartheta$ . Within about  $20\ \mu\text{m}$  the displacement dropped below the experimental resolution limit of about  $0.05\ \mu\text{m}$ . Displacement and particle position vectors were mainly parallel to each other. This is shown in the inset of Fig. 5.9 in terms of the projection  $\vec{r} \cdot \vec{d}(\vec{r}) / (|\vec{r}| |\vec{d}(\vec{r})|)$  defined as the normalized scalar product of both vectors. The histogram has a maximum at 1 corresponding to fully parallel position and displacement vectors.

More detailed information could be obtained from the strain tensor. The high degree of symmetry in the displacement fields encouraged an averaging not only over the  $(3\ \mu\text{m})^3$  subvolumes but over all azimuthal angles. This procedure already compensated for the larger uncertainties in the strain components compared to the displacements and suited our main focus on the average distribution of the deformation. Therefore, only the positive  $x$ -axis is depicted in the graphs of  $\varepsilon_{\alpha\beta}$  at an indentation depth of  $3\ \mu\text{m}$  in Fig. 5.10.<sup>18</sup>

Just like the absolute displacement the absolute values for the strain components decreased with increasing distance to the indenter tip. Besides, there was a distinct patterning of positive and negative strains. In case of the diagonal elements  $\varepsilon_{\alpha\alpha}$  positive and negative values represent dilation and compression of the local structure in direction of  $\alpha$ , respectively. Directly below the indenter the structure was strongly compressed in  $z$ -direction and dilated in  $x$ - and  $y$ -



**Fig. 5.8.:** Distribution of absolute particle displacements  $d(\vec{r})$  in the (a)  $xz$ -plane at  $y = 0$  and (b)  $xy$ -plane at a depth of  $z = 3\ \mu\text{m}$  in case of an amorphous structure. The indenter is located at its deepest position of  $h = 3\ \mu\text{m}$  inside the film.

<sup>18</sup>In order to compare the strain components of different azimuthal angles  $\phi$  the strain tensor needs to be transformed according to  $\varepsilon' = R^T \varepsilon R$  with the rotation matrix  $R = \begin{bmatrix} \cos(-\phi) & \sin(-\phi) & 0 \\ -\sin(-\phi) & \cos(-\phi) & 0 \\ 0 & 0 & 1 \end{bmatrix}$

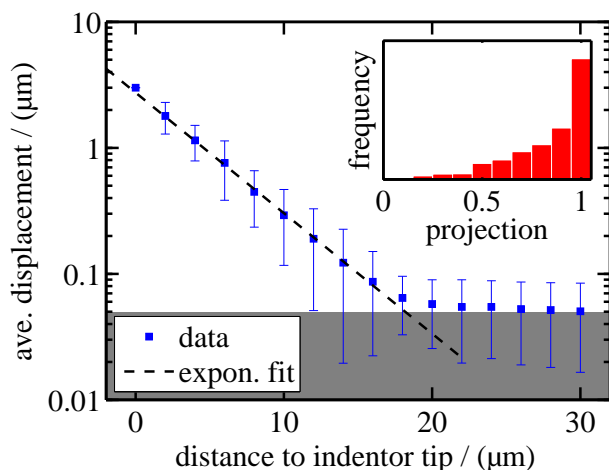


**Fig. 5.9.:** The average absolute displacement shows an exponential dependency on the distance to the indenter tip. Due to the resolution limit a determination of particle displacements is not possible for distances exceeding  $20 \mu\text{m}$ . The position vector  $\vec{r}$  and the cumulative displacement vector  $\vec{d}(\vec{r})$  are mainly parallel as depicted in the inset in terms of the histogram of the projection  $\vec{r} \cdot \vec{d}(\vec{r}) / (|\vec{r}| |\vec{d}(\vec{r})|)$ .

directions. The opposite was the case for polar angles  $\vartheta \geq 55^\circ$  closer to the sample surface. Here the local particle arrangement was compressed in x-direction and dilated in y- and z-direction. Dilation and compression partially canceled each other inducing spatial fluctuations in the volume change

$$\Delta v = (1 + \varepsilon_{xx})(1 + \varepsilon_{yy})(1 + \varepsilon_{zz}) - 1 \quad (5.8)$$

whose absolute values decayed faster than the pure strain components. Shear deformations also took place. The corresponding strain components in the xz-plane of Fig. 5.10 were dominated by the xz-component. It was maximal at polar angles  $\vartheta$  of about  $55^\circ$  for which the absolute values of  $\varepsilon_{xx}$  and  $\varepsilon_{zz}$  were minimal.

### 5.3.2. Comparison to continuum models

The lack of exact information about reorganizations processes complicates the application of any microscopic mechanical model that is based on contact forces between the particles. On the contrary the observed homogeneous average distributions of particle displacements and strain components may be interpreted in terms of a continuum mechanical model.

In the simplest case the amorphous film is regarded as a spatially homogeneous and isotropic material. If the film behaves elastically the force applied by the indenter gives rise to a distribution of stresses  $\sigma_{\alpha\beta}$  that can be calculated analytically according to Huber [Hub06, Dav49] (see appendix D). These stress components in turn are related to the strain components  $\varepsilon_{\alpha\beta}$  via Hooke's law:

$$\varepsilon_{\alpha\beta} = \frac{1}{E} \sigma_{\alpha\beta} - \frac{\nu}{E} \left( \sum_k \sigma_{\gamma\gamma} \delta_{\alpha\beta} - \sigma_{\alpha\beta} \right) \quad (5.9)$$

Here  $E$  and  $\nu$  denote the effective Young's modulus and Poisson ratio of the colloidal film, respectively. These calculated strain components strongly resemble the experimentally obtained strain distributions with respect to the separation in positive and negative strains as well as

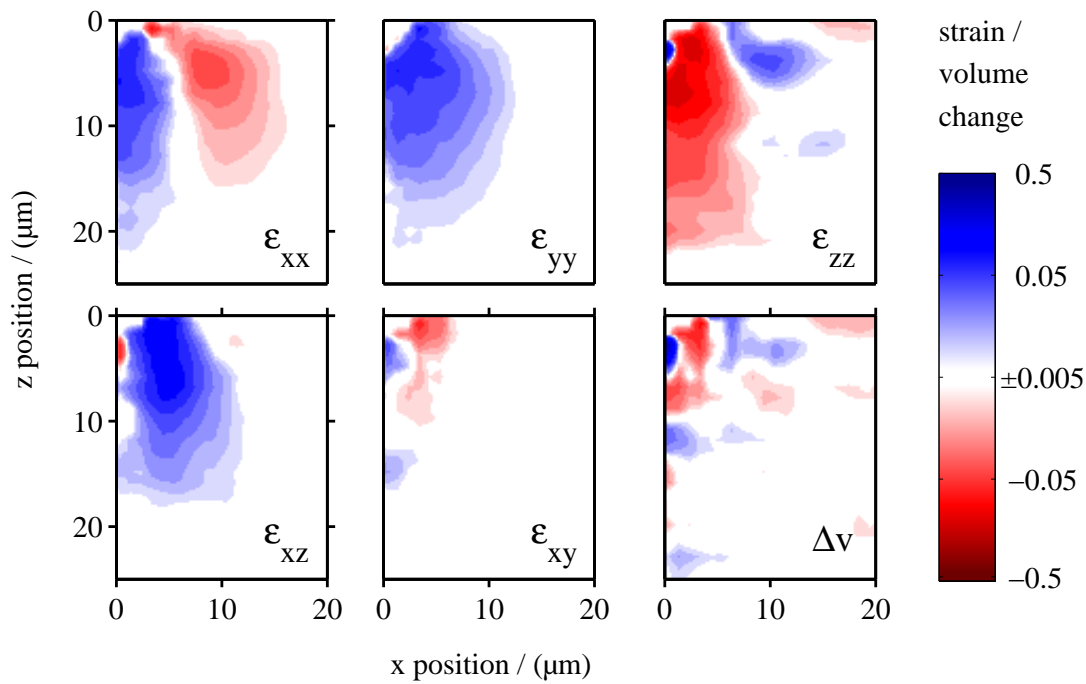


**Fig. 5.10.:** Spatial distribution of the strain tensor elements  $\varepsilon_{\alpha\beta}$  at a depth of  $3\ \mu\text{m}$  for the case of a spherical tip indented in an amorphous film: The data is averaged for all possible values of  $\phi \in [0^\circ, 360^\circ]$  and therefore only shown for positive  $x$ -coordinates.

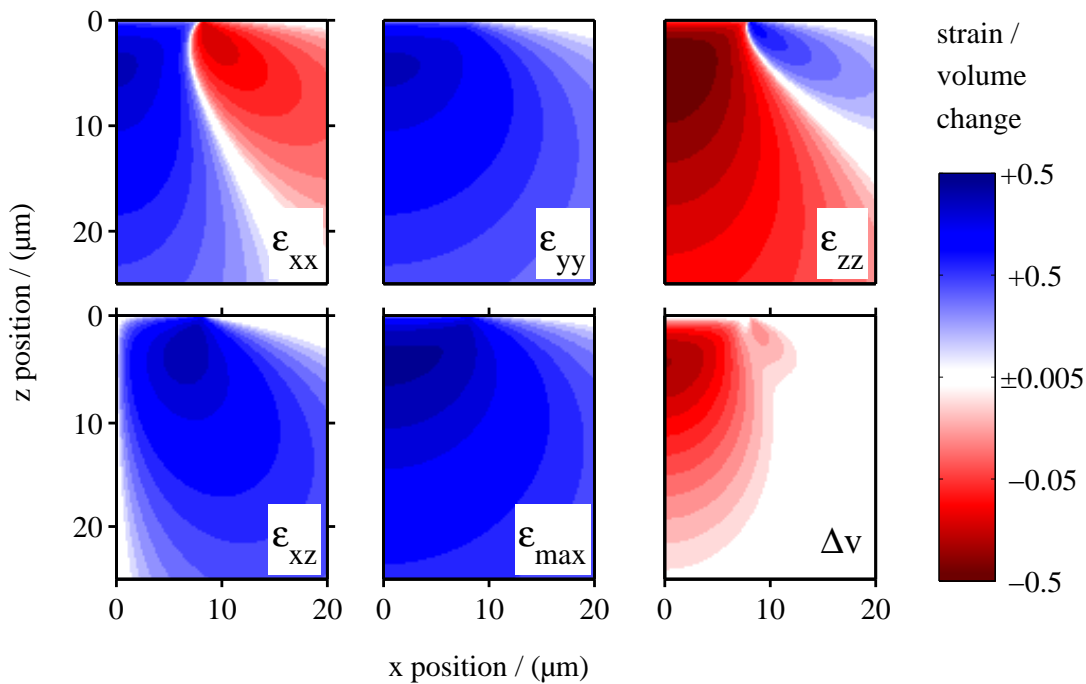


**Fig. 5.11.:** Simulation of the spatial distribution of the strain tensor elements  $\varepsilon_{\alpha\beta}$  according to Huber [Hub06]. The colloidal film is assumed to be an isotropic, homogeneous material with a Poisson ratio of  $\nu = 0.6$  and the indentation is purely elastic. The indentation depth was chosen to be  $3\ \mu\text{m}$  and the spherical indenter has a diameter of  $25\ \mu\text{m}$ .

the general shape of the equi-strain levels. Since any quantitative information about applied force is missing  $E$  cannot be obtained at this point. But relative changes in  $\varepsilon_{\alpha\beta}$  for different values of  $\nu$  allow for an estimation of the effective Poisson ratio of the film. The best congruence of experimental and calculated values was obtained for the maximal value of  $\nu_{\text{film}} = 0.5$  corresponding to an incompressible material (see Fig. D.6).

Despite this good agreement in the spatial characteristics the calculated strain decayed much slower with increasing distance to the indenter than in the experiments. Two effects might explain this discrepancy. The colloidal film had a finite thickness and was supported by the glass substrate which imposed restrictions to the deformation in particular close to the substrate. So the experimental strain is likely to be reduced compared to the theoretical prediction. Second, yielding, *i. e.* plastic deformations, of the film and the individual particles need to be considered and become most apparent in the remnant imprint when the indenter is retracted from the sample. During the indentation process the applied load rises steadily and so does the stress inside the film. When the stress exceeds the yield stress of the film irreversible particle reorganizations take place. The stress-strain relation becomes non-linear and more stress is required for further deformation. Following Tresca's criterion for yielding such plastic deformations first take place where the principal stress difference  $\sigma_{\text{max}}$  is maximal [Dav49]. Formally  $\sigma_{\text{max}}$  is calculated from

$$\sigma_{\text{max}} = \max(|\sigma_1 - \sigma_2|, |\sigma_1 - \sigma_3|, |\sigma_2 - \sigma_3|) \quad (5.10)$$

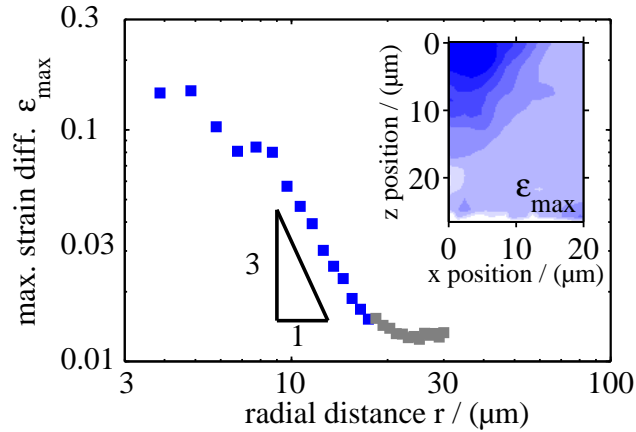
Here  $\sigma_1$ ,  $\sigma_2$  and  $\sigma_3$  denote the principle stresses that are obtained from a principal axes transformation of the symmetric stress tensor. Following the model from above this calculations predicts a maximum in  $\sigma_{\text{max}}$  at a distance of  $0.63 a$  below the indenter tip whereas  $a$  is the radius of the projected contact area (see Fig. 5.5). [Joh04a] Indeed such a localized yielding was already observed for other mesoscopic systems such as crystalline assemblies of soap bubbles [Gou01]. In our case the yielding point is close to the indenter tip even for the largest indentation depth ( $0.63 a \approx 5 \mu\text{m}$ ) and masked by the limited spatial resolution after averaging. Furthermore yielding can already take place at smaller indentation depth and therefore even closer to the tip.

Hence, it is more appropriate to describe the amorphous colloidal structure as an elasto-plastic solid. In the initial phase of the indentation the deformation is fully elastic until the imposed stress exceeds the yield stress. The stress is partially released via plastic deformations and rises again upon further indentation. In the end of the loading cycle the stress is divided into two regions. Close to the indenter the stress decreases moderately with increasing distances from the tip  $r$  until the elastic-plastic boundary is reached [Joh04b, Cho08]. For larger distances the stress is stored in elastic deformations and decays much faster according to a  $r^{-3}$  dependency. Moreover, the distribution is virtually independent on  $\vartheta$ .

Experimentally this stress characteristics is best mapped by the maximal strain difference  $\varepsilon_{\text{max}}$  defined in analogy to  $\sigma_{\text{max}}$ . If cylindrical symmetry is assumed the components  $\varepsilon_{xy}$  and



**Fig. 5.12.:** The transition from a weak dependency of the maximal shear strain on the distance to the indenter tip to a power law behavior with a slope of approximately -3 in the semi-logarithmic plot is a hallmark of an elasto-plastic solid. The gray data points for the larger distances are masked by the resolution limit of the strain analysis. The complete  $xz$ -view is shown in the inset with a color-scale identical to Fig. 5.10



$\varepsilon_{yz}$  can be neglected with regard to  $\varepsilon_{xz}$  and  $\varepsilon_{max}$  is more easily obtained from

$$\varepsilon_{max} = \sqrt{(\varepsilon_{xx} - \varepsilon_{zz})^2/4 + \varepsilon_{xz}^2} \quad (5.11)$$

Fig. 5.12 shows the spatial distribution of  $\varepsilon_{max}$  as well as the distance profile which are in reasonable agreement with this model.

### 5.3.3. Microscopic processes

The comparison with the continuum model does not provide any information about the exact nature of the microscopic processes that lead to the observed strain field. In particular the azimuthal averaging makes it impossible to keep track of the individual particle rearrangements and evaluate their contribution to the total strain. Still we try to relate the insights from the average strain field to microscopic processes that potentially play a role in the indentation.

Obviously the mechanical nature of the particle contacts plays a crucial role on the microscopic processes. If the particles stick together via cohesion a certain binding force need to be overcome to separate two particles in axial directions. Rolling or sliding movements, however, are more complicated and depend on the particle surface properties. In case of smooth particles such transversal motions are expected to require smaller compared to rough particles. Aggregates with solid particle bridges behave differently. If the applied forces are small the bonds are elastically deformed but when stressed beyond the yield point irreversible deformation of bonds occur. At even higher stresses and strains above the strength the bond breaks and again frictional sliding of particles occur. Obviously the behavior strongly depends on the used materials. Glassy PS and PMMA are rather brittle materials that show failure at small strains and large stresses compared to ductile materials. Moreover, the direction of the acting forces need to be considered. While the strengths for transversal and tensional loads are similar in case of PS the compressive strength is larger by a factor of almost two.

The measured compressive strains might also have a contribution from deformations of the particles themselves. This deformation  $d$  is maximal for the particles that are in contact with the indenter tip. Under the assumption that a typical maximal load of 1.5 mN (see Fig. 2.12)

is distributed over roughly 25 particles, Hertzian contact theory [Her26, Joh04a] predicts a particle deformation of:

$$d = \left( \frac{9 P_o^2}{16 R^* E_r^2} \right)^{1/3} \approx 140 \text{ nm} \quad (5.12)$$

Here  $R^* = (1/R_p + 1/R_{\text{ind}})^{-1}$  denotes the effective contact radius defined by the radii  $R_p$  and  $R_{\text{ind}}$  of the particle and indenter, respectively.  $P_o$  is the force applied to particle and  $E_r \approx 2.5 \text{ GPa}$  is the reduced Young's Modulus defined in analogy of equation (2.19). However, the corresponding contact pressure

$$p = \frac{2}{\pi} E^* \left( \frac{d}{R^*} \right)^{1/2} \approx 500 \text{ MPa} \quad (5.13)$$

by far exceeds the compressive strength of PMMA ( $\approx 80 \text{ MPa}$ ). So, the particles themselves are plastically deformed which most likely manifest in a flattening of the particle surface at the contact point and the calculated deformation of 140 nm is overestimated.

For particle sizes in the micrometer range surface tension can contribute to the stiffness of the individual particles as any deformation of the spherical particle increases its surface energy. According to the Young-Laplace equation the pressure difference between the particle and the environment amounts to  $\Delta p = 2\gamma/R \approx 0.1 \text{ MPa}$ . In this approximation a value of  $\gamma = 40 \text{ mJ/m}^2$  was chosen for the surface tension of PMMA at room temperature [Jan90].  $\Delta p$  is already a measure of the resistance of the particle upon any deformation from its spherical shape. Hence, effects of surface tension are negligible compared to the elastic modulus of PMMA.

These approximations are only valid for the upper most particle layers since the force on the particles decays steeply when going deeper in the film. The lower particles show predominantly elastic deformations below the resolution limit of 50 nm. Consequently, plastic deformations of the particles cannot account for the compressive strains in Fig. 5.10 but still must be considered in the mechanical description of the indentation.

In summary, the interplay of particle contact type, material properties as well as geometrical factors determines the microscopic behavior of the deformed film. However, the intrinsic complexity as well as the lack of more accurate single particle data prevents a clear assignment of certain microscopic processes to the elastic and plastic contributions of the measured strain field. Further parameter variations might help a better understanding. Therefore, we continue with the deformation analysis in semi-crystalline structures.

### 5.3.4. Heterogeneities in semi-crystalline structures

The semi-crystalline structure consisted of extended crystalline domains with hexagonal close-packed and cubic face centered lattices that are separated by stacking faults or larger amorphous regions. Due to these defects the average volume density for all indentation spots was reduced to a value of about 67% compared to the value of 74% for perfectly closed packed

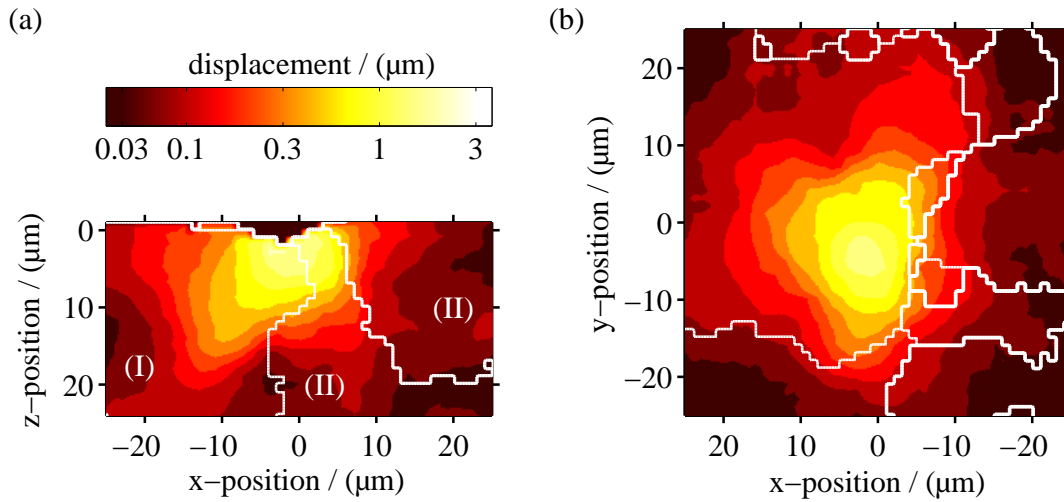


**Fig. 5.13.:** Distribution of absolute particle displacements for a xz- (a) and a xy-cut (b) through a crystalline sample. The borders of the crystalline domains are shown as contour lines. In the direct vicinity of the indentation region the stress is transmitted through domain borders. At larger distances defects between the domain walls hinder the transmission of stress and the displacement is contained in the crystalline domains.

spheres. Also the average number of nearest neighbors of was reduced to 10.5.

When comparing the absolute displacement field for the amorphous and semi-crystalline structure (Fig. 5.13) no significant differences were found in the vicinity of the indenter tip. Particles in immediate contact with the tip were exposed to large stresses that led to large strains and partial destruction of the crystal structure. With increasing distances the crystal lattice was less distorted revealing heterogeneities in the displacement field that were not observed in the amorphous case.

These heterogeneities were partially related to presence of multiple crystalline domains in the sample. In addition to the displacement field the borders of crystalline domains are shown in Fig. 5.13. At the domain borders a transmission of stresses seemed to be hindered while the range of the displacement field was increased within the domains like for domain (I) in the left part of Fig. 5.13(a). This effect is further visualized in Fig. 5.14 that shows the distance profiles of the particle displacement averaged over a small range of polar and azimuthal angles. While the displacement for the amorphous and semi-crystalline structure close to the domain borders (region A) decayed similarly, the displacement extends much farther within the domains (region B). This increase in stress transmission efficiency was related to the close packing within the domain. Sliding and rolling of individual particles past each other was hindered because of the limitations in free space and thus groups of particles were collectively displaced. The slight increase in the number of nearest neighbors and bonds further stabilized the relative positions of the particles and thus aided cooperative motions.

The orientation of the crystalline domain also affected the stress transmission. If the acting force was collinear with high symmetry planes of the crystal lattice the particle bonds were preferentially loaded in normal direction. As discussed above the bonds can sustain larger

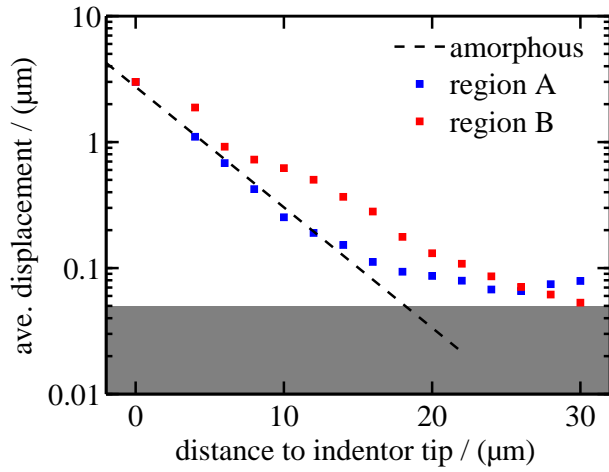


**Fig. 5.14.:** The radial distribution of the absolute displacement in the semi-crystalline structure is heterogeneous. In the amorphous regions and crystalline domains with unfavorable lattice orientation the displacements are comparable to those of the completely amorphous structure. That is the case for region A that averages over all particles with  $\vartheta \in [20, 50]^\circ$  and  $\phi \in [-15, 15]^\circ$  (pos. x-axis). When the crystal lattice is orientated along with the acting forces the displacements are significantly increased like for region B with  $\vartheta \in [20, 50]^\circ$  and  $\phi \in [165, 195]^\circ$  (neg. x-axis).

stresses in this direction. This scenario is depicted as a computer reconstruction in Fig. 5.15 of the same xz-cut like in Fig. 5.13 (a). The overall crystalline order of domain (I) is clearly visible with a high symmetry lattice plane (Miller's Indexes:  $\{\bar{1}, 0, 2\}$ ) crossing the xz-plane in the dashed line. This dashed line is nearly perpendicular to the spherical indenter tip. In this geometrical configuration indentation forces were effectively transmitted along straight lines of particles.

The collective motion of particles was not only observed for elastic deformations but also for yielding events. In case of domain (I) a cooperative yielding manifested as a sliding dislocation along the above mentioned lattice plane. Such a sliding motion is a frequent defect because of reduced energy barriers [Sch05] perpendicular to the high symmetry lattice planes and were also observed in DEM simulations of e.g. sheared crystals [Kaw11]. Furthermore, in the present case the defect generation was favored by maximal shear stresses  $\varepsilon_{xz}$  at polar angles  $\vartheta$  of about  $45^\circ$ .

As a result of the dislocation, particles left to the dashed line in Fig. 5.15 were elevated while the particles closer to the z-axis were displaced downwards. This elevation of particle above the initial film surface is called pile-up and is a direct consequence of limited compressibility of

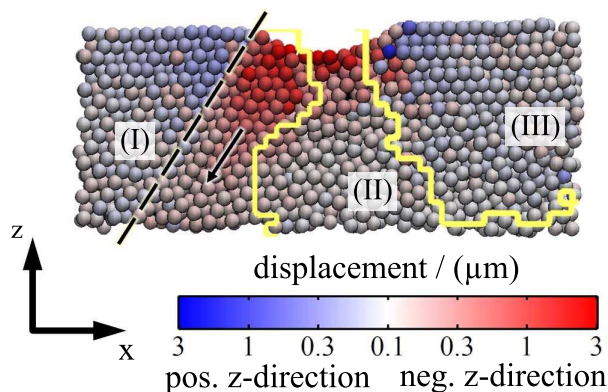


**Fig. 5.15.:** 3D computer reconstruction of a XZ-cut through a poly-crystalline film indented with a spherical tip. The color code represent the absolute displacement for each individual particle distinguishing between particles, that move in positive and negative z-directions. The collective movement of particle along high-symmetry crystal directions (arrow) and the resulting gliding dislocation (dashed line) are clearly visible.

the sample. It is well-known for atomic matter and enforced for crystals as larger amounts of material is involved. The orientation of the crystal plays an important role [Smi03]. If it does not favor stress transmission along high symmetry planes piling-up is reduced like for domain (III) in Fig. 5.15.

## 5.4. Macroscopic material properties

### 5.4.1. Deformation works and elastic recovery

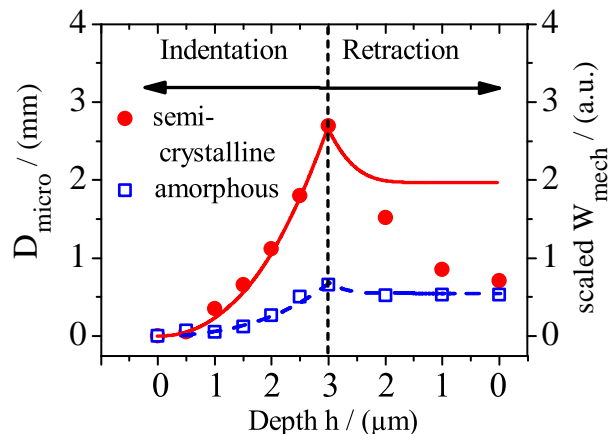
As no quantitative information about the contact forces could be gained from the live indentation experiments we could not calculate plastic and elastic deformation works associated with the indentation. Yet, we could observe plastic and elastic particle displacements. When the indenter tip was retracted the stored elastic deformation energy recovered via partial relaxation of the particles back to their initial configuration before the indentation. We monitored this recovery as well as the deformation in the loading cycle by the following quantity in dependence on the indentation depth  $h$ :

$$D_{\text{micro}}(h) = \sum_{i, d^{(i)} > 0.15 \mu\text{m}} d^{(i)}(h) \quad (5.14)$$

$D_{\text{micro}}$  sums up the absolute values of the cumulated displacements. Due to the finite resolution of the displacements we cut the sum and reject those displacements with absolute values smaller than  $0.15 \mu\text{m}$  corresponding to 5% of the total indentation depth.

Fig. 5.16 shows the result of this analysis for an exemplary amorphous and crystalline structure.  $D_{\text{micro}}$  rose with increasing indentation depth up to a maximum value at the deepest indenter position. Coinciding with the extended displacement field in case of the crystalline structure  $D_{\text{micro}}(3 \mu\text{m})$  exceeded that of the amorphous structure. The relative factor depended on the indentation position and is on the order of 2 – 4. The difference is even more increased for the elastic recovery. While the amorphous structure showed almost exclusively plastic deformation a large amount of the cumulative displacements was recovered for the crystalline structure. This recovery is visualized in the computer reconstruction of Fig. 5.17.

**Fig. 5.16.:** The maximal total displacement  $D_{\text{micro}}$  (symbols) is largely increased for the crystalline structure compared to the amorphous one. The same is true for the elastic recovery under retraction of the indenter tip. The rescaled total deformation work  $W_{\text{mech}}$  (lines) shows the same functional dependency for the indentation process for both structures. However, differences are found under retraction for the crystalline structure.



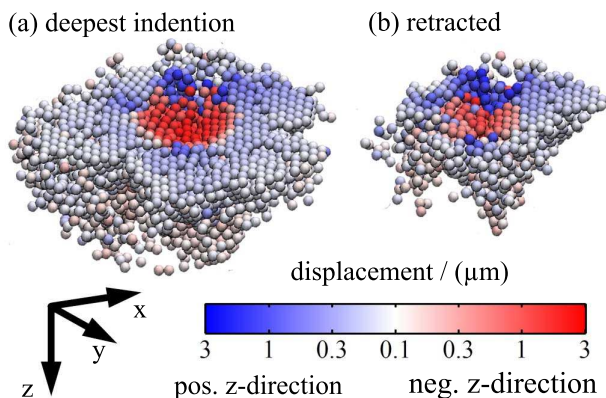


**Fig. 5.17.:** Computer reconstructions of a semi-crystalline colloidal film at the deepest indenter position of  $h = 3 \mu\text{m}$  (a) and after retracting the tip (b). Only those particles with absolute cumulative displacements larger than  $0.15 \mu\text{m}$  are shown. Although the depth of the indent is reduced after retraction of the tip, it is still clearly visible.

We compared the displacement data with the deformation work

$$W_{\text{mech}}(h) = \begin{cases} \int_0^h P_{\text{ind}}(h') dh' & \text{Indentation} \\ W_{\text{tot}} - \int_h^{h_{\text{max}}} P_{\text{ret}}(h') dh' & \text{Retraction} \end{cases} \quad (5.15)$$

defined in analogy to the set of equations (2.27). For the indentation process  $W_{\text{mech}}$  gives the total deformation work. Upon retraction the elastic part is recovered and thus the deformation work is reduced again.  $W_{\text{mech}}$  was calculated for exemplary force-depth curves (see section 2.2.2) of an amorphous and a semi-crystalline structure and added to the graph in Fig. 5.16. The absolute values of  $W_{\text{mech}}(h)$  were rescaled to make the maximal deformation work  $W_{\text{mech}}(3 \mu\text{m})$  and maximal summed displacements  $D_{\text{micro}}(3 \mu\text{m})$  overlap in the graph.

For both, the amorphous and the semi-crystalline structure,  $D_{\text{mech}}(h)$  and  $W_{\text{mech}}(h)$  coincided for the loading part showing the same dependency on the indentation depth. This is quite surprising as  $W_{\text{mech}}(h)$  is a measure of the deformation work while  $D_{\text{mech}}(h)$  only sums up the displacements. In order to get an estimation for the deformation energy from particle displacements, assumptions about the acting forces are required. In the most trivial model the force that is necessary for a infinitesimal displacement is constant for all particles. Although the ratio between  $D_{\text{mech}}(h)$  and  $W_{\text{mech}}(h)$  indeed was almost constant this model is clearly oversimplified. In case of the amorphous structure  $W_{\text{mech}}$  and  $D_{\text{micro}}$  also overlapped for the unloading cycle. The semi-crystalline film, however, shows a displacement recovery that is strongly enhanced compared to the retrieved elastic deformation work.

At this point we restrict ourselves to this qualitative description of the relation between  $W_{\text{mech}}$  and  $D_{\text{micro}}$ . In addition to the already mentioned difficulties of an appropriate comparison, experimental issues complicate the discussion. A fast reduction of the contact area between indenter and sample upon retraction would limit the force transmission of the sample to the tip. A reduced force on the indenter would lead to a reduced elastic recovery of  $W_{\text{mech}}(h)$  while the particle displacements are not necessarily altered. Differences in the sample preparation and the experimental procedure also must be considered. When the indenter tip is retracted from the sample in the live indentation experiments a possible hydrodynamic

drag on the particle caused by the viscous oil might act as an additional effective restoring force and contribute to the elastic recovery of the displacements.

### 5.4.2. Hardness and effective elastic modulus

In the following we focus on the analysis of the force-depth curves in order to extract average mechanical properties of the films such as the hardness and the effective elastic modulus. Beside to the variations in film structure we investigate the influence of an enforced bond strength between the particles.

Before force-depth curves like *e. g.* in Fig. 2.12 can be analyzed the raw data need to be corrected for a possible deformation of the glass substrate. In case of a 1 mm thick substrate this deformation is negligible. However, the used glass substrates had a thickness of  $170\ \mu\text{m}$  which was required in order to image the films after indentation with the confocal microscope. Indentation on a bare glass substrate showed that the deformation is highly elastic and an effective spring constant of  $20\ \text{N/mm}$  was obtained from the unloading part of the indentation process. Assuming validity of Hook's law the deformation of the substrate was calculated from the applied force and subtracted from the raw indentation depth. This procedure just rescales the depth axis and thusly does not change the general appearance of the force-depth curves.

The corrected force-depth curves were analyzed following the method by Oliver and Pharr described in section 2.2.2. While the characteristic quantities of maximal force  $P_{\text{max}}$  and contact stiffness  $S$  could be determined from the retraction data, the contact area  $A_c$  is not accessible from the mechanical data. The proposed solution to calculate  $A_c$  from  $h_c$  fails for the colloidal films because the starting point of the indentation process is not well defined.

Upon approaching to the sample surface the tip may indent directly on top of a particle or into the interstice between them. After the initial contact with the tip the upper most particles will rearrange to fit the shape of the indenter causing a shift in the onset of indentation. As only few particles are involved, this first consolidation process has a diffuse mechanical response that differs strongly from one indentation spot to the other. Corresponding large strains in the vicinity of the indenter tip were observed in live indentation experiments and eventually led to the two small humps in Fig. 2.12 in the early stage of the indentation. Given the fact that the particle radius of  $0.8\ \mu\text{m}$  is not far off the total indentation depth  $h_{\text{max}}$  these onset uncertainties give rise to large errors in  $h_c$  and even more pronounced in  $A_c$ .

The problem of an unclear total indentation depth is even more intensified when adhesion comes into play and single particles are pulled out of the film and adhere to the indenter tip. This effect manifests in small negative indentation forces shortly before the tip loses contact with the sample. Further indications can be found in the confocal images showing few elevated particles next to the indents. These adhered particles can cause a premature start of the measurement at the subsequent indentation spot and with this again give another source of errors in  $h_{\text{max}}$ .

We bypass these difficulties by choosing the second possibility to determine the contact area  $A_c$  by imaging the remnant indent. As already discussed before this method disregards the

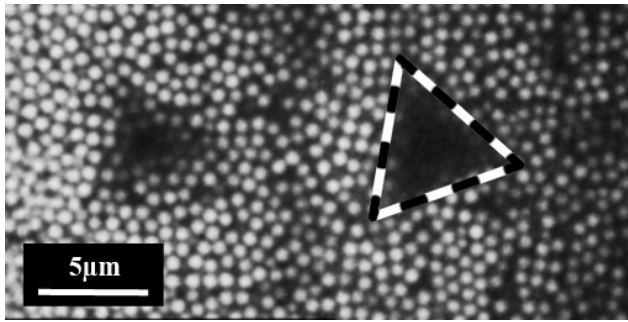


**Fig. 5.18.:** The confocal image shows the colloidal film after indentation. Two neighboring indents appear as dark areas devoid of bright particles allowing for a measurement of the contact area. The triangle indicates the shape of the used Berkovich indenter.

elastic recovery of the material upon unloading. Yet, the live indentation experiments showed that only particles with small displacements at larger distances to the tip return to their initial locations. On the contrary particles in direct contact with the indenter are largely irreversibly displaced and map the tip geometry. Fig. 5.18 shows a xy slice of a complete 3D confocal data set showing two neighboring indent positions. The triangular shape of the Berkovich indenter used in this part of the study is clearly visible and a determination of  $A_c$  is feasible.

The extracted values for hardness  $H$  and effective elastic modulus  $E_{\text{eff}}$  of the amorphous and semi-crystalline structures are shown in Fig. 5.19 and Fig. 5.20, respectively. The ordinate was chosen to be the product of the number of nearest neighbours  $N_n$  and the order parameter  $\bar{q}_6$ . In case of the amorphous structure  $\bar{q}_6 \cdot N_n$  as well as the mechanical quantities were narrowly

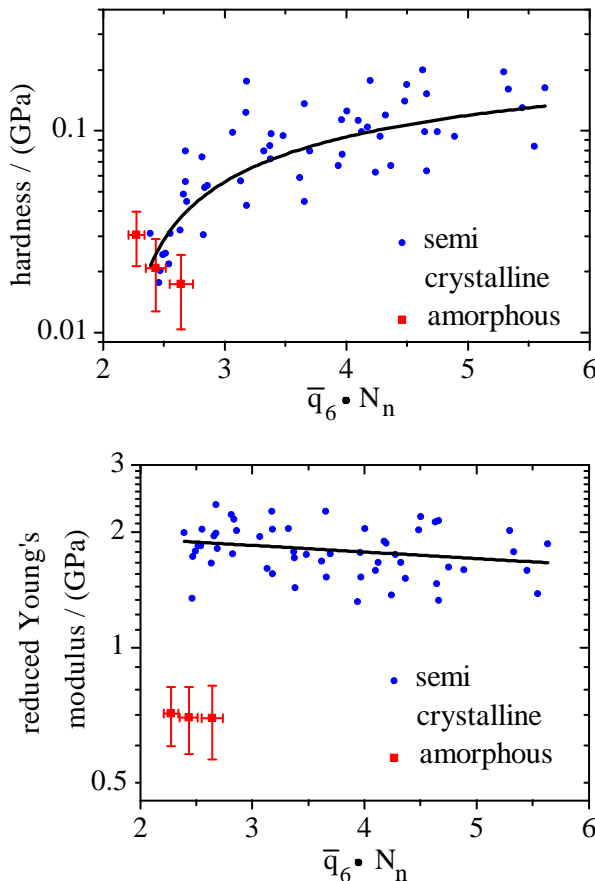
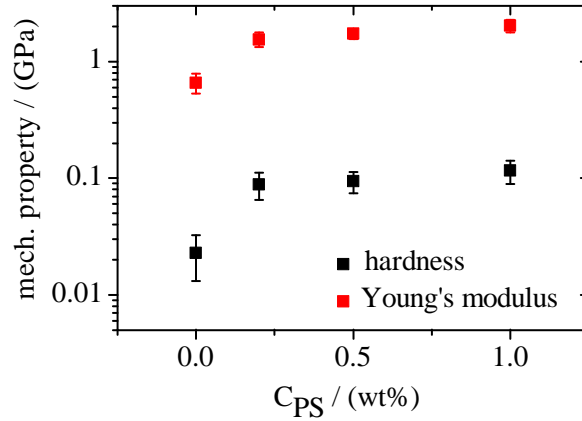


**Fig. 5.19.:** Dependency of the film hardness on its colloidal structure. The hardness increases monotonic with higher order parameters and number of nearest neighbors and saturates for highly crystalline films.

**Fig. 5.20.:** Within the semi-crystalline sample only a slight dependency of the effective elastic modulus  $E_{\text{eff}}$  on the local order  $\bar{q}_6 N_n$  was observed. Though,  $E_{\text{eff}}$  for semi-crystalline and amorphous structures with similar values of  $\bar{q}_6 N_n$  differ significantly. Instead, this difference in elasticity coincides with variations in the film thicknesses (see Fig. 5.4).



**Fig. 5.21.:** Hardness and Young's modulus show the same behavior for a variation of binding strength between the particles in the film. Upon a sharp increase for the weakest binding, both quantities similarly saturate at a value comparable to the crystalline films.



distributed and only averaged values are shown. On the contrary the semi-crystalline film revealed larger variations in  $H$  and  $E_{\text{eff}}$  as well as  $\bar{q}_6 \cdot N_n$ .

Two effects were responsible for this scatter. The live indentation experiments showed that structural heterogeneities in the semi-crystalline films led to a non-isotropic displacement and strain field which directly manifested in enlarged statistical variations of the mechanical properties. Secondly,  $\bar{q}_6 \cdot N_n$  strongly depended on the film thickness as it was discussed in Fig. 5.4. Along with the reduction of the film thickness,  $\bar{q}_6 \cdot N_n$  as well as the crystallinity *i. e.* the fraction of particles belonging to a crystal domain is reduced. At the indentation spots with the lowest film thickness no crystal domains were found at all and the corresponding hardness fitted well with the data of the amorphous samples. At high values of  $\bar{q}_6 \cdot N_n$  the hardness finally saturated at a mean value of about 0.15 GPa. An analogous trend was not found for  $E_{\text{eff}}$ . Irrespective of sample thickness and values for  $\bar{q}_6 \cdot N_n$  an almost constant value of about 1.8 GPa was extracted for all indentation spots of the semi-crystalline sample. The amorphous structures were significantly off with a mean value of  $(0.65 \pm 0.10)$  GPa.

The variation of the particle bond strength resulted in a similar change in the mechanical properties. By introducing only small amounts of PS as solid bridges between the particles, hardness as well as effective elastic modulus rose by a factor of 5 and 2.5 respectively compared to the amorphous films without fortified bonds. The values are comparable to those of the thick semi-crystalline films. Addition of further PS however did not change both quantities significantly.

### 5.4.3. Correlation of microscopic deformation and macroscopic material properties

The live indentation experiments showed that the averaged distribution of strains in the amorphous structure can be understood with continuum theories of the indentation process. Therefore we suppose that the analysis of the force-depth curves according to Oliver and Pharr provides average material properties just like in case of nanoindentation of atomic matter. Indeed hardness (Fig. 5.19) and effective elastic modulus (Fig. 5.20) at different indentation spots

of the amorphous structure follow a reasonably<sup>19</sup> narrow distribution around a well defined mean value. The increased data scatter for the semi-crystalline structures has already been related to enlarged spatial heterogeneities in the deformation field that have been identified in the live indentation experiments.

Yet, the extracted values for the hardness and effective elastic modulus need to be motivated. The hardness of a material is defined as the force per contact area that is needed to deform the specimen irrespective of the type of deformation. Plastic rearrangements of particles are not distinguished from elastic deformation of particles and bonds. In the semi-crystalline structure particle reorganization and the relaxation of stresses are hindered due to high particle densities. The number of displaced particles increases fast while the indenter tip is pressed deeper into the sample. Larger groups of particles are elevated above the sample surface to compensate for the volume blocked by the tip. All these effects contribute to large indentation forces and thus a large value of the hardness. In the amorphous film structural rearrangement of rather small groups of particles are still possible. Comparatively small forces are needed to break the existing weak bonds and displace the particles via frictional sliding. As a result the hardness is reduced compared to the semi-crystalline structure.

$\bar{q}_6 \cdot N_n$  seems to be a suitable parameter to map the structural differences. It accounts for changes in the particle density that is proportional to the  $N_n$  as well as for the geometrical assembly of the particles reflected by the order parameter  $\bar{q}_6$ . However, this argument does not hold if the particles bonds are strong and withstand larger applied loads. This was the case when PS was introduced into the film to form solid bridges between the particles. Only small amounts were required to increase the hardness significantly. Still the hardness of the particulate films turned out to be about one order of magnitude smaller than the literature value of 1.9 GPa for bulk PMMA [Lu01].

The Young's modulus  $E$  measures the changes in elastic energy density  $w_{\text{elas}}$  when a material is deformed upon an external load. Since the total deformation energy can also have plastic contribution  $E$  is more reliably obtained from the elastic recovery when the applied stress is taken away  $E = dw_{\text{elas}}/d\varepsilon$ . In case of the colloidal film  $w_{\text{elas}}$  scales with the number of deformed particles and bonds as well as the type of deformation. Both parameters are different for the amorphous and crystalline structures. In the amorphous film less particles are displaced and enhanced plastic rearrangements during the indentation process reduce the stored elastic energy and therewith  $E_{\text{eff}}$ . Moreover, there is a considerable amount of elastic energy that is stored in transversal deformations of particle bonds. On the contrary, in the semi-crystalline structure particles rearrangements are hindered due to close-packing and particles and bonds are deformed in the normal directions that can sustain larger stresses. All in all  $w_{\text{elas}}$  rises more steeply when the film is deformed resulting in greater values for  $E_{\text{eff}}$ .

Like for the hardness  $\bar{q}_6 \cdot N_n$  seems to be a suitable parameter to quantify these differences between the different structures. Though, within the group of semi-crystalline films  $E_{\text{eff}}$  did not reveal a dependency on  $\bar{q}_6 \cdot N_n$ . This behavior can be explained by coincidentally decrea-

---

<sup>19</sup>Still one has to consider that the number of involved particles is much much smaller than for atomic matter which causes an larger statistical scatter.

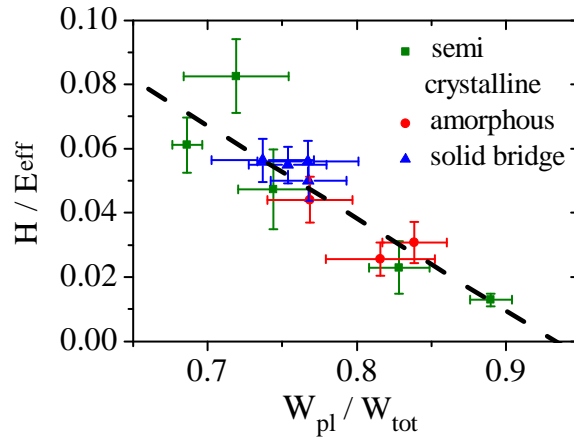


**Fig. 5.22.:** Irrespective of structure or binding strength the mechanical properties of all samples can be universally related with each other in a plot of the ratio  $H/E_{eff}$  versus the fraction of plastic deformation work  $W_{pla} / W_{tot}$ .

sing film thickness and  $\bar{q}_6 \cdot N_n$ . The proximity of the particles to the substrate for the thin films effectively limits the amount of possible plastic rearrangements and thus enhances the contribution of elastic deformations. So an equally high value of  $E_{eff}$  was maintained. In the amorphous structures with induced solid bridges reorganization of particles is also hindered and again  $E_{eff}$  exceeds that of the amorphous sample without solid bridges.

Considering that the volume density of the colloidal film even for the thick semi-crystalline films is lowered to 70 % of a continuous PMMA film the observed values for  $E_{eff}$  are quite close to the literature values for bulk PMMA [(1.8 – 3.1) GPa]. This supports the assumption that the deformation of particles and bonds is the dominant contribution to  $E_{eff}$  as effectively the materials of the constituent particles and bonds are tested.

#### 5.4.4. Universality

Further checks for the consistency of the analysis according to Oliver and Pharr can be found in the previous works [Che98] that related the mechanical quantities  $H$  and  $E$  to the elastic and plastic fractions of the deformation work. Scaling arguments predict a linear correlation of  $H/E$  and  $W_{pla}/W_{tot}$  irrespective of the used materials. Via this relation metals, sapphire and silica could be universally superimposed on a single curve. The same behavior was found for our colloidal films. Films with solid bridges as well as semi-crystalline and amorphous structures collapsed to a single line with a slope of  $(-0.29 \pm 0.02)$  (Fig. 5.22). The discrepancy to the corresponding literature value of  $-0.2$  [Oli04] may be based on the choice of  $E_{eff}$  instead of the true Young's modulus  $E$ .

## 5.5. Conclusions and Outlook

### 5.5.1. Nanoindentation as a mechanical test method for colloidal aggregates

We presented a study of the mechanical properties of stiff colloidal aggregates tested via nanoindentation. Although the sample was tested only very locally the induced deformation was in semi-quantitative agreement with the predictions of a continuum theory and thus behaved

comparable to atomic matter. This result lines up with similar observations in other colloidal systems that were tested via nanoindentation. One example are soft colloidal crystals for which the thermal energy of the constituent particles still is large enough to induce position fluctuations about their mean crystal lattice positions. In this system the dynamics of dislocation generation could be explained analogous to atomic crystal. By balancing the energy cost for defect nucleation and the energy gain due to relaxation of the indentation stress the critical parameters like dislocation radius, defect energies and indentation stresses were obtained [Sch05, Sch04]. In weak and fractal colloidal aggregates the indentation could be modeled with Hertzian theory. The applied force rose with increasing indentation depth  $d$  following a  $d^{3/2}$  power law as it is expected for atomic matter. From the fit an estimate of the average elastic modulus of the aggregate was obtained. Moreover, stress relaxation experiments revealed plastic particle reorganizations which were successfully modeled by a stick-slip behavior of particles as they slide past each other [Fil06a, Fil06b]. What is most remarkable about these common similarities to continuum theory and atomic matter is the huge difference in the type and strength of dominant interactions present in the different colloidal systems. While the soft crystals are formed by sedimentation and Brownian motion of the particles the weak aggregates originated from an attractive depletion interaction that is strong enough to withstand gravitation forces. Though, the particles easily slide past each other compared to the dense aggregates in the present study that require more than 1000 times larger indentation forces.

The comparability with the continuum model might arise from the fact that a sufficiently large ensemble of particles are tested during the indentation. The shown computer reconstructions such as Fig. 5.17 typically contain 1.000 to 10.000 particles which is also a typical number of particles in simulations [Kaw11, Kad09]. Consequently, heterogeneities caused by the particulate nature of the colloidal film are averaged and the theory of Oliver and Pharr was successfully applied to obtain average material properties. Hardness and effective elastic modulus were found to be dominated by aggregate structure and the particle bond strength as these properties decide on the relevant particle reorganization processes during the indentation. This opens up new possibilities for a standardized mechanical characterization of particle based materials via nanoindentation.

This test of applicability of nanoindentation methods for mechanical characterization of colloids was one of our main goals. The other studies from above primarily focus on the similarities in the description of colloids and atomic matter. Colloids are used as a model for atomic systems as increased lengthscales and slowed down kinetics provide means for new experimental insights [Poo04]. Phase separation kinetics, capillary waves of crystallization processes can be resolved almost at a single particle level. In this sense, the present and further studies of colloidal films via indentation might aid the understanding of plasticity in atomic matter in terms of shear bands or other cooperative reorganization processes of the atoms under applied stress [Pha06, Sch03c].

### 5.5.2. Further insight into microscopic processes

Confocal microscopy and single particle tracking were essential tools to uncover the average strain field and helped to define the material properties. Though, the microscopic reorganization processes could not be enlightened in detail. Only the dependency of hardness and elastic modules on the bond strengths or the particulate structure allowed for some vague statements about the relative importance of different types of bond and particle deformations. Yet, the resolution limits in particle coordinates were not the only reason for this lack of information. Bare particle coordinates and translative displacements are simply insufficient to determine bond yield stresses or distinct between rolling and sliding motions of particles. The following two ways out will be applied in future work.

It has already been proven that the discrete element method is a suitable method for the simulation of granular matter [Cun79, Oda00]. In this algorithm the Newtonian equation of motion is solved numerically for each individual particle as it is subject to different acting forces. Beside to central inter-particle (electrostatic, van der Waals, depletion) and friction forces, solid bridges between the particles can be implemented which makes this method very versatile. A comparison of the experimental results with a simulation of the indentation process will give further insight into the microscopic properties of the colloidal aggregates.

A different route to characterize particle reorganizations relies on the usage of specialized particles and microscopic imaging techniques in order to obtain more detailed information about the single particle motions. Hollow spheres can be utilized as local force sensors [Zha09] and anisotropic labeled particles reveal rotational motions [Rot11a] if the probe beam of the confocal microscope is polarized. In the following chapter we will go into detail on these new techniques.



## 6. Deformation and rotation of single particles

In the majority of studies on the mechanical behavior of colloidal and granular matter experiments quantify the macroscopic material properties. In combination with theoretical models and simulations these experimental results lead to conclusions on the microscopic particle interactions and dynamics. While this procedure often worked successfully like *e. g.* in case of the investigation of the colloidal glass transition with the help of mode coupling theory there are also scenarios where the insight into the microscopic processes is limited. The nanoindentation on colloidal aggregates and the unclear microscopic particle reorganizations in the preceding chapter is one example.

Recently, several experimental methods have been developed in order to pursue the opposite approach and directly investigate the behavior of single particles. In particular measurements of the forces that act on the particle have been of interest. In force spectroscopy micrometer-sized particles were glued to micro-cantilevers with a known spring constant. In doing so adhesion [Hei05, Hei99] and frictional [Tyk07] forces acting on the particle could be measured by means of the restoring force generated by the deflection of the cantilever. In a similar manner optical tweezers were used to trap single particles in a well defined attractive potential. By adjusting the strength of this potential other forces acting on the particle can be balanced and thus quantified [Ash70, Gri97]. These methods are well suited for single or at least a limited number of particles and therefore are used for a general characterization of particle interactions.

However, the distribution and transmission of forces in aggregates is inaccessible. In kinetically arrested systems movements are largely suppressed because acting forces nearly cancel out [Cat98]. Colloidal gels only slowly rearrange [Cat98] and may collapse with time [Wee00b] or under external forces [Var01]. If such systems are further compressed the loading force is heterogeneously transmitted through the particle contacts along so called force chains [Ast02]. This process has been simulated [Kad09] and studied experimentally in case of 2D granular systems, *e. g.* using materials that show stress-induced birefringence [Liu95]. However, smaller particles and 3D samples are inaccessible with this method. Another approach uses soft particles that deform under external forces [Bru03]. In other words it is not a cantilever or an optical trap but the particle itself which is used to quantify the acting forces on basis of the deformation of the particle. From a practical point of view, in particular hollow spheres are suitable, since their elastic constants can be tuned by the shell thickness and choice of materials [Zha09, Fer07]. Here we present a method to automatically determine 3D coordinates as well as the deformation state of such hollow particles from confocal images. The analysis is based on the already existing algorithm to locate fully labeled spheres by Crocker, Grier

[Cro96] and Weeks [Wee00a].

In case of non-vanishing forces reorganization of the local particle structure occur. Bare 3D coordinates however are not sufficient to fully describe the involved processes. Rolling particles cannot be distinguished from those that sliding past each other [Aga08]. Clearly frictional forces between particles in contact are essential in this question. Unfortunately, conventional confocal microscopy cannot distinguish between rolling and sliding particles because both processes manifest in translational motions in the confocal images. Only additional information about the rotational state of the particles will resolve this ambiguity and help to answer basic questions like: Can rotation be enforced for rough or irregularly shaped particles? How do particle-particle interactions influence rolling and sliding?

Rotational movements have been studied experimentally for anisotropically shaped particles or groups of bound particles. [Hon06] However, such grouped particles are hardly recognizable in dense suspensions. In addition, this approach immediately limits the choice of particle shapes. In particular spherical particles cannot be used. A possibility to solve this problem are particles with anisotropic optical properties. Spatial variations of fluorescent dye concentrations or incomplete metal coatings on homogeneously labeled particles [Ant06] are directly reflected in the microscopic images and thus can be used to determine the rotational state of the particle. However, at the same time such variations lead to inevitable complications in the localization of the particles.

In order to circumvent this problem, we induce an anisotropy in the orientational distribution of the chromophores embedded in the particle. This is done by selectively bleaching chromophores with specific orientations to non-fluorescent states. If imaged with the confocal microscope the anisotropy leads to a total fluorescence intensity that depends on the rotational state of these particles. The same bleaching approach was used in (polarized) fluorescence after photobleaching [(p)FRAP] [Rig84] for the investigation of the rotational diffusion of large particle ensembles in solution [Let04] and the incorporation of dye molecules in membranes [Smi81, Arb06]. It relies on the effect, that chromophores preferentially absorb and emit light of specific polarization [Zan99].

We introduce two new methods to get mechanical information of colloidal systems on a single particle level via confocal microscopy. Hollow spheres are used to sense local forces. Rotational motions are accessible via optically anisotropic particles. The chapter is organized as follows. The first part presents the deformation analysis of hollow particles. After discussing the special case of localizing hollow particles we introduce the algorithms for extracting the orientation and deformation state of these particles. The method is tested for a sample data set. In the second part we describe the rotation analysis, beginning with the preparation of anisotropically bleached particles. We present a theoretical calculation of the expected fluorescence intensity variations when these particles rotate and compare this modeling with experimental results.



## 6.1. Deformation analysis of hollow spheres

The deformation analysis of hollow spheres comprises the localization of the individual particles, the determination of their orientations and finally their deformation state. Due to the

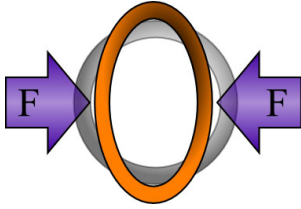


**Fig. 6.1.:** Deformation of a hollow sphere upon an uniaxial Force  $F$ .

large number of particles it is essential that each step is carried out automatically by a computer without any human interaction required. The algorithm relies on the assumption that the spheres are deformed as a whole resulting in a roughly ellipsoidal shape. So, in particular strong localized buckling or fracture of the particle cannot be handled which can be prevented by choosing suitable particle materials and shell thicknesses. In the following we will describe the different stages of the analysis and demonstrate the performance of the used algorithms by means of sample data sets and computer simulations.

### 6.1.1. Sample preparation

The sample data are 3D confocal images of a suspension of partially sedimented core-shell particles obtained with the home-made confocal microscope described in section 2.1.2. The non-labeled polystyrene (PS) template particles ( $1.97\ \mu\text{m}$  in diameter and a polydispersity of 5%) were coated with a 60 nm silica shell [Zha09]. Rhodamine B was covalently incorporated only into the silica matrix. The particles were dispersed without any further surface modification in a modified PDMS melt (Laser liquid<sup>TM</sup> with defined refractive index of  $n = 1.5780 \pm 0.0002$ , Cargille Laboratories) to match the refractive index of PS.

We did not use real hollow spheres for a number of reasons. At first, the confocal representation of the core-shell particles is identical to that of hollow particles as can be seen in the exemplary image of Fig. 6.2 (b). Second, the synthesis of hollow particles and the preparation of the suspension is rather complicated compared to core-shell particles. At last we want to preserve the spherical shape of the test particles which is only guaranteed for rigid particle cores. In this case the expected outcome of the deformation analysis is clearly defined. Hollow particle on the other side might already be partially deformed due to interactions present in the system or the sample preparation. These influences, however, are hard to estimate and therefore should be avoided during the testing of the analysis.

Beside to the confocal data of perfectly spherical particles the analysis needs to be verified for particles with a fixed and well-known deformation and orientation. Therefore, not the particles but rather the 3D confocal image was deformed and rotated. In doing so the stretching ratios and rotation angles can be easily compared to the results of the analysis.

### 6.1.2. Localization of hollow particles

The localization of the hollow particles, *i. e.* the determination of their 3D coordinates, is the first step of the deformation analysis. The used method is adopted from the algorithm

by Crocker, Grier and Weeks to localize homogeneously labeled particles which was already described in section 2.1.3: After an initial spatial filtering by means of a 3D convolution with a Gaussian distribution the confocal data is scanned for local intensity maxima that are identified with the particles. The Gaussian distribution is used to mimic the intensity distribution of homogeneously labeled particles in the confocal images. By analogy, in order to process the confocal data of hollow particles, the Gaussian distribution is replaced by a mask distribution  $g_{\text{mask}}$  that resembles the intensity distribution of a hollow sphere.

As an example of the general performance of this modified convolution we present in Fig. 6.2 (b) a  $64 \times 64$  pixel<sup>2</sup> sized subsection of a xy-slice of a complete 3D data set. The intensity mask  $g_{\text{mask}}$  in Fig. 6.2 (a) was modeled according to the appearance of the particles in the image. The convolution intensity  $C$  in Fig. 6.2 (c) shows well separated maxima at the positions of the hollow sphere that can be easily localized. Two aspects are worth mentioning: An additional mask normalization according to equation (2.12) and a restriction to positive convolution intensities effectively reduced the background. Second, the maxima in the convolved image are sharp with extensions comparable to the thickness of the particle shells in the original image. This becomes more obvious when looking at the intersections in Fig. 6.2 (c)

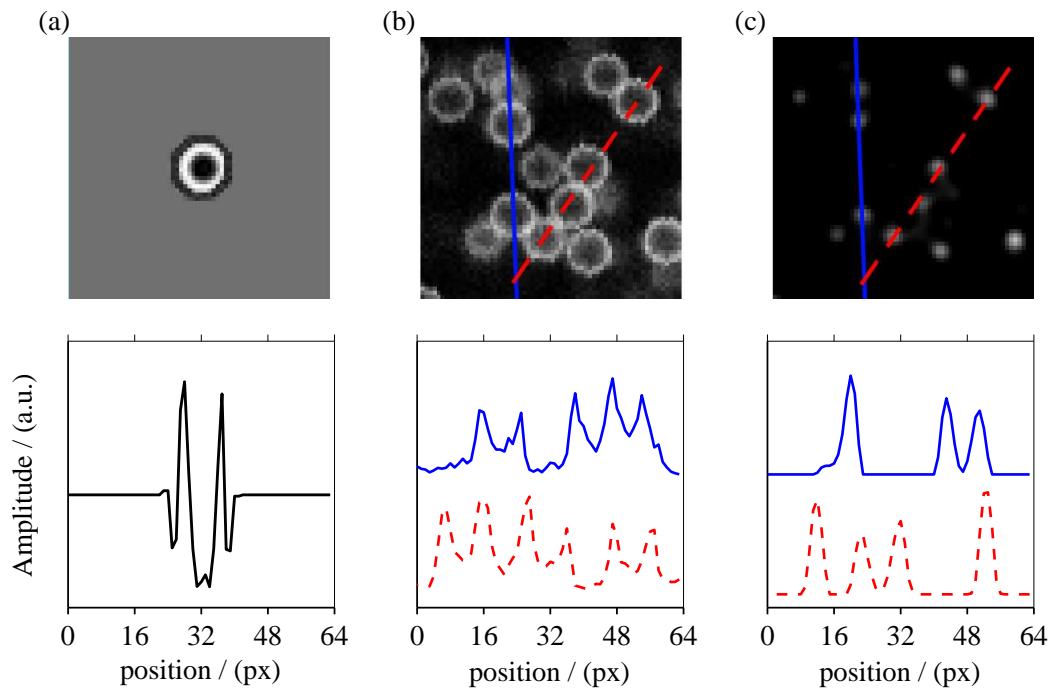


**Fig. 6.2.:** xy-slices of the hollow sphere mask (a), raw  $I_d$  (b) and convolved  $C$  (c) 3D fluorescence intensity of hollow spheres. The intensity scale is linear and in arbitrary units. The asymmetry in the line profile of the mask is caused by the finite spatial resolution that was adapted from the real data. The line profiles in the lower part of the images represent cross sections through the images. Even small deviations of the line from the center of the particle lead to significant reduction of the convolution intensity for both, lateral (x,y) and vertical (z) directions. Hence, separation distances are large in the convolved data and positioning is easy and reliable. For the given combination of materials and refractive index matching, spatial resolution, background level and optical artifacts in (b) are representative for confocal images.

that do not cross all particles perfectly in the middle plane. Already small lateral (x,y) and/or vertical (z) deviations from the center lead to a significant reduction of convolution intensity. Moreover, the convolution implicates a local averaging which is why the profiles in Fig. 6.2 (c) show less noise compared to the original data. This smoothness aids the subsequent localization process.

Any variation of the measured intensity distribution to the modeled mask profile  $g_{\text{mask}}$  gives rise to a broadened and distorted convolution signal. If the deviations, *e. g.* in particle size, are too large the maximum of the convolution intensity is no longer located in the center of the particle but still has the shape of a hollow object. This is shown in the right part of Fig. 6.3 (a) for computer simulated data. However, for relative variations in the extensions of test particle  $R_p$  and mask  $R_m$  below 25 % a localization is still possible. This is also true if the particles are no longer spherical but rather are deformed to ellipsoids. In this case the broadening does mainly affect those directions where a deformation actually is present. In directions for which mask and real particles image have the same extension the extension of the convolution intensity is minimal as can be seen in the right part of Fig. 6.3 (b) for  $A = 1.28$ . This directional broadening can be used to determine the orientation of deformed particles and thus the direction of the forces acting on the particle.

Before we proceed we shortly comment on the computational implementation of the localization algorithm. Although a fast implementation of the algorithm was already available in IDL and Matlab computing languages, the code for the 3D-convolution was rewritten in IDL using 3D-fast fourier transform (FFT) methods. The original implementation can only cope with Gaussian intensity profiles since the 3D convolution is separated into three individual one-dimensional calculations. This limitation is removed for a 3D calculation and thusly arbitrary mask distributions can be used. Yet, the 3D calculation demands for increased memory capacities and therefore is limited to smaller data sets. However, the total computation time does not change significantly if the whole 3D data set is split up into sufficiently small fractions to reduce memory occupation. The coordinate data is recombined after processing each sub-image separately. The part of the implementation for the final localization of the particles was not changed.

### 6.1.3. Main axes of deformation

We extract the orientation of the deformed particle from its representation in the convolved image. As we already mentioned above any discrepancy of the measured intensity distribution and the mask distribution causes a broadening of the convolved intensity  $C$ . This broadening can be quantified in terms of the intensity weighted inertia tensor  $\Theta$  with the components

$$(\Theta)_{ab} \equiv \Theta_{ab} = \frac{1}{\sum_p C_p} \cdot \sum_p C_p \cdot (a_p - \bar{a}) \cdot (b_p - \bar{b}) \quad (6.1)$$

with  $a, b$  being one of the directions  $x, y, z$  and  $\bar{a}, \bar{b}$  as the intensity weighted mean positions.

$$\bar{a} = \frac{1}{\sum_p C_p} \cdot \sum_p C_p \cdot a_p \quad (6.2)$$

The summations extends over all pixels  $p = (i, j, k)$  whose convolution intensity  $C_p$  exceeds a pre-defined threshold value and lies in the region where the particle is localized. The definition of  $\Theta_{ab}$  is analogous to the definition of the inertia tensor in classical mechanics with the mass replaced by the convolved intensity. By definition  $\Theta_{ab}$  is a symmetric matrix that can be transformed to its diagonal form  $\Theta'_{ab}$ . The principal axes  $\hat{u}_m$  ( $m = 1, 2, 3$ ) obtained from this mathematical procedure can be directly identified with the major axes of the ellipsoid [Gol80] and thus define the orientation of the deformed hollow particle.

Yet this procedure relies on the fact that the particle deformation is unambiguously transferred into the broadening of the convolution signal. This is not always the case as it is shown in Fig. 6.3 (a) for the above mentioned variation of the particle radius  $R_p$  at a fixed mask radius  $R_m$ . Since the particles are still spherical in the convolved image [see right in Fig. 6.3a)]  $\Theta_{ab}$  is already diagonal with equal elements  $\Theta_{xx}$ ,  $\Theta_{yy}$  and  $\Theta_{zz}$ . We normalize these components to the corresponding tensor element  $\Theta_{\alpha\alpha}^{\text{mask}}$  when replacing  $C_p$  by  $g_{\text{mask}}$  in equation (6.1):

$$\Theta'_{\text{norm}} = \frac{\Theta_{\alpha\alpha}}{\Theta_{\alpha\alpha}^{\text{mask}}} \quad (6.3)$$

At first this normalization quantifies the sharpening of the particle representation when switching from the confocal raw data to the convolved intensity.  $\Theta'_{\text{norm}}$  drops by one order of magnitude ending at a level of 0.1. Second,  $\Theta'_{\text{norm}}$  is minimal for  $R_p/R_m = 1$  and rises irrespective of whether the particle is smaller or larger than the mask distribution. So, a particle that is compressed in one direction and stretched in the other can also lead to a spherical convolution signal for which the orientation cannot be extracted.

This effect is demonstrated in Fig. 6.3 (b). The shape of an initially spherical particle was varied regarding its x-deformation  $\Delta x/R_p$  at a fixed compression in y-direction  $\Delta y/R_p = 0.76$ . Here  $\Delta x$  and  $\Delta y$  denote the particle extensions in x and y direction, respectively. After the calculation of  $\Theta_{ab}$  the ratio  $\Theta_{xx}/\Theta_{yy}$  gives a measure of this eccentricity of the convolution intensity. If the eccentricity deviates from 1 the particle orientation can be determined. The mask distribution was chosen to exactly fit the original particle size  $R_p/R_m = 1$ . As expected  $\Theta_{xx}/\Theta_{yy}$  equals 1 for identical deformations  $\Delta x/R_p = \Delta y/R_p = 0.76$ . But for a x-deformation of about  $\Delta x/R_p = 1.12$  corresponding to an aspect ratio of  $A = \Delta x/\Delta y = 1.5$  the tensor elements even out again. Hence, no orientation can be extracted from the convolved image although it is clearly visible in the initial image [see right in Fig. 6.3b)].

In order to resolve this ambiguity the mask distribution properties can be chosen to on purpose mismatch the particle properties. This was tested in Fig. 6.3b) for a size mismatch of  $R_p/R_m = 1.14$ , again at a constant deformation  $\Delta y/R_p = 0.8$ . For this particular set of parameters the eccentricity  $\Theta_{xx}/\Theta_{yy}$  rises monotonically with increasing x-deformation allowing for an unambiguous determination of the particle orientation. As a rule of thumb

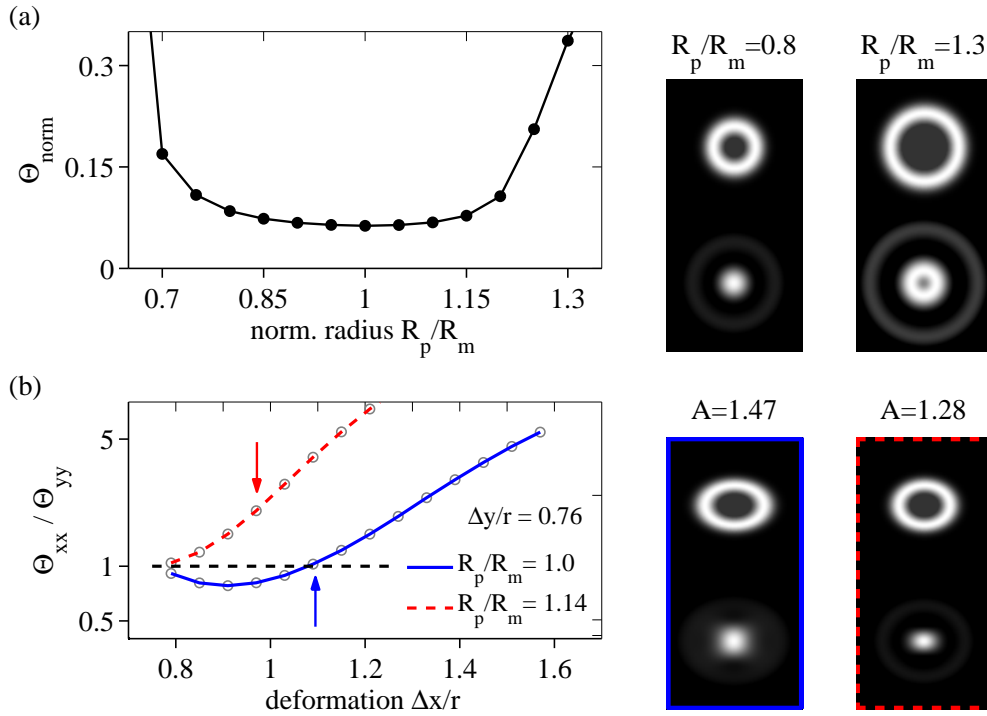


**Fig. 6.3.:** (a) Deviations in the particle extension of the measured intensity  $R_p$  and the modeled mask  $R_m$  lead to a broadening of the convolved image which is equivalent to an increase of  $\Theta_{\text{norm}}$  (see text for the definition). Two xy-slices of the computer generated 3D particle images (top) and the convolution (bottom) are shown on the right. If the relative deviation is too large  $R_p/R_m \geq 1.25$  the convolved intensity is no longer maximal in the center but shows a local minimum. (b) Deformed hollow particles appear as filled ellipses in the convolved image. The eccentricity of these ellipses is quantified by  $\Theta_{xx}/\Theta_{yy}$ . This ratio is shown for varying deformations  $\Delta x/R_p$  in x-direction at a constant deformation in y-direction  $\Delta y/R_p$ . For matching mask and particle distributions  $R_p/R_m = 1$ ,  $\Theta_{xx}/\Theta_{yy}$  does not increase monotonously with increasing aspect ratio  $A = \Delta x/\Delta y$ . This ambiguity can be resolved via a mismatch  $R_p/R_m \neq 1$ . The arrows indicate parameter configuration for which real (top) and convolved (bottom) images are shown on the right.

the mask extension should be reduced to the smallest extension of the deformed particles. A variation of other mask distribution properties like the shell thickness alters the slope of the curves in Fig. 6.3 (b) and hence may be used to adjust the sensitivity in aspect ratios.

In summary, an orientation analysis is possible for moderate deformations. Although the actual numbers depend on the confocal resolution, spatial sampling rate and particle properties, variations in the aspect ratio and deformation of up to 25% can be handled without any restriction.

#### 6.1.4. Particle extensions along principal directions

Once the orientation of the deformed particle is known the actual deformation along the principal axes can be extracted. However, this cannot be done on basis of the diagonal tensor elements  $\Theta'_{aa}$  because these quantities are mathematically not fully decoupled. Instead the deformation is measured from the original confocal images (Fig. 6.4). The projection of the

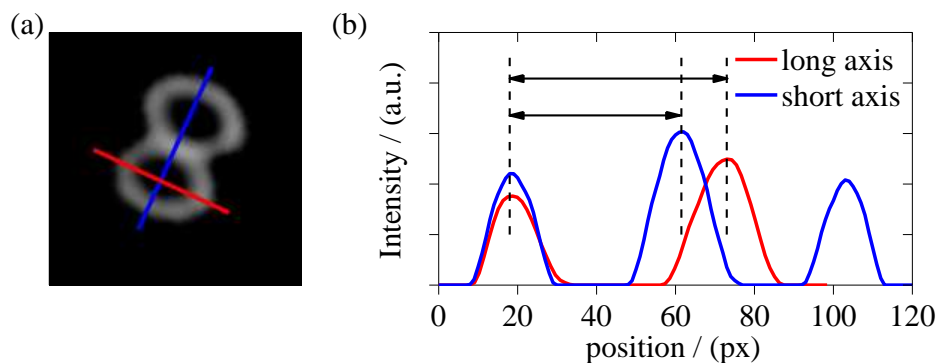


**Fig. 6.4.:** (a) XY-Slice of an exemplary confocal image showing two touching hollow particles. The principal axes of deformation are indicated by red and blue lines. (b) The line profiles show distinct maxima that are used to define the extension of the particle along the principal axes. The asymmetry of the particles is clearly visible.

intensity distribution along each of the principal axes shows two distinct maxima resulting from the particle shell. The separation distance of these two maxima is a direct measure of the particle extension and also its deformation.

### 6.1.5. Sample data set

The complete orientation and deformation analysis was tested for a real confocal data set of undeformed spheres. More than 99% of all particles, about 1000 in total, were located with a sub-pixel accuracy ( $\leq 5\%$  of radius). After extraction of the principal axes of  $\Theta$  the particles extensions were measured in the original unfiltered image giving the same mean value for all three directions [see Fig. 6.5a)] as it is expected for spherical particles. Beside the particle extensions the orientations of the principal axes was tested. Each of the three principal axes  $\hat{u}_m$  was assigned to the axes of the laboratory frame  $\hat{e}_a$  with a maximal projection  $|\hat{u}_m \cdot \hat{e}_a|$ . In this sense the projection is a measure of the orientational correlation of the principal axes and the laboratory frame. Due to the explicit assignment of axes the projection cannot drop below  $1/\sqrt{3} \approx 0.58$ . Moreover, the distribution of the projections is expected to be flat since there is no preferential direction for the principle axes. Indeed the experimental distribution in the inset in Fig. 6.5a) is rather flat and its average value compares reasonably well the theoretical value of 0.83.

In order to test the performance of the algorithm for a known deformation and rotation the same data set was stretched along the x- and y-direction with ratios of  $\Delta x/r = 1.15$  and  $\Delta y/r = 1.3$ , respectively. Additionally, the data set was rotated to exclude a possible influence of the choice of the laboratory system. In the statistical analysis the stretching ratios were reproduced and the principal axes aligned with the axes of the rotated coordinates system giving a maximum in the histogram of the projections at 1 [Fig. 6.5 (b)].

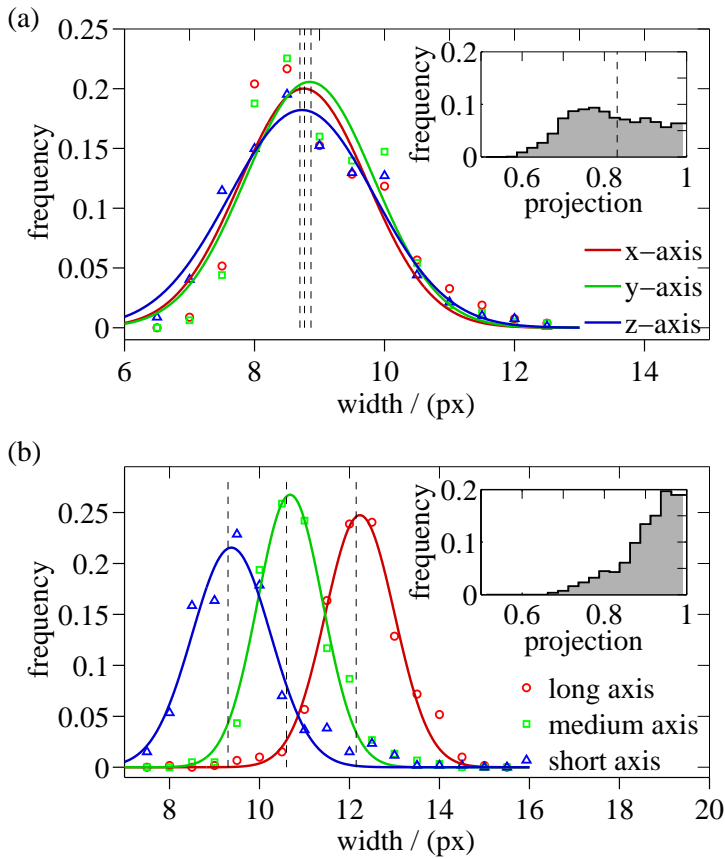


**Fig. 6.5.:** (a) Normalized distribution of particle extensions for spherical particles. The extracted principal axes lead to identical mean particle extensions (dashed lines). As expected the orientational correlation with the outer coordinate system is flat and is centered around the theoretical value of 0.83 (dashed line in the inset). (b) The analysis of the stretched and rotated data set reproduced the stretching factors of 1, 1.15 and 1.3. The main axes correlate with the rotated coordinate system axes (see inset).

### 6.1.6. General remarks

The only requirement for this analysis to work is a homogeneous fluorescence intensity across the labeled parts of the particle since  $\Theta_{ab}$  is sensitive to intensity fluctuations. That is, also fully labeled particles can be used. However, here the variations in  $\Theta_{ab}$  for deformed particles are less pronounced handicapping the analysis.

There are some potential difficulties of the analysis that arise from the finite size of the PSF (compare section 2.1.1). If the extension of the laser focus largely exceeds the thickness of the labeled shell the measured intensity in the vicinity of two adjacent particles is enhanced (Fig. 6.4). This directly affects the convolved image  $C$  as well as the calculation of  $\Theta_{ab}$ . An effective solution to this problem is to clip the maximal intensity by introducing an upper threshold. The situation is getting even worse when the shell thickness is comparable to the size of the PSF. In this case the shells of two adjacent particles merge in the confocal images and the determination of the particle extension after the orientation analysis is hindered. This case should be avoided by an appropriate choice of particle properties and spatial resolutions.

The confocal images are also distorted by the anisotropy of the PSF that is broader in  $z$ -direction compared to  $x$  and  $y$ -directions. As a consequence the particle appears blurred in  $z$ -directions. We circumvent this problem by blurring the whole 3D intensity data in  $x$ - and  $y$ -directions via an additional convolution with a suitable Gaussian distribution mimicking an equally bad resolution in  $x$ - and  $y$ -directions.

## 6.2. Rotation analysis

After the deformation analysis we present a method to quantify the rotational movement of a particle with embedded fluorescent chromophores. As discussed above it relies on the fact that the interaction of photons with chromophores in course of a fluorescence process follow an approximate dipole characteristic [Let04, Smi81]. Hence, the probability to excite the chromophore into a fluorescent state and therewith to emit a fluorescence photon depends on the polarization of the incoming laser beam and the orientation of the chromophore. However, large numbers<sup>20</sup> and random orientations of chromophores in a particle lead to negligible differences in the total fluorescence intensity for different particle orientations and probe laser beam polarizations. If, on the other side, for any reason the dipole axis of the chromophores exhibit a preferential orientation, the fluorescence intensity depends on the relative angle between probe beam polarization and the mean dipole axis. Consequently, if the incorporated chromophores are immobile, a rotating particle will show modulations in its fluorescence intensity. Vice versa, these modulations allow for a characterization of the particle rotation.

Various methods for the preparation of particles with such an anisotropic chromophore orientation exist. Here we follow the principle that is used in pFRAP-experiments (Fig. 6.6). Again the preferred absorption of light with special polarization is used to selectively bleach chromophores with parallel orientation to a non-fluorescent state. This bleaching process generates an anisotropy in the orientation distribution of remaining fluorescent chromophores. In the following we go into detail on the sample preparation and the theoretical modeling of the bleaching process as well as the expected polarization contrast in the confocal images. Afterwards we provide an experimental proof of principle.

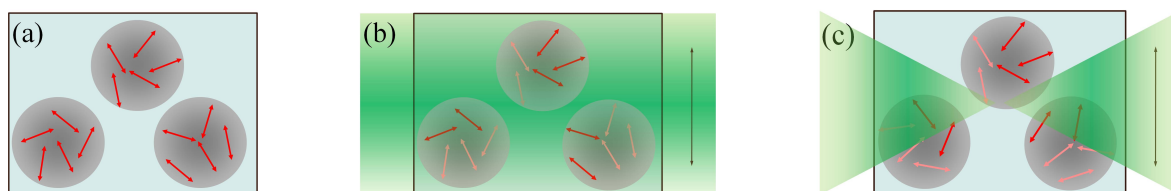


**Fig. 6.6.:** Schematic illustration of the preparation of particle with an anisotropic distribution of chromophores (red arrow: dipole axis). (a) Initially the spatial and orientational distributions of chromophores is homogeneous. As the chromophores are covalently bound to the silica matrix of the particles they do not alter their orientation and position over time. (b) An incoming parallel laser beam with a wavelength in the absorption range of the chromophores does not only induce the emission of fluorescence light but also irreversibly transforms the dye molecule into a non-fluorescent state. This bleaching process is more probable for orientations that are parallel to the polarization direction (black arrow) if a dipole interaction of the photons with the chromophores is assumed. The orientational distribution of the chromophores becomes anisotropic. (c) If the particles are now imaged with the confocal microscope the emitted intensity depends on the relative angle of the probe beam polarization and the average orientation of active chromophores.

<sup>20</sup> Assuming an moderate efficiency for the incorporation of chromophores into the particles the number of chromophores per particle is in the order of  $10^7$  molecules per particle



### 6.2.1. Sample preparation

We used silica particles with a diameter of 780 nm (polydispersity of 10 %) that were synthesized according to the Stöber method in the presence of Rhodamine B. The dye molecules and thus also the chromophores were covalently bound to the silica matrix [Ver94] and thus did not show a significant reorientation with time.<sup>21</sup> Due to the stepwise growth of the particle the chromophores are incorporated only in the core of the particles while the shell is unlabeled (see also appendix C). The particles were dried in a observation cell made of glass and infiltrated with refractive index matching mixture of glycerol and water. The system was sealed with UV-curing glue to prevent evaporation.

### 6.2.2. Preparation of orientation anisotropic particles via selective bleaching and theoretical polarization contrast

Assuming an isotropic orientation of chromophores before the bleaching process [Fig. 6.6 (a)] the absorption dipole moment<sup>22</sup> follows the normalized distribution

$$\vec{\mu}_A^{\text{init}}(\vartheta, \phi) = \frac{\mu_A \hat{e}_r}{4\pi \sin(\vartheta)} = \frac{\mu_A}{4\pi \sin(\vartheta)} \begin{bmatrix} \cos(\phi) \sin(\vartheta) \\ \sin(\phi) \sin(\vartheta) \\ \cos(\vartheta) \end{bmatrix} \quad (6.4)$$

with  $\mu_A$  denoting the absolute absorption dipole moment and  $\vartheta$  and  $\phi$  polar and azimuthal angles. In the presence of the electric field

$$\vec{E}_B = E_B \begin{bmatrix} 1 \\ 0 \\ 0 \end{bmatrix} \exp[i(\omega t - k z)] \quad (6.5)$$

of a linearly polarized laser beam<sup>23</sup> the probability of one molecule to be optically excited is proportional to  $|\vec{\mu}_A \cdot \vec{E}_B|^2$  [Let04]. This relation is not only valid for the absorption of photons but also for the bleaching of chromophores if a single photon process is involved<sup>24</sup>. So, the laser beam bleaches predominantly those molecules with orientations parallel to the beam polarization [Fig. 6.6 (b)]. Moreover, if the bleaching is irreversible the number of chromophores decays exponentially resulting in an anisotropic distribution

$$\vec{\mu}_A^{\text{bleach}}(\vartheta, \phi, a) = \vec{\mu}_A^{\text{init}}(\vartheta, \phi) \exp[-a(E_B, \mu_A) \cos(\phi)] \quad (6.6)$$

<sup>21</sup>Chromophores that were incorporated into polymeric particles by swelling with a co-solvent cannot be regarded as immobile. Therefore such kind of particles are not suitable for the rotation analysis.

<sup>22</sup>We omit any dependencies on the spatial distribution of chromophores within the particles

<sup>23</sup>Without restricting generality the polarization of  $\vec{E}_B$  was set parallel to the x-direction with a propagation direction of the laser beam along the z-axis

<sup>24</sup>In most cases the exact bleaching mechanism is not understood [Ton03]. It can be a transition into a metastable non-fluorescent electronic state or a photon-induced chemical conversion of the chromophore. If multi-photon processes are involved the theoretical modeling is more complicated and strongly depends on the incident laser intensity.

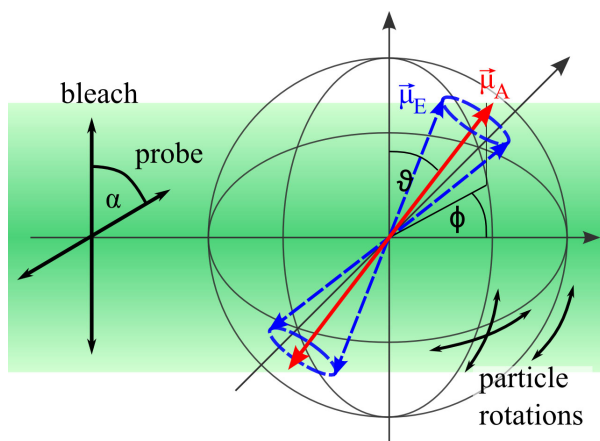


**Fig. 6.7.:** Bleaching geometry: The polarizations of bleach and probe beam enclose an angle  $\alpha$ . The orientation of the absorption dipole  $\vec{\mu}_A$  of the chromophore is homogeneously distributed on the unit sphere parametrized by polar  $\vartheta$  and azimuthal  $\phi$  angles. The emission dipole  $\vec{\mu}_E$  encloses a constant angle with  $\vec{\mu}_A$  that depends on the chromophore. Therefore, all possible orientations of  $\vec{\mu}_E$  lie on a cone around  $\vec{\mu}_A$ .

The proportionality constant  $a$  will be regarded as the bleaching strength and is a linear function in  $\mu_A^2$ ,  $E_B^2$  and the irradiation time  $t$ .

During the subsequent confocal imaging with a probe laser beam

$$\vec{E}_P(\alpha) = E_P \begin{bmatrix} \cos(\alpha) \\ \sin(\alpha) \\ 0 \end{bmatrix} \exp[i(\omega t - k z)] \quad (6.7)$$

[Fig. 6.6 (c)], enclosing an angle  $\alpha$  to the polarization of the bleach beam  $\vec{E}_B$ , the emitted fluorescence intensity is proportional to

$$I_f(a) \sim \int_0^{2\pi} \int_0^\pi |\vec{\mu}_A^{\text{bleach}}(\vartheta, \phi, a) \cdot \vec{E}_P(\alpha)|^2 \sin(\vartheta) d\vartheta d\phi \quad (6.8)$$

In the experimental realization the probe beam polarization was adjusted by a polarizer that was placed between the dichroic mirror and the scanning unit in the confocal microscope (compare section 2.1.2). Since the excitation and collected fluorescence light share the same optical path in this part of the setup the fluorescence intensity in (6.8) is modified by an additional factor  $|\vec{\mu}_E(\vartheta, \phi) \cdot \vec{E}_P|^2$  whereas  $\vec{\mu}_E$  denotes the direction of the emission dipole of the chromophore.  $\vec{\mu}_E$  and  $\vec{\mu}_A$  are not necessarily parallel. In case of Rhodamine-B both vectors enclose an angle of about  $23^\circ$  [Bee72]. This restricts the number of possible orientations of  $\vec{\mu}_E$  to a cone about  $\vec{\mu}_A$  (Fig. 6.7) which is taken into account by an additional integration:

$$I_f(a, \alpha) \sim \int_0^{2\pi} \int_0^\pi \left[ |\vec{\mu}_A^B(\vartheta, \phi, a) \cdot \vec{E}_P(\alpha)|^2 \cdot \int_0^{2\pi} \left[ |\mathbf{R}(\vartheta, \phi) \vec{\mu}_A^{\text{init}}(23^\circ, \psi) \cdot \vec{E}_P(\alpha)|^2 d\psi \right] \sin(\vartheta) d\vartheta d\phi \quad (6.9)$$

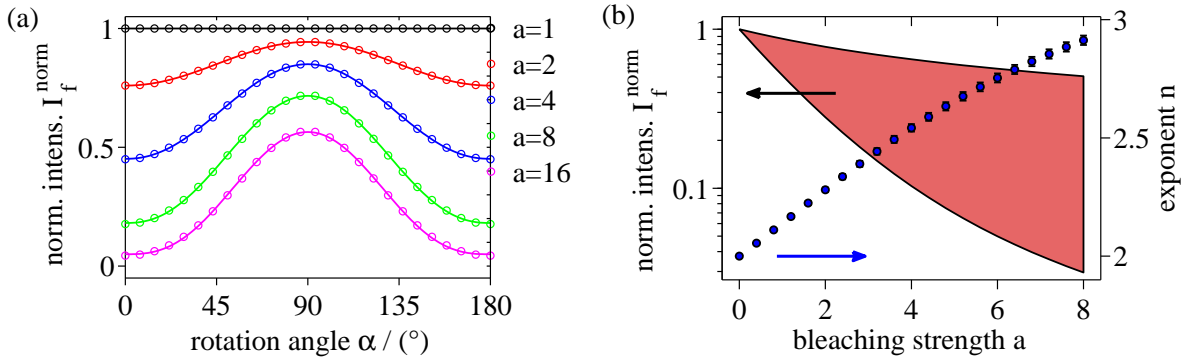


**Fig. 6.8.:** (a) Simulated ratio of the fluorescence intensity  $I_B/I_{NB}$  of bleached and non-bleached particles as a function of the relative angle between the polarizations of bleach and probe beam for various bleaching strengths  $a$ . The data was fitted by a biased  $\text{abs}[\sin(\alpha)]^n$  dependency. (b) With increasing bleaching strengths  $a$  the polarization contrast  $I_B(90^\circ)/I_B(0^\circ)$  increased strongly (red shaded area) whereas the exponent  $n$  varied moderately.

with the combined rotation matrix

$$(\mathbf{R}(\vartheta, \phi))_{\alpha\beta} = \begin{bmatrix} \cos(\vartheta) & 0 & -\sin(\vartheta) \\ 0 & 1 & 0 \\ \sin(\vartheta) & 0 & \cos(\vartheta) \end{bmatrix} \cdot \begin{bmatrix} \cos(\phi) & -\sin(\phi) & 0 \\ \sin(\phi) & \cos(\phi) & 0 \\ 0 & 0 & 1 \end{bmatrix} \quad (6.10)$$

The results of this calculation are illustrated in Fig. 6.8 (a) in dependency on the bleaching strength  $a$  and the relative polarization angle  $\alpha$ . The fluorescence intensity normalized to the initial state before bleaching could be fitted by

$$I_f^{\text{norm}}(a, \alpha) = \frac{I_f(a, \alpha)}{I_f(0, 0)} = I_o - \Delta I \cdot \text{abs}[\sin(\alpha)]^n \quad (6.11)$$

The variation of the fit parameters are depicted in Fig. 6.8 (b). Whereas the exponent  $n$  varies moderately and is of minor interest, the fluorescence intensity contrast  $\Delta I = I_f^{\text{norm}}(a, 0^\circ) - I_f^{\text{norm}}(a, 90^\circ)$  between bleached and non-bleached orientations needs to be optimized by choosing an appropriate bleaching strength  $a$ . If  $a$  is too small  $\Delta I$  is small and the resolution in the particle rotation is bad. On the other side, if  $a$  is too large the fluorescence intensity in the bleached orientation is too small to localize the particle in the confocal image.

### 6.2.3. Experimental verification

Instead of rotating particles we demonstrate the usability of this approach by changing the relative polarization of bleaching and probe beam for immobilized particles. Bleaching and confocal imaging was done with the same laser beam enabling for an easy control of the bleaching strength. After selecting a suitable sample area with about 500 particles a fraction of the particles were bleached to a level of about 30% of the initial fluorescence intensity equivalent to a total energy dose of  $0.16 \mu\text{J}/\text{particle}$  (Fig. 6.9). After bleaching the laser intensity was reduced to prevent further significant bleaching during imaging of the sample. Fig. 6.10

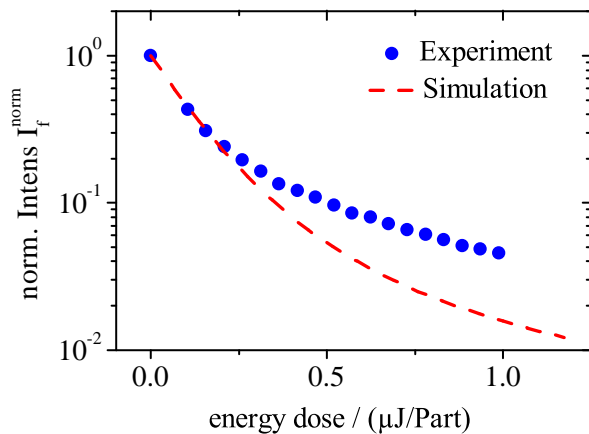


**Fig. 6.9.:** For the given particles an energy dose of about  $0.5 \mu\text{J}/\text{particle}$  is required to reduce the fluorescence intensity by a factor of 10. The experimental data coincide with the simulation only for low doses.

compares confocal images of the unbleached particles alone and in relation to the bleached particles under relative polarization angles  $\alpha$  of  $0^\circ$  and  $90^\circ$ . The differences in the fluorescence intensity are clearly visible.

Beside to these two extreme values 3D confocal images were taken for various relative polarization angles. From each image the position and total fluorescence intensity of each bleached particle was extracted and averaged (Fig. 6.11). The fluorescence contrast  $\Delta I$  amounted to about 40% and the functional dependency on  $\alpha$  could be fitted to equation (6.11) when fixing the exponent to  $n = 2$ .

Although the theoretical modeling disregards the strong focusing of bleach and probe laser beam by the objective the dependency on  $\alpha$  is reasonably well described. The large statistical scatter in the relative intensities might be an indication of this discrepancy to the model as the divergence of the beam tends to blur the bleaching contrast. More pronounced differences between experiment and simulation were observed for the reduction of fluorescence intensity in dependency on the deposited energy dose per particle that is assumed to be proportional

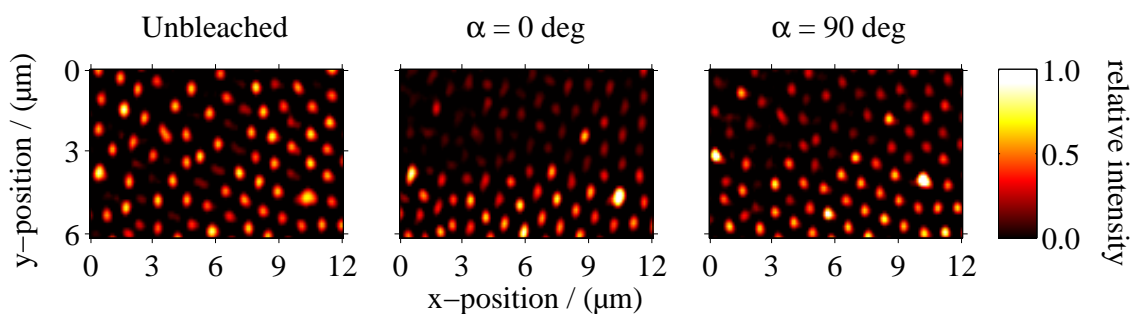
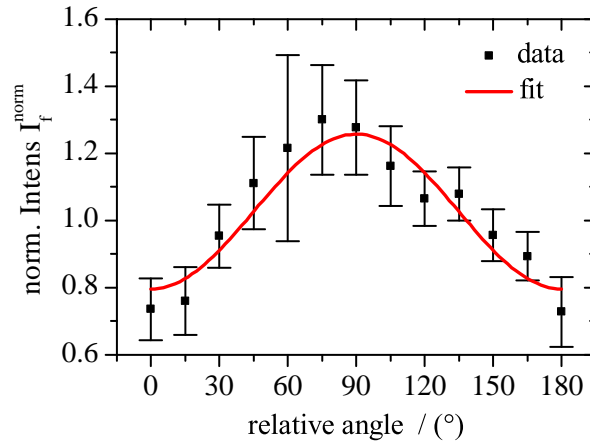


**Fig. 6.10.:** Spatially filtered confocal images of a single layer of silica core-shell particles. Before bleaching the measured fluorescence intensity per particle was constant. After bleaching the particles in the upper part of the image the intensity of these particles dropped down by a factor of about 5 compared to unbleached particles. After changing the relative angle between the polarizations of bleach and probe beam from  $\alpha = 0^\circ$  to  $\alpha = 90^\circ$  the detected intensity contrast to the unbleached particles decreased.

**Fig. 6.11.:** Rotation of the laser polarization leads to a variation of the fluorescence intensity that can be fitted by a  $\sin^2$  behavior. The intensity is normalized to the average intensity for all angles.



to the bleaching strength in Fig. 6.9. Though, the quality of this data might also be limited due to the finite detection threshold for fluorescence intensity in our set-up.

#### 6.2.4. General remarks

A parallel bleach beam is certainly more advantageous than a focused bleach beam as variations in the bleach polarization are minimal and thus the bleaching process is optimized. However, the energy density in the laser focus exceeds that of a wide parallel laser beam by a factor of roughly  $5 \cdot 10^8$ .<sup>25</sup> Consequently, bleaching takes long time and even an enhancement of the overall laser power from  $20 \mu\text{W}$  in the confocal microscope to  $20 \text{mW}$  for the wide beam cannot compensate the mismatch in the energy densities. Hence, the particles need to be immobilized during the bleaching procedure and redispersed afterwards. As we have shown such cumbersome procedures can be avoided by selectively bleaching smaller groups of particle with a focused beam. Moreover, the bleaching progress can be directly monitored.

One major drawback of the presented method is that the rotation state cannot be defined unambiguously. While rotations around the bleaching direction do not result in a variation of the fluorescence intensity at all rotations around the two orthogonal axes cannot be distinguished (Fig. 6.7). Other methods to resolve particle rotations also struggle with this problem and eventually solve it by introducing an particle shape anisotropy [Hon06]. In our case incorporation of a second type of chromophore that is sensitive to another laser wavelength and bleached in a perpendicular direction to the first type immediately resolves this ambiguity.

### 6.3. Conclusions

We have shown that fluorescent confocal microscopy cannot only be used to obtain 3D coordinates of a particle but at the same time can deliver information about its deformation and rotation. This can be done on a single particle level in a fully automated procedure. There are few mandatory demands on the particles. Hollow particles are in particular suitable for the deformation analysis as they provide a moderate compliance that allow for a reasonable

<sup>25</sup> Assuming an diffraction limited focus of  $250 \text{nm}$  in diameter and an width of  $1 \text{mm}$  for the unfocused beam

level of deformation. In case of the rotation analysis the chromophores must be homogeneously distributed in the particles and most importantly immobile. Besides, the algorithms work for confocal images with standard resolution and quality and are easily adaptable because of their simple underlying principles.

As an example, hollow spheres might be replaced by particles that show pressure induced enhanced fluorescence which have been presented recently by Peter Schall and the Molecular Photonics Group at the University of Amsterdam.<sup>26</sup> These particles have the same appearance like the particles used in this study but instead of being deformed by a contact force they show a local enhancement in the fluorescence intensity when being stressed. This anisotropic intensity distribution behaves similarly to the deformed spheres as they induce an anisotropy in the filtered images that can be quantified by the intensity weighted inertia tensor.

Nevertheless, we think that hollow particles with homogeneous fluorescence are most suitable for the deformation analysis. It is worth mentioning that such particles can also be used for the rotation analysis and thus provide a chance to ultimately measure contact forces and rotations at the same time. If, in addition, the shell is thin compared to the used excitation wavelength ( $d \leq \lambda/10$ ) there is no need for exact matching of the refractive indexes of particle and solvent as scattering at the interfaces is significantly reduced. Hence, the choice of compatible materials is increased facilitating an easier sample preparation.

---

<sup>26</sup><http://staff.science.uva.nl/~pschall/Research/FluorescentProbes/fluorescentprobes.html>, 19.04.2011

## 7. Summary and final conclusions

Due to the thematic diversity of the individual chapters most of the conclusions has already been stated. Therefore, we do not want to reiterate these arguments but rather go back and evaluate our findings with respect to the basic motivation of the presented work. In a nutshell, the main objective was to investigate the rheology of arrested colloids with the emphasis on the mutual interplay of the dominant interaction mechanisms in the system, its structural characteristics and the properties of the bare particles. The choice of vastly different model systems helped to represent the diversity of colloidal systems and at the same time addressed new advances in the field. One example are colloids with an anisotropic solvent phase that attracted increasing fundamental interest because of their novel types of particle-solvent interactions. Our rheological description of colloidal-LC dispersions showed that the plastification of the particles by the LC induced a polymer-like visco-elasticity in the system. The observed pronounced temperature dependency was related to the ongoing phase separation that already led to the formation of system spanning particle network. The intense usage of colloids in industry was part of our motivation to study the non-linear rheology of colloidal films. Used as a model system for dense and stiff particle clusters our findings contribute to a better understanding of their mechanical properties and therewith might aid the improvement of fragmentation and dispersion methods.

Novel combinations of experimental methods turned out to be highly beneficial. Low strain amplitudes used in the piezo-rheometer were essential not to disturb the network formation in colloidal-LC dispersions and thus guaranteed measurements in the linear rheological regime. This condition could be further verified by the simultaneous confocal microscopy which in addition delivered structural information about the network. In the nanoindentation experiments of the colloidal films this combined structural and mechanical testing was even more important as it allowed for a proper adaption of the analysis method by Oliver and Pharr and the extraction of average mechanical quantities. Along with particle localization methods the live indentation experiments complemented these macroscopic data by the microscopic deformation field within the film. Finally, we showed that specifically designed particles can give even more detailed insights about the forces within the aggregate and the nature of the microscopic particle reorganizations.

In the end, we shortly comment on the dilemma of treating colloids microscopically as an assembly of individual, interacting particles or macroscopically as a large ensemble that can be used to define averaged quantities. Both cases reflect the attempts to model colloids in analogy to atomic systems or granular matter. Obviously, the sample volume and therewith the total number of involved particles is a deciding parameter. In case of the LC-colloidal

dispersions the sampled volume was large and the extracted shear modulus clearly represent an average macroscopic quantity of the system. In the nanoindentation experiments, however, the number of particles that contribute to the mechanical response was rather low. Still a macroscopic approach by means of continuum deformation theory was suitable to describe the average strain field. So it remains questionable at which sample volumes averaging is no longer reasonable. Although we cannot answer this question right now, we want to point out that the new micro-rheological techniques can be the starting point to further elucidate this problem. The direct measurement of the contact forces and particle rotations will help to evaluate the role of individual particle motions in the restructuring of large clusters.



# Appendix

## A. Hardware architecture and Labview interface of the combined piezo-rheometer and LSCM setup

The Labview interface for controlling the home-made piezo-rheometer and LSCM consists of six main programs `LAB_Schedule.vi`, `RHEO_Module.vi`, `TEMP_Module.vi`, `TIME_Module.vi`, `LSCM_Module.vi`, and `LCTR_Module.vi`. Their interrelation and the incorporation of the electronic hardware components are schematically shown in the flow chart of Fig. A.1. The program architecture is fully modular as only the user and `LAB_Schedule.vi` directly interacts with the other programs. `LAB_Schedule.vi` [Fig. A.1 (a)] somewhat stands apart from the other programs as it is used to control the other programs without intervention by the user. On basis of a pre-defined list and commands are subsequently assigned to the corresponding programs and executed. This allows for an automated execution of the measurements and thus for accurate control during long-time experiments. `TIME_Module.vi` is solely implemented for this automation purpose as it helps the user to adjust waiting times between the individual measurements [Fig. A.1 (b)].

`RHEO_Module.vi` is designed for the rheological measurements with the piezo-rheometer. In the container tab ‘settings’ [Fig. A.1 (f)] the user explicitly defines the important parameters of the measurement, such as the covered frequency range, the applied deformation in terms of the voltage at the waveform generator, the number of captured data points in course of a frequency or strain sweep and the numbers of oscillation periods and data points recorded by the digital oscilloscope. Various other options for managing the recording file as well as the evaluation and adjustment of the signal quality are included, too. In the tab ‘parameters and status’ [Fig. A.1 (g)] the user starts the actual measurement. Various displays give information about the current state of the measurement. After recording the excitation  $V_e(t)$  and detection  $V_d(t)$  voltages for a fixed frequency  $f$  and strain and averaging over all periods the signals are displayed in the ‘signal’ tab [Fig. A.1 (h)]. In the following the complex frequency components  $V_e(f)$  and  $V_d(f)$  of both voltages are calculated via FFT:

$$V_{e/d}(f) = \frac{1}{2\pi} \int_0^T V_{e/d}(t) \exp(i 2\pi f t) dt \quad (\text{A.1})$$

The relative amplitude and phase of these components

$$A = \frac{|V_d(f)|}{|V_e(f)|} \quad \psi = \arctan\left(\frac{\text{Im}(V_e(f))}{\text{Re}(V_e(f))}\right) - \arctan\left(\frac{\text{Im}(V_d(f))}{\text{Re}(V_d(f))}\right) \quad (\text{A.2})$$

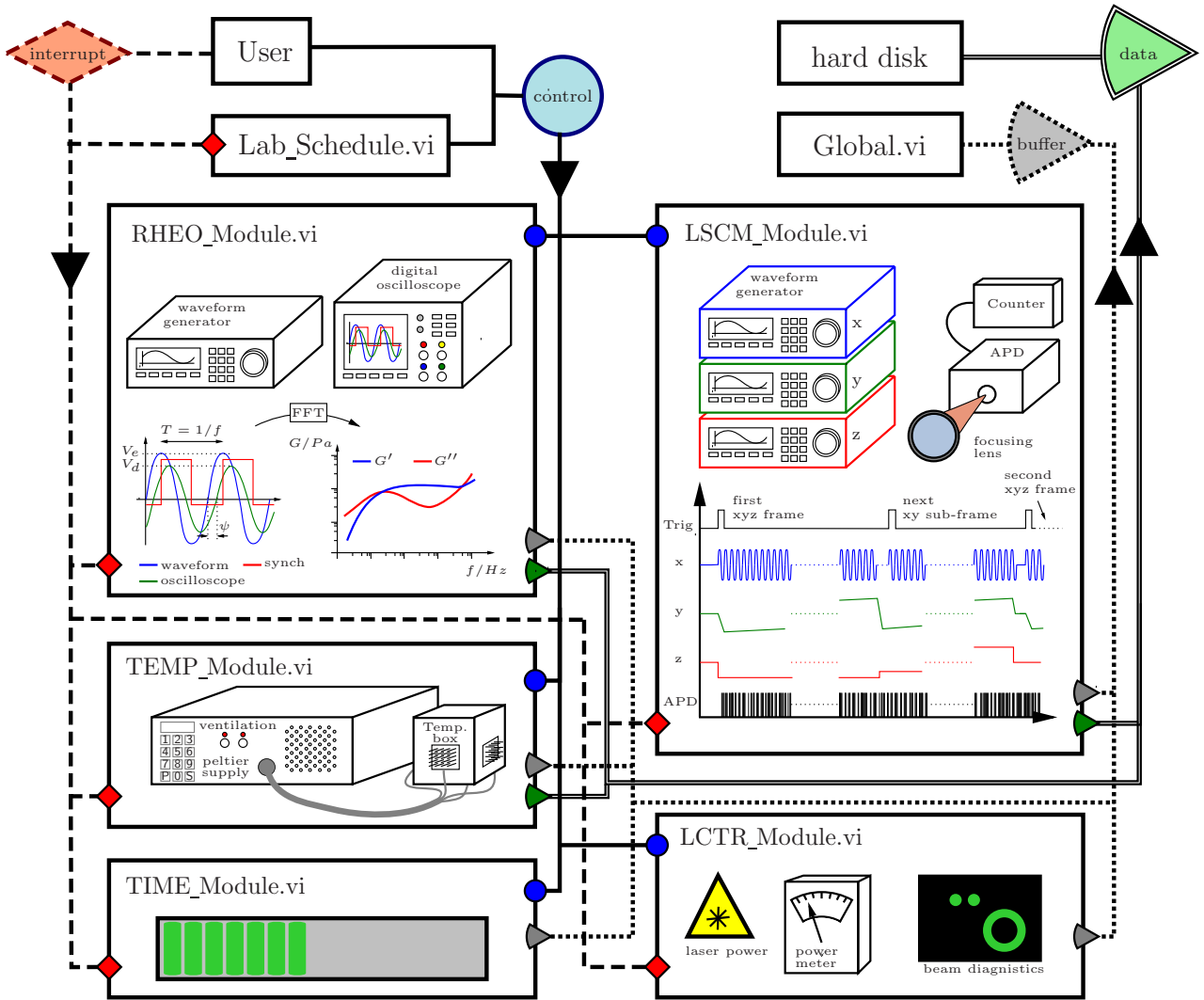
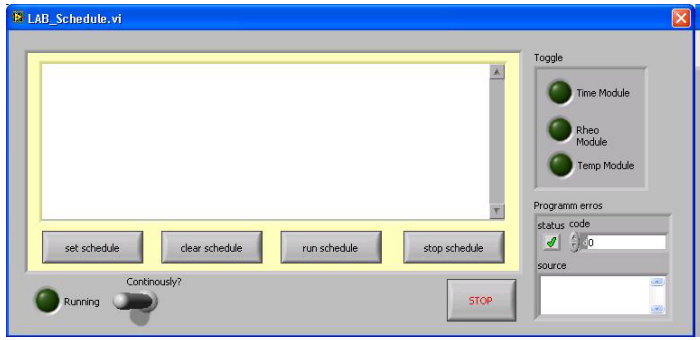


**Fig. A.1.:** The Labview interface is set up modularly. Beside to the modules used for confocal imaging and the rheometric measurement, auxiliary modules control the laser beam quality and power as well as the sample temperature and time delays.

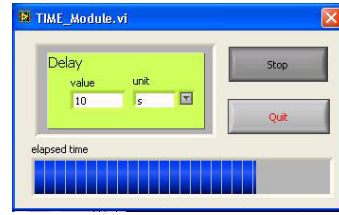
are depicted in the corresponding tabs [Fig. A.1 (i) and Fig. A.1 (j)].

`TEMP_Module.vi` controls the operation of the Peltier elements which are used to heat and cool the brass cube and the rheometer cell. The tab ‘graph’ shows a time graph of the temperature that is set by the electronic temperature control, the actual temperature in the walls of the brass cube which is used as the temperature feedback and the temperature at cooling fins of the temperature box Fig. A.1 (l)]. If this last temperature gets too high or low, a temperature balance with the environment exclusively via radiation takes too long and additional ventilation is activated. The desired temperature is set in the tab ‘control’ in terms of a specified temperature and temperature rate or a pre-defined list of times and temperature that is loaded by the program Fig. A.1 (m)].

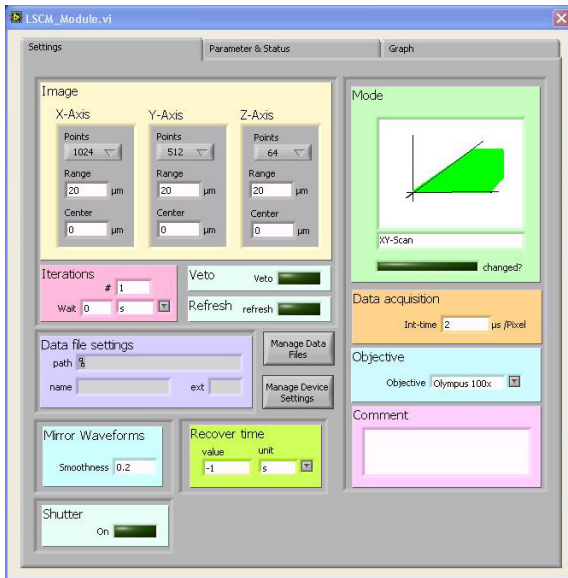
The LSCM is mainly controlled by `LSCM_Module.vi`. In the tab ‘settings’ the user can adjust spatial resolution, type (xy, xyz and xz) and number of the confocal images that will



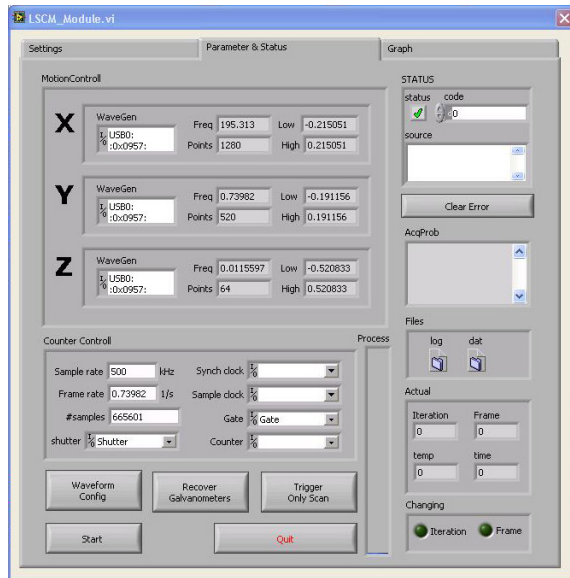
(a) LabSchedule.vi



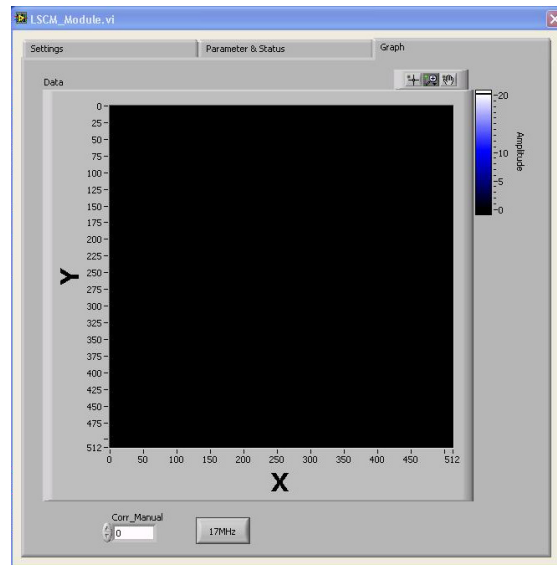
(b) TimeModule.vi



(c) LSCM\_Module.vi - Settings

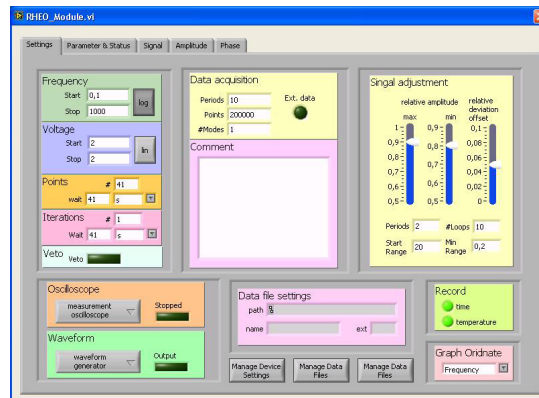


(d) LSCM\_Module.vi - Parameters & Status

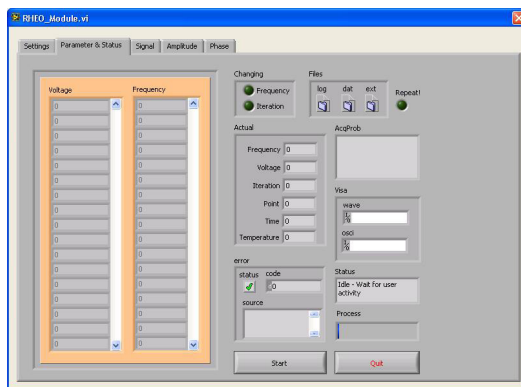


(e) LSCM\_Module.vi - Graph

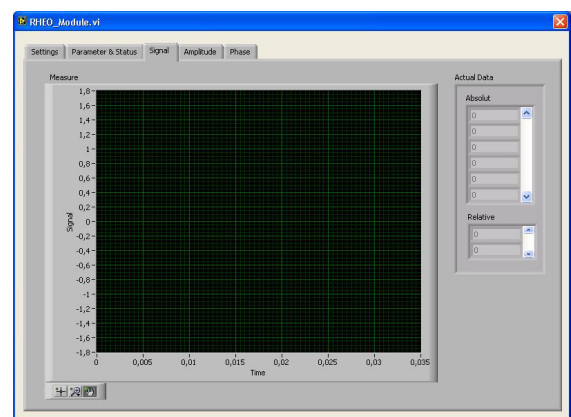
Fig. A.1.: Labview graphical user interface for confocal microscope and piezo-rheometry



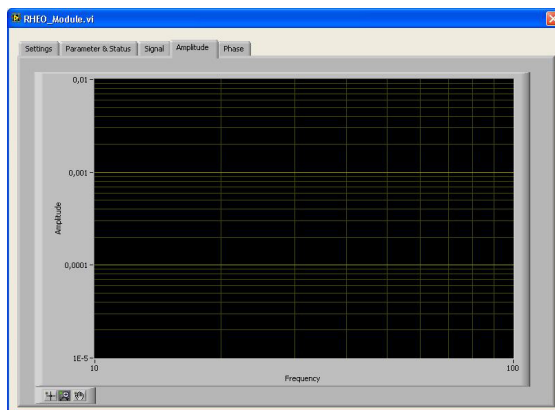
(f) Rheo\_Module.vi - Settings



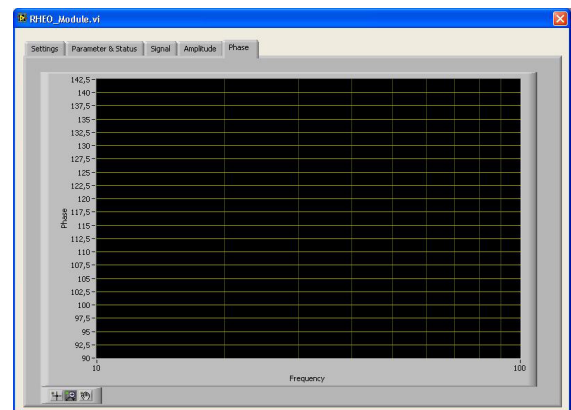
(g) Rheo\_Module.vi - Parameter &amp; Status



(h) Rheo\_Module.vi - Signal



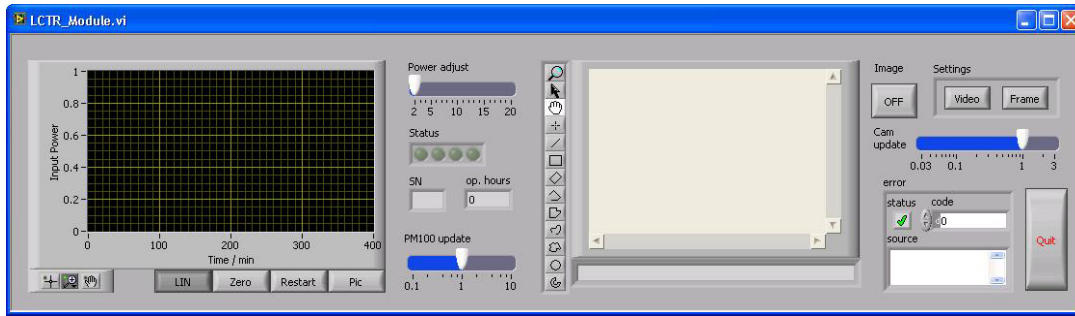
(i) Rheo\_Module.vi - Amplitude



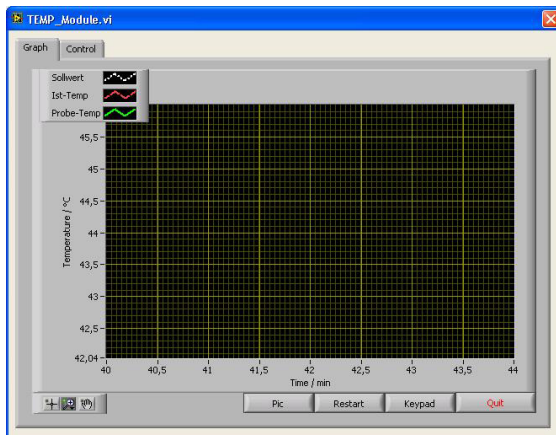
(j) Rheo\_Module.vi - Phase

**Fig. A.1.:** Labview graphical user interface for confocal microscope and piezo-rheometry (continued)

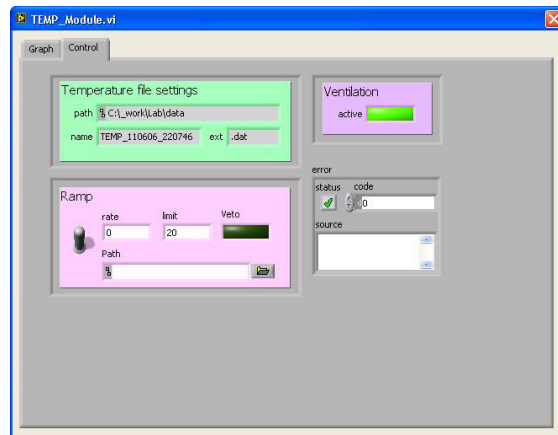
be recorded. The integration time per pixel is set explicitly, typically from  $2 \mu\text{s}$  to  $20 \mu\text{s}$ , and defines the total recording time of the image. The integration time also controls the frequencies at the three waveform generators used for the scanning of the laser focus across the sample. These frequencies and the voltages applied to the piezo-positioning and the scanning unit are summarized in the tab 'parameters and status' together with other control parameters like



(k) LCTR\_Module



(l) Temp\_Module - Graph



(m) Temp\_Module - Control

**Fig. A.1.:** Labview graphical user interface for confocal microscope and piezo-rheometry (continued)

*e. g.* the sampling and frame rate. The voltage profiles during the recording of a xyz-image are schematically shown in Fig. A.1. The fast x-axis works at a frequency of typically 200 Hz at which inertia effects of the mirrors in the scancube become important. Therefore, the voltage profile is not an asymmetric sawtooth-like which corresponds to a unidirectional scanning mode from left to right in the sample. Rather we used an symmetric and slightly smoothed sawtooth modulation and scan the sample alternating from left to right and right to left. In case of the y-axis inertial effects do no longer play a role and an asymmetric sawtooth-like modulation is applied. Finally, the voltage applied to the piezo-actuator of the objective is varied stepwise leaving the z-position of focus constant during the xy-scans. For a better synchronization all three waveform generators are synchronized and the measurement is started by setting a trigger signal at the beginning of each xy sub-frame. The fluorescence intensity data of the xy sub-frames are consecutively illustrated in the tab 'graph' [Fig. A.1 (e)].

Finally, `LCTR_Module.vi` provides means to control the output power of the laser and to check the optical power that is actually coupled into the objective [Fig. A.1 (k)]. Moreover, it shows the image of the CCD camera which is used for beam diagnostics and a coarse relative positioning of the sample and the laser focus.

## B. Rheology of polymer solutions and melts [Fer80a]

The rheology of dilute polymer solutions is greatly influenced by the nature of the polymer chains. Consisting of a more or less flexible backbone there is a large number of interchangeable conformations of the polymer chain. If the monomers interact with each other only via a fixed separation distance and excluded volume effects, the chain can easily switch from one conformation to the other via Brownian motion of the monomers. Therefore, the chain is not characterized by its actual conformation but by their root-mean-square of the end-to-end distance  $\sqrt{\langle r_{1N}^2 \rangle}$ . In equilibrium this quantity is proportional to  $\sqrt{N}$ , with  $N$  denoting the number of monomers in the chain. However, any flow in the surrounding solvent will displace the monomers and force the chain out of equilibrium. It is the interplay of these distorting forces and Brownian motion that defines whether the chain can switch to another conformation and relax the internal stress or is bound to its deformed state. This behavior of the chain is expressed in the pronounced visco-elasticity of polymer solutions and melts. Moreover, it directly becomes clear why the visco-elasticity shows a strong dependency on temperature. As the temperature rises the diffusional motion and thus the rate for conformational changes increases, too. Hence, the polymer chain relaxes faster for higher temperatures.

The bead-spring model is a simple model of the polymer chain. In this model the total chain is divided in smaller units, the beads, that contain several monomeric units. The beads are connected with each other via springs that represent the entropic forces driving the chains back to equilibrium. Moreover, the beads are subject to a viscous drag by the surrounding medium. The resulting equations of motion of the  $M$  individual beads of the chain are strongly coupled. Following standard procedures for decoupling these equations any motion of the chain can be expressed as a superposition of  $M$  different principle modes characterized by a set of resonance frequencies  $\omega_p$  or more commonly a set of relaxation times  $\tau_p = 2\pi/\omega_p$ . Assuming an exponential relaxation behavior of these modes the polymer related contribution to the shear relaxation modulus can be expressed by

$$G(t) = n k_B T \sum_{p=1}^M \exp(-t/\tau_p) \quad (\text{B.3})$$

and the complex shear modulus as

$$\begin{aligned} G'(\omega) &= n k_B T \sum_{p=1}^M \frac{\omega^2 \tau_p^2}{1 + \omega^2 \tau_p^2} \\ G''(\omega) &= n k_B T \sum_{p=1}^M \frac{\omega \tau_p}{1 + \omega^2 \tau_p^2} \end{aligned} \quad (\text{B.4})$$

The distribution of relaxation times depends on the question whether hydrodynamic interaction between the beads play a role. In the Rouse approximation these interactions are neglected and the distribution

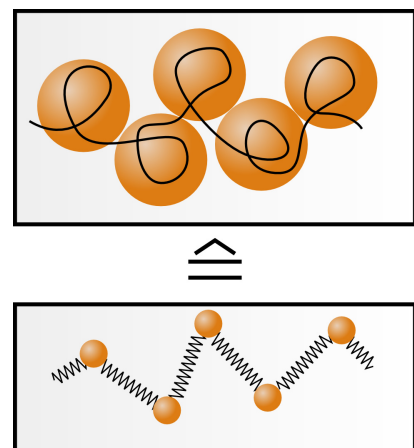


**Fig. B.2.:** Spring-bead model of a polymer chain

of relaxation times is given by

$$\tau_p \propto \sin^{-2} \left[ \frac{p\pi}{2(N+1)} \right] \quad (\text{B.5})$$

With increasing  $p$  the relaxation times become smaller and approach closer to each other. At some point the discrete set of relaxation times might be replaced by a continuous distribution for which equations (B.4) are simplified

$$G'(\omega) = G''(\omega) \propto \omega^{1/2} \quad (\text{B.6})$$

Hence, for oscillatory deformations at frequencies above a  $\omega_1 = 2\pi/\tau_1$   $G'$  and  $G''$  will follow a power law with an exponent of 1/2. Due to the Kramers-Kronig relation both modules fall over each other.

In the other case of dominant hydrodynamic interactions the Zimm model applies. Using the same formalism  $G'$  and  $G''$  again follow a power law, but this time with an exponent of 2/3:

$$\begin{aligned} G'(\omega) &\propto \omega^{2/3} \\ G''(\omega) &\propto \omega^{2/3} \end{aligned} \quad (\text{B.7})$$

At low concentrations and in particular for  $\Theta$ -solvent<sup>27</sup> mostly a Zimm-like behavior is observed. At higher concentrations and stronger monomer solvent interactions the dissolved polymer chains start to overlap and thus constrict the motions of the beads. Consequently, hydrodynamic effects are reduced and the Rouse model applies. This regime is often denoted as semi-dilute in contrast to the dilute regime and the Zimm case. Although this distinction between both cases is oversimplified it grants a good insight into the underlying physical principles.

At even higher concentrations the interpenetration of the polymer chains increases. Eventually the chains form loops and other topological constraints that severely alters the relaxation behavior of the polymer. These so called entanglements split the relaxation times into two separate sets. At low frequencies *i. e.* long times the stressed polymer chain can escape the entanglement. The polymer behaves like a Newtonian Fluid with the standard proportionalities  $G' \propto \omega^2$  and  $G'' \propto \omega$ . The frequency region is also called the terminal zone. The terminal relaxation time  $\tau_1$  is the longest relaxation time in the system and separates the terminal zone from the rubbery plateau. Here  $G'$  is almost independent of  $\omega$  while  $G''$  shows a minimum. The plateau is caused by the entanglements. The escape dynamics of the polymer chain is too slow to relax the applied stress. The interconnected chains behave like a stationary network with a high degree of elasticity. The separation of  $G'$  and  $G''$  actually depends on the molecular weight of the polymer as the number of entanglements along the chain rises with the chain length. If this number is too small the constraining effect is reduced and the mechanical

---

<sup>27</sup>In a  $\Theta$ -solvent the interaction between two monomers is equal to the interaction of a monomer with a solvent molecule

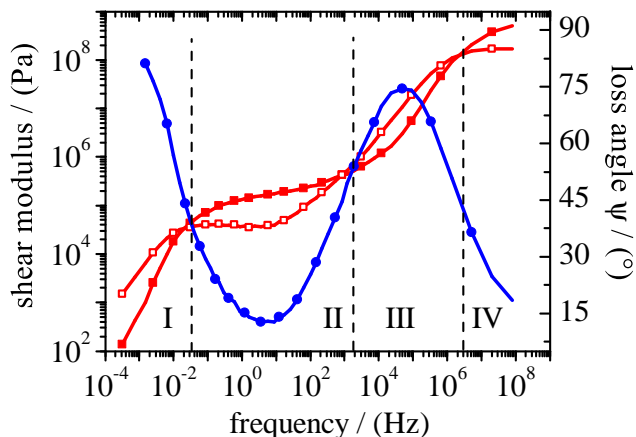


**Fig. B.3.:** Master Curve of polystyrene at a reference temperature of  $T_{o,tTS} = 170^\circ\text{C}$ . The curves may be separated into terminal zone (I), rubbery plateau (II), transition zone (III) and glassy plateau (IV). For the shear modulus filled and open symbols denote  $G'$  and  $G''$ , respectively.

spectra are described by the Rouse model. In between the entanglement points the polymer chain still is mobile. This motion corresponds to frequencies above the rubbery plateau. In the so called transition zone  $G'$  and  $G''$  again approach each other and rise simultaneously towards the glass transition. The glass transition is caused by a steady reduction of the free volume that is available for conformation changes. Suddenly, at very high frequencies no motion is possible any more. The polymer is kinetically arrested in the glassy state.  $G'$  levels off again and  $G''$  drops down.

The complete polymer spectrum for PS is shown in Fig. B.3. Each of the regimes from above can be clearly identified. The spectrum was obtained from measurements with an oscillatory rheometry in plate-plate geometry. Obviously, there is no device that can test the sample over a frequency range of 12 decades. The spectrum was generated from several spectra over a reduced frequency range of about 3 decades with the help of the time-temperature superposition (tTS). tTS relies on the above mentioned temperature dependency of the relaxation behavior of polymers. Increased temperatures give rise to a speed-up in the dynamics of the polymer chain. So, if the accessible frequency range of the rheometer is limited, the internal timescales of the polymer relaxation can be shifted by a change in the sample temperature. This scaling behavior is expressed as follows:

$$T \varrho G^*(\omega, T) = T_o \varrho_o G^*(\omega \cdot a_T, T_o) \quad (\text{B.8})$$

Equation (B.8) not only accounts for a change in the dynamics but also for a change in the absolute values of the complex shear modulus due to variations in the mass density  $\varrho$ . Yet, the shift factor  $a_T$  is the central element in equation (B.8).  $a_T$  obviously depends on the actual temperature  $T$  as well as the so called reference temperature  $T_o$  according to the semi-empirical William-Landel-Ferry (WLF) equation:

$$\log(a_T) = -\frac{c_1(T - T_o)}{c_2 + T - T_o} \quad (\text{B.9})$$

The WLF equation fits experimental data only at temperature above the glass transition as

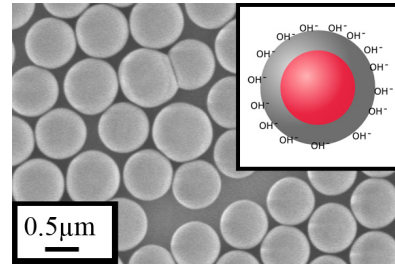


it relies on a constant thermal expansion coefficient  $\beta_T$ . At the glass transition however,  $\beta_T$  describes a kink which prevents a continuation of the WLF equation to lower temperatures.

## C. Particle description

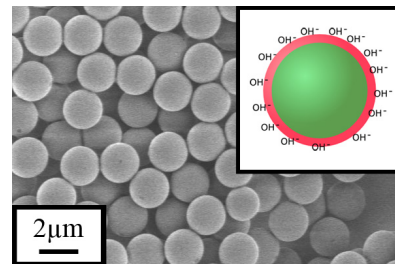
### C.1. Silica core-shell particles

The silica core-shell particles were synthesized in a single-batch reaction according to Stöber [Ver94]. Modified Rhodamine-B [9-(2-Carboxyphenyl)-3, 6-bis(diethylamino) xanthyliumchlorid] was added to the reaction mixture and covalently bound to the silica matrix. Due to the stepwise addition of the main reactant tetraethy orthosilicate the dye was incorporated only in the core of the particles while the shell is essentially free of Rhodamine.



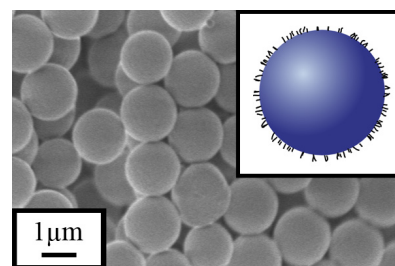
### C.2. PMMA particles

The PMMA particles are synthesized via dispersion polymerization in the presence of Nile Red (7-diethylamino-3,4-benzophenoxazine-2-one) as fluorescent dye [Pat97]. As far as we can judge, the dye molecules were uniformly distributed throughout the particle. A comb-like graft copolymer with a backbone of methyl methacrylate and glycidyl methacrylate and teeth made from PHSA [Ant86] was also added to the reaction mixture and co-polymerized with the PMMA. This polymerization steps also caused the formation of crosslinks between the PMMA chains. The graft copolymer assembled predominantly at the surface of the particles to act as steric stabilization layer ( $\approx 15$  nm). Hence, the surface was at least to some degree crosslinked. Instead of the graft copolymer with PHSA groups also pure PDMS was used as a stabilizing agent. Compared to the PHSA stabilized particles these particles were not crosslinked, rather rough and not perfectly spherical.



### C.3. PS-silica core-shell particles

Two types of fluorescent labeled polystyrene-silica core-shell particles were used. In both cases PS particles were first synthesized via dispersion polymerization [Zha09]. Poly(Acrylic acid) was added the reaction mixture to provide an electrostatic stabilization. Azobisisobutyronitrile was used as a catalyst of the polymerization. After the reaction the particles were swollen with a mixture of toluene and Nile Red to produce the first type of core-shell particles. After swelling the toluene was given



time to evaporate leaving the Nile Red over in the particles. Afterwards the particles were coated with poly(allylamine hydrochloride) and poly(vinylpyrrolidone). This step aided the subsequent synthesis of a smooth silica shell on the particles analog to the Stoeber method. For the second type of particles not the PS core but rather the shell was labeled. Like for the silica particles above Rhodamine-B was used as the fluorescent dye.

## D. Stress distribution for the indentation of a sphere in an elastic half-space

The elastic deformation  $d$  of two spheres with the radii  $R_1$  and  $R_2$  upon an applied contact force  $P$  is given by Hertzian contact mechanics [Her26] and equation (5.12). The projected contact area is characterized by the length

$$a = \sqrt[3]{\frac{3PR^*}{4E_r}} \quad (\text{D.10})$$

with  $1/R^* = 1/R_1 + 1/R_2$  and  $1/E_r = (1 - \nu_1^2)/E_1 + (1 - \nu_2)/E_2$  and the Poisson ratios  $\nu_1, \nu_2$  and Young's modules  $E_1, E_2$  of both spheres, respectively.

These equations are also valid for the indentation of an elastic half-sphere ( $R_1 \rightarrow \infty$ ) with an spherical indenter ( $R_2 \rightarrow R$ ). A derivation of the stress distribution within the half-space is rather lengthy. It is based on the assumption that the total stress at each point in the half-space is a superposition of all stresses that are generated by the points of the contact area. The spatial distribution of forces along the projected contact area is assumed to be

$$p(r) = p_o \sqrt{1 - \frac{r^2}{a^2}} \quad (\text{D.11})$$

with

$$r = \sqrt{x^2 + y^2} \quad \text{and} \quad p_o = \frac{3P}{2\pi a} \quad (\text{D.12})$$

After lengthy mathematical calculations the stress components for the points in the  $xz$ -plane are given by

$$\begin{aligned} \sigma_{xx} = p \left\{ \frac{1 - 2\nu_{\text{sam}}}{3} \frac{a^2}{r^2} \left[ 1 - \left( \frac{z}{\sqrt{u}} \right)^3 \right] \right. \\ \left. + \frac{z}{\sqrt{u}} \left[ 2\nu + \frac{(1-\nu)u}{a^2 + u} - (1+\nu) \frac{\sqrt{u}}{a} \arctan \left( \frac{a}{\sqrt{u}} \right) \right] \right\} \quad (\text{D.13}) \end{aligned}$$

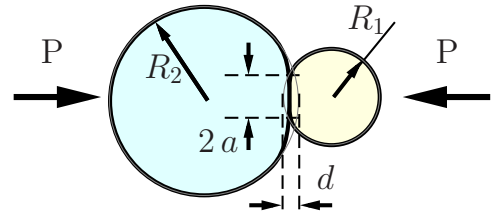
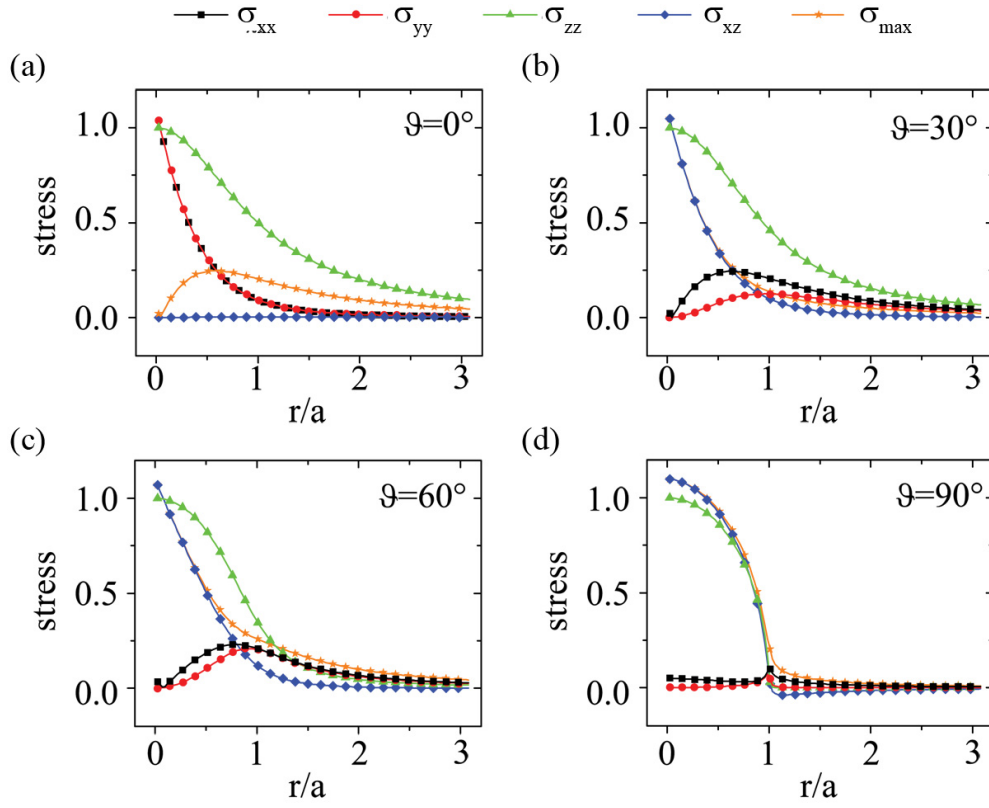


Fig. D.4.: Two spheres in contact under an applied force  $P$ .



**Fig. D.5.:** Stress components  $\sigma_{xx}$ ,  $\sigma_{yy}$ ,  $\sigma_{zz}$  and  $\sigma_{xz}$  as a function of distance to the indenter for polar angles of (a)  $\vartheta = 0^\circ$ , (b)  $\vartheta = 30^\circ$ , (c)  $\vartheta = 60^\circ$  and (d)  $\vartheta = 90^\circ$ .

$$\sigma_{yy} = p \left\{ \frac{1 - 2\nu_{\text{sam}}}{3} \frac{a^2}{r^2} \left[ 1 - \left( \frac{z}{\sqrt{u}} \right)^3 \right] + \left( \frac{z}{\sqrt{u}} \right)^3 \frac{a^2 u}{u^2 + a^2 z^2} + \frac{z}{\sqrt{u}} \left[ \frac{(1 - \nu)u}{a^2 + u} + (1 + \nu) \frac{\sqrt{u}}{a} \arctan \left( \frac{a}{\sqrt{u}} \right) - 2 \right] \right\} \quad (\text{D.14})$$

$$\sigma_{zz} = p \left( \frac{z}{\sqrt{u}} \right)^3 \frac{a^2 u}{u^2 + a^2 z^2} \quad (\text{D.15})$$

$$\sigma_{xz} = p \frac{r z^2}{u^2 + a^2 z^2} \frac{a^2 \sqrt{u}}{a^2 + u} \quad (\text{D.16})$$

Since the system is symmetric with respect to the indentation axis the other shear stresses  $\sigma_{yz}$  and  $\sigma_{xy}$  will vanish.

In order to get a better insight into their relative magnitude we do not show the stress components in 2D plots like in Fig. 5.10 or Fig. 5.11 but as a function of distance to the indenter for several polar angles  $\vartheta$  (Fig. D.5). Using Hooke's law (5.9) the strain components can be calculated. Their spatial distribution is compared exemplary for  $\epsilon_{xx}$  and  $\epsilon_{zz}$  for different Poisson ratios  $\nu$  in Fig. D.6.

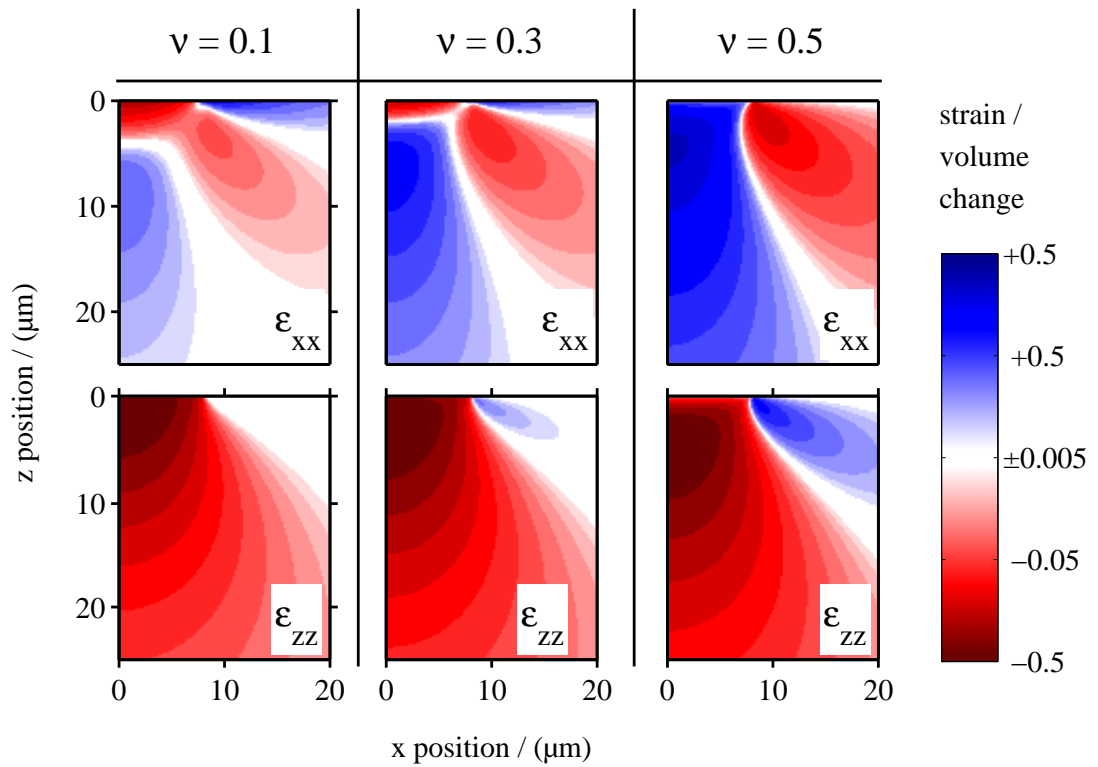


**Fig. D.6.:** Simulation of the spatial distribution of the strain tensor elements  $\epsilon_{\alpha\beta}$  according to Huber[Hub06] for different values of the Poisson ratio  $\nu$ . The material is assumed to be isotropic and homogeneous and the indentation is purely elastic. The indentation depth was chosen to be  $3\nu\text{m}$  and the spherical indenter has a diameter of  $25\nu\text{m}$ .

## Bibliography

- [Aar02] D. G. A. L. Aarts, R. Tuinier, and H. N. W. Lekkerkerker. ‘Phase behaviour of mixtures of colloidal spheres and excluded-volume polymer chains’. *J. Phys.: Cond. Matt.* **14**, pp. 7551–7561 (2002).
- [Aar04] D. G. A. L. Aarts, M. Schmidt, and H. N. W. Lekkerkerker. ‘Direct Visual Observation of Thermal Capillary Waves’. *Science* **304**, pp. 847–850 (2004).
- [Ada13] K. Adachi, I. Fujihara, and Y. Ishida. ‘Diluent effects on molecular motions and glass transition in polymers. I. Polystyrene-toluene’. *J. Poly. Sci.: Poly. Phys. Ed* **1975**, pp. 2155–2171 (13).
- [Ada95] M. Adam and D. Lairez. ‘Physical Properties of Polymeric Gels’ Chap. 4. Sol-Gel Transition, pp. 88–139. John Wiley & Sons (1995).
- [Aga08] R. R. Agayan, R. G. Smith, and R. Kopelman. ‘Slipping friction of an optically and magnetically manipulated microsphere rolling at a glass-water interface’. *J. Appl. Phys.* **104**, pp. 054915 1–11 (2008).
- [And00a] V. Anderson and E. Terentjev. ‘Cellular solid behaviour of liquid crystal colloids 2. Mechanical properties’. *Eur. Phys. Rev. E* **4**, p. 21 (2000).
- [And00b] V. Anderson, E. Terentjev, S. Meeker, J. Crain, and W. Poon. ‘Cellular solid behaviour of liquid crystal colloids 1. Phase separation and morphology’. *Eur. Phys. Rev. E* **4**, p. 11 (2000).
- [Ant06] S. M. Anthony, L. Hong, M. Kim, and S. Granick. ‘Single-Particle Colloid Tracking in Four Dimensions’. *Langmuir* **22**, pp. 9812–9815 (2006).
- [Ant86] L. Antl, J. W. Goodwin, R. D. Hill, R. H. Ottewill, S. M. Owens, S. Papworth, and J. A. Waters. ‘The preparation of poly(methyl methacrylate) latices in non-aqueous media’. *Coll. Surf.* **17**, pp. 67 – 78 (1986).
- [Arb06] F. L. Arbeloa and V. M. Martinez. ‘New fluorescent polarization method to evaluate the orientation of adsorbed molecules in uniaxial 2D layered materials’. *J. Photochem. Photobio. A* **181**, pp. 44–49 (2006).
- [Arb93] S. Arbabi and M. Sahimi. ‘Mechanics of disordered solids. I. Percolation on elastic networks with central forces’. *Phys. Rev. B* **47**, pp. 695–702 (1993).
- [Arc05] A. J. Archer, R. Evans, R. Roth, and M. Oettel. ‘Solvent mediated interactions close to fluid-fluid phase separation: Microscopic treatment of bridging in a soft-core fluid’. *J. Chem. Phys.* **122**, p. 084513 (2005).
- [Asa58] S. Asakura and F. Oosawa. ‘Interaction between particles suspended in solutions of macromolecules’. *J. Poly. Sci.* **33**, pp. 183–192 (1958).
- [Ash70] A. Ashkin. ‘Acceleration and Trapping of Particles by Radiation Pressure’. *Phys. Rev. Lett.* **24**, pp. 156–159 (1970).

- [Ash83] M. F. Ashby. *'The mechanical properties of cellular solids'*. Metall. Mat. Trans. A **14**, pp. 1755–1769 (1983).
- [Ast02] T. Aste, T. D. Matteo, and E. G. d'Agliano. *'Stress transmission in granular matter'*. J. Phys.: Cond. Matt. **14**, p. 2391 (2002).
- [Aue06] G. K. Auernhammer, D. Collin, and P. Martinoty. *'Viscoelasticity of suspensions of magnetic particles in a polymer: Effect of confinement and external field'*. J. Chem. Phys. **124**, p. 204907 (2006).
- [Bar10] R. Bartali, V. Michelia, G. Gottardia, A. Vaccaria, and N. Laidania. *'Nanoindentation: Unload-to-load work ratio analysis in amorphous carbon films for mechanical properties'*. Surface and Coatings Technology **204**, pp. 2073–2076 (2010).
- [Bar77] R. Bartolino and G. Durand. *'Plasticity in a Smectic-A Liquid Crystal'*. Phys. Rev. Lett. **39**, pp. 1346–1349 (1977).
- [Bat77] G. K. Batchelor. *'The effect of Brownian motion on the bulk stress in a suspension of spherical particles'*. J. Fluid Mech. **83**, pp. 97–117 (1977).
- [Bau00] C. Bauer, T. Bieker, and S. Dietrich. *'Wetting-induced effective interaction potential between spherical particles'*. Phys. Rev. E **62**, pp. 5324–5338 (2000).
- [Bau96] M. Baumgärtel and N. Willenbacher. *'The relaxation of concentrated polymer solutions'*. Rheo. Acta **35**, pp. 168–185 (1996).
- [Bee72] D. Beer and J. Weber. *'Photobleaching of organic laser dyes'*. Opt. Comm. **5**, pp. 307–309 (1972).
- [Bes07] R. Besseling, E. R. Weeks, A. B. Schofield, and W. C. K. Poon. *'Three-Dimensional Imaging of Colloidal Glasses under Steady Shear'*. Physical Review Letters **99**, p. 028301 (2007).
- [Bey99] D. Beysens and T. Narayanan. *'Wetting-Induced Aggregation of Colloids'*. Journal of Statistical Physics **95**, pp. 997–1008 (1999).
- [Bin00] B. P. Binks and S. O. Lumsdon. *'Influence of Particle Wettability on the Type and Stability of Surfactant-Free Emulsions'*. Langmuir **16**, pp. 8622–8631 (2000).
- [Bin01] B. P. Binks and P. D. I. Fletcher. *'Particles absorbed at the Oil-Water Interface: A Theoretical Comparison between Spheres of Uniform Wettability and "Janus" Particles'*. Langmuir **17**, pp. 4708–4710 (2001).
- [Bin02] B. P. Binks. *'Particles as surfactants—similarities and differences'*. Curr. Op. Coll. Interf. Sci. **7**, pp. 21 – 41 (2002).
- [Bla05] J.-F. Blach, A. Daoudi, J.-M. Buisine, and D. Bormann. *'Raman mapping of Polymer Dispersed Liquid Crystal'*. Vibr. Spectr. **39**, pp. 31 – 36 (2005).
- [Bon09] D. Bonn, J. Otwinowski, S. Sacanna, H. Guo, G. Wegdam, and P. Schall. *'Direct Observation of Colloidal Aggregation by Critical Casimir Forces'*. Phys. Rev. Lett. **103**, p. 156101 (2009).
- [Bos02] G. Bosma, C. Pathmamanoharan, E. H. A. de Hoog, W. K. Kegel, A. van Blaaderen, and H. N. W. Lekkerkerker. *'Preparation of Monodisperse, Fluorescent PMMA-Latex Colloids by Dispersion Polymerization'*. J. Coll. Int. Sci. **245**, pp. 292–300. (2002).

- [Bou01] T. Bouchaour, F. Benmouna, F. Roussel, J.-M. Buisine, Coqueret, M. Benmouna, and U. U. Maschke. ‘*Equilibrium phase diagram of poly(2-phenoxyethylacrylate) and 5CB*’. *Polymer* **42**, pp. 1663–1667 (2001).
- [Bra06] A. R. E. Brás, M. T. Viciosa, C. M. Rodrigues, C. J. Dias, and M. Dionísio. ‘*Changes in molecular dynamics upon formation of a polymer dispersed liquid crystal*’. *Phys. Rev. E* **73**, p. 061709 (2006).
- [Bra07] A. R. Brás, M. Dionísio, H. Huth, C. Schick, and A. Schönhal. ‘*Origin of glassy dynamics in a liquid crystal studied by broadband dielectric and specific heat spectroscopy*’. *Physical Review E (Statistical, Nonlinear, and Soft Matter Physics)* **75**, p. 061708 (2007).
- [Bra93] J. F. Brady. ‘*The rheological behavior of concentrated colloidal dispersions*’. *J. Chem. Phys.* **99**, pp. 567–581 (1993).
- [Bru03] J. Brujic, S. Edwards, I. Hopkinson, and H. A. Makse. ‘*Measuring the distribution of interdroplet forces in a compressed emulsion system*’. *Physica A: Stat. Mech. Appl.* **327**, pp. 201 – 212 (2003).
- [But06a] H.-J. Butt, K. Graf, and M. Kappl. ‘*Physics and Chemistry of Interfaces*’ Chap. 7. Contact angle phenomena and wetting, pp. 125–152. Wiley-VHC (2006).
- [But06b] H.-J. Butt, K. Graf, and M. Kappl. ‘*Physics and Chemistry of Interfaces*’ Chap. 2. Liquid surfaces, pp. 5–26. Wiley-VHC (2006).
- [Cag80] M. Cagnon and G. Durand. ‘*Mechanical Shear of Layers in Smectic-A and Smectic-B Liquid Crystal*’. *Phys. Rev. Lett.* **45**, pp. 1418–1421 (1980).
- [Cam05] A. I. Campbell, V. J. Anderson, J. S. van Duijneveldt, and P. Bartlett. ‘*Dynamical Arrest in Attractive Colloids: The Effect of Long-Range Repulsion*’. *Phys. Rev. Lett.* **94**, p. 208301 (2005).
- [Car69] N. F. Carnahan and K. E. Starling. ‘*Equation of State for Non attracting Rigid Spheres*’. *J. Chem. Phys.* **51**, p. 635 (1969).
- [Cas48] H. B. G. Casimir. ‘*On the attraction between two perfectly conducting plates*’. *Proc. Koninklijke Nederlandse Akad. van Wetenschappen* **B 51**, pp. 793–796 (1948).
- [Cat04a] M. E. Cates. ‘*Mode Coupling Theories for Jamming and Gelation*’. *AIP Conf. Proc.* **708**, pp. 33–39 (2004).
- [Cat04b] M. E. Cates, M. Fuchs, K. Kroy, W. C. K. Poon, and A. M. Puertas. ‘*Theory and simulation of gelation, arrest and yielding in attracting colloids*’. *J. Phys.: Cond. Matt.* **16**, p. S4861 (2004).
- [Cat06] K. J. V. V. Catherine A. Tweedie. ‘*On the indentation recovery and fleeting hardness of polymers*’. *J. Mater. Res.* **21**, pp. 3029–3036 (2006).
- [Cat08] M. E. Cates. ‘*Arrest and Flow of Colloidal Glasses*’. *Annales Henri Poincare* **4**, pp. 647–661 (2008).
- [Cat98] M. E. Cates, J. P. Wittmer, J.-P. Bouchaud, and P. Claudin. ‘*Jamming, Force Chains, and Fragile Matter*’. *Phys. Rev. Lett.* **81**, pp. 1841–1844 (1998).

- [Cav87] J. Y. Cavaille, C. J. J. Perez, L. Monnerie, and G. P. Johari. ‘*Time-Temperature Superposition and Dynamic Mechanical Behavior of Atactic Polystyrene*’. J. Poly. Sci. **25**, pp. 1099–0488 (1987).
- [Ceb83] D. J. Cebula, J. W. Goodwin, R. H. Ottewill, G. Jenkin, and J. Tabony. ‘*Small angle and quasi-elastic neutron scattering studies on polymethylmethacrylate lattices in nonpolar media*’. Coll. Poly. Sci. **261**, pp. 555–564 (1983).
- [Cha95] S. Challa, S. Wang, and J. Koenig. ‘*Thermal induced phase separation of E7/PMMA PDLC system*’. J. Therm. Ana. Cal. **45**, pp. 1297–1312 (1995). 10.1007/BF02547424.
- [Che07] T. Chen, L. Zhang, T. Li, J. Lin, and S. Lin. ‘*Phase equilibria of polymer dispersed liquid crystal systems in the presence of an external electrical field*’. J. Poly. Sci. B: Poly. Phys. **45**, pp. 1898 – 1906 (2007).
- [Che10] D. Chen, D. Semwogerere, J. Sato, V. Breedveld, and E. R. Weeks. ‘*Microscopic structural relaxation in a sheared supercooled colloidal liquid*’. Phys. Rev. E **81**, p. 011403 (2010).
- [Che11] Q. Chen, Q. Li, and J. Lin. ‘*Synthesis of Janus composite particles by the template of dumbbell-like silica/polystyrene*’. Mat. Chem. Phys. (2011).
- [Che97] C.-M. Cheng and Y.-T. Cheng. ‘*On the initial unloading slope in indentation of elastic-plastic solids by an indenter with an axisymmetric smooth profile*’. Appl. Phys. Lett. **71**, pp. 2623–2625 (1997).
- [Che98] Y.-T. Cheng and C.-M. Cheng. ‘*Relationships between hardness, elastic modulus, and the work of indentation*’. Appl. Phys. Lett. **73**, pp. 614–616 (1998).
- [Cho04] S. Chowdhury and M. T. Laugier. ‘*The use of non-contact AFM with nanoindentation techniques for measuring mechanical properties of carbon nitride thin films*’. Appl. Surf. Sci. **233**, pp. 219 – 226 (2004).
- [Cho08] I. S. Choi, M. Dao, and S. Suresh. ‘*Mechanics of indentation of plastically graded materials*’. J. Mech. Phys. Sol. **56**, pp. 157–171 (2008).
- [Cho10] E. Choppe, F. Puaud, T. Nicolai, and L. Benyahia. ‘*Rheology of xanthan solutions as a function of temperature, concentration and ionic strength*’. Carbohydrate Polymers **82**, pp. 1228 – 1235 (2010).
- [Cla06] C. Clasen, B. P. Gearing, and G. H. McKinley. ‘*The flexure-based microgap rheometer (FMR)*’. J. Rheo. **50**, pp. 883–905 (2006).
- [Cle04a] J. Cleaver and W. C. K. Poon. ‘*Network formation in colloid - liquid crystal mixtures studied by confocal microscopy*’. J. Phys.: Cond. Matt. **16**, pp. S1901–S1909 (2004).
- [Cle04b] J. A. Cleaver, D. Vollmer, J. Crain, and W. Poon. ‘*Self-supporting liquid crystal composite*’. Mol. Cryst. Liquid Cryst. **409**, pp. 59–68 (2004).
- [Cle07] P. S. Clegg, E. M. Herzig, A. B. Schofield, S. U. Egelhaaf, T. S. Horozov, B. P. Binks, M. E. Cates, and W. C. K. Poon. ‘*Emulsification of Partially Miscible Liquids Using Colloidal Particles: Nonspherical and Extended Domain Structures*’. Langmuir **23**, pp. 5984–5994 (2007).



- [Coa95] D. Coates. *'Polymer-dispersed liquid crystals'*. J. Mater. Chem. **5**, pp. 2063 – 2072 (1995).
- [Col03] D. Collin, G. K. Auernhammer, O. Gavtat, P. Martinoty, and H. R. Brand. *'Frozen-In Magnetic Order in Uniaxial Magnetic Gels: Preparation and Physical Properties'*. Macromol. Rap. Comm. **24**, pp. 737 – 741 (2003).
- [Col89] R. H. Colby. *'Breakdown of time-temperature superposition in miscible polymer blends'*. Polymer **30**, pp. 1275 – 1278 (1989).
- [Con06] J. C. Conrad, P. P. Dhillon, E. R. Weeks, D. R. Reichman, and D. A. Weitz. *'Contribution of Slow Clusters to the Bulk Elasticity Near the Colloidal Glass Transition'*. Phys. Rev. Lett. **97**, p. 265701 (2006).
- [Con09] M. Conradi, M. Ravnik, M. Bele, M. Zorko, S. Zumer, and I. Muevi. *'Janus nematic colloids'*. Soft Matter **5**, pp. 3905 – 3912 (2009).
- [Cou02] P. Coussot, Q. D. Nguyen, H. T. Huynh, and D. Bonn. *'Avalanche Behavior in Yield Stress Fluids'*. Phys. Rev. Lett. **88**, p. 175501 (2002).
- [Cra05] J. J. Crassous, R. Regisser, M. Ballauff, and N. Willenbacher. *'Characterization of the viscoelastic behavior of complex fluids using the piezoelectric axial vibrator'*. J. Rheo. **49**, pp. 851–863 (2005).
- [Cra06] J. J. Crassous, M. Siebenbürger, M. Ballauff, M. Drechsler, O. Henrich, and M. Fuchs. *'Thermosensitive core-shell particles as model systems for studying the flow behavior of concentrated colloidal dispersions'*. J. Chem. Phys. **125**, p. 204906 (2006).
- [Cra08] J. J. Crassous, M. Siebenbürger, M. Ballauff, M. Drechsler, D. Hajnal, O. Henrich, and M. Fuchs. *'Shear stresses of colloidal dispersions at the glass transition in equilibrium and in flow'*. J. Chem. Phys. **128**, p. 204902 (2008).
- [Cra97] C. Cramer, T. Cramer, F. Kremer, and R. Stannarius. *'Measurement of orientational order and mobility of a nematic liquid crystal in random nanometer confinement'*. J. Chem. Phys. **106**, pp. 3730–3742 (1997).
- [Cro96] J. C. Crocker and D. G. Grier. *'Methods of Digital Video Microscopy for Colloidal Studies'*. J. Coll. Int. Sci. **179**, pp. 298–310 (1996).
- [Cun79] P. A. Cundall and O. D. L. Strack. *'A discrete numerical model for granular assemblies'*. Géotechnique **29**, pp. 47–65 (1979).
- [Cuv86] G. Cuvelier and B. Launay. *'Concentration regimes in xanthan gum solutions deduced from flow and viscoelastic properties'*. Carbohydrate Polymers **6**, pp. 321 – 333 (1986).
- [DAc10] M. D'Acunzi, M. Mammen, L. Singh, X. Deng, M. Roth, G. K. Auernhammer, H.-J. Butt, and D. Vollmer. *'Superhydrophobic surfaces by hybrid raspberry-like particles'*. Faraday Discuss. **146**, pp. 35–48 (2010).
- [Dav49] R. M. Davies. *'The Determination of Static and Dynamic Yield Stresses Using a Steel Ball'*. Proc. R. Soc. Lond. A **197**, pp. 416–432 (1949).

- [Daw01] K. A. Dawson, G. Foffi, F. Sciortino, P. Tartaglia, and E. Zaccarelli. ‘*Mode-coupling theory of colloids with short-range attractions*’. *J. Phys.: Cond. Matt.* **13**, pp. 9113–9126 (2001).
- [Doe86] M. Doerener and W. Nixa. ‘*A method for interpreting the data from depth-sensing indentation instruments*’. *J. Mat. Res.* **1**, pp. 601–609 (1986).
- [Don82] E. Donth. ‘*The size of cooperatively rearranging regions at the glass transition*’. *J. Non-Cryst. Sol.* **53**, pp. 325 – 330 (1982).
- [Dro02] A. Drozd-Rzoska and S. J. Rzoska. ‘*Complex dynamics of isotropic 4-cyano-4-n-pentylbiphenyl (5CB) in linear and nonlinear dielectric relaxation studies*’. *Phys. Rev. E* **65**, p. 041701 (2002).
- [Drz86] P. S. Drzaic. ‘*Polymer dispersed nematic liquid crystal for large area displays and light valves*’. *J. Appl. Phys.* **60**, p. 2142 (1986).
- [Dul06] R. P. A. Dullens, D. G. A. L. Aarts, and W. K. Kegel. ‘*Dynamic Broadening of the Crystal-Fluid Interface of Colloidal Hard Spheres*’. *Phys. Rev. Lett.* **97**, p. 228301 (2006).
- [Eck02] T. Eckert and E. Bartsch. ‘*Re-entrant Glass Transition in a Colloid-Polymer Mixture with Depletion Attractions*’. *Phys. Rev. Lett.* **89**, p. 125701 (2002).
- [Ein06] A. Einstein. ‘*Eine neue Bestimmung der Moleküldimensionen*’. *Annalen der Physik* **324**, pp. 289–306 (1906).
- [Fen07] Z. Feng, Z. Wang, C. Gao, and J. Shen. ‘*Hollow microcapsules with a complex polyelectrolyte shell structure fabricated by polymerization of 4-vinylpyridine in the presence of poly(sodium 4-styrenesulfonate) and silica particles*’. *Mat. Lett.* **61**, pp. 2560 – 2564 (2007).
- [Fer07] A. Fery and R. Weinkamer. ‘*Mechanical properties of micro- and nanocapsules: Single-capsule measurements*’. *Polymer* **48**, pp. 7221 – 7235 (2007).
- [Fer80a] J. D. Ferry. ‘*Viscoelastic properties of Polymers*’. John Wiley & Sons 3 Ed. (1980).
- [Fer80b] J. Ferry. ‘*Viscoelastic properties of Polymers*’ Chap. 17. Concentrated solutions, Plasticized Polymer, and Gels, pp. 486–544. John Wiley & Sons (1980).
- [Fer80c] J. Ferry. ‘*Viscoelastic properties of Polymers*’ Chap. 11. Dependence of Viscoelastic Behavior on Temperature and Pressure, pp. 486–544. John Wiley & Sons (1980).
- [Fil06a] D. Filip, M. H. G. Duits, V. I. Uricanu, and J. Mellema. ‘*Plastic-to-Elastic Transition in Aggregated Emulsion Networks, Studied with Atomic Force Microscopy-Confocal Scanning Laser Microscopy Microrheology*’. *Langmuir* **22**, pp. 4558–4566 (2006).
- [Fil06b] D. Filip, V. I. Uricanu, M. H. G. Duits, D. van den Ende, J. Mellema, W. G. M. Agterof, and F. Mugele. ‘*Microrheology of Aggregated Emulsion Droplet Networks, Studied with AFM-CSLM*’. *Langmuir* **22**, pp. 560–574 (2006).
- [Flo92] G. Floudas, G. Fytas, and W. Brown. ‘*Solvent mobility in poly(methyl methacrylate)/toluene solutions by depolarized and polarized light scattering*’. *J. Chem. Phys.* **96**, p. 2164 (1992).

- [Flo93a] G. Floudas, W. Steffen, E. W. Fischer, and W. Brown. ‘*Solvent and polymer dynamics in concentrated polystyrene/toluene solutions*’. J. Chem. Phys. **99**, p. 695 (1993).
- [Flo93b] G. Floudas, W. Steffen, L. Giebel, and G. Fytas. ‘*Polymer and solvent dynamics in a polystyrene/di-2-ethylhexyl phthalate solution*’. Pro. Coll. Poly. Sci. **91**, pp. 124–126 (1993).
- [Fox56] T. Fox. Bull. Am. Phys. Soc. **1**, p. 123 (1956).
- [Fri01] B. J. Frisken. ‘*Revisiting the Method of Cumulants for the Analysis of Dynamic Light-Scattering Data*’. Applied Optics **24**, pp. 4087–4091 (2001).
- [Fuc02a] M. Fuchs and M. E. Cates. ‘*Theory of Nonlinear Rheology and Yielding of Dense Colloidal Suspensions*’. Phys. Rev. Lett. **89**, p. 248304 (2002).
- [Fuc02b] M. Fuchs and K. S. Schweizer. ‘*Structure of colloid-polymer suspensions*’. J. Phys.: Cond. Matt. **14**, p. R239 (2002).
- [Gam09] A. Gambassi, A. Maciołek, C. Hertlein, U. Nellen, L. Helden, C. Bechinger, and S. Dietrich. ‘*Critical Casimir effect in classical binary liquid mixtures*’. Phys. Rev. E **80**, p. 061143 (2009).
- [Gib97a] L. J. Gibson and M. F. Ashby. ‘*Cellular solids - Structure and properties*’ Chap. 1. Introduction, pp. 175–282. Cambridge University Press (1997).
- [Gib97b] L. J. Gibson and M. F. Ashby. ‘*Cellular solids - Structure and properties*’ Chap. 5. The mechanics of foams: basic results, pp. 175–282. Cambridge University Press (1997).
- [Gog01] N. Gogibus, U. Maschke, F. Benmouna, B. Ewen, X. Coqueret, and M. Benmouna. ‘*Phase diagrams of poly(dimethylsiloxane) and 5CB blends*’. J. Poly Sci. B **39**, pp. 581–588 (2001).
- [Gog03] N. Gogibus, F. Benmouna, B. Ewen, T. Pakula, X. Coqueret, M. Benmouna, and U. Maschke. ‘*Phase diagrams of poly(siloxane)/liquid crystal blends*’. J. Poly. Sci. B **41**, pp. 39–43 (2003).
- [Gol80] H. Goldstein. ‘*Classical mechanics*’. Addison-Wesley series in physics Addison-Wesley Pub. Co. (1980).
- [Gou01] A. Gouldstone, K. J. Van Vliet, and S. Suresh. ‘*Nanoindentation: Simulation of defect nucleation in a crystal*’. Nature **411**, p. 656 (2001).
- [Gra93] M. C. Grant and W. B. Russel. ‘*Volume-fraction dependence of elastic moduli and transition temperatures for colloidal silica gels*’. Phys. Rev. E **47**, pp. 2606–2614 (1993).
- [Gri97] D. G. Grier. ‘*Optical tweezers in colloid and interface science*’. Curr. Op. Coll. Interf. Sci. **2**, pp. 264 – 270 (1997).
- [Guo08] H. Guo, T. Narayanan, M. Sztuchi, P. Schall, and G. H. Wegdam. ‘*Reversible Phase Transition of Colloids in a Binary Liquid Solvent*’. Phys. Rev. Lett. **100**, p. 188303 (2008).

- [Gur] M. van Gorp and J. Palmen. ‘*Time-Temperature-Superposition for Polymeric Blends*’. Soc. Rheol. News.
- [Han93] C. D. Han and J. K. Kim. ‘*On the use of time-temperature superposition in multi-component/multiphase polymer systems*’. Polymer **34**, pp. 2533 – 2539 (1993).
- [Hay09] J. Hay. ‘*Introduction to instrumented indentation testing*’. Exp. Tech. **33**, pp. 66–72 (2009).
- [Hei05] L. Heim, M. Farshchi, M. Morgeneyer, J. Schwedes, H.-J. Butt, and M. Kappl. ‘*Adhesion of carbonyl iron powder particles studied by atomic force microscopy*’. J. Adh. Sci. Tech. **19**, pp. 199–213 (2005).
- [Hei99] L.-O. Heim, J. Blum, M. Preuss, and H.-J. Butt. ‘*Adhesion and Friction Forces between Spherical Micrometer-Sized Particles*’. Phys. Rev. Lett. **83**, pp. 3328–3331 (1999).
- [Hel81] A. V. Helden, J. Jansen, and A. Vrij. ‘*Preparation and characterization of spherical monodisperse silica dispersions in nonaqueous solvents*’. J. Coll. Int. Sci. **81**, pp. 354 – 368 (1981).
- [Her07] E. M. Herzig, K. A. White, A. B. Schofield, W. C. K. Poon, and P. S. Clegg. ‘*Bicontinuous emulsions stabilized solely by colloidal particles*’. Nat. Mat. **6**, pp. 966–971 (2007).
- [Her26] H. Hertz. ‘*Ueber die Berührung fester elastischer Körper*’. J. reine angew. Math. pp. 156–171 (1826).
- [Hon06] L. Hong, S. M. Anthony, and S. Granick. ‘*Rotation in Suspension of a Rod-Shaped Colloid*’. Langmuir **22**, pp. 7128–7131 (2006).
- [Hor04] H. Hori, O. Urakawa, and K. Adachi. ‘*Dielectric Relaxation in Phase-Segregated Mixtures of Polystyrene and Liquid Crystal 5CB*’. Macromolecules **37**, pp. 1583–1590 (2004).
- [Hub06] M. T. Huber. ‘*Zur Theorie der Berührung fester elastischer Körper*’. Annalen der Physik **316**, pp. 153–163 (2006).
- [Hun07] R. J. Hunter. ‘*Foundations of Colloid Science*’. Oxford University Press (2007).
- [Jan90] B. Janczuk and T. Bialopiotrowicz. ‘*The total surface free energy and the contact angle in the case of low energetic solids*’. J. Coll. Int. Sci. **140**, pp. 362 – 372 (1990).
- [Jea00] P. B. Jean-Christophe Loudet and P. Poulin. ‘*Colloidal ordering from phase separation in a liquid- crystalline continuous phase*’. Nature **407**, pp. 611–613 (2000).
- [Jee10] A.-Y. Jee and M. Lee. ‘*Comparative analysis on the nanoindentation of polymers using atomic force microscopy*’. Polymer Testing **29**, pp. 95–99 (2010).
- [Joh04a] K. L. Johnson. ‘*Contact mechanics*’ Chap. 4. Normal contact of elastic solids: Hertz theory, pp. 84–106. Cambridge University Press (2004).
- [Joh04b] K. L. Johnson. ‘*Contact mechanics*’ Chap. 6. Normal contact of inelastic solids, pp. 153–201. Cambridge University Press (2004).

- [Jon77] A. K. Jonscher. ‘*The ‘universal’ dielectric response*’. Nature **267**, pp. 673 – 679 (1977).
- [Jon91] D. A. R. Jones, B. Leary, and D. V. Boger. ‘*The rheology of a concentrated colloidal suspension of hard spheres*’. J. Coll. Int. Sci. **147**, pp. 479 – 495 (1991).
- [Kad09] D. Kadau, J. J. Andrade, and H. Herrmann. ‘*Collapsing granular suspensions*’. Eur. Phys. J. E **30**, pp. 275–281 (2009).
- [Kal99] A. K. Kalkar, V. V. Kunte, and A. A. Deshpande. ‘*Electro-optic studies on polymer-dispersed liquid crystal composite films. I. Composites of PVB-E7*’. J. Appl. Poly. Sci. **74**, pp. 3485–3491 (1999).
- [Kar02] S. Kara-Slimane, U. Maschke, F. Benmouna, M. Bacquet, F. Roussel, J.-M. Buisine, X. Coqueret, and M. Benmouna. ‘*Thermophysical behaviour of monofunctional acrylate and liquid crystal systems*’. Eur. Poly. J. **38**, pp. 461 – 466 (2002).
- [Kaw11] T. Kawasaki and A. Onuki. ‘*Plastic deformations in crystal, polycrystal and glass in three-dimensional binary mixtures under stretching*’. Arxiv. cond-mat. soft. **1103**, p. 1051 (2011).
- [Ken92] K. Kendall and T. P. Weihs. ‘*Adhesion of nanoparticles within spray dried agglomerates*’. J. Phys. D **25**, pp. A3–A8 (1992).
- [Kim06] J.-W. Kim, R. J. Larsen, and D. A. Weitz. ‘*Synthesis of Nonspherical Colloidal Particles with Anisotropic Properties*’. J. Am. Chem. Soc. **128**, pp. 14374–14377 (2006).
- [Kim93] D. Kim, J. M. Caruthers, and N. Peppas. ‘*Viscoelastic properties of dodecane/polystyrene systems*’. Polymer **34**, pp. 3638–3647 (1993).
- [Kim98] A. Kim, S.-J. Park, and J.-R. Lee. ‘*Stabilization of Liquid Crystal-in-Water Dispersion with Polymer/Surfactant Mixture: Nematic Curvilinear Aligned Phase Composite Film*’. J. Coll. Int. Sci. **197**, pp. 119 – 125 (1998).
- [Kin87] R. King. ‘*Elastic analysis of some punch problems for a layered medium*’. Int. J. Sol. Struct. **23**, pp. 1657 – 1664 (1987).
- [Kir02] L. Kirschenmann and W. Pechhold. ‘*Piezoelectric rotary vibrator (PRV): a new oscillating rheometer for linear viscoelasticity*’. Rheo. Acta **41**, pp. 362–368 (2002).
- [Kle03] S. M. Klein, V. N. Manoharan, D. J. Pine, and F. F. Lange. ‘*Preparation of monodisperse PMMA microspheres in nonpolar solvents by dispersion polymerization with a macromonomeric stabilizer*’. Coll. Poly. Sci. **282**, pp. 7–13 (2003).
- [Kon07] J. Konnerth, A. Valla, and W. Gindl. ‘*Nanoindentation mapping of a wood-adhesive bond*’. Appl. Phys. A **88**, pp. 371–375 (2007). 10.1007/s00339-007-3976-y.
- [Kop72] D. E. Koppel. ‘*Analysis of Macromolecular Polydispersity in Intensity Correlation Spectroscopy: The Method of Cumulants*’. J. Chem. Phys. **57**, p. 4814 (1972).
- [Kra10] R. C. Kramb, R. Zhang, K. S. Schweizer, and C. F. Zukoski. ‘*Glass Formation and Shear Elasticity in Dense Suspensions of Repulsive Anisotropic Particles*’. Phys. Rev. Lett. **105**, (2010).

- [Kre03a] F. Kremer and A. Schönhal. *'Broadband Dielectric Spectroscopy'*. Springer Verlag (2003).
- [Kre03b] F. Kremer and A. Schönhal. *'Broadband Dielectric Spectroscopy'* Chap. 2 Broadband Dielectric Measurement Techniques ( $10^{-6}$  Hz to  $10^{12}$  Hz), pp. 385–432. Springer Verlag (2003).
- [Kre03c] F. Kremer and A. Schönhal. *'Broadband Dielectric Spectroscopy'* Chap. 10 Molecular and Collective Dynamics of (Polymeric) Liquid Crystals, pp. 385–432. Springer Verlag (2003).
- [Kri72] I. M. Krieger. *'Rheology of monodisperse latices'*. Adv. Coll. Interf. Sci. **3**, pp. 111 – 136 (1972).
- [Kro04] K. Kroy, M. E. Cates, and W. C. K. Poon. *'Cluster Mode-Coupling Approach to Weak Gelation in Attractive Colloids'*. Phys. Rev. Lett. **92**, p. 148302 (2004).
- [Kur10] R. Kurita and E. R. Weeks. *'Experimental study of random-close-packed colloidal particles'*. Phys. Rev. E **82**, p. 011403 (2010).
- [Kyu93] T. Kyu, I. Ilies, and M. Mustafa. *'Phase separation dynamics of a polymer dispersed liquid crystal'*. Journal de Physique IV **3**, pp. 37–40 (1993).
- [Kyu96] T. Kyu, C. Shen, and H. W. Chiu. *'Effect of Molecular Weight on Miscibility Phase Diagrams in Mixtures of Polymer and Liquid Crystals'*. Mol. Cryst. Liq. Cryst. **287**, pp. 27 – 34 (1996).
- [Le 08] A. Le Grand and G. Petekidis. *'Effects of particle softness on the rheology and yielding of colloidal glasses'*. Rheo. Acta **47**, pp. 579–590 (2008). 10.1007/s00397-007-0254-z.
- [Lec08] W. Lechner and C. Dellago. *'Accurate determination of crystal structures based on averaged local bond order parameters'*. J. Chem. Phys. **129**, p. 114707 (2008).
- [Let04] M. P. Lettinga, G. H. Koenderink, B. W. M. Kuipers, E. Bessels, and A. P. Philipse. *'Rotational dynamics of colloidal spheres probed with fluorescence recovery after photobleaching'*. J. Chem. Phys. **120**, pp. 4517–4529 (2004).
- [Li02] J. Li, K. J. Van Vliet, T. Zhu, S. Yip, and S. Suresh. *'Atomistic mechanisms governing elastic limit and incipient plasticity in crystals'*. Nature **418**, pp. 307–310 (2002).
- [Lin37] K. Lindstrom-Lang. *'Dilatometric ultra-micro-estimation of peptidase activity'*. Nature pp. 713–714 (1937).
- [Lin90a] M. Y. Lin, H. M. Lindsay, D. A. Weitz, R. C. Ball, R. Klein, and P. Meakin. *'Universal reaction-limited colloid aggregation'*. Phys. Rev. A **41**, pp. 2005–2020 (1990).
- [Lin90b] M. Y. Lin, H. M. Lindsay, D. A. Weitz, R. Klein, R. C. Ball, and P. Meakin. *'Universal diffusion-limited colloid aggregation'*. J. Phys.: Cond. Matt. **2**, p. 3093 (1990).
- [Liu95] C. h. Liu, S. R. Nagel, D. A. Schecter, S. N. Coppersmith, S. Majumdar, O. Narayan, and T. A. Witten. *'Force Fluctuations in Bead Packs'*. Science **269**, p. 513 (1995).

- [Liu98] A. J. Liu and S. R. Nagel. ‘*Nonlinear dynamics: Jamming is not just cool any more*’. *Nature* **396**, pp. 21–22 (1998).
- [Lu01] K.-P. Lu, S. Lee, and C. P. Cheng. ‘*Hardness of irradiated poly(methyl methacrylate) at elevated temperatures*’. *J. Appl. Phys.* **90**, pp. 1745–1749 (2001).
- [Lu06] P. J. Lu, J. C. Conrad, H. M. Wyss, A. B. Schofield, and D. A. Weitz. ‘*Fluids of Clusters in Attractive Colloids*’. *Phys. Rev. Lett.* **96**, p. 028306 (2006).
- [Lu07] P. J. Lu, P. A. Sims, H. Oki, J. B. Macarthur, and D. A. Weitz. ‘*Target-locking acquisition with real-time confocal (TARC) microscopy*’. *Opt. Express* **15**, pp. 8702–8712 (2007).
- [Mac94] C. W. Macosko. ‘*Rheology Principles, Measurements, and Application*’. Wiley-VCH (1994).
- [Mal02] J. Malzbender and G. de With. ‘*Indentation load-displacement curve, plastic deformation, and energy*’. *J. Mater. Res.* **17**, pp. 502–511 (2002).
- [Man02] T. Mansar, R. Decressain, C. Gors, and V. K. Dolganov. ‘*Phase Transformations And Dynamics Of 4-Cyano-4'-Pentylbiphenyl (5cb) By Nuclear Magnetic Resonance, Analysis Differential Scanning Calorimetry, And Wideangle X-Ray Diffraction Analysis*’. *Mol. Cryst. Liq. Cryst.* **382**, pp. 97 – 111 (2002).
- [Man05] S. Manley, H. M. Wyss, K. Miyazaki, J. C. Conrad, V. Trappe, L. J. Kaufman, D. R. Reichman, and D. A. Weitz. ‘*Glasslike Arrest in Spinodal Decomposition as a Route to Colloidal Gelation*’. *Phys. Rev. Lett.* **95**, p. 238302 (2005).
- [Mar76] D. E. Martire, G. A. Oweimreen, G. I. Agren, S. G. Ryan, and H. T. Peterson. ‘*The effect of quasispherical solutes on the nematic to isotropic transition in liquid crystals*’. *J. Chem. Phys.* **64**, p. 1456 (1976).
- [Mar98] P. Martinoty, J. L. Gallani, and D. Collin. ‘*Hydrodynamic and Nonhydrodynamic Behavior of Layer-Compression Modulus B at the Nematic–Smectic- A Phase Transition in 8 OCB*’. *Phys. Rev. Lett.* **81**, pp. 144–147 (1998).
- [Mas02] U. Maschke, X. Coqueret, and M. Benmouna. ‘*Electro-Optical Properties of Polymer-Dispersed Liquid Crystals*’. *Macromol. Rap. Comm.* **23**, pp. 159–170 (2002).
- [Mas95] T. G. Mason, J. Bibette, and D. A. Weitz. ‘*Elasticity of Compressed Emulsions*’. *Phys. Rev. Lett.* **75**, pp. 2051–2054 (1995).
- [McN99] J. G. McNally, T. Karpova, J. Cooper, and J. A. Conchello. ‘*Three-Dimensional Imaging by Deconvolution Microscopy*’. *Methods* **19**, pp. 373–385 (1999).
- [Mea83] P. Meakin. ‘*Formation of Fractal Clusters and Networks by Irreversible Diffusion-Limited Aggregation*’. *Phys. Rev. Lett.* **51**, pp. 1119–1122 (1983).
- [Mee00] S. P. Meeker, W. C. K. Poon, J. Crain, and E. M. Terentjev. ‘*Colloid-liquid-crystal composites: An unusual soft solid*’. *Phys. Rev. E* **61**, pp. R6083–R6086 (2000).
- [Min88] M. Minski. ‘*Double focussing Stage scanning microscope*’. *Scanning* **10**, pp. 128–138 (1988).

- [Mus06] I. Musevic, M. Skarabot, U. Tkalec, M. Ravnik, and S. Zumer. ‘*Two-Dimensional Nematic Colloidal Crystals Self-Assembled by Topological Defects*’. *Science* **313**, p. 954 (2006).
- [Nas07] M. J. Nasse, J. C. Woehl, and S. Huant. ‘*High-resolution mapping of the three-dimensional point spread function in the near-focus region of a confocal microscope*’. *Appl. Phys. Lett.* **90**, p. 031106 (2007).
- [Nij97] K. te Nijenhuis. ‘*Thermoreversible Networks*’ Chap. 1 Introduction, pp. 1–11. Springer (1997).
- [Nob08] S. Nobukawa, O. Urakawa, T. Shikata, and T. Inoue. ‘*Component Dynamics in Polystyrene/4-Pentyl-4'-Cyanobiphenyl Blend*’. *AIP Conf. Proc.* **1027**, pp. 561–563 (2008).
- [Oda00] M. Oda and K. Iwashita. ‘*Study on couple stress and shear band development in granular media based on numerical simulation analyses*’. *Int. J. Eng. Sci.* **38**, pp. 1713 – 1740 (2000).
- [Oht08] C. P. Ohtsuka, T. Royall and H. Tanaka. ‘*Local structure and dynamics in colloidal fluids and gels*’. *Eur. Phys. Lett.* **84**, p. 46002 (2008).
- [Oli04] W. Oliver and G. M. Pharr. ‘*Measurement of hardness and elastic modulus by instrumented indentation: Advances in understanding and refinements to methodology*’. *J. Mater. Res.* **19**, pp. 3–20 (2004).
- [Oli85] N. H. Oliver, R. Pecora, and A. C. Ouano. ‘*Restricted rotational diffusion of a rodlike solvent in a polymeric matrix*’. *Macromolecules* **18**, pp. 2208–2215 (1985).
- [Oli92] W. Oliver and G. M. Pharr. ‘*An improved technique for determination hardness and elastic modulus using load and displacement sensing indentation experiments*’. *J. Mater. Res.* **7**, pp. 1564–1583 (1992).
- [Ono05] H. Ono and N. Kawatsuki. ‘*Effects of molecular weight on morphology and electrooptical properties of polymethylmethacrylate/liquid crystal composites fabricated by a solvent-induced phase separation method*’. *Polymer Bulletin* **35**, pp. 365–370 (2005).
- [Owe80] G. A. Oweimreen and D. E. Martire. ‘*The effect of quasispherical and chainlike solutes on the nematic to isotropic phase transition in liquid crystals*’. *J. Chem. Phys.* **72**, pp. 2500–2510 (1980).
- [Pat08] C. Patrick Royall, S. R. Williams, T. Ohtsuka, and H. Tanaka. ‘*Direct observation of a local structural mechanism for dynamic arrest*’. *Nat. Mat.* **7**, pp. 556 – 561 (2008).
- [Pat97] C. Pathmamanoharan, K. Groot, and J. K. G. Dhont. ‘*Preparation and characterization of crosslinked PMMA latex particles stabilized by grafted copolymer*’. *Coll. Poly. Sci.* **275**, pp. 897–901 (1997).
- [Paw06] J. B. Pawley. ‘*Handbook of biological confocal microscopy*’ Chap. Fundamental limits in confocal microscopy. Springer Science + Business Media, LLC (2006).
- [Pec85] R. Pecora. ‘*Dynamic light scattering*’. Plenum Press (1985).



- [Pes06] S. Pestov. ‘*Landolt-Börnstein - Group VIII Advanced Materials and Technologies*’ Chap. Two ring systems without bridge, pp. 24–65. Springer-Verlag (2006).
- [Pet01] P. Petrov and E. Terentjev. ‘*Formation of Cellular Solid in Liquid Crystal Colloids*’. *Langmuir* **17**, pp. 2942–2949 (2001).
- [Pha06] K. N. Pham, G. Petekidis, D. Vlassopoulos, S. U. Egelhaaf, P. N. Pusey, and W. C. K. Poon. ‘*Yielding of colloidal glasses*’. *Europhys. Lett.* **75**, p. 624 (2006).
- [Pic07] S. U. Pickering. ‘*CXCVI.-Emulsions*’. *J. Chem. Soc., Trans.* **91**, pp. 2001–2021 (1907).
- [Pin88] D. J. Pine, D. A. Weitz, P. M. Chaikin, and E. Herbolzheimer. ‘*Diffusing wave spectroscopy*’. *Phys. Rev. Lett.* **60**, pp. 1134–1137 (1988).
- [Pla79] D. J. Plazek, E. Riande, H. Markovitz, and N. Raghupathi. ‘*Concentration dependence of the viscoelastic properties of polystyrene-tricresyl phosphate solutions*’. *J. Poly. Sci.: Poly Phys Ed.* **17**, pp. 2189–2213 (1979).
- [Poo04] W. Poon. ‘*Colloids as Big Atoms*’. *Science* **304**, pp. 830–831 (2004).
- [Pou97] P. Poulin, H. Stark, T. C. Lubensky, and D. A. Weitz. ‘*Novel Colloidal Interactions in Anisotropic Fluids*’. *Science* **275**, pp. 1770–1773 (1997).
- [Pra03] V. Prasad, V. Trappe, A. D. Dinsmore, P. N. Segre, L. Cipelletti, and D. A. Weitz. ‘*Universal features of the fluid to solid transition for attractive colloidal particles*’. *Faraday Discuss.* **123**, pp. 1–12 (2003).
- [Pue02] A. M. Puertas, M. Fuchs, and M. E. Cates. ‘*Comparative Simulation Study of Colloidal Gels And Glasses*’. *Phys. Rev. Lett.* **88**, p. 098301 (2002).
- [Pue04] A. M. Puertas, A. Fernández-Barbero, F. Javier de las Nieves, and L. F. Rull. ‘*Colloidal Aggregation Induced by Long Range Attractions*’. *Langmuir* **20**, pp. 9861–9867 (2004).
- [Pus09] P. N. Pusey, E. Zaccarelli, C. Valeriani, E. Sanz, W. C. K. Poon, and M. E. Cates. ‘*Hard spheres: crystallization and glass formation*’. *Phil. Trans. R. Soc. A* **367**, pp. 4993–5011 (2009).
- [Pus86] P. N. Pusey and W. van Megen. ‘*Phase behaviour of concentrated suspensions of nearly hard colloidal spheres*’. *Nature* **320**, pp. 340 – 342 (1986).
- [Rai06] Y. Raichman, M. Kazakevich, E. Rabkin, and Y. Tsur. ‘*Inter-Nanoparticle Bonds in Agglomerates Studied by Nanoindentation*’. *Adv. Mat.* **18**, pp. 2028–2030 (2006).
- [Ram04] S. Ramakrishnan, Y.-L. Chen, K. S. Schweizer, and C. F. Zukoski. ‘*Elasticity and clustering in concentrated depletion gels*’. *Phys. Rev. E* **70**, p. 040401 (2004).
- [Rei05] D. R. Reichman and P. Charbonneau. ‘*Mode-coupling theory*’. *Journal of Statistical Mechanics: Theory and Experiment* **2005**, p. P05013 (2005).
- [Reu09] M. Reufer, P. Diaz-Leyva, I. Lynch, and F. Scheffold. ‘*Temperature-sensitive poly(N-Isopropyl-Acrylamide) microgel particles: A light scattering study*’. *Eur. Phys. J. E* **28**, pp. 165–171 (2009).

- [Rib85] J. L. G. Ribelles and R. D. Calleja. ‘*The  $\beta$  dielectric relaxation in some methacrylate polymers*’. J. Poly. Sci.: Poly. Phys. Ed: **23**, pp. 1297–1307 (1985).
- [Rig84] W. A. W. T. R. Rigler. ‘*Separation of translational and rotational contributions in solution using fluorescence photobleaching*’. Biophys. J. **46**, pp. 787–793 (1984).
- [Rom00] S. Romer, F. Scheffold, and P. Schurtenberger. ‘*Sol-Gel Transition of Concentrated Colloidal Suspensions*’. Phys. Rev. Lett. **85**, pp. 4980–4983 (2000).
- [Rot10] M. Roth, M. D’Acunzi, D. Vollmer, and G. K. Auernhammer. ‘*Viscoelastic rheology of colloid-liquid crystal composites*’. J. Chem. Phys. **132**, p. 124702 (2010).
- [Rot11a] M. Roth, M. Franzmann, M. d’Acunzi, M. Kreiter, and G. K. Auernhammer. ‘*Experimental analysis of contact forces and rotation in colloidal and granular systems*’. in preparation (2011).
- [Rot11b] M. Roth, C. Schilde, P. Lellig, A. Kwade, and G. K. Auernhammer. ‘*Colloidal aggregates tested via nanoindentation and simultaneous 3D imaging*’. Arxiv. cond-mat. soft. **1102.4233v1**, (2011).
- [Rou00] F. Roussel, J.-M. Buisine, U. Maschke, X. Coqueret, and F. Benmouna. ‘*Phase diagrams and morphology of polymer dispersed liquid crystals based on nematic-liquid-crystal-monofunctional-acrylate mixtures*’. Phys. Rev. E **62**, pp. 2310–2316 (2000).
- [Roz96] S. A. Rozanski, R. Stannarius, H. Groothues, and F. Kremer. ‘*Dielectric properties of the nematic liquid crystal 4-n-pentyl-4’-cyanobiphenyl in porous membranes*’. Liquid Crystals **20**, pp. 59–66 (1996).
- [Rss85] E. Rössler, H. Sillescu, and H. Spiess. ‘*Deuteron n.m.r. in relation to the glass transition in polymers*’. Polymer **26**, pp. 203 – 207 (1985).
- [Rue97] C. J. Rueb and C. F. Zukoski. ‘*Viscoelastic properties of colloidal gels*’. J. Rheol. **41**, p. 197 (1997).
- [Rue98] C. J. Rueb and C. F. Zukoski. ‘*Rheology of suspensions of weakly attractive particles: Approach to gelation*’. J. Rheo. **42**, pp. 1451–1476 (1998).
- [Sac07] S. Sacanna, W. K. Kegel, and A. P. Philipse. ‘*Thermodynamically Stable Pickering Emulsions*’. Phys. Rev. Lett. **98**, p. 158301 (2007).
- [Sah93] M. Sahimi and S. Arbabi. ‘*Mechanics of disordered solids. II. Percolation on elastic networks with bond-bending forces*’. Phys. Rev. B **47**, pp. 703–712 (1993).
- [Sch01] F. Scheffold, S. E. Skipetrov, S. Romer, and P. Schurtenberger. ‘*Diffusing-wave spectroscopy of nonergodic media*’. Phys. Rev. E **63**, p. 061404 (2001).
- [Sch03a] A. Schausberger and I. V. Ahrer. ‘*On the time-concentration superposition of the linear viscoelastic properties of plasticized polystyrene melts using the free volume concept*’. Macromol. Chem. Phys. **196**, pp. 2161 – 2172 (2003).
- [Sch03b] F. Schlesener, A. Hanke, and S. Dietrich. ‘*Critical Casimir Forces in Colloidal Suspensions*’. J. Stat. Phys. **110**, pp. 981–1013 (2003). 10.1023/A:1022184508016.
- [Sch03c] C. Schuh and A. Lund. ‘*Atomistic basis for the plastic yield criterion of metallic glass*’. Nat. Mat. **2**, pp. 449–452 (2003).

- [Sch04] P. Schall, I. Cohen, D. A. Weitz, and F. Spaepen. ‘*Visualization of Dislocation Dynamics in Colloidal Crystals*’. *Science* **305**, pp. 1944–1948 (2004).
- [Sch05] P. Schall, I. Cohen, D. A. Weitz, and F. Spaepen. ‘*Visualizing dislocation nucleation by indenting colloidal crystals*’. *Science* **440**, pp. 319–323 (2005).
- [Sch07] C. Schilde, S. Breitung-Faes, and A. Kwade. ‘*Dispersing and Grinding of Alumina Nano Particles by Different Stress Mechanisms*’. *Ceramic Forum Int.* **84**, pp. 12–17 (2007).
- [Sch09a] C. Schilde, T. Gothsch, K. Quarch, M. Kind, and A. Kwade. ‘*Effect of Important Precipitation Process Parameters on the Redispersion Process and the Micromechanical Properties of Precipitated Silica*’. *Chem. Eng. Tech.* **32**, pp. 1078–1087 (2009).
- [Sch09b] C. Schilde and A. Kwade. ‘*Mikromechanische Eigenschaften und Dispergierbarkeit unterschiedlich gefällter nanostrukturierter Aggregate*’. *Chem. Ing. Tech.* **81**, pp. 1155–1155 (2009).
- [Sch10a] F. Scheffold, P. Díaz-Leyva, M. Reufer, N. Ben Braham, I. Lynch, and J. L. Harden. ‘*Brushlike Interactions between Thermoresponsive Microgel Particles*’. *Phys. Rev. Lett.* **104**, p. 128304 (2010).
- [Sch10b] C. Schilde, I. Kampen, and A. Kwade. ‘*Dispersion kinetics of nano-sized particles for different dispersing machines*’. *Chem. Eng. Sci.* **65**, pp. 3518 – 3527 (2010).
- [Sch94] K. Schmidt-Rohr, A. S. Kulik, H. W. Beckham, A. Ohlemacher, U. Pawelzik, C. Boeffel, and H. W. Spiess. ‘*Molecular Nature of the .beta. Relaxation in Poly(methyl methacrylate) Investigated by Multidimensional NMR*’. *Macromolecules* **27**, pp. 4733–4745 (1994).
- [Sem05] D. Semwogerere and E. R. Weeks. ‘*Confocal Microscopy*’. *Encyclopedia of Biomaterials and Biomedical Engineering* (2005).
- [Sha03] S. A. Shah, Y.-L. Chen, K. S. Schweizer, and C. F. Zukoski. ‘*Viscoelasticity and rheology of depletion flocculated gels and fluids*’. *J. Chem. Phys.* **119**, pp. 8747–8760 (2003).
- [Shi94] M. Shima, M. Sato, M. Atsumi, and K. Hatada. ‘*Dipole Moments of Isotactic and Syndiotactic Poly(methyl methacrylate) and their Temperature Dependence*’. *Poly. J.* **26**, pp. 579–585 (1994).
- [Sie09] M. Siebenbürger and M. Ballauff. ‘*Viscoelasticity and shear flow of concentrated, noncrystallizing colloidal suspensions: Comparison with mode-coupling theory*’. *J. Rheol.* **53**, p. 707 (2009).
- [Smi03] R. Smith, D. Christopher, S. D. Kenny, A. Richter, and B. Wolf. ‘*Defect generation and pileup of atoms during nanoindentation of Fe single crystals*’. *Phys. Rev. B* **67**, p. 245405 (2003).
- [Smi81] L. M. Smith, R. M. Weis, and H. M. McConnell. ‘*Measurement of rotational motion in membranes using fluorescence recovery after photobleaching*’. *Biophys. J.* **36**, pp. 73–91 (1981).

- [Sne65] I. N. Sneddon. ‘*The relation between load and penetration in the axisymmetric boussinesq problem for a punch of arbitrary profile*’. Intern. J. of Eng. Sci. **3**, pp. 47 – 57 (1965).
- [Sok10] M. Sokuler, G. K. Auernhammer, M. Roth, C. Liu, and H.-J. Bonaccorso, E. and Butt. ‘*The Softer the Better: Fast Condensation on Soft Surfaces*’. Langmuir **26**, pp. 1544–1547 (2010).
- [Sta01] H. Stark. ‘*Physics of colloidal dispersions in nematic liquid crystals*’. Phys. Rep. **351**, pp. 387–474 (2001).
- [Sta04] H. Stark, J. Fukuda, and H. Yokoyama. ‘*Capillary condensation in liquid-crystal colloids.*’. Phys Rev Lett **92**, p. 205502 (2004).
- [Ste83] P. J. Steinhardt, D. R. Nelson, and M. Ronchetti. ‘*Bond-orientational order in liquids and glasses*’. Phys. Rev. B **28**, pp. 784–805 (1983).
- [Sur06] S. Suresh. ‘*Crystal deformation: Colloid model for atoms*’. Nat. Mat. **5**, pp. 253–254 (2006).
- [Tab54] D. Tabor. ‘*Mohs’s Hardness Scale - A Physical Interpretation*’. Proc. Phys. Soc. B **67**, p. 249 (1954).
- [Tak08] K. Takahashi, M. Ichikawa, and Y. Kimura. ‘*Force between colloidal particles in a nematic liquid crystal studied by optical tweezers*’. Phys. Rev. E **77**, p. 020703 (2008).
- [Tak93] S. Takigami, M. Shimada, P. A. Williams, and G. O. Phillips. ‘*E.s.r. study of the conformational transition of spin-labelled xanthan gum in aqueous solution*’. Int. J. Bio. Macromol. **15**, pp. 367 – 371 (1993).
- [Tam94] D. E. Tambe and M. M. Sharma. ‘*The effect of colloidal particles on fluid-fluid interfacial properties and emulsion stability*’. Adv. Coll. Interf. Sci. **52**, pp. 1 – 63 (1994).
- [Tan00] H. Tanaka. ‘*Viscoelastic phase separation*’. J. Phys.: Cond. Matt. **12**, pp. R207–R264 (2000).
- [Tar04] S. Tarimala, S. R. Ranabothu, J. P. Verneti, and L. L. Dai. ‘*Mobility and In Situ Aggregation of Charged Microparticles at Oil-Water Interfaces*’. Langmuir **20**, pp. 5171–5173 (2004).
- [Thi10] J. H. J. Thijssenab and P. S. Clegg. ‘*Demixing, remixing and cellular networks in binary liquids containing colloidal particles*’. Soft Matter **6**, p. 1182 (2010).
- [Tim70] S. P. Timoshenko and J. N. Goodier. ‘*Theory of Elasticity*’. McGraw-Hill, New York 3rd Ed. (1970).
- [Tob45] A. V. Tobolsky and R. D. Andrews. ‘*Systems Manifesting Superposed Elastic and Viscous Behavior*’. J. Chem. Phys. **13**, pp. 3–27 (1945).
- [Tob55] A. V. Tobolsky and J. R. McLoughlin. ‘*Viscoelastic Properties of Crystalline Polymers: Polytrifluorochloroethylene*’. J. Chem. Phys. **59**, pp. 989–990 (1955).
- [Tob56] A. V. Tobolsky. ‘*Stress Relaxation Studies of the Viscoelastic Properties of Polymers*’. J. Appl. Phys. **27**, pp. 673–685 (1956).

- [Ton03] C. Tong-Sheng, Z. Shao-Qun, Z. Wei, and L. Qing-Ming. ‘*A Quantitative Theory Model of a Photobleaching Mechanism*’. *Chin. Phys. Lett.* **20**, p. 1940 (2003).
- [Tor07] L. Torres, R. Iturbe, M. Snowden, B. Chowdhry, and S. Leharne. ‘*Preparation of o/w emulsions stabilized by solid particles and their characterization by oscillatory rheology*’. *Coll. Surf. A* **302**, pp. 439 – 448 (2007).
- [Tra01] V. Trappe, V. Prasad, L. Cipelletti, P. N. Segre, and D. A. Weitz. ‘*Jamming phase diagram for attractive particles*’. *Nature* **411**, pp. 772–775 (2001).
- [Tra04] V. Trappe and P. Sandkühler. ‘*Colloidal gels—low-density disordered solid-like states*’. *Curr. Op. Coll. Interf. Sci.* **8**, pp. 494 – 500 (2004).
- [Tyk07] R. Tykhoniuk, J. Tomas, S. Luding, M. Kappl, L. Heim, and H.-J. Butt. ‘*Ultrafine cohesive powders: From interparticle contacts to continuum behaviour*’. *Chem. Eng. Sci.* **62**, pp. 2843 – 2864 (2007).
- [Ull09] B. Ullrich, G. K. Auernhammer, E. M. Sam, and D. Vollmer. ‘*Tracer colloids close to an isotropic-nematic domain interface with phase transition-induced solute transport*’. *Coll. Surf. A* **354**, pp. 298–307 (2009).
- [Var01] P. Varadan and M. J. Solomon. ‘*Shear-Induced Microstructural Evolution of a Thermoreversible Colloidal Gel*’. *Langmuir* **17**, pp. 2918–2929 (2001).
- [Ver94] N. A. M. Verhaegh and A. van Blaaderen. ‘*Dispersions of Rhodamine-Labeled Silica Spheres: Synthesis, Characterization, and Fluorescence Confocal Scanning Laser Microscopy*’. *Langmuir* **10**, pp. 1427–1438 (1994).
- [Vie08] D. C. Viehman and K. S. Schweizer. ‘*Theory of gelation, vitrification, and activated barrier hopping in mixtures of hard and sticky spheres*’. *J. Chem. Phys.* **128**, p. 084509 (2008).
- [Vla01] Y. A. Vlasov, X.-Z. Bo, J. C. Sturm, and D. J. Norris. ‘*On-chip natural assembly of silicon photonic bandgap crystals*’. *Nature* **414**, pp. 289–293 (2001).
- [Vol04] D. Vollmer, G. Hinze, W. C. K. Poon, J. Cleaver, and M. E. Cates. ‘*The origin of network formation in colloid-liquid crystal composites*’. *J. Phys.: Cond. Matt.* **16**, pp. L227–L233 (2004).
- [Vol05] D. Vollmer, G. Hinze, B. Ullrich, W. Poon, M. E. Cates, and A. Schofield. ‘*Formation of Self-Supporting Reversible Cellular Networks in Suspensions of Colloids and Liquid Crystals*’. *Langmuir* **21**, pp. 4921–4930 (2005).
- [Vri76] A. Vrij. ‘*Polymers at Interfaces and the Interactions in Colloidal Dispersions*’. *Pure Appl. Chem.* **48**, pp. 471–483 (1976).
- [Wal08] A. Walther and A. H. E. Muller. ‘*Janus particles*’. *Soft Matter* **4**, pp. 663–668 (2008).
- [Wan80] C. C. Wang and R. Pecora. ‘*Time-correlation functions for restricted rotational diffusion*’. *J. Chem. Phys.* **72**, p. 5333 (1980).
- [Wee] E. Weeks. ‘*Explanation of tracking macros*’.

- [Wee00a] E. R. Weeks, J. C. Crocker, A. C. Levitt, A. Schofield, and D. A. Weitz. ‘*Three-Dimensional Direct Imaging of Structural Relaxation Near the Colloidal Glass Transition*’. *Science* **287**, pp. 627–631 (2000).
- [Wee00b] J. R. Weeks, J. S. van Duijneveldt, and B. Vincent. ‘*Formation and collapse of gels of sterically stabilized colloidal particles*’. *J. Phys.: Cond. Matt.* **12**, pp. 9599–9606 (2000).
- [Wee02] E. R. Weeks and D. A. Weitz. ‘*Subdiffusion and the cage effect studied near the colloidal glass transition*’. *Chem. Phys.* **284**, pp. 361 – 367 (2002).
- [Wes02] J. L. West, A. Glushchenko, G. Liao, Y. Reznikov, D. Andrienko, and M. P. Allen. ‘*Drag on particles in a nematic suspension by a moving nematic-isotropic interface*’. *Phys. Rev. E* **66**, p. 012702 (2002).
- [Wes90] J. L. West. ‘*Polymer-Dispersed Liquid Crystals*’ Chap. 33, pp. 475–495. Am. Chem. Soc. (1990).
- [Wil07] N. Willenbacher and C. Oelschlaeger. ‘*Dynamics and structure of complex fluids from high frequency mechanical and optical rheometry*’. *Curr. Op. Coll. Interf. Sci.* **12**, pp. 43–49 (2007).
- [Wil55] M. L. Williams, R. F. Landel, and J. D. Ferry. ‘*The Temperature Dependence of Relaxation Mechanisms in Amorphous Polymers and Other Glass-forming Liquids*’. *J. Am. Chem. Soc.* **77**, pp. 3701–3707 (1955).
- [Win97] H. H. Winter and M. Mours. ‘*Advances in Polymer Science*’ Chap. Rheology of Polymers Near Liquid-Solid Transitions, pp. 165–234. Vol. 134 Springer Berlin/Heidelberg (1997).
- [Wit83] T. A. Witten and L. M. Sander. ‘*Diffusion-limited aggregation*’. *Phys. Rev. B* **27**, pp. 5686–5697 (1983).
- [Yam86] Y. Yamamoto, H. Nakamura, and K. Okano. ‘*Apparatus for Measurement of Complex Shear Modulus of Liquid Crystals at Low Frequencies*’. *Jap. J. Appl. Phys.* **26-1**, pp. 29–31 (1986).
- [Yam90] J. Yamamoto and K. Okano. ‘*Anomalous Hydrodynamic Behaviors of Smectic Liquid Crystals at Low Frequencies*’. *Jap. J. Appl. Phys.* **30**, pp. 754–763 (1990).
- [Zac09] A. Zaccone, M. Soos, M. Lattuada, H. Wu, M. U. Bäbler, and M. Morbidelli. ‘*Breakup of dense colloidal aggregates under hydrodynamic stresses*’. *Phys. Rev. E* **79**, p. 061401 (2009).
- [Zan99] M. A. M. J. van Zandvoort, D. L. J. Vossen, G. van Ginkel, R. Torre, P. Bartolini, M. Ricci, J. Thomas-Oates, and H. Zuillhof. ‘*Spectral characterization of fluorescent 5-iodoacetamidotetramethylrhodamine and its N-acetylcysteine derivative*’. *Phys. Chem. Chem. Phys.* **1**, p. 4571E4582 (1999).
- [Zau08] J. Zausch, J. Horbach, M. Laurati, S. U. Egelhaaf, J. M. Brader, T. Voigtmann, and M. Fuchs. ‘*From Equilibrium to Steady State: The Transient Dynamics of Colloidal Liquids under Shear*’. *J. Phys.: Cond. Matt.* **20**, p. 404210 (2008).
- [Zel82] H. R. Zeller. ‘*Dielectric Relaxation and the Glass Transition in Nematic Liquid Crystals*’. *Phys. Rev. Lett.* **48**, pp. 334–337 (1982).

- [Zen06] C. Zeng, H. Bissig, and A. Dinsmore. ‘*Particles on droplets: From fundamental physics to novel materials*’. Sol. State Comm. **139**, pp. 547 – 556 (2006). Soft Condensed Matter, Soft Condensed Matter.
- [Zha09] L. Zhang, M. D’Acunzi, M. Kappl, G. K. Auernhammer, and D. Vollmer. ‘*Hollow Silica Spheres: Synthesis and Mechanical Properties*’. Langmuir **25**, pp. 2711–2717 (2009).
- [Zho03] Z. Z. Zhong, D. E. Schuele, W. L. Gordon, K. J. Adamic, and R. B. Akins. ‘*Dielectric properties of a PMMA/E7 polymer-dispersed liquid crystal*’. J. Poly Sci. B **30**, pp. 1443 – 1449 (2003).
- [Zum10] S. Zumer, M. Ravnik, T. Porenta, G. P. Alexander, and J. M. Yeomans. ‘Blue phases as templates for 3D colloidal photonic crystals’. SPIE (2010).